Polycrystalline Elasto-Viscoplasticity: Application to B.C.C. Metals

by

Manish Kothari

B.Tech., Mechanical Engineering, Indian Institute of Technology, Madras, 1992
S.M., Mechanical Engineering, Massachusetts Institute of Technology, 1995

Submitted to the Department of Mechanical Engineering
in partial fulfillment of the requirements for the degree of

Doctor of Philosophy

at the

MASSACHUSETTS INSTITUTE OF TECHNOLOGY

June 1997

Author .....
Department of Mechanical Engineering
May 9, 1997

Certified by .....
Lallit Anand
Professor
Thesis Supervisor

Accepted by .....
Ain Sonin
Chairman, Departmental Committee on Graduate Students

Polycrystalline Elasto-Viscoplasticity: Application to B.C.C. Metals

by

Manish Kothari

Submitted to the Department of Mechanical Engineering
on May 9, 1997, in partial fulfillment of the
requirements for the degree of
Doctor of Philosophy

Abstract

It has been recently established that a Taylor-type large deformation, rate-dependent crystal plasticity model can accurately predict both the evolution of the crystallographic texture and the stress-strain response of initially isotropic, as well as pre-textured polycrystalline f.c.c. materials (Kalidindi, Bronkhorst and Anand, 1992). The aim of this study has been to extend this model to polycrystalline b.c.c. materials. We shall use tantalum as the model b.c.c. material, and also evaluate the applicability of the model to iron.

A physically-motivated constitutive function based on the thermally-activated theory for plastic flow, together with appropriate hardening equations have been incorporated in a Taylor-type crystal plasticity model. This model has been implemented in a finite element code to facilitate simulations of quasi-static as well as dynamic non-homogeneous deformations of polycrystalline b.c.c. materials. We have fit available experimental data to calibrate the model for tantalum at high strain-rates and large strains.

To evaluate the accuracy of the crystal plasticity-based model, the following experiments have been performed :

1. Nominally homogenous experiments : simple compression, tension, plane-strain compression and torsion.

2. Non-homogenous experiments :

   - Quasi-static cup-drawing experiments on sheets of pure tantalum as well as a tantalum - 2.5% tungsten alloy.
   - Dynamic rod-impact experiments on pre-textured tantalum cylinders.

In all cases, the agreement between the predictions from the theory and the corresponding experimental measurements is shown to be very good.

The applicability of the constitutive equations to b.c.c iron has also been evaluated by comparing the predictions with (a) simple compression, tension and plane-strain compression experiments on iron, and (b) cup-drawing experiment on a low carbon steel sheet under quasi-static conditions.

Thesis Supervisor: Lallit Anand
Title: Professor

Acknowledgments

I would like to express my sincere thanks to all those people, whose input and advice over the past five years has been invaluable. First and foremost, I am forever indebted to my advisor and mentor, Prof. Lallit Anand, for his guidance, patience and encouragement. I am very grateful to him for his effort in helping me build a solid foundation. The various experiences at MIT has given me the confidence necessary to build a successful career and I owe this to my advisor. Thanks to Professors David Parks and Rohan Abeyaratne for serving on my committee. Discussions with them have always been very helpful and educative. I would also like to thank Dr. Vasily Bulatov and Prof. Ali Argon for the discussions on asymmetry of slip in b.c.c. crystals, and Dr. Ting at Textron Defense Systems who kindly provided us with his rod-impact specimens.

Research support for this work was provided by ARO under contract number DAAH04-A4-G-0060 and NSF under contract number DMI-9215246.

It has been a great pleasure and privilege to be a part of the Mechanics and Materials group with people who have been great friends as well as good sources of discussion, techinical and otherwise. Christine Allan, my mentor in experimental work, provided invaluable help and guidance during my early years at MIT. I would like to thank Srihari Balasubramanian for his important contributions to this thesis. I have worked very closely with him and significantly improved my computational skills Thanks to Mary Joseph who performed all the experiments on Iron. I am grateful to my colleagues Clarence Chui, Hong Dai, Brian Gally, Suryaprakash Ganti, Brian Gearing, Chunguang Gu, Michael Kim, Chuang-Chia Lin, Ronald Rezac, Alexander Staroselsky and Prakash Thamburaja for the fruitful discussions on research as well as other issues. Special thanks to Michael Kim and Oscar Yeh for their incessant enthusiasm in keeping the group alive and active.

Thanks to Ray Hardin for providing with all the information necessary to make things run smoothly. Leslie Regan and the staff of graduate office were always there for help and most of us would not get things organized as well without them. Peter, at the LNS machine shop, was very helpful with his ideas and suggestions on machining and experimental setup on many occasions.

My special thanks go to my parents, brother and sister who have always been a source of inspiration, support and encouragement.

Contents

Chapter 1

Introduction

Most of the commonly used metals today have either face-centered or a body-centered cubic crystal structure. The main differences in the plastic deformation due to crystallographic slip between the pure b.c.c. and f.c.c. crystals are the following:

- At low homologous temperatures, the rate-controlling mechanism in b.c.c. crystals for plastic flow is the thermal activation of dislocations to overcome the lattice resistance, also called the Peierls stress. In f.c.c. crystals, the rate-controlling mechanism for plastic flow is governed by the interactions with localized forest dislocations (Conrad, 1964; Kocks *et al.*, 1975).

- The slip systems in f.c.c crystals are the twelve $\{111\} < 110 >$ type. Plastic deformation in b.c.c. crystals due to crystallographic slip is found to occur in the $< 111 >$ direction, but unlike the f.c.c. materials with only one set of planes, the possible slip planes in b.c.c. materials are of the $\{110\}$, $\{112\}$, and $\{123\}$ type.

- While the slip on the $\{111\}$ planes in f.c.c. crystals is symmetric, slip on the $\{112\}$ planes in b.c.c. crystals may be asymmetric with respect to the direction of shearing. Note that the possible twin systems in b.c.c. crystals are also of the $\{112\} < 111 >$ type. Slip is found to be easier in the twinning sense on the $\{112\}$ planes rather than in the anti-twinning sense (Christian, 1970; Carpay *et al.*, 1975; Franciosi, 1983; Hull and Bacon, 1984).

The theory of finite plastic deformation due to crystallographic slip in f.c.c. materials at low homologous temperatures (< 0.3 of the melting temperature) and low strain-rates

(10^{-3} — 10^{1}/s) is now well established. This theory can accurately predict the evolving crystallographic texture, the stress-strain response and the macroscopic shape change in homogeneous as well as non-homogeneous deformations of polycrystalline f.c.c. materials (e.g., Mathur and Dawson, 1989, 1990; Kalidindi *et al.*, 1992; Bronkhorst *et al.*, 1992; Anand and Kalidindi, 1994; Beaudoin *et al.*, 1994; Balasubramanian and Anand, 1996). The three central features of these polycrystalline models are :

1. A power-law type kinetic relation for the plastic shearing rates $\dot{\gamma}^\alpha$ on the slip systems (Asaro and Needleman, 1985):

$$\dot{\gamma}^\alpha = \dot{\gamma}_0 \left| \frac{\tau^\alpha}{s^\alpha} \right|^{(1/m)} \operatorname{sign}(\tau^\alpha) \,. \tag{1.1}$$

   In the equation above, τ^α is the resolved shear stress on the slip system, and $s^\alpha (> 0)$ is the slip system deformation resistance. The parameter $\dot{\gamma}_0$ is a reference rate of shearing, and the parameter m characterizes the material rate sensitivity. The rate-independent limit is $m \to 0$. The slip system shear rate is uniquely specified by this equation, and is nonvanishing as long as the resolved shear stress τ^α on that system is not identically equal to zero.

2. The hardening rule for the slip systems:

$$\dot{s}^\alpha = \sum_\beta h^{\alpha\beta} \dot{\gamma}^\beta, \tag{1.2}$$

$$h^{\alpha\beta} = \left[q_l + (1 - q_l)\delta^{\alpha\beta} \right] h^\beta. \tag{1.3}$$

   In this equation, the matrix $h^{\alpha\beta}$ describes the rate of increase of the deformation resistance on slip system α due to shearing on slip system β. The self-hardening rate is denoted by h^β, and q_l is the latent hardening parameter.

3. A polycrystalline averaging scheme based on the classical Taylor assumption (Taylor, 1938b) : All the grains in an aggregate have equal volume and the deformation gradient is uniform throughout the aggregate. In this assumption, compatibility is satisfied and equilibrium holds in each grain, but equilibrium is usually violated between grains.

The theory of finite plastic deformation due to crystallographic slip in b.c.c. materials is less well developed. Most of the early theoretical work on studying the texture evolution in b.c.c. materials was based on the rate-independent Taylor-Bishop-Hill modeling principle (Taylor, 1938a, 1938b; Bishop and Hill, 1951a, 1951b); for example, see Chin and Mammel (1967) and Piehler and Backofen (1971). The recent work on crystal plasticity has concentrated on texture evolution in rolling, especially in b.c.c. iron and steel; see the various proceedings of ICOTOM (e.g., Lucke and Holscher, 1991; Royer *et al.*, 1991; and Wagner *et al.*, 1991). Comparisons of the predicted and the experimentally-measured rolling textures have been made, and the results seem to suggest that the Taylor-type averaging scheme is reasonably accurate for b.c.c. materials.

Finite element modeling of polycrystalline materials is a useful technique to evaluate the accuracy of Taylor and other averaging schemes. Bronkhorst *et al.* (1992) compared the stress-strain response, the crystallographic texture and the macroscopic shape change observed in their experiments on initially isotropic, annealed OFHC copper against the predictions of (1) the rate-dependent Taylor model, and (2) the finite element model where equilibrium and compatibility is satisfied. They found that the Taylor-type model was in reasonable first-order agreement with the experiments for the texture formation and also the overall stress-strain response for the high symmetry f.c.c. materials. The textures predicted by the Taylor model was found to be sharper than the experiments, a feature they did not observe in their finite element calculations. The first such attempt in evaluating the accuracy of the Taylor-assumption in b.c.c. materials is by Dawson *et al.* (1994). They performed plane-strain compression calculations using the rate-dependent Taylor and the finite element model. Qualitative comparisons between the two models indicated that the Taylor assumption gave sharper textures. However, no experiments were performed. Clearly there is a need for a complete set of experimental data on stress-strain response and texture evolution in b.c.c. materials similar to that obtained by Bronkhorst *et al.* (1992) which can be used to evaluate the accuracy of crystal plasticity-based models.

There are numerous situations where materials are subjected to dynamic loading (Meyers, 1994). Understanding the anisotropic response of the material in these situations is of considerable interest. One such example is that of explosively formed penetrators (EFPs). The material obtained in the form of a plate or a circular disc is first formed into saucer, hemispherical and conical shaped warhead liners. These warhead liners are

then explosively formed into long rod-shaped penetrators as they are accelerated towards the target. In this operation, strain-rates are of the order of 10^5sec^{-1} and strains can get to be of the order of $300 - 500\%$. Tantalum, a b.c.c. metal, because of its high density $\rho = 16.6 \text{Mg/m}^3$ and high ductility is currently of interest to the Army as a possible liner material for explosively formed penetrators (EFPs).

Some other examples of b.c.c. materials are iron, tungsten, niobium and molybdenum. Although these metals have a b.c.c. crystal lattice, significant differences exist in their plastic behavior. At a nominal strain-rate of $\approx 10^{-4} \, \text{sec}^{-1}$, the temperature above which the lattice resistance is completely overcome by thermal activation is around $400°K$ for iron (Leslie, 1972) and around $800°K$ for tantalum (Hoge and Mukherjee, 1977). At high strain-rates and low temperatures, twinning is also a major contributor to plastic deformation in iron, while in tantalum the contribution of twinning to plastic deformation is found to be neglibile (Bolling and Richman, 1965; Mitchell and Spitzig, 1965; Reid, 1981; Qiang, 1993). Iron shows a transition from brittle to ductile fracture at a temperature of $-150°C$, while tantalum is found to be ductile at temperatures down to $-195°C$ (Bechtold, 1955). The ductility of tantalum at low temperatures is associated with the absence of mechanical twinning. In this work we model the plastic deformation of b.c.c. materials due to crystallographic slip alone. For some recent work on modeling of plastic deformation due to both crystallographic slip and twinning, see Staroselsky and Anand (1997). Tantalum is the model b.c.c. material in this work. We shall also evaluate the applicability of our constitutive model to the important b.c.c. metal iron.

Although there has been considerable work in modeling the dynamic behavior of tantalum based on the classical isotropic models for viscoplasticity (e.g., Hoge and Mukherjee, 1977; Zerilli and Armstrong, 1990; Meyers *et al*, 1995; Nemat-Nasser and Isaacs, 1996; and Chen and Gray, 1996), no crystal-plasticity based model for the high-rate deformation of b.c.c. materials has been previously reported. The simple power-law description (equation 1.1) used previously in the crystal plasticity models is a useful simplification of the viscoplastic response of crystals in a narrow range of strain-rates and temperatures. However, as we shall see, it cannot capture the real strain-rate and temperature sensitivity of flow of tantalum under dynamic loading conditions. There is a need for an improved kinetic equation for the plastic shearing rates, and we shall address this issue in this work.

The temperature and rate-sensitivity of the flow stress of tantalum has been widely studied by performing quasi-static and high-rate experiments between a wide range of temperatures. Some of the earlier experiments on tantalum is by Bechtold (1955) who studied the temperature dependence of the flow stress of tantalum. Hoge and Mukherjee (1977) were the first to characterize the temperature and strain-rate dependence of the flow stress of tantalum for a wide range of temperatures (between 78 to $800°K$) and strain rates (from 10^{-5} to $2 \times 10^4\,\mathrm{sec}^{-1}$). In their experiments, they found that tantalum exhibited a high temperature-sensitivity but a moderate rate-sensitivity of plastic flow. They postulated that the rate-controlling mechanism for plastic flow in tantalum is governed by the thermal activation of dislocations past Peierls-Nabarro barriers and a viscous drag mechanism, viewing the latter mechanism as rate-controlling at strain-rates above $10^3\,\mathrm{sec}^{-1}$. In view of the importance of strain-rates of $10^5\,\mathrm{sec}^{-1}$ and higher in applications such as EFPs, and the possibility of the change in the rate-controlling mechanism of plastic deformation in this regime, Duprey and Clifton (1995) carried out pressure-shear plate impact experiments on tantalum foil. In their experiments, they did not find the *linear* increase in flow stress with increasing strain-rate, as predicted by the viscous drag mechanism and concluded that thermal activation of dislocations past Peierls-Nabarro barriers is the rate-controlling mechanism at strain-rates of the order of $10^6\,\mathrm{sec}^{-1}$.

The strain-hardening behavior of tantalum at various strain-rates and temperatures has also been previousy studied. Gray and Rollet (1992) and Rajendran and Garrett (1992) measured the dynamic stress-strain response of tantalum up to strain-rates of $10^3\,\mathrm{sec}^{-1}$, but the strains were limited to less than 30%. Tantalum in EFP's must undergo extensive plastic deformation (strains of the order of 500%) at strain-rates of $10^5\,\mathrm{sec}^{-1}$. Since most high strain-rate research on tantalum had previously focused on low strains, Vecchio (1994) measured the stress-strain response of tantalum up to strain-rates of the order of $10^4\,\mathrm{sec}^{-1}$ and a final strain of the order of 60%. The high strain-rate tests to large strains showed pronounced thermal softening associated with the temperature rise due to adiabatic heating. Based on a technique developed by Nemat-Nasser *et al.* (1994), Meyers *et al.* (1995) and Nemat-Nasser and Isaacs (1996) measured the isothermal stress-strain response of tantalum at high rates, large strains and at elevated temperatures. The isothermal stress-strain curves showed the hardening that is masked by thermal softening.

With this as background, the following has been accomplished in this thesis:

1. A physically-motivated constitutive function based on thermally-activated theory for plastic flow, together with the hardening equations are presented in Chapter 2. These constitutive equations have been incorporated in a Taylor-type crystal plasticity model which has been implemented in the finite element codes ABAQUS/Standard and ABAQUS/Explicit to facilitate simulations of quasi-static as well as dynamic non-homogeneous deformations of polycrystalline b.c.c. materials.

2. In chapter 3, the slip systems to be used in the crystal plasticity calculations for the b.c.c. metals are identified. We begin first by evaluating the accuracy of the Taylor assumption by comparing the predicted plane-strain compression textures against those predicted by the finite element method with different choices for the operative slip systems. In these simulations the initial texture was chosen to be random and the material was modeled as non-hardening. These calculations show that the Taylor model is reasonably accurate for the texture formation and the stress-strain response for b.c.c. metals. Next, Taylor model plane-strain compression simulations are performed on a pre-textured tantalum with the different assumptions for the number of slip systems, and the predicted textures are compared with the experimentally-measured texture to determine the operative slip systems. These comparisons show that that the textures predicted with the 24 slip systems, twelve $\{110\} < 111 >$ and twelve $\{112\} < 111 >$, are in reasonable agreement with the experiment. Therefore, we use these 24 slip systems for the crystal plasticity calculations on b.c.c. metals in this work.

3. In chapter 4, we demonstrate the ability of the crystal plasticity-based model to reproduce the recently-published stress-strain response of b.c.c. tantalum for strains up to 60%, at strain-rates from quasi-static to $30{,}000\,s^{-1}$, and temperatures from -200 to 525°C (Hoge and Mukherjee, 1977; Vecchio, 1994; Meyers *et al.*, 1995; Nemat-Nasser and Isaacs, 1996).

4. In chapter 5, we evaluate the accuracy of the Taylor-type crystal plasticity model for tantalum by comparing the predictions of the evolution of crystallographic texture and the corresponding stress-strain curves in nominally homogeneous simple-compression, tension, plane-strain compression, and torsion experiments under quasi-static conditions at room temperature.

5. In chapter 6, we evaluate the accuracy of the crystal plasticity model for tantalum undergoing non-homogeneous quasi-static, as well as dynamic deformations. (i) Quasi-static cup-drawing experiments have been performed on sheets of pure tantalum as well as a tantalum - 2.5% tungsten alloy with different initial textures. The predictions of the resulting ear heights and location, as well as the load-displacement response have been compared against the experimental measurements. (ii) Numerical simulations of the dynamic Taylor-rod impact experiments of Ting (1992) on pre-textured tantalum cylinders have also been performed and the measurements of the deformed shape, including the ovalized macroscopic shape of the impact end of the cylinders are compared against the predictions. The model is shown to reasonably accurately predict the results from both the cup-drawing and the rod-impact experiments.

6. Finally, the applicability of the constitutive model to b.c.c iron is evaluated by (a) comparing the predictions against the measurements of texture evolution and the stress-strain response in simple-compression, simple tension, and plane-strain compression experiments under quasi-static conditions, and (b) comparing the simulations of cup-drawing against corresponding experiments on a low-carbon steel sheet. These results are presented in Chapter 7.

The conclusions are summarized in Chapter 8, where some suggestions for future research are also presented.

Chapter 2

Constitutive Model

We use the following notation: $\mathbf{F}$, deformation gradient; $\mathbf{L}$, velocity gradient; $\mathbf{T}$, Cauchy stress. Also, the inner product of two vectors $\mathbf{u}$ and $\mathbf{v}$ will be denoted by $\mathbf{u} \cdot \mathbf{v}$. The tensor product of two vectors $\mathbf{u}$ and $\mathbf{v}$ will be denoted by $\mathbf{u} \otimes \mathbf{v}$; it is the tensor which assigns to each vector $\mathbf{w}$ the vector $(\mathbf{v} \cdot \mathbf{w})\, \mathbf{u}$. The inner product of two (second rank) tensors $\mathbf{S}$ and $\mathbf{T}$ is defined by $\mathbf{S} \cdot \mathbf{T} = \text{trace}\left(\mathbf{S}^T \mathbf{T}\right)$.

The foundations of the constitutive model for single crystal elasto-plasticity considered here may be traced to the papers by Teodosiu [1970], Rice [1971], Hill and Rice [1972], Mandel [1974], Teodosiu and Sidoroff [1976], Asaro and Rice [1977] and Asaro [1983b, 1983a] from a continuum mechanics viewpoint, and Conrad [1964], Kocks *et al.* [1975], Frost and Ashby [1982], and Argon [1995] from a materials science viewpoint.

The governing variables in the constitutive model are: (*i*) The Cauchy stress, $\mathbf{T}$. (*ii*) The deformation gradient, $\mathbf{F}$. (*iii*) The absolute temperature, θ. (*iv*) Crystal slip systems, labeled by integers α. Each slip system is specified by a unit normal $\mathbf{n}_o^\alpha$ to the slip plane, and a unit vector $\mathbf{m}_o^\alpha$ denoting the slip direction. The slip systems $(\mathbf{m}_o^\alpha, \mathbf{n}_o^\alpha)$ are assumed to be known in the reference configuration. (*iv*) A plastic deformation gradient, $\mathbf{F}^p$, with $\det \mathbf{F}^p = 1$. (*v*) The slip system deformation resistance $s^\alpha > 0$, with units of stress.

We define an elastic deformation gradient by

$$\mathbf{F}^e \equiv \mathbf{F}\, \mathbf{F}^{p-1}, \qquad \det \mathbf{F}^e > 0. \tag{2.1}$$

This equation may be rearranged as $\mathbf{F} = \mathbf{F}^e\, \mathbf{F}^p$. The plastic part $\mathbf{F}^p$ in this multiplicative decomposition of $\mathbf{F}$ represents the cumulative effect of dislocation motion on the active slip

systems in the crystal, and the elastic part $\mathbf{F}^e$ describes the elastic distortion of the lattice.

Next, with $\bar{\mathbf{S}} = (\det \mathbf{F})\mathbf{T}\mathbf{F}^{-T}$ denoting the first Piola-Kirchoff stress, the stress power per unit reference volume is $\dot{\omega} = \bar{\mathbf{S}} \cdot \dot{\mathbf{F}}$, which, since $\det \mathbf{F}^p = 1$, is also equal to the stress power per unit volume of the isoclinic relaxed configuration. This stress power may be additively decomposed as $\dot{\omega} = \dot{\omega}^e + \dot{\omega}^p$, where $\dot{\omega}^e = \mathbf{T}^* \cdot \dot{\mathbf{E}}^e$ is the elastic stress power per unit volume of the relaxed configuration, with

$$\mathbf{E}^e \equiv (1/2)\left\{\mathbf{F}^{eT}\mathbf{F}^e - 1\right\} \quad \text{and} \quad \mathbf{T}^* \equiv (\det \mathbf{F}^e)\, \mathbf{F}^{e-1}\mathbf{T}\mathbf{F}^{e-T} \tag{2.2}$$

the Green elastic strain measure and the symmetric second Piola-Kirchoff stress tensor relative to the relaxed configuration, respectively, and

$$\dot{\omega}^p = (\mathbf{C}^e\, \mathbf{T}^*) \cdot \left(\dot{\mathbf{F}}^p\, \mathbf{F}^{p-1}\right), \qquad \mathbf{C}^e \equiv \mathbf{F}^{eT}\mathbf{F}^e, \tag{2.3}$$

is the plastic stress power per unit volume of the relaxed configuration.

Constitutive Equation For Stress:

Elastic stretches in metallic single crystals are generally small. Temperature changes need not be small, but for simplicity of presentation we restrict our attention here to small temperature changes about a reference temperature θ_0. Accordingly, the constitutive equation for the stress in a metallic single crystal is taken as the linear relation

$$\mathbf{T}^* = \boldsymbol{\mathcal{C}}\left[\mathbf{E}^e - \mathbf{A}\ (\theta - \theta_0)\right], \tag{2.4}$$

where $\boldsymbol{\mathcal{C}}$ is a fourth-order anisotropic elasticity tensor, and $\mathbf{A}$ is a second-order anisotropic thermal expansion tensor. Also, $\mathbf{E}^e$ and $\mathbf{T}^*$ are the strain and stress measures defined in equation (2.2).

Flow Rule:

The evolution of the plastic deformation gradient is given by

$$\dot{\mathbf{F}}^p\mathbf{F}^{p-1} = \sum_\alpha \dot{\gamma}^\alpha\, \mathbf{S}_0^\alpha, \qquad \mathbf{S}_0^\alpha \equiv \mathbf{m}_0^\alpha \otimes \mathbf{n}_0^\alpha, \tag{2.5}$$

where $\mathbf{S}_0^\alpha$ is the Schmid tensor, and

$$\dot{\gamma}^\alpha = \rho_m^\alpha\, b\, \bar{v}^\alpha \tag{2.6}$$

is the plastic shearing rate on the α-th slip system. The expression $\dot{\gamma} = \rho_m\, b\, \bar{v}$ is due to Orowan [1940], and it represents the physical picture that the strain rate $\dot{\gamma}$ is produced by a density ρ_m of mobile dislocations with Burgers vector magnitude b (in the slip direction $\mathbf{m}_0$), moving with an average velocity $\bar{v}$ through a field of obstacles.

Using (2.5) and (2.3), we define a *resolved shear stress* τ^α for the slip system α through the relation $\dot{\omega}^p = \sum_\alpha \tau^\alpha \dot{\gamma}^\alpha$, which yields

$$\tau^\alpha \equiv (\mathbf{C}^e\, \mathbf{T}^*) \cdot \mathbf{S}_0^\alpha. \tag{2.7}$$

With the resolved shear stress so defined, the average dislocation velocity on the slip system α is taken to be governed by a constitutive function,

$$\bar{v}^\alpha = \hat{\bar{v}}^\alpha\,(\tau^\alpha, \theta, s^\alpha)\,, \tag{2.8}$$

where

$$s^\alpha = \hat{s}^\alpha(\theta, \text{microstructural state}) > 0$$

is a temperature dependent *critical slip resistance* (units of stress) for the slip system α. The average dislocation velocity $\bar{v}^\alpha$ at applied shear stress τ^α and a temperature θ depends on the waiting time of mobile dislocations at obstacles, and s^α reflects the strength, density and arrangement of these obstacles. Whenever convenient, we will simply write $\hat{s}^\alpha(\theta)$ for the function $\hat{s}^\alpha(\theta, \text{microstructural state})$.

The constitutive equation for the average dislocation velocity is formulated as follows. At a temperature of absolute zero let $\hat{s}^\alpha(0)$ denote the critical slip resistance; then the sign of $\bar{v}^\alpha$ is the same as that of the resolved shear stress τ^α, and its magnitude is idealized as

$$|\bar{v}^\alpha| = \left\{ \begin{array}{lll} 0 & & \text{if } |\tau^\alpha| < \hat{s}^\alpha(0), \\ > 0 \quad \text{(and large)} & & \text{if } |\tau^\alpha| = \hat{s}^\alpha(0), \end{array} \right\} \tag{2.9}$$

with stress levels $|\tau^\alpha| > \hat{s}^\alpha(0)$ unattainable. The slip resistance $\hat{s}^\alpha(0)$ at absolute zero is called the *mechanical threshold* (Kocks *et al.* [1975]; Argon [1995]). Because of the usual variability of the microstructural state of real materials the transition from no dislocation velocity to a high velocity will not be as sharp as idealized in equation (2.9), but it should still exhibit a "threshold" behavior. At a temperature $\theta > 0$ this response is modified in

two important ways. First, since the underlying mechanism which governs the magnitude of s^α is an elastic interaction on the atomic scale of a mobile dislocation segment with the microstructural state, an increase in temperature results in a decrease in the magnitude of s^α, primarily due to the attendant decrease in the elastic moduli, that is $\hat{s}^\alpha(\theta) < \hat{s}^\alpha(0)$. Second, and more importantly, with increasing temperature the local energy barriers to dislocation motion due to *short-range* obstacles (less than $\approx$10 atomic diameters) can be overcome at a lower applied shear stress with the help of thermal fluctuations, and a finite dislocation velocity should be observable below the slip resistance s^α. Accordingly, it is useful to distinguish between barriers that can be overcome with the aid of thermal fluctuations, and those that cannot — *thermal* and *athermal*, respectively; and to assume that the slip resistance s^α is decomposable as

$$s^\alpha = s^\alpha_*(\theta, \text{microstructural state}) + s^\alpha_a(\theta, \text{microstructural state}), \tag{2.10}$$

where s^α_* represents the part of the resistance due to thermally-activatable obstacles to slip, and s^α_a the part of the resistance due to the athermal obstacles to slip. Typical examples of athermal barriers are dislocation groups and large incoherent precipitates, whereas the Peierls resistance, solute atoms, and forest dislocations typify thermally-activatable barriers. In pure f.c.c. and h.c.p. materials the dislocations glide easily without any appreciable Peierls resistance, and s^α_* is governed by interactions with localized forest dislocations. In pure b.c.c. and diamond-cubic crystals, and in oxides and carbides, s^α_* is controlled by the interactions with the Peierls resistance which increases rapidly with decreasing temperature.

Let

$$\tau^\alpha_* \equiv |\tau^\alpha| - s^\alpha_a \tag{2.11}$$

denote an *effective stress*, then equation (2.8) is modified as

$$\bar{v}^\alpha = \hat{\bar{v}}^\alpha\left(\tau^\alpha_*, \theta, s^\alpha_*\right), \tag{2.12}$$

and we recognize that at temperatures $\theta > 0$ the motion of the mobile dislocation segments is thermally activated. Using the framework of transition-state theory (e.g. Krausz and Eyring [1975]), with ΔG^α_* denoting the difference in the free enthalpy between the saddle point and the ground point for a shear increment, the quantity $\left[\exp\left\{-\frac{\Delta G^\alpha_*}{k_B\theta}\right\}\right]$ is the

probability that a thermal fluctuation of the required energy (or larger) for a shear increment can be supplied at a temperature $\theta > 0$. ΔG_*^α is called the *activation free enthalpy* or the *Gibb's free energy for activation*, and k_B is the Boltzmann's constant. The rate at which dislocations overcome the obstacles is given by $\nu \left[\exp\left\{-\frac{\Delta G_*^\alpha}{k_B \theta}\right\}\right]$, where ν is a characteristic frequency factor of the order of 10^{12}sec^{-1} (10^{-2} - 10^{-1} times the Debye frequency of atoms). Then, with $\bar{l}^\alpha$ denoting the mean distance of advance of a mobile dislocation segment, the magnitude of the average dislocation velocity may be written as

$$|\bar{v}^\alpha| = \left\{ \begin{array}{ll} 0 & \text{if } \tau_*^\alpha \leq 0, \\ \bar{l}^\alpha \, \nu \, \exp\left\{-\frac{\Delta G_*^\alpha(\tau_*^\alpha, s_*^\alpha)}{k_B \theta}\right\} & \text{if } 0 < \tau_*^\alpha < s_*^\alpha, \end{array} \right\} \tag{2.13}$$

using which, the shearing rates may be written as

$$\dot{\gamma}^\alpha = \left\{ \begin{array}{ll} 0 & \text{if } \tau_*^\alpha \leq 0, \\ \dot{\gamma}_0^\alpha \exp\left\{-\frac{\Delta G_*^\alpha(\tau_*^\alpha, s_*^\alpha)}{k_B \theta}\right\} \text{sign}(\tau^\alpha) & \text{if } 0 < \tau_*^\alpha < s_*^\alpha, \end{array} \right\}, \tag{2.14}$$

with

$$\dot{\gamma}_0^\alpha = \rho_m^\alpha \, b \, \bar{l}^\alpha \, \nu.$$

Henceforth, for simplicity, we take the pre-exponential term $\dot{\gamma}_0^\alpha$ to be the same for all slip systems, and denote it by $\dot{\gamma}_0$. This pre-exponential term has a typical magnitude of $\dot{\gamma}_0 \approx 10^6$ to 10^7sec^{-1}. Also, the mobile dislocation density, which contributes to $\dot{\gamma}_0$, is expected to be a function of the applied stress and the temperature (Kocks *et al.* [1975]), but we neglect any such dependence here.

The considerations of Kocks *et al.* [1975] (also see Frost and Ashby [1982]) concerning the nature of the activation free enthalpy suggest that ΔG_*^α may be expressed as

$$\Delta G_*^\alpha = \Delta F_* \left[1 - \left(\frac{\tau_*^\alpha}{s_*^\alpha}\right)^p\right]^q, \tag{2.15}$$

where ΔF_*, the activation free energy required to overcome the obstacles to slip without the aid of an applied shear stress, is taken to be the same for all slip systems and is expected to remain constant provided the character of the obstacles does not change. ΔF_* typically lies in the range

$$0.05 \leq \frac{\Delta F_*}{\mu b^3} \leq 2, \tag{2.16}$$

with μ denoting an appropriate shear modulus for anisotropic materials; for example, $\mu \approx C_{44}$ for a b.c.c. material, where (C_{11}, C_{12}, C_{44}) are the elastic moduli for a cubic crystal. The quantities p and q are suggested to lie in the ranges

$$0 \leq p \leq 1, \quad \text{and} \quad 1 \leq q \leq 2, \tag{2.17}$$

and they control the shape of the ΔG_*^α versus $\left(\frac{\tau_*^\alpha}{s_*^\alpha}\right)$ curve.

Note that for the case of non-zero plastic shearing rates we may write

$$|\tau^\alpha| = s_a^\alpha + Z\left(\theta, |\dot{\gamma}^\alpha|\right) s_*^\alpha, \tag{2.18}$$

where

$$Z = \left[1 - \left(\frac{\theta}{\theta_c}\right)^{1/q}\right]^{1/p} \leq 1, \quad \text{with} \quad \theta_c = \left\{\frac{\Delta F_*}{k_B \ln\left(\frac{\dot{\gamma}_0}{|\dot{\gamma}^\alpha|}\right)}\right\}. \tag{2.19}$$

These equations show the temperature and strain rate sensitivity of resolved shear stress at a *fixed* value of the deformation resistance $s^\alpha = s_*^\alpha + s_a^\alpha$. At $\theta = 0$ the parameter $Z = 1$, and at $\theta = \theta_c$ we have $Z = 0$. That is, at temperatures above θ_c there is enough thermal energy for the barriers to be overcome by thermal activation alone, without the aid of a stress. At a given strain rate $\dot{\gamma}^\alpha$, the temperature θ_c sets the limit of applicability of the thermal-activation model for the plastic flow of metals at low homologous temperatures.

Evolution Equations For Slip System Resistances:

In crystal plasticity theories, the slip system resistance parameters s^α are taken to evolve according to

$$\dot{s}^\alpha = \sum_\beta h^{\alpha\beta} \left|\dot{\gamma}^\beta\right|,$$

where $\dot{\gamma}^\beta$ is the shearing rate on slip system β, and the matrix $h^{\alpha\beta}$ describes the rate of increase of the deformation resistance on slip system α due to shearing on slip system β; it describes both self-hardening and latent hardening of the slip systems. The use of the absolute value of $\dot{\gamma}^\beta$ in the hardening equation reflects the assumption that the hardening behavior is not significantly affected by the direction of shearing on a slip system. Each element $h^{\alpha\beta}$ depends on the deformation history.

Since we have decomposed s^α as

$$s^\alpha = s^\alpha_*(\theta, \text{microstructural state}) + s^\alpha_a(\theta, \text{microstructural state}),$$

it is important to distinguish whether the source of macroscopic strain hardening is due to the change of s^α_* or s^α_a, or both. For pure b.c.c. materials, since s^α_* is controlled by the interactions with the Peierls lattice resistance, it is reasonable to assume that

$$s^\alpha_* \approx s_* \equiv \text{constant}, \tag{2.20}$$

and

$$\dot{s}^\alpha \doteq \dot{s}^\alpha_a = \sum_\beta h^{\alpha\beta} \left|\dot{\gamma}^\beta\right|. \tag{2.21}$$

Several simple phenomenological forms for the hardening matrix have been proposed in the past; these have been reviewed by Peirce *et al.* [1982], and more recently by Havner [1992], and Bassani [1993]. In their numerical calculations Peirce *et al.* [1982] (also see Asaro and Needleman [1985]) used the following simple form for the hardening moduli:

$$h^{\alpha\beta} = \left[q_l + (1 - q_l)\delta^{\alpha\beta}\right] h^\beta, \tag{2.22}$$

with h^β denoting the self-hardening rate and the parameter q_l representing a latent-hardening parameter. The latent hardening parameter q_l is not necessarily a constant, and may of course be history-dependent just as the self-hardening parameter h^β is. This simple form for $h^{\alpha\beta}$ yields an acceptable description of the physical phenomena of latent hardening, and we adopt it here without modification.

Our eventual goal in this study is to formulate constitutive equations for polycrystalline ductile metals undergoing complex deformations encountered in dynamic metal-forming operations. Thus we do not focus on the typical fine-scale description of hardening (Stage I, Stage II, etc.) during single slip of single crystals; instead, motivated by the work of Brown *et al.* [1989]), we adopt the following specific form:

$$h^\beta = h^\beta_0 \left|1 - \frac{s^\beta_a}{s^\beta_{a,s}}\right|^r \text{sign}\left(1 - \frac{s^\beta_a}{s^\beta_{a,s}}\right), \tag{2.23}$$

where

$$h_0^\beta = \hat{h}_0^\beta \left(\left| \dot{\gamma}^\beta \right|, \theta \right) \tag{2.24}$$

is the initial hardening rate, and

$$s_{a,s}^\beta = \hat{s}_{a,s}^\beta \left(\left| \dot{\gamma}^\beta \right|, \theta \right) \tag{2.25}$$

is a saturation value of s_a^β. Our notation indicates that both h_0^β and $s_{a,s}^\beta$ are in general expected to be strain rate- and temperature-dependent.

For polycrystalline materials we adopt the Taylor assumption (Taylor [1938b, 1938a]), according to which the local deformation gradient in each grain is homogeneous and identical to the macroscopic deformation gradient at the continuum material point level. For such a model, straight-forward considerations (Asaro and Needleman [1985]) show that with $\mathbf{T}^{(k)}$ denoting the constant Cauchy stress in each grain, the volume-averaged Cauchy stress is given by

$$\bar{\mathbf{T}} = \sum_{k=1}^{N} v^{(k)} \mathbf{T}^{(k)}, \tag{2.26}$$

where $v^{(k)}$ is the volume fraction of each grain in a representative volume element. When all grains are assumed to be of equal volume, the stress $\bar{\mathbf{T}}$ is just the number average over all the grains:

$$\bar{\mathbf{T}} = \frac{1}{N} \sum_{k=1}^{N} \mathbf{T}^{(k)}. \tag{2.27}$$

The accuracy of such an approximate Taylor-type polycrystal constitutive model (with a simple power-law type of flow rule) has been previously evaluated by Bronkhorst *et al.* [1992]. Their experiments and calculations showed that the Taylor-type model is in reasonable agreement with experiments for the texture formation and also with the overall stress-strain response of single-phase f.c.c materials. We expect the Taylor-type polycrystal model to also be reasonably accurate for b.c.c. tantalum which possesses numerous slip systems. This will be verified in Chapter 5.

The constitutive model has been implemented in a finite element program ABAQUS [1994], which contains capabilities for both "static, implicit," and " dynamic, explicit" solution procedures. Our implementation is at present limited to the isothermal case for ABAQUS/Standard, and the isothermal or completely adiabatic case for

ABAQUS/Explicit. For the adiabatic case the temperature rise is calculated using

$$\rho c \dot{\theta} = \xi \sum_{k=1}^{N} v^{(k)} \left(\sum_{\alpha} \tau^{\alpha} \dot{\gamma}^{\alpha} \right)^{(k)} . \tag{2.28}$$

Here, the first sum is over all slip systems in a grain, and the second sum is over all grains in a polycrystalline aggregate comprising a material point. Also, $\rho = \hat{\rho}(\theta)$ denotes the mass density, $c = \hat{c}(\theta)$ the specific heat, and $0.85 \leq \xi \leq 1$ denotes the fraction of plastic work converted to heat.

In the next chapter we determine the number of slip systems to be be used in the Taylor-type simulations of b.c.c. tantalum.

Chapter 3

Identification of the Slip Systems in B.C.C. Crystals

A widely discussed issue in the plastic deformation of b.c.c. crystals due to crystallographic glide is the identification of the operative slip systems. For a summary on this topic, see Havner (1992). Slip in b.c.c. crystals occurs in the close-packed direction $< 111 >$. However, there is no close-packed plane in b.c.c. crystals. The macroscopic slip traces observed from the experiments on b.c.c. single crystals are interpreted as composed of elementary translations on the {110}, {112} and {123} planes (Hull and Bacon [1984]).

It has also been found from experiments on b.c.c. single crystals that the slip on the {112} planes may be asymmetric with respect to the $< 111 >$ direction of shearing (e.g., Christian [1970]; Carpay *et al.* [1975]; Franciosi [1983]). Twinning in b.c.c. crystals also occurs on the {112} planes and in the $< 111 >$ directions. Fig. 3-1 shows the stacking sequence of {112} planes in a b.c.c. crystal (Hull and Bacon [1984]). From the atom positions in Fig. 3-1, it is clear that a $\frac{1}{6} < 111 >$ translation which displaces E to C, F to D, etc., produces a different result from a $\frac{1}{6} < 111 >$ translation in the opposite sense. The latter translation which moves E to D, etc., produces a structure of high energy. Therefore, there is a potential asymmetry of slip resistance with respect to $< 111 >$ translations on the {112} planes. Atomistic calculations of the core structure of screw dislocations and their mobility in b.c.c. crystals performed by Vitek and co-workers (Duesbery *et al.* [1973]; Vitek [1976]) also confirm the possibility of asymmetry of slip on the {112} planes.

Numerical simulations have been carried out by Chin [1972] to study the relative

competition among the {110}, {112} and {123} slip modes and their effect on the evolution of texture in b.c.c. crystals. Van Houtte [1978] peformed plane strain compression simulations on a random aggregate of a polycrystalline b.c.c. metal by considering crystallographic slip on the {110} and {112} planes in the {111} direction and studied the effect of the asymmetry of slip of the $\{112\} < 111 >$ slip systems on the resulting rolling textures. Referring to the slip resistance on the {112} planes in the *soft* direction as $s_0^{\{112\}s}$, and in the *hard* direction as $s_0^{\{112\}h}$, we define two ratios :

$$\alpha_s = \frac{s_0^{\{112\}s}}{s_0^{\{110\}}} \quad \text{and} \quad \alpha_h = \frac{s_0^{\{112\}h}}{s_0^{\{110\}}}; \quad \alpha_s \leq \alpha_h, \tag{3.1}$$

where $s_0^{\{110\}}$ denotes the slip resistance on the {110} planes. Van Houtte performed numerical simulations for different values of α_s and α_h in the framework of a rigid perfectly-plastic, rate-independent theory based on the Taylor-assumption. In his parameteric study, he found that different values of α_s and α_h influenced the predicted rolling textures in b.c.c. metals. However, no comparison was made against experiments to justify the different values of α_s and α_h used in thc simulations.

Dawson *et al.* [1994] performed plane strain compression simulations on a polycrystalline b.c.c. material using the Taylor and the finite element model (FEM) to study the influence of the choice of slip systems. Comparisons between the predicted textures for the Taylor and the FEM model between the simulation with 12 and 48 slip systems showed that the availibility of large number of slip systems slows the rate of texture evolution. The overall texture as well as the specific texture components were found to be the same with 12 and 48 slip systems.

In this chapter, we first evaluate the accuracy of the Taylor assumption for b.c.c. metals, and then identify the operative slip systems for tantalum. In both instances, we focus on the results of plane-strain compression simulations.

3.1 Evaluation of the Accuracy of Taylor Assumption

Plane-strain compression simulations was performed on a random aggregate of 343 polycrystalline grains using the Finite Element Model (Bronkhorst *et al.* [1992]) and the Taylor model for different choices of operative slip systems. Since the flow parameters in our

kinetic equation (2.14) for the plastic shearing rates are yet to be determined, we use the simple power-law relation for the plastic shearing rates, equation (1.1). The deformation was modeled to be perfectly-plastic. The flow parameters used are the following:

$$\dot{\gamma}_0 = 1.0 \times 10^{-3}\,\mathrm{sec}^{-1},\ m = 0.024,\ s_0 = 50\mathrm{MPa}. \tag{3.2}$$

The simulations were carried out for each of the following cases (see Table 3.1) :

(a) 12 symmetric slip systems : 12 $\{110\} < 111 >$,

(b) 24 symmetric slip systems : 12 $\{110\} < 111 >$ and 12 $\{112\} < 111 >$,

(c) 36 slip systems : 12 $\{110\} < 111 >$, 12 $\{112\} < 111 > s$, and 12 $\{112\} < 111 > h$, and

(d) 48 symmetric slip systems : 12 $\{110\} < 111 >$, 12 $\{112\} < 111 >$ and 24 $\{123\} < 111 >$.

The slip systems for which we do not distinguish between the positive and negative directions of slip on the slip plane are referred to as symmetric slip systems. The slip systems with asymmetric slip on the $\{112\}$ planes are distinguished by $\{112\}s$ for the soft slip directions of slip, and those with the hard slip directions are denoted by $\{112\}h$.

The initial value of the slip system resistance s_0 is assumed to be the same on all the slip systems for the simulations with 12, 24 and 48 slip systems. Henceforth, we shall refer to these cases by (12), (24) and (48), respectively. In the simulations with 36 slip systems, we distinguish between the positive and negative directions of slip. Carpay *et al.* [1975] have performed tension experiments on single crystals of b.c.c. molybdenum and measured the slip resistances on the $\{112\}$ planes. They estimate that

$$\frac{s_0^{\{112\}h}}{s_0^{\{110\}}} \approx 1.0, \quad \frac{s_0^{\{112\}s}}{s_0^{\{110\}}} \approx 0.77.$$

For single crystals of b.c.c. iron, Franciosi [1983] estimates

$$\frac{s_0^{\{112\}h}}{s_0^{\{110\}}} \approx 1.14, \quad \frac{s_0^{\{112\}s}}{s_0^{\{110\}}} \approx 1.04.$$

Motivated by these results, the simulations with 36 slip systems are performed for the following two sets of flow parameters :

$$s_0^{\{110\}} = 50\mathrm{MPa},\ \frac{s_0^{\{112\}h}}{s_0^{\{110\}}} = 1 \text{ and } \frac{s_0^{\{112\}s}}{s_0^{\{110\}}} = 0.77, \tag{3.3}$$

and

$$s_0^{\{110\}} = 50\text{MPa}, \ \frac{s_0^{\{112\}h}}{s_0^{\{110\}}} = 1.15 \text{ and } \frac{s_0^{\{112\}s}}{s_0^{\{110\}}} = 1.0, \tag{3.4}$$

We shall refer to the simulations with the 36 slip systems for the two cases as (36a) and (36b), respectively.

The plane-strain compression simulations with the FEM model are performed using ABAQUS/Standard. The mesh consists of 343 (= 7^3) ABAQUS-C3D8 elements, Fig. 3-2(a). Each element represents a single crystal and is assigned a orientation which is chosen randomly from a set of 343 grains whose pole figures are shown in Fig. 3-3. The compression, constraint, and the free directions in the simulations are denoted by 3, 1 and 2, respectively. All the nodes on the planes $x_1 = 0, x_2 = 0$ and $x_3 = 0$ have zero displacements in the 1, 2 and 3 directions, respectively. The nodes on the outer face of the specimen in the x_1 direction have zero displacement in the 1 direction; all the nodes on the top x_3 face are moved in the negative 3 direction at a constant true strain rate of $0.001s^{-1}$. The simulation is carried out to a final strain of 1.0. The deformed mesh for the simulation with 12 slip systems is shown in Fig. 3-2(b). The deformation in the aggregate is non-homogenous and this is evident from the shape of the deformed elements.

For the simulations with the Taylor-type model, a single four noded ABAQUS-CPE4 element is used. The element is deformed at a constant true strain rate of 0.001 s^{-1} to a final strain of 1.0 in the compression direction. Each integration point in the element is assigned the 343 orientations which represent an initially random texture, Fig. 3-3.

The predicted macroscopic stress-strain curves by the FEM and the Taylor model for the the cases (12), (24), (36a), (36b) and (48) is presented in Figs. 3-4 and 3-5 respectively. As expected, the stress levels in the finite element calculations are slightly lower than the Taylor model because of the stronger kinematic constraint on the deformation in the Taylor model. In both methods, the order of the stress-strain response for the different choices of the slip systems is preserved. The stress-strain response with 24 slip systems is straddled by that of 12 and 48 slip systems. As the number of available slip systems increases, the stress-strain response becomes softer. However, the stress-strain response for the case (36b) with 36 slip systems is slightly lower than the simulation with 48 slip systems due to a lower value of the deformation resistance on the $\{112\}s$ planes as compared to the $\{110\}$ and $\{112\}h$ planes. Note that the differences in the stress levels for the cases (24), (36a),

and (36b) is of the order of $\pm 3\%$.

The crystallographic texture after a deformation of 100% for the FEM and the Taylor-type model are compared in Figs. 3-6 through 3-10 for the different choices of the slip systems. The following observations can be made:

1. The Taylor model predicts sharper textures when compared with the FEM model.

2. The Taylor model predicts a "hole", a region of low intensities, in the center of the {222} pole figures for the cases (12) (Fig. 3-6) and (48) (Fig. 3-10) while the FEM model does not predict a "hole" in the center of the {222} pole figures.

The differences between the FEM and the Taylor model as described above are due to the richer displacement fields in the individual grains in the finite element method than the Taylor method. Overall, the textures predicted by the Taylor model are reasonably close to that predicted by the FEM model for each of the 5 cases, (12), (24), (36a), (36b) and (48), respectively. Therefore, we expect the Taylor model to be reasonably accurate for use in simulations of polycrystalline b.c.c. materials.

Table 3.1 Slip Systems

α	$\mathbf{n}_o^\alpha$	$\mathbf{m}_o^\alpha$	α	$\mathbf{n}_o^\alpha$	$\mathbf{m}_o^\alpha$	α	$\mathbf{n}_o^\alpha$	$\mathbf{m}_o^\alpha$	α	$\mathbf{n}_o^\alpha$	$\mathbf{m}_o^\alpha$
1	$01\bar{1}$	111	13	$2\bar{1}\bar{1}$	111	25	$12\bar{3}$	111	37	$1\bar{2}3$	$\bar{1}11$
2	$\bar{1}01$	111	14	$1\bar{2}1$	111	26	$1\bar{3}2$	111	38	$13\bar{2}$	$\bar{1}11$
3	$1\bar{1}0$	111	15	$\bar{1}\bar{1}2$	111	27	$21\bar{3}$	111	39	$2\bar{1}3$	$\bar{1}11$
4	011	$\bar{1}\bar{1}1$	16	$\bar{2}1\bar{1}$	$\bar{1}\bar{1}1$	28	$2\bar{3}1$	111	40	$23\bar{1}$	$\bar{1}11$
5	101	$\bar{1}\bar{1}1$	17	$1\bar{2}\bar{1}$	$\bar{1}\bar{1}1$	29	$\bar{3}12$	111	41	$3\bar{1}2$	$\bar{1}11$
6	$\bar{1}10$	$\bar{1}\bar{1}1$	18	112	$\bar{1}\bar{1}1$	30	$\bar{3}21$	111	42	321	$\bar{1}11$
7	$01\bar{1}$	$\bar{1}11$	19	$\bar{2}1\bar{1}$	$\bar{1}11$	31	123	$\bar{1}\bar{1}1$	43	$\bar{1}23$	$1\bar{1}1$
8	101	$\bar{1}11$	20	$12\bar{1}$	$\bar{1}11$	32	$\bar{1}32$	$\bar{1}\bar{1}1$	44	132	$1\bar{1}1$
9	$\bar{1}\bar{1}0$	$\bar{1}11$	21	$1\bar{1}2$	$\bar{1}11$	33	213	$\bar{1}\bar{1}1$	45	$\bar{2}13$	$1\bar{1}1$
10	$0\bar{1}\bar{1}$	$1\bar{1}1$	22	$21\bar{1}$	$1\bar{1}1$	34	$\bar{2}31$	$\bar{1}\bar{1}1$	46	231	$1\bar{1}1$
11	$\bar{1}01$	$1\bar{1}1$	23	$\bar{1}2\bar{1}$	$1\bar{1}1$	35	$3\bar{1}2$	$\bar{1}\bar{1}1$	47	$31\bar{2}$	$1\bar{1}1$
12	110	$1\bar{1}1$	24	$\bar{1}12$	$1\bar{1}1$	36	$3\bar{2}1$	$\bar{1}\bar{1}1$	48	$32\bar{1}$	$1\bar{1}1$

Table 3.1: Components of $\mathbf{m}_0^\alpha$ and $\mathbf{n}_0^\alpha$ with respect to an orthonormal basis associated with the crystal lattice for f.c.c. crystals. (Indices as printed for the $\{112\} < 111 >$ systems correspond to positive shear in the *soft* direction.)

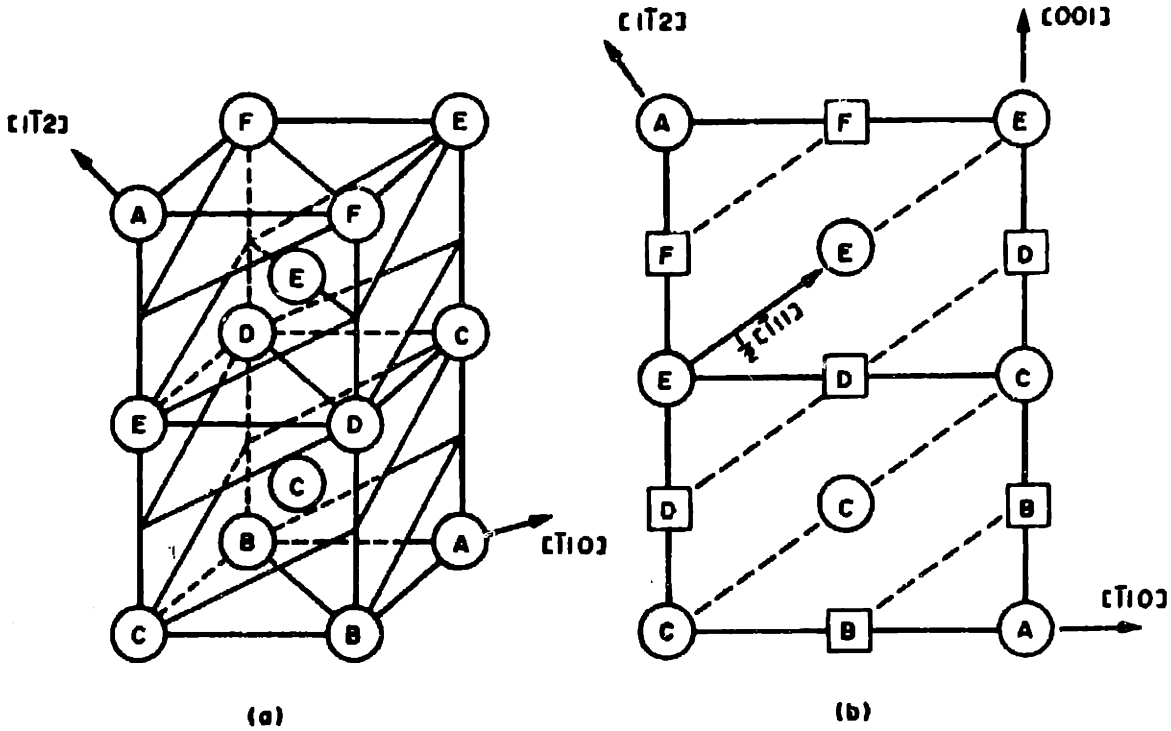

Figure 3-1: Stacking sequence of {112} planes in a b.c.c. crystal. (a) Two unit cells showing positions of atoms in $(1\bar{1}2)$ planes. (b) Traces of the $(1\bar{1}2)$ planes on a (110) projection: atom sites marked by circles lie in the plane of the diagram; those marked by squares lie above and below (From Hull and Bacon, 1984).

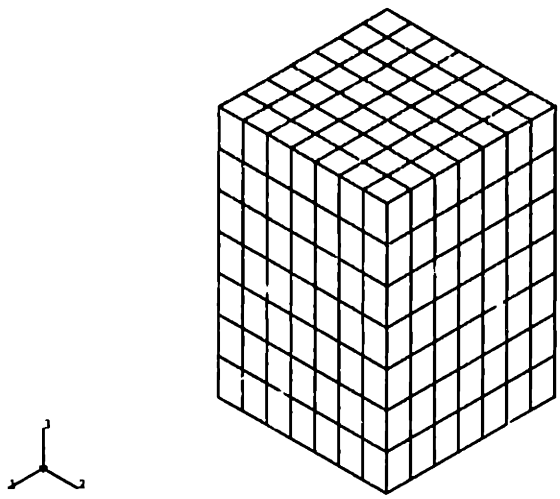

(a)

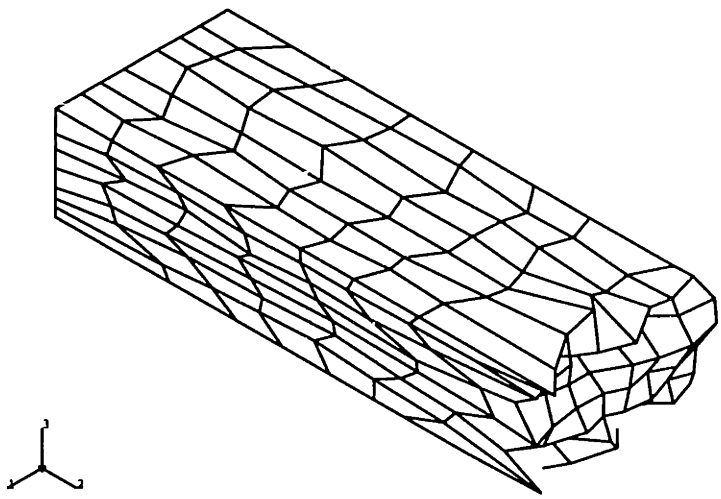

(b)

Figure 3-2: (a) Initial finite element mesh. (b) Deformed finite element mesh after a plane strain compression to a strain of 100% with 12 slip systems.

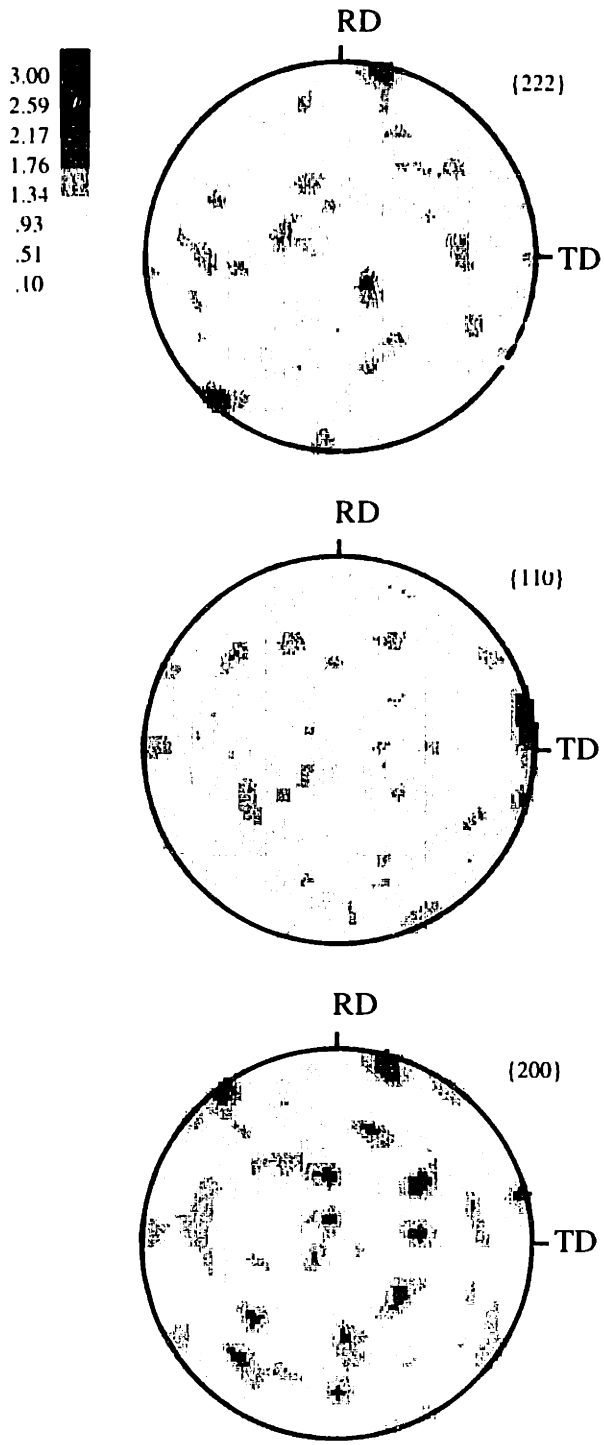

Figure 3-3: Initially random texture as represented by 343 grain orientations.

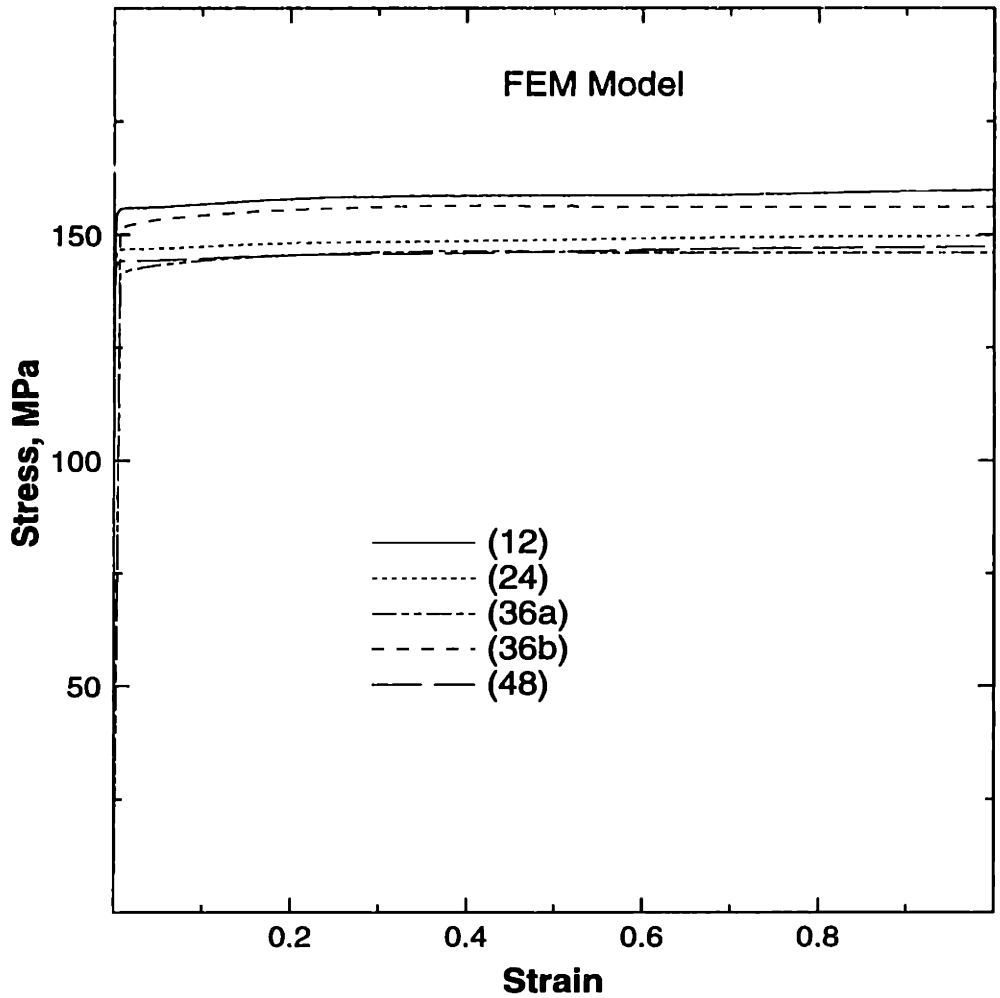

Figure 3-4: Numerically predicted macroscopic stress-strain curve in the plane-strain compression simulation by the finite element model for the cases (12), (24), (36a), (36b) and (48), respectively.

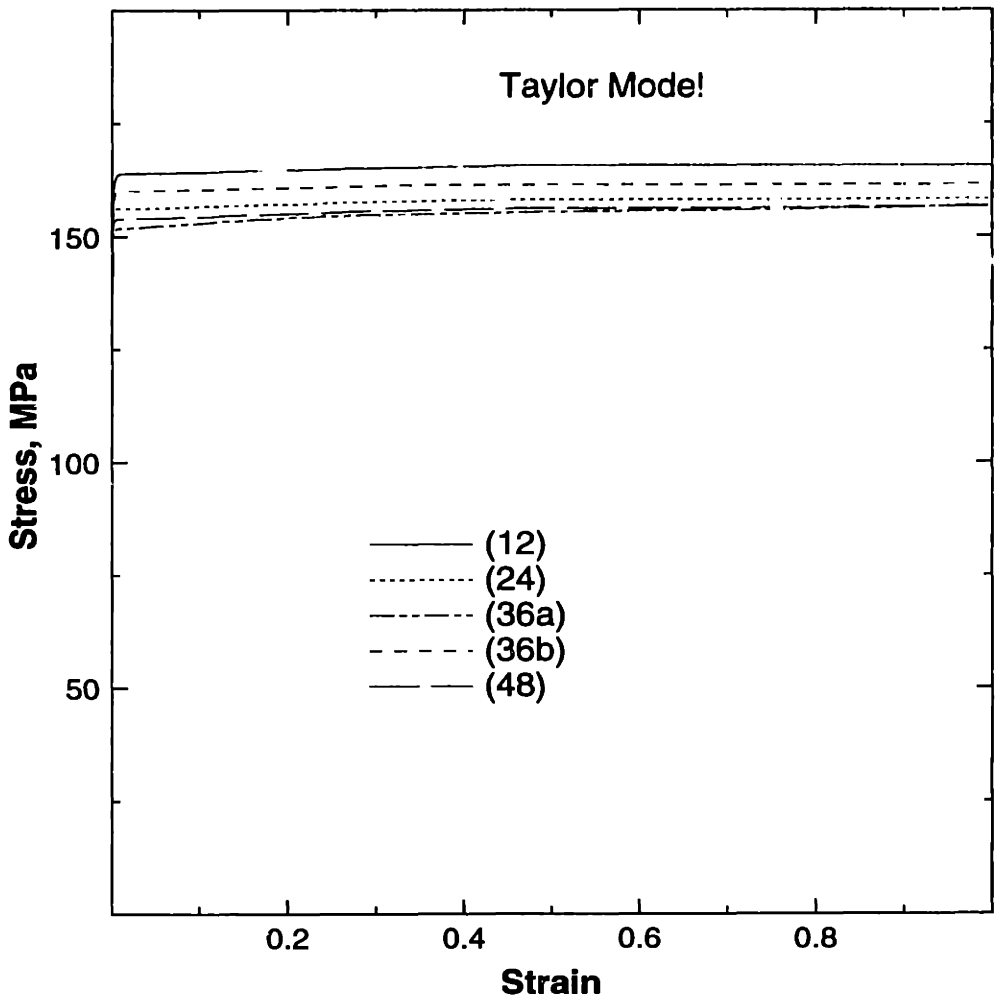

Figure 3-5: Numerically predicted macroscopic stress-strain curve in the plane-strain compression simulation by the Taylor model for the cases (12), (24), (36a), (36b) and (48), respectively.

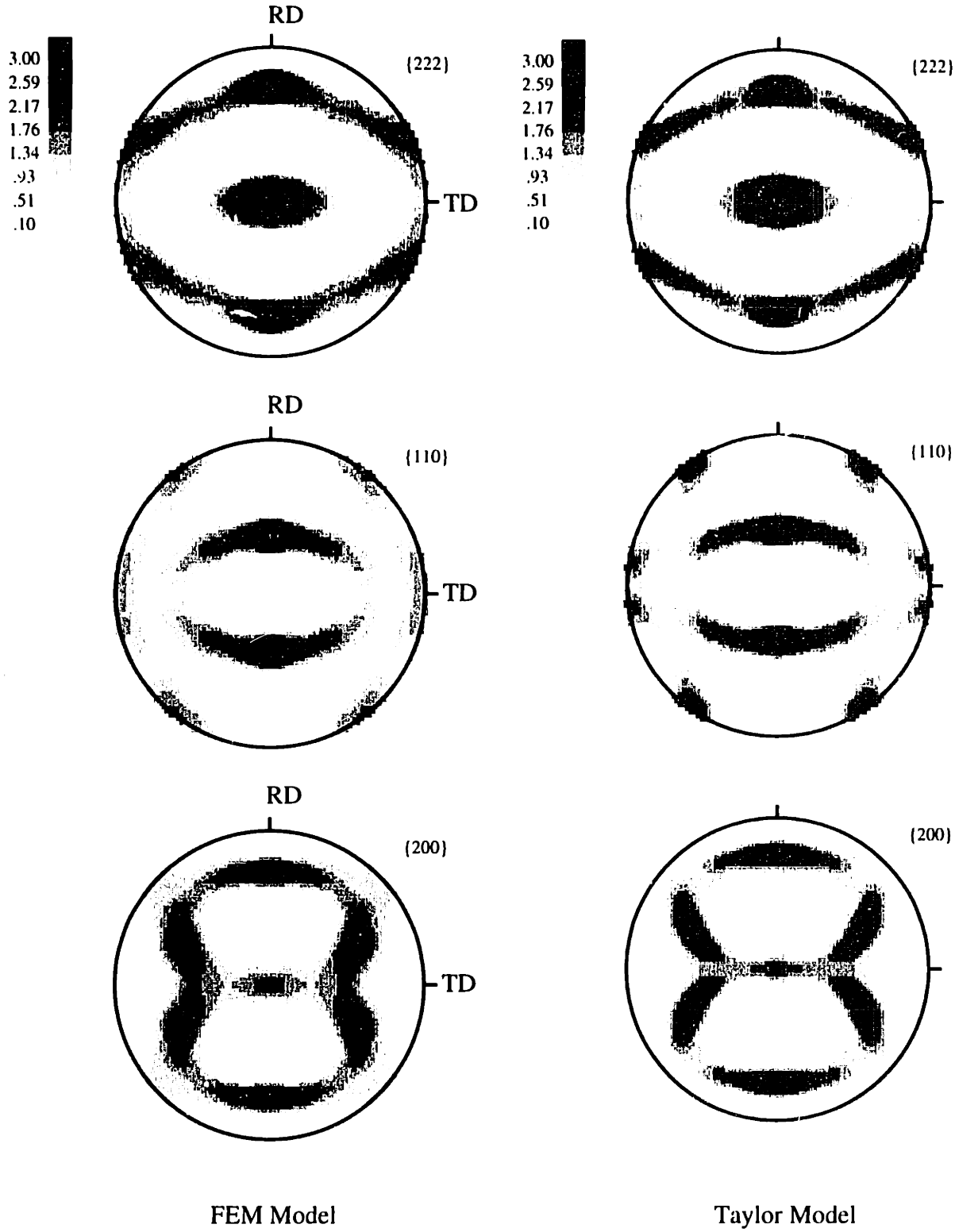

Figure 3-6: Comparison of the predicted textures in the plane-strain compression simulation on a initially random, polycrystalline b.c.c. material by the FEM and the Taylor model with 12 slip systems (case (12)).

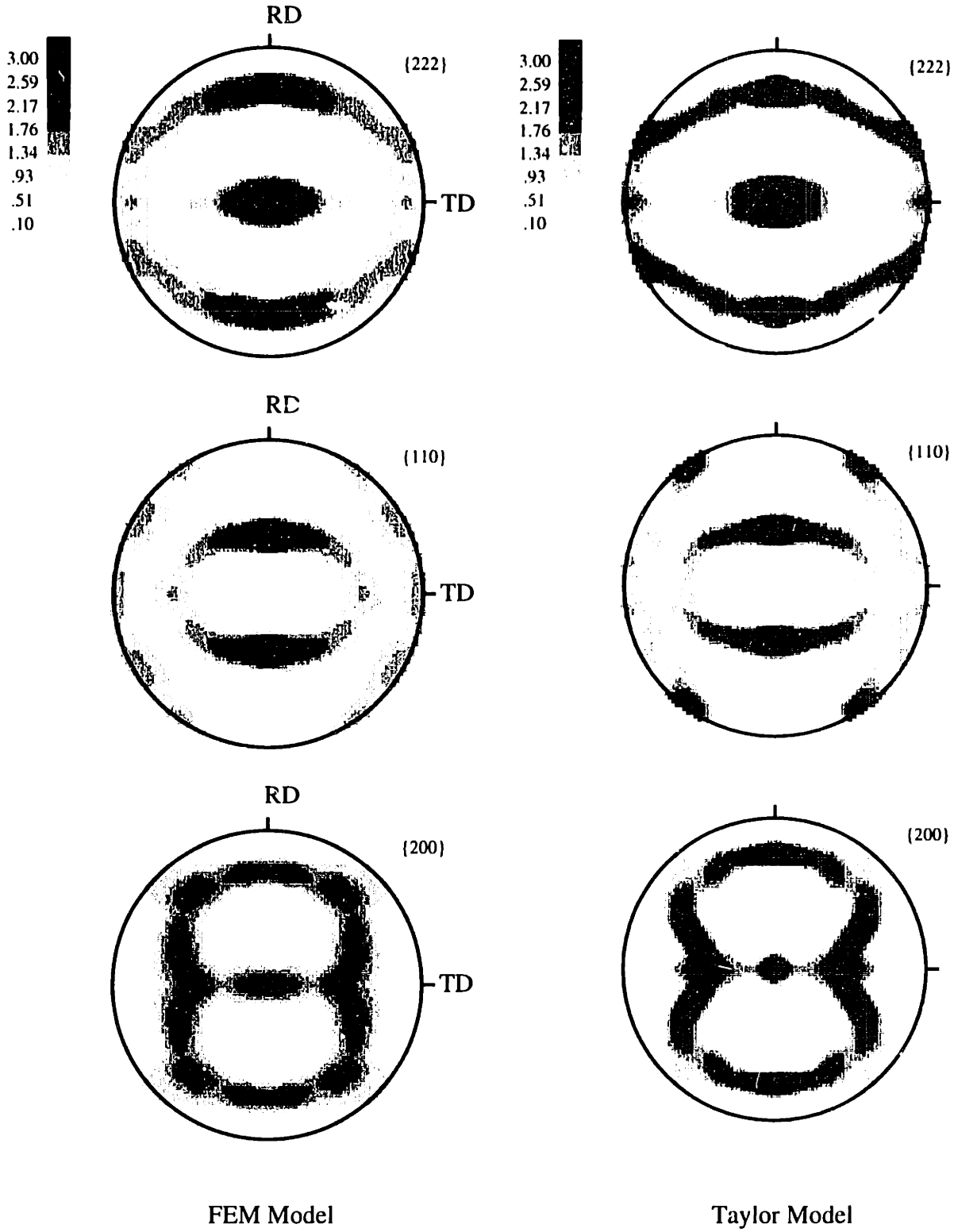

Figure 3-7: Comparison of the predicted textures in the plane-strain compression simulation on a initially random, polycrystalline b.c.c. material by the FEM and the Taylor model with 24 slip systems (case (24)).

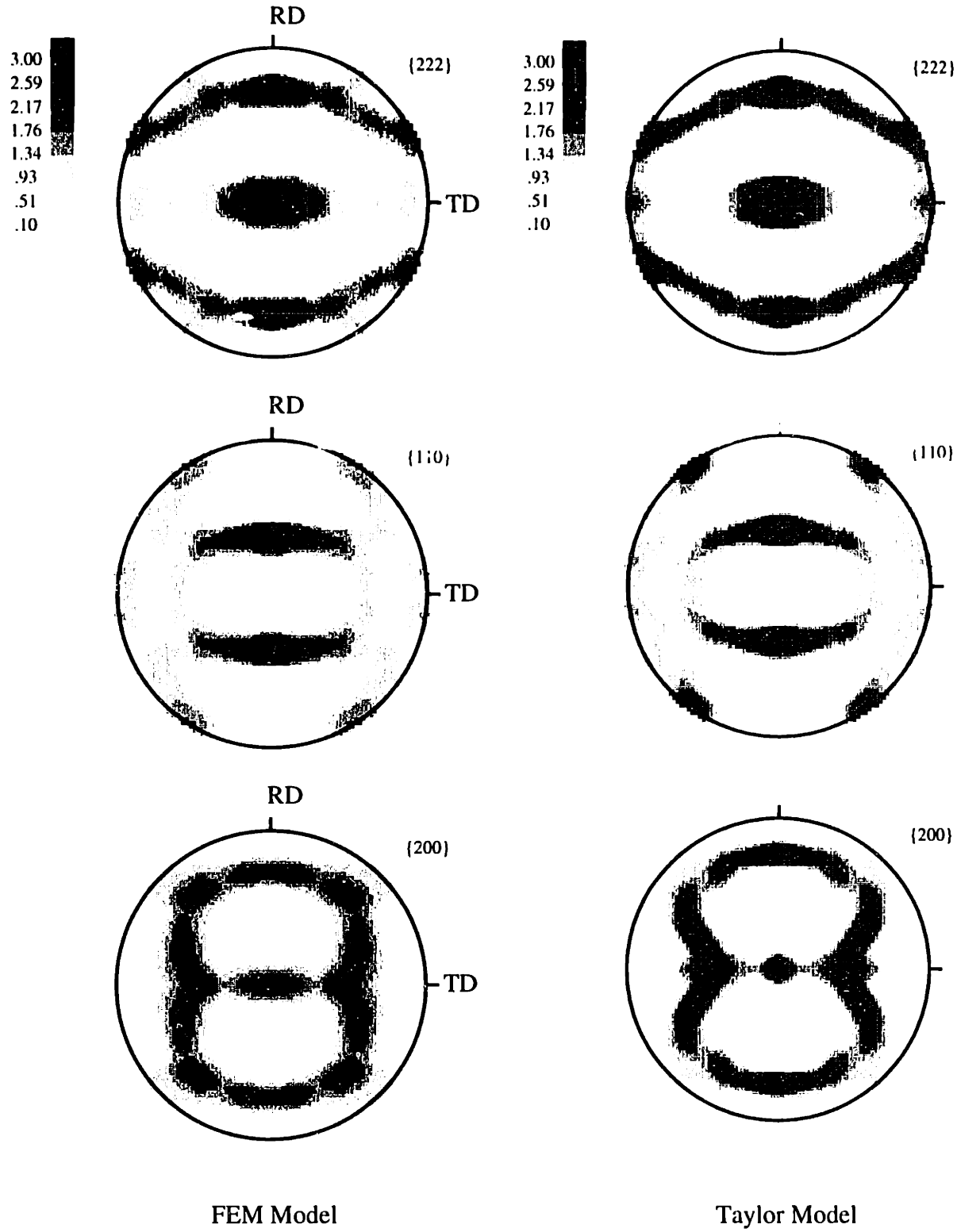

Figure 3-8: Comparison of the predicted textures in the plane-strain compression simulation on a initially random, polycrystalline b.c.c. material by the FEM and the Taylor model with 36 slip systems (case (36a)).

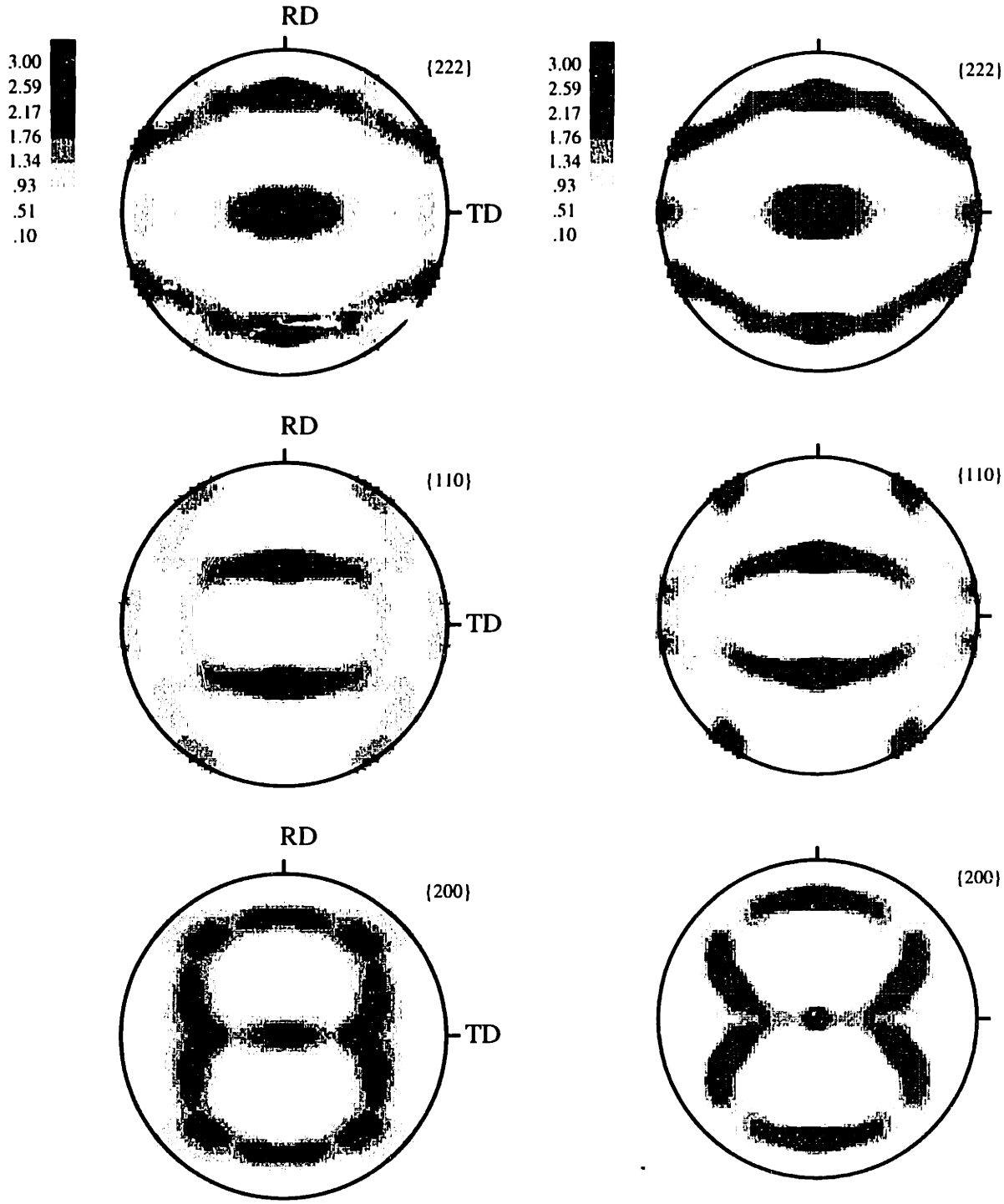

Figure 3-9: Comparison of the predicted textures in the plane-strain compression simulation on a initially random, polycrystalline b.c.c. material by the FEM and the Taylor model with 36 slip systems (case (36b)).

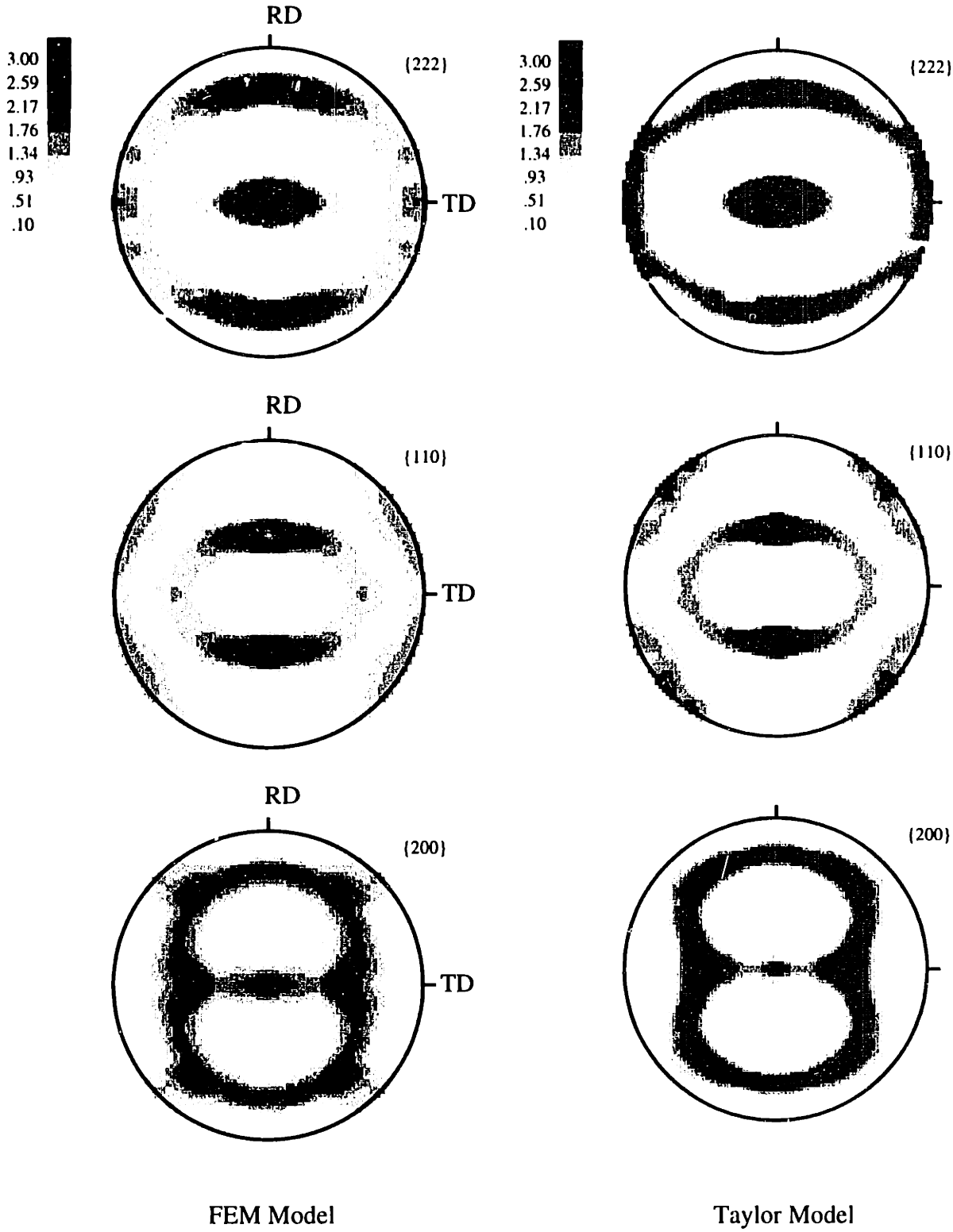

Figure 3-10: Comparison of the predicted textures in the plane-strain compression simulation on a initially random, polycrystalline b.c.c. material by the FEM and the Taylor model with 48 slip systems (case (48)).

3.2 Identification of Operative Slip Systems for Tantalum

A plane-strain compression experiment was carried out on an initially pre-textured tantalum specimen at a strain-rate of $0.001\,s^{-1}$ to a final strain of 1.0. Fig. 3-11 shows the initial texture of tantalum and its numerical representation using 400 weighted grain orientations. The experimentally-measured {200} pole figure is shown in Fig. 3-12. Also shown in this figure is a {200} pole figure with some ideal orientations typically observed in b.c.c. metals : A ((100)[011]), B ((115)[011]), C ((113)[011]), D ((112)[011]), E ((111)[011]) and F ((111)[112]) (From Barret *et al.* [1937]). As seen from this figure, the rolling texture of tantalum contains components of A ((100)[011]) and F ((111)[112]), and a relatively weaker component E ((111)[011]).

Ideally, plane-strain compression simulations should be performed using the FEM model with the different choices of the slip systems. However, the finite element calculations for an initially pre-textured polycrystalline aggregate is rather difficult due to the following reasons : (a) A large number of grains are needed to represent the initial texture. The representation of an initial texture obtained from popLA (Kallend, *et al.* [1994]) consists of a set of weighted grain orientations which are replaced by a number of grain orientations equal to the weight (that is rounded off to the nearest integer); these grains are then distributed in a small neighbourhood of the given orientation in the Euler angle space (Kalidindi [1992]). To illustate the problems in this approach, consider a situation where rounding the weight to the nearest integer results in too few grains as there are considerable number of crystals with weights less than 0.5. In order to retain these crystals, the complete set of weighted grain orientations have to be multiplied by a factor of two and the procedure as described before has to be repeated. (b) The sensitivity of the finite element calculations to the manner in which a grain orientation is assigned to an element may be significant for an initially pre-textured polycrystalline aggregate. Due to these reasons, we performed Taylor-type crystal plasticity calculations on the pre-textured tantalum to decide on the operative slip systems by comparing the measured-texture components in the simulations with the experiments.

The Taylor model calculations were carried out on a ABAQUS-CPE4 element, with each integration point assigned the 400 weighted orientations, Fig. 3-11. The flow parameters for the different calculations are the same as used in the previous section, equations (3.2),

(3.3), and (3.4). The numerically predicted stress-strain curves for the different choices of the slip systems is presented in Fig. 3-13. As seen from this figure, the stress levels is highest for the case (12) and lowest for the case (48). The difference in the stress levels for the cases (24), (36a) and (36b) is of the order of $\pm 3\%$.

Fig. 3-14 shows a comparison of the {200} pole figures predicted by Taylor model for the cases (12), (24) and (48). The predicted textures for the cases (36a) and (36b) are shown in Fig. 3-15. From these two figures, we can identify the texture components in the five cases as :

- (12) : strong component (F) and weak component (A)
- (24) : strong component (A,F) and weak component (E)
- (36a) : strong component (A,F) and weak component (E)
- (36b) : strong component (A,F) and weak component (E)
- (48) : strong component (E,F) and weak component (A)

The texture of tantalum consisted of the components of A ((100)[011]) and F ((111)[112]), and a relatively weaker component E ((111)[011]). The presence of the texture component A in the experiment immediately rules out the cases (12) and (48). The texture components in the cases (24), (36a) and (36b) are similar to that measured in the experiment.

Given the small differences between the textures and the stress-strain response in the cases (24), (36a) and (36b), it is computationally less expensive to use 24 in comparison to 36 slip systems in Taylor-type crystal plasticity calculations. Hence, we shall use use 24 slip systems for our simulations on tantalum in this work.

In the next chapter, we determine the material parameters in our constitutive model for tantalum.

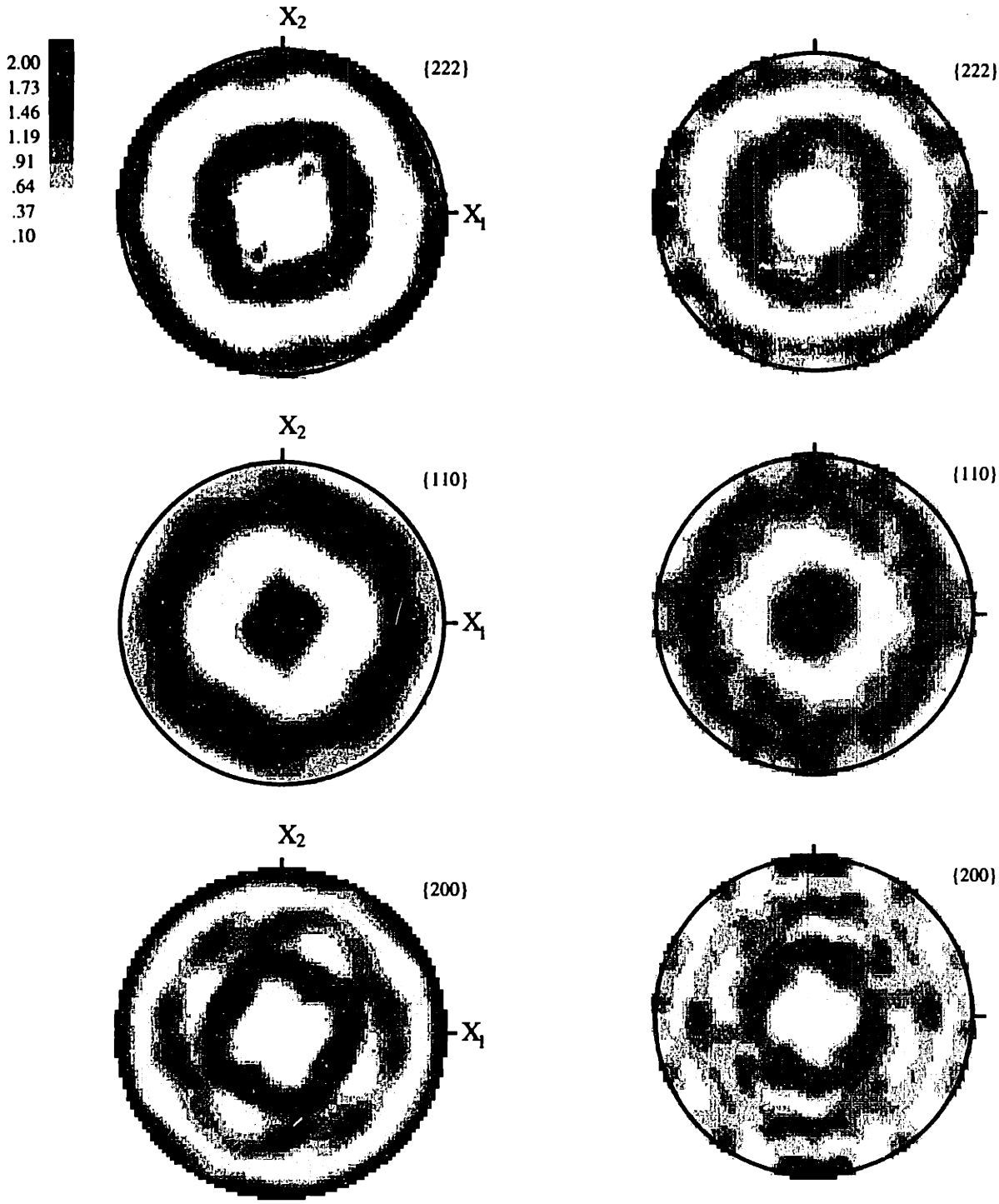

Figure 3-11: Representation of the initial texture of tantalum with 400 weighted grains.

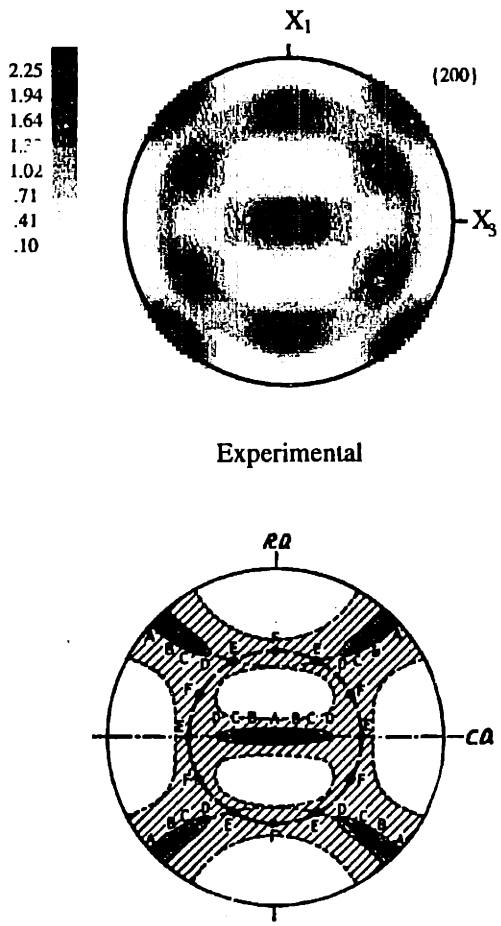

Figure 3-12: Experimentally-measured plane-strain compression texture in tantalum compared against the pole figures showing some ideal orientations measured in b.c.c. materials (Barret *et al.* [1937]) : A ((100)[011]), B ((115)[011]), C ((113)[011]), D ((112)[011]), E ((111)[011]) and F ((111)[112].

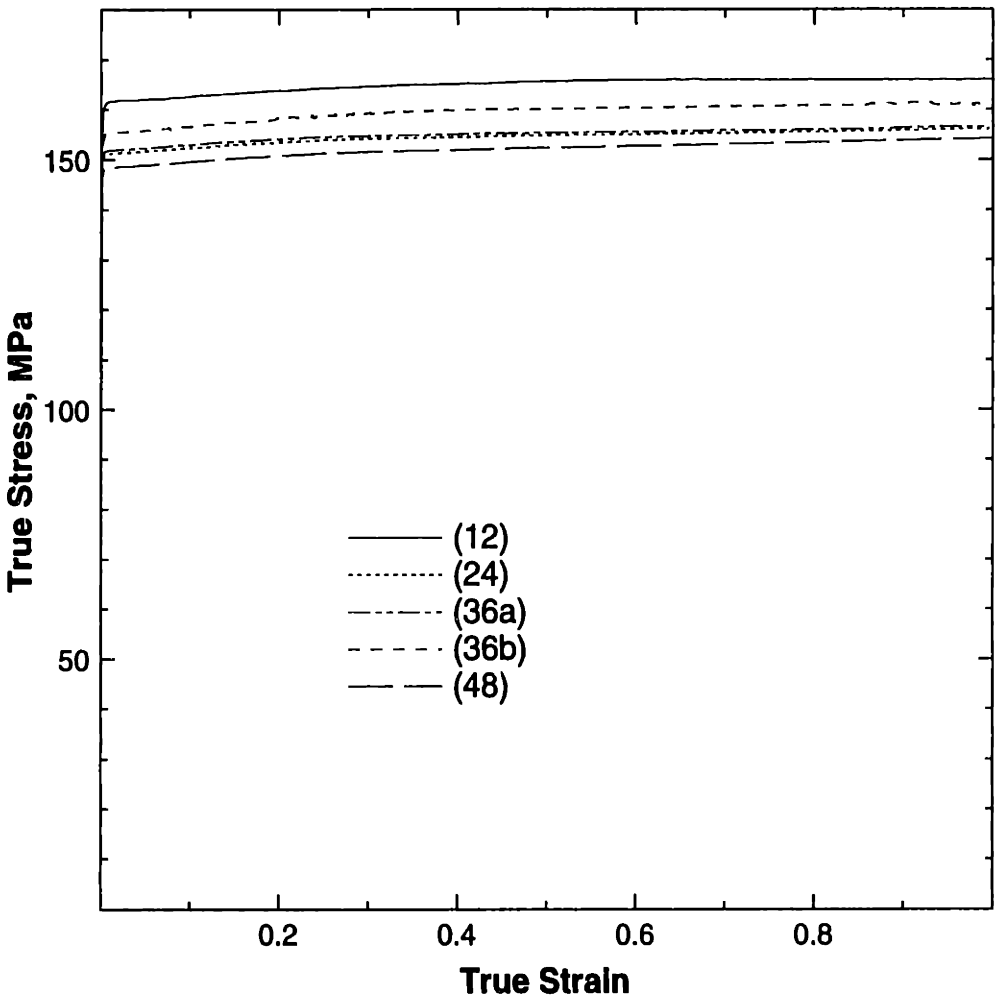

Figure 3-13: Numerically predicted macroscopic stress-strain curve in the plane-strain compression simulation on tantalum by the Taylor model for the cases (12), (24), (36a), (36b) and (48), respectively.

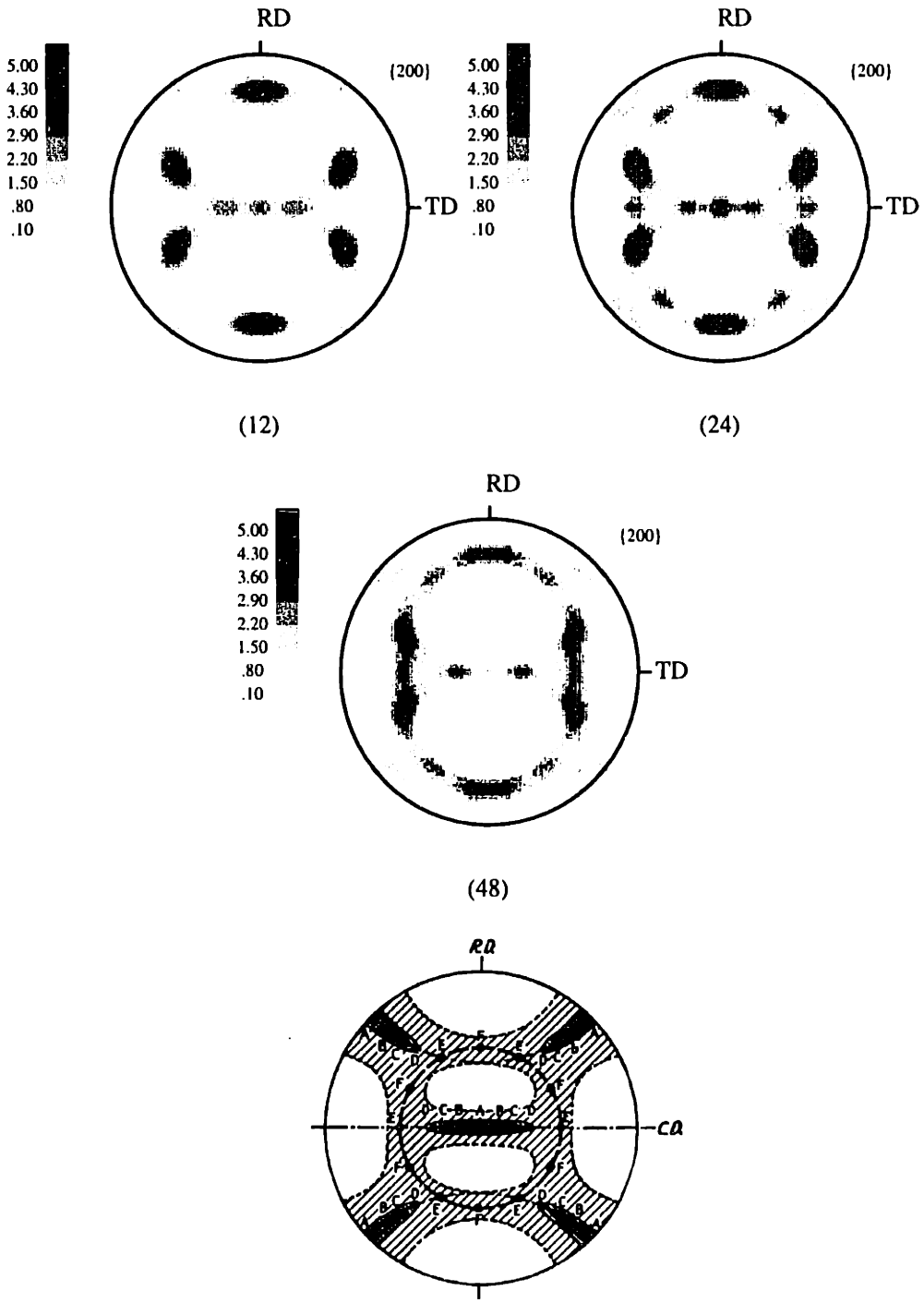

Figure 3-14: Numerically predicted {200} pole figures by the Taylor model for cases (12), (24), and (48) compared against the pole figures showing some ideal orientations measured in b.c.c. materials (Barret *et al.* [1937]) : A ((100)[011]), B ((115)[011]), C ((113)[011]), D ((112)[011]), E ((111)[011]) and F ((111)[112].

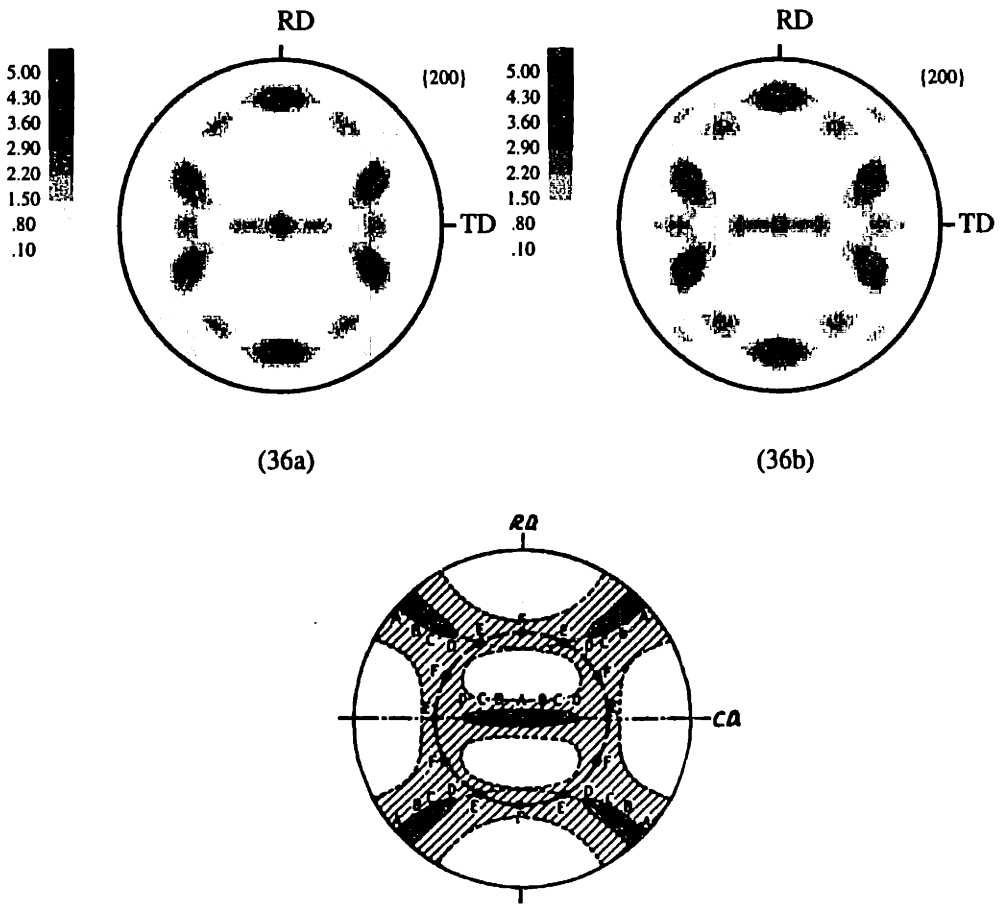

Figure 3-15: Numerically predicted {200} pole figures by the Taylor model for the cases (36a) and (36b) compared against the pole figures showing some ideal orientations measured in b.c.c. materials (Barret *et al.* [1937]) : A ((100)[011]), B ((115)[011]), C ((113)[011]), D ((112)[011]), E ((111)[011]) and F ((111)[112].

Chapter 4

Material Parameters For Tantalum

In this chapter, we evaluate the material parameters in the crystal plasticity model for polycrystalline tantalum. The material parameters are first determined for the isotropic model (see Appendix A), and these values are then used as guides to determine the parameters for the crystal plasticity model.

For b.c.c. crystals the anisotropic elasticity tensor $\boldsymbol{C}$ may be specified in terms of three stiffness parameters, C_{11}, C_{12} and C_{44}. The values of the elastic parameters for tantalum as a function of temperature (in degree Kelvin) are taken as (Simmons and Wang [1971]):

$$\begin{aligned} C_{11} &= (268.2 - 0.024\,\theta)\ \text{GPa}, \\ C_{12} &= (159.6 - 0.011\,\theta)\ \text{GPa}, \\ C_{44} &= (87.1 - 0.015\,\theta)\ \text{GPa}. \end{aligned}$$

We have modeled the plastic deformation of b.c.c. tantalum to occur solely due to crystallographic slip on the twelve $\{110\} < 111 >$, plus the twelve $\{112\} < 111 >$ slip systems, and have neglected any small asymmetry of slip on the $\{112\}$ planes. As we shall see, the assumption of these slip systems captures the macroscopic stress-strain response and the evolution of the crystallographic texture in b.c.c. tantalum reasonably well. The slip systems have been listed in Table 3.1.

The other necessary material parameters are the quantities $\{\dot{\gamma}_0, \Delta F^*, p, q, s_*\}$ in the

flow equations (2.14, 2.15), the quantities $\{\hat{h}_0^\alpha(|\dot{\gamma}^\alpha|,\theta), r, \hat{s}_{a,s}^\alpha(|\dot{\gamma}^\alpha|,\theta), q_l\}$ in the hardening equations (2.22, 2.23, 2.24, 2.25), and the initial value of the athermal slip-system resistance $s_{a,0}$, which are taken to be identical for all the slip systems. These material parameters and functions are determined by calibrating the model against existing experimental results of Hoge and Mukherjee [1977], Vecchio [1994] and Nemat-Nasser and Issacs [1996] on commercially pure tantalum.

The flow parameters are determined by fitting the experimental data of Hoge and Mukherjee [1977] for the strain rate and temperature sensitivity of the yield strength of a tantalum rod. The initial texture of the tantalum rod was not reported by Hoge and Mukherjee. Here, to approximate this initial texture, we measured the texture of our own commercially-procured and annealed tantalum rod and represented this texture by a set of 400 weighted grain orientations by using the texture conversion program popLA (Kallend, *et al.* [1994]). The as-received tantalum rod was annealed at 1200°C for 30 minutes. This annealing procedure produced an equi-axed grain structure with a grain size of $\approx 50\mu$m, but it did not remove the previous texture. The crystallographic texture was measured by X-ray diffraction using a diffractometer with a pole figure goniometer. The experimentally-measured and numerically-represented pole figures are presented in Fig. 4-1.

For the curve-fitting procedure, the yield strength of tantalum at different temperatures and strain rates is calculated by performing a Taylor-model simple compression ABAQUS/Explicit simulation on a single ABAQUS-C3D8R (continuum, 3-D, eight-noded, reduced integration) element subjected to the appropriate strain rate and initial temperature in the experiment. The integration point in the element is assigned the 400 weighted grain orientations corresponding to the initial texture of the rod, Fig. 4-1. The flow parameters obtained by the fitting procedure are: [1]

$$\dot{\gamma}_0 = 1.73 \times 10^7\,\mathrm{sec}^{-1},\ \Delta F^* = 2.77 \times 10^{-19}\mathrm{J},\ p = 0.28,\ q = 1.34,\ s_* = 400\mathrm{MPa}, \quad (4.1)$$

[1]The curve-fitting exercise is quite time-consuming. To speed up the process, the data is first fit to an isotropic version of the model (see Appendix A), and the values of the material parameters so determined are then used as guides for initial estimates for the numerical calculations based on the crystal-plasticity model. In particular, the flow parameters $\{\Delta F^*, p, q\}$ are taken to be equal to those obtained for the isotropic model, and the parameter $\dot{\gamma}_0$ is obtained from the corresponding quantity $\dot{\epsilon}_0$ in the isotropic model by setting $\dot{\gamma}_0 = \sqrt{3}\,\dot{\epsilon}_0$. Initial estimates for the resistance parameters s_* and $s_{a,0}$ are taken as the values obtained for the isotropic model, divided by a "Taylor Factor" of $M \approx 3$.

with

$$s_{a,0} = 22\text{MPa}.$$

The quantities s_* and $s_{a,0}$ are taken to be the same for all slip systems. The fit of the model against the experimental data of Hoge and Mukherjee [1977] for the strain rate and temperature sensitivity of the yield strength of tantalum is presented in Figs. 4-2 and 4-3, respectively. Fig. 4-2 also show two data points form the recent plate-impact experiments of Duprey and Clifton [1994] on tantalum foil, at room temperature and a strain rate of approximately 10^5sec^{-1}. The initial texture for these calculations was chosen to be random. The data at this high rate falls on an extrapolation of the curve for the data of Hoge and Mukherjee, indicating that there is no change in mechanism from thermally-activated dislocation glide to dislocation drag, for strain rates up to $\approx 10^5\text{sec}^{-1}$.

As noted before, most of the previous work on crystal plasticity has been based on a power-law description (1.1) for the shearing rates. This simple flow rule with a *constant* rate sensitivity parameter m is not able to represent the real strain-rate and temperature sensitivity of flow of tantalum. To emphasize this point, using (2.18, 2.19) we may define a rate-sensitivity parameter m by

$$m \equiv \left.\frac{\partial \ln \tau^\alpha}{\partial \ln|\dot{\gamma}^\alpha|}\right|_{s^\alpha=\text{const.}} = \left(\frac{k_B\,\theta}{\Delta F_*}\right)\left(\frac{1}{pq}\right)\left(\frac{\left(\frac{\theta}{\theta_c}\right)^{\frac{1}{q}-1}}{1-\left(\frac{\theta}{\theta_c}\right)^{\frac{1}{q}}}\right). \tag{4.2}$$

Using the flow parameters for tantalum (4.1), the variation of the parameter m defined in (4.2) is plotted against strain rate at fixed representative temperatures in Fig. 4-4(a), and as a function of temperature at fixed strain rates Fig. 4-4(b). These figures show that in order to accurately represent the flow behavior of tantalum we would need to use a rate- and temperature- dependent m in the power-law relation (1.1), rather than a constant m as has been customary in most previous crystal plasticity calculations.

The hardening parameters are determined by fitting the predictions from the crystal plasticity model against the "isothermal" and "adiabatic" data from the compression split Hopkinson bar experiments of Vecchio [1994] and Nemat-Nasser and Isaacs [1996]. The experimental data was obtained by digitizing the curves presented in the paper of Vecchio [1994] and Nemat-Nasser and Isaacs [1996]. The technique used by Nemat-Nasser and co-workers to deduce the isothermal stress-strain curves at high rates is to strain the

specimen incrementally and unload, allow the specimen to cool to the test temperature, and then re-load at the same initial strain rate. The curve connecting the peaks of these incremental tests provides an estimate of the isothermal stress-strain curve at a high strain rate. The compression split Hopkinson bar experiments were performed on specimens cored from tantalum discs which were produced by cross-rolling the initial ingots. These authors do not report on quantitative information concerning the initial texture of their material. Accordingly, we approximated their initial texture by using our own texture measurements on a similarly-produced tantalum plate, and representing this texture by a set of 400 weighted grain orientations by using popLA, Fig. 4-5.

For the curve-fitting procedure to determine the hardening parameters, both the isothermal and adiabatic stress-strain curves of tantalum at different temperatures and strain rates are calculated by performing Taylor-model simple compression ABAQUS/Explicit simulations on a single ABAQUS-C3D8R element subjected to the appropriate strain rate and initial temperature in the experiment. The integration point in the element is assigned the 400 weighted grain orientations corresponding to the initial texture of the rod, Fig. 4-5. The adiabatic stress-strain curves are simulated by computing the temperature rise according to equation (2.28), by assuming that all the plastic work is converted into heat ($\xi = 1.0$). In the simulations, the flow parameters are the same as those determined above from the data of Hoge and Mukherjee [1977], equation (4.1). As indicated earlier, the hardening quantities $\{\hat{h}_0^\alpha(|\dot{\gamma}^\alpha|, \theta), \hat{s}_{a,s}^\alpha(|\dot{\gamma}^\alpha|, \theta)\}$ are in general expected to be strain rate and temperature-dependent. However, for tantalum in the range of strain rates and temperatures examined, these quantities are adequately described by taking the initial hardening rate h_0 and the saturation value of the athermal slip-system resistance $s_{a,s}$ to be independent of both temperature and strain rate. The values of the hardening parameters estimated by the fitting procedure for the two sets of data are: [2]

[2] As for the flow parameters, the hardening parameters are also first estimated for the isotropic model, and the values so determined are used as initial estimates for the corresponding quantities in the anisotropic model. Specifically, initial estimates for $s_{a,s}$ and $s_{a,0}$ are taken to be equal to those obtained in the isotropic model divided by a Taylor factor of $M \approx 3$, and the initial estimate for h_0 is taken to be equal to the value obtained in the isotropic model divided by $M^2 \approx 9$.

Table 4.1 Hardening Parameters

	$s_{a,0}$	h_0	$s_{a,s}$	r	q_l
Nemat-Nasser and Isaacs (1996)	20 MPa	80 MPa	110 MPa	1.1	1.4
Vecchio (1994)	49 MPa	160 MPa	100 MPa	1.1	1.4

The different values of the hardening parameters in Table 4.1 may be attributed to the fact that the data used to determine these parameters are from different sources. Ideally, data from a single set of well-pedigreed experiments should be used to determine both the flow and hardening parameters, but no such data over a broad range of strains, strain rates, and temperatures is available. Recall that the flow parameters were determined from the data of Hoge and Mukherjee [1977], whereas the hardening parameters were obtained form the data of Vecchio [1994] and Nemat-Nasser and Issacs [1996]. The main reason for the discrepancy in the values of the hardening parameters is due to the fact that the initial state, as characterized by the initial crystallographic texture and the dislocation microstructure, is probably different in the specimens used by the different authors. Although, we have attempted to account for some of the differences in the initial texture, there is essentially no information reported in the papers of Hoge and Mukherjee [1977], Vecchio [1994] and Nemat-Nasser and Issacs [1996], which would allow us to satisfactorily account for the differences in the initial crystallographic texture that probably existed in the specimens used in these studies. With this limitation in mind, the quality of the fit using the material parameters in Table 4.1, to the strain-hardening data is shown in Figs. 4-6 through 4-8. Considering the broad range of strains up to 60%, strain rates of 10^{-4} to 30,000/s, and temperatures from room temperature to 500°C, the fit is very good.

In the next chapter we evaluate the ability of the crystal plasticity model to predict the texture evolution and the stress-strain response of tantalum in some *quasi-static* experiments.

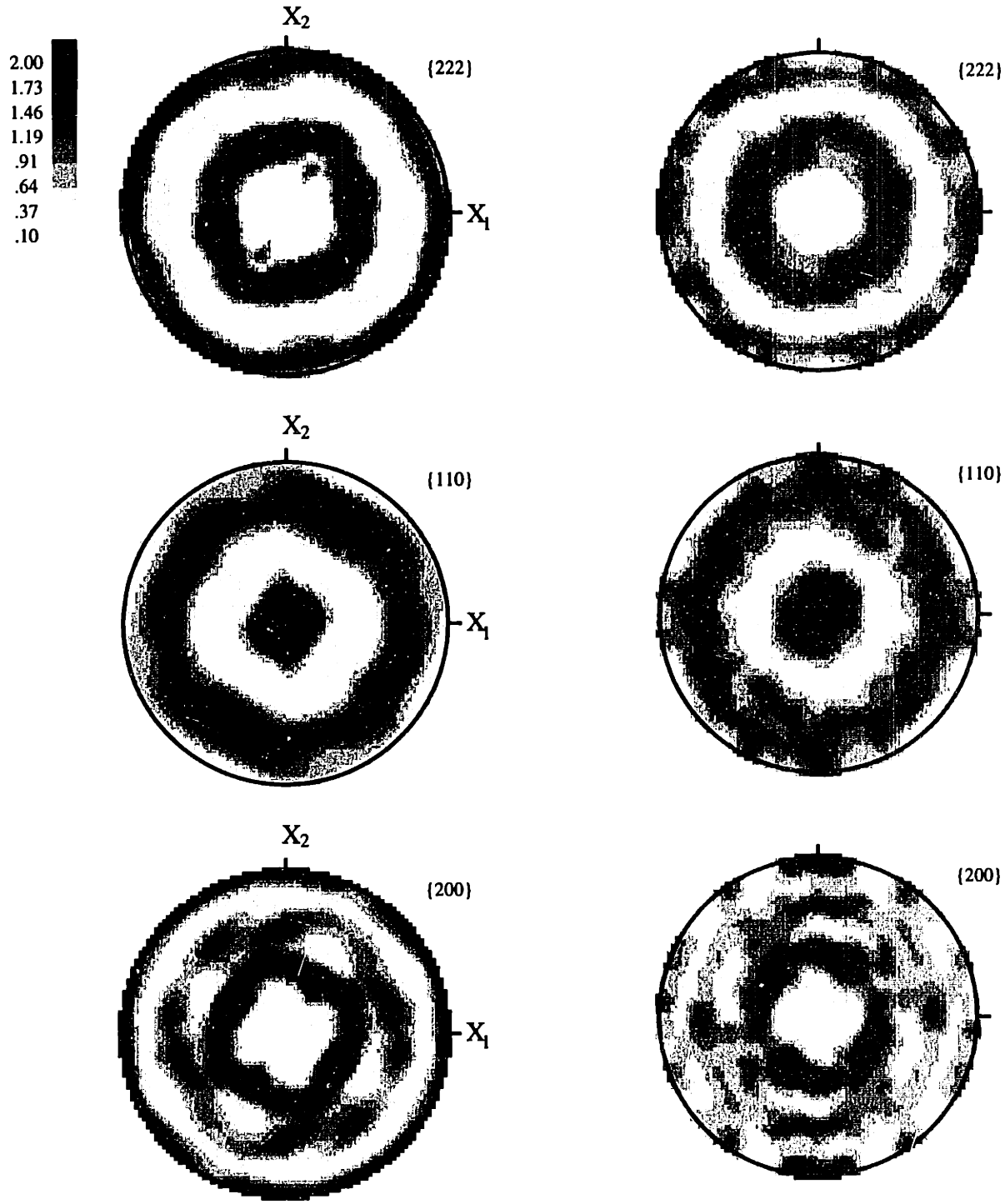

Figure 4-1: Representation of the texture of annealed b.c.c. tantalum with 400 weighted grains.

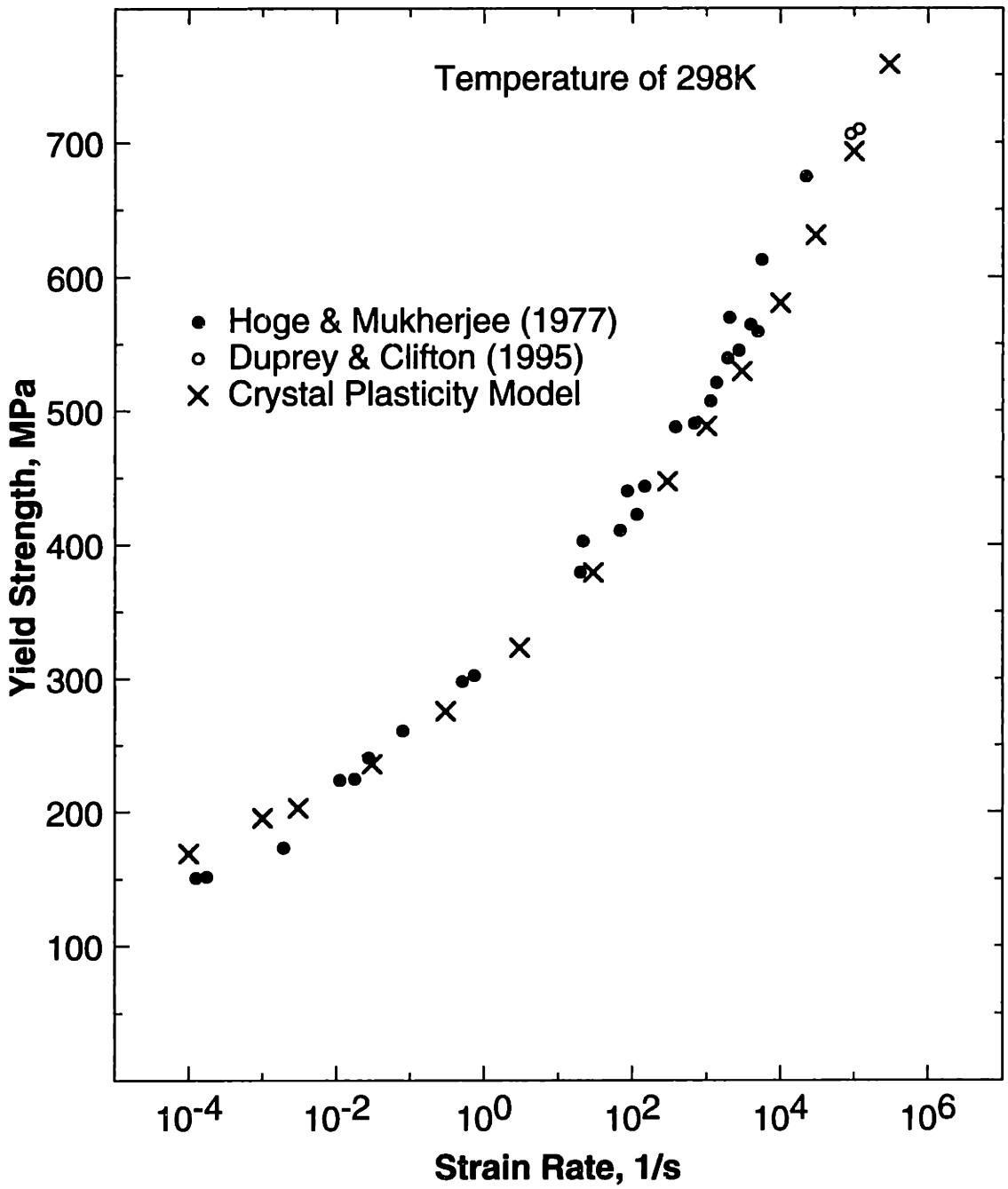

Figure 4-2: Fit of the Taylor-type crystal plasticity model to the data of Hoge and Mukherjee (1977) and Duprey and Clifton (1995) on the strain rate dependence of the yield strength of b.c.c. tantalum.

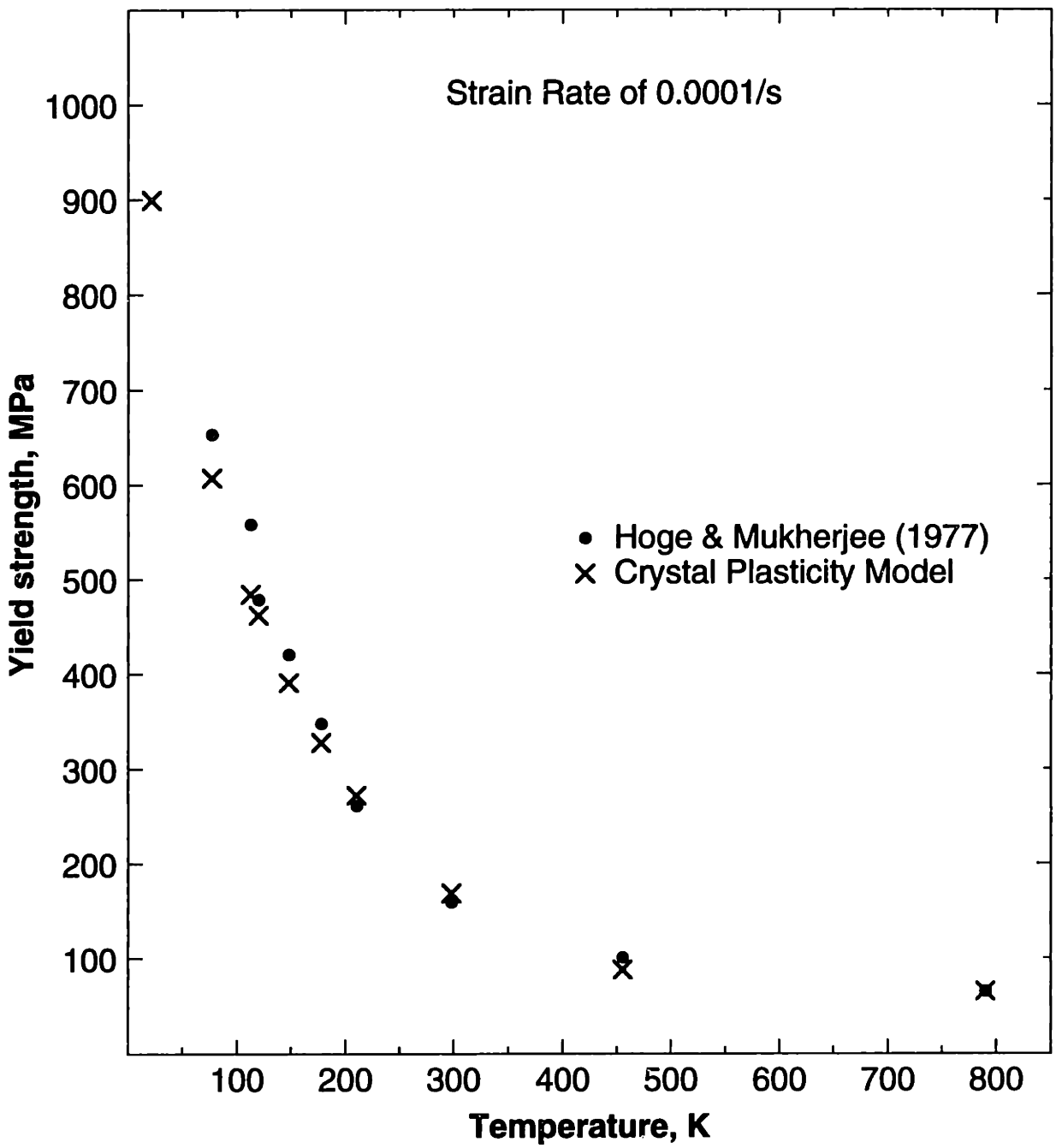

Figure 4-3: Fit of the Taylor-type crystal plasticity model to the data of Hoge and Mukherjee (1977) on the temperature dependence of the yield strength of b.c.c. tantalum.

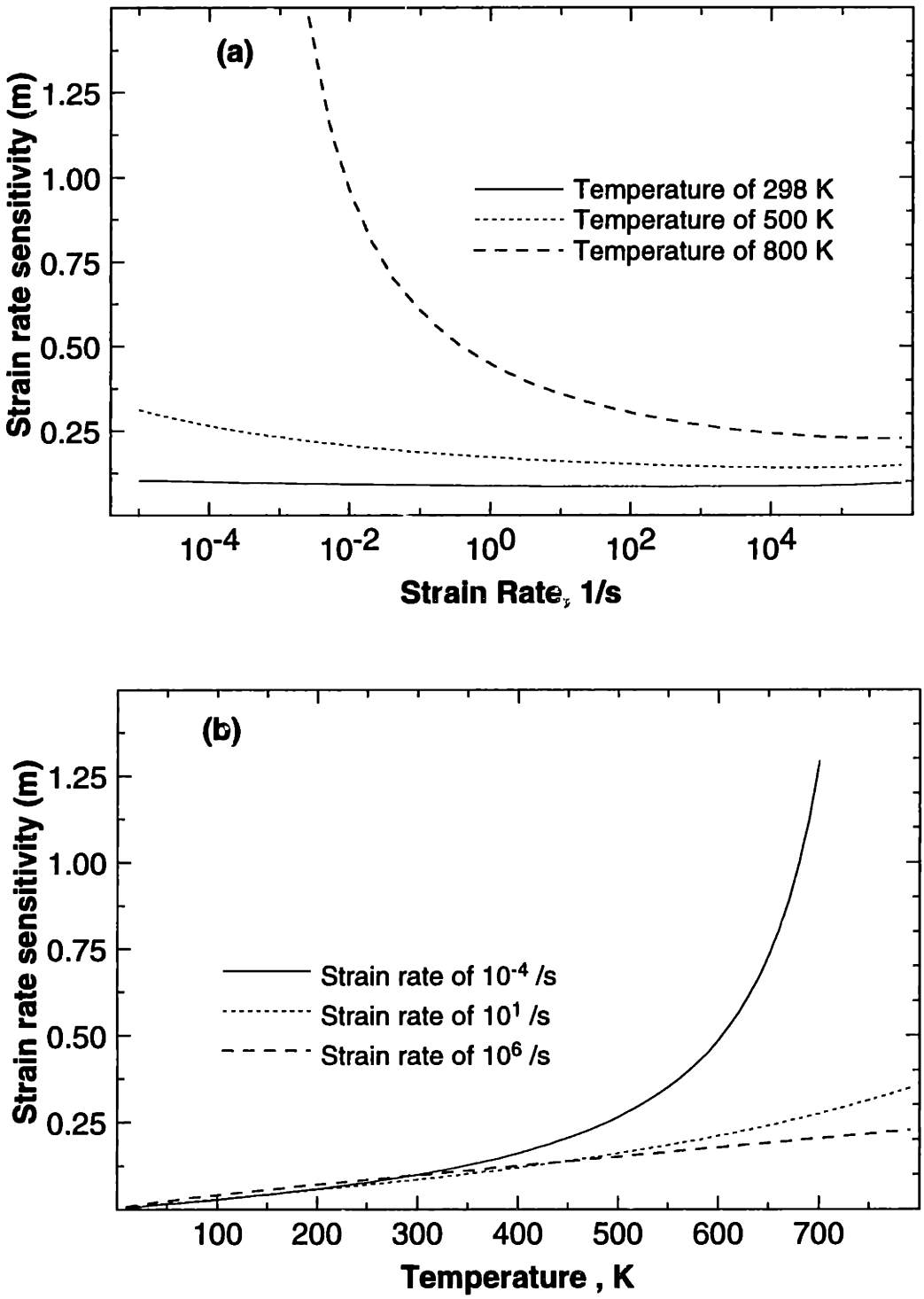

Figure 4-4: The variation of the strain rate sensitivity parameter m for tantalum with (a) strain rate at fixed temperatures, and (b) temperature at fixed strain rates.

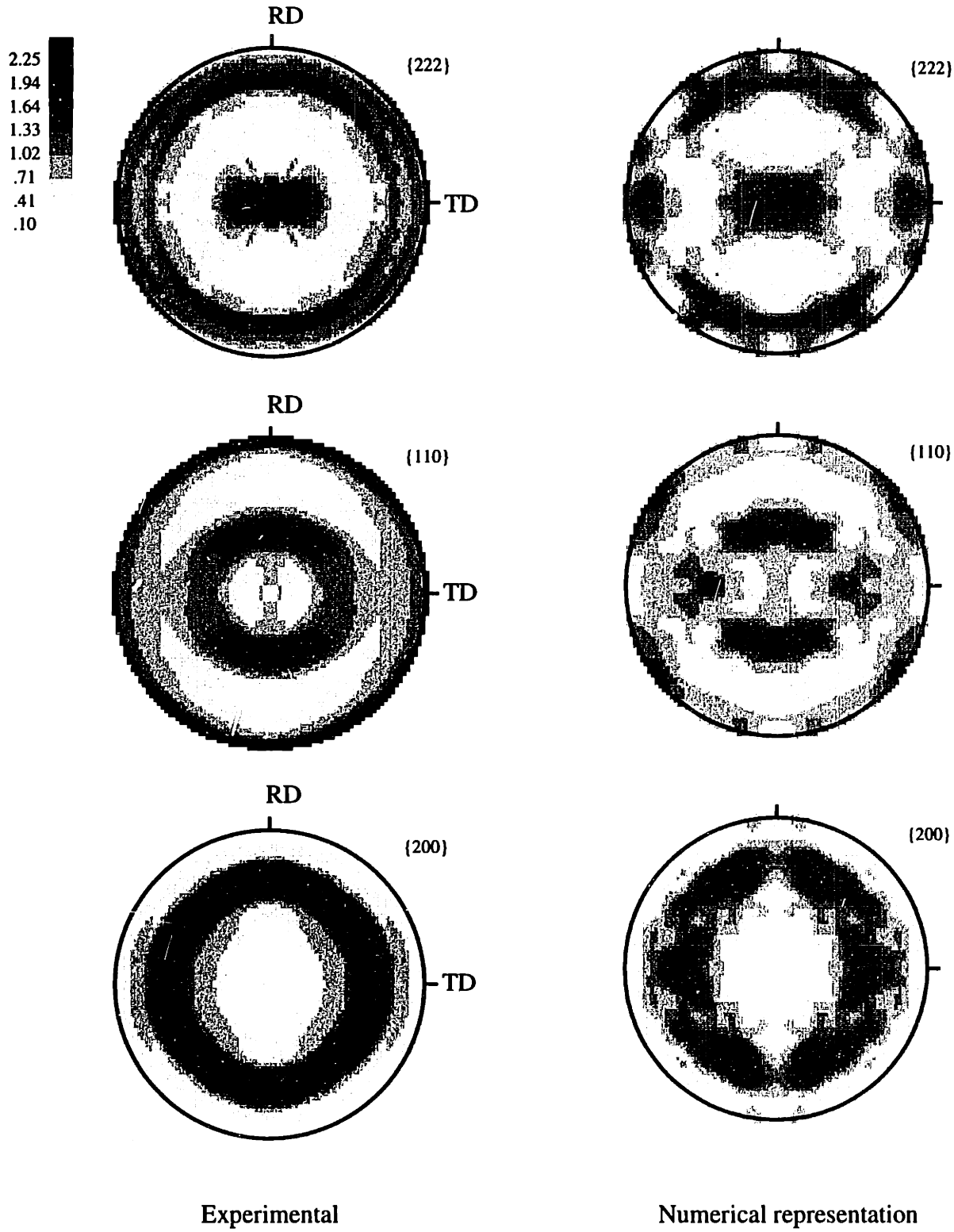

Figure 4-5: Representation of the texture of a tantalum plate with 400 weighted grains.

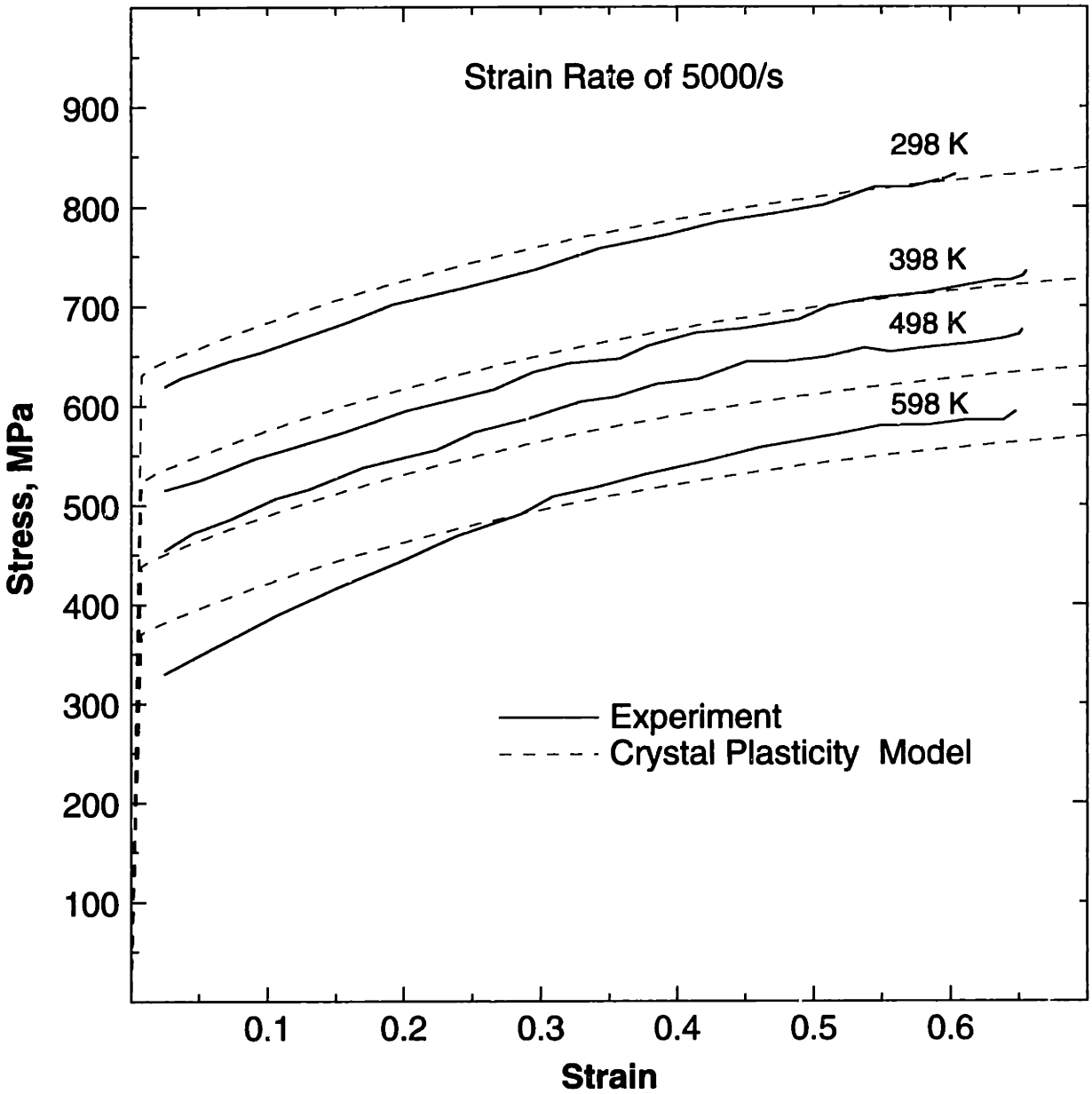

Figure 4-6: Comparison of the predictions from the Taylor-type crystal plasticity model against the *isothermal* experiments of Nemat-Nasser and Issacs (1996).

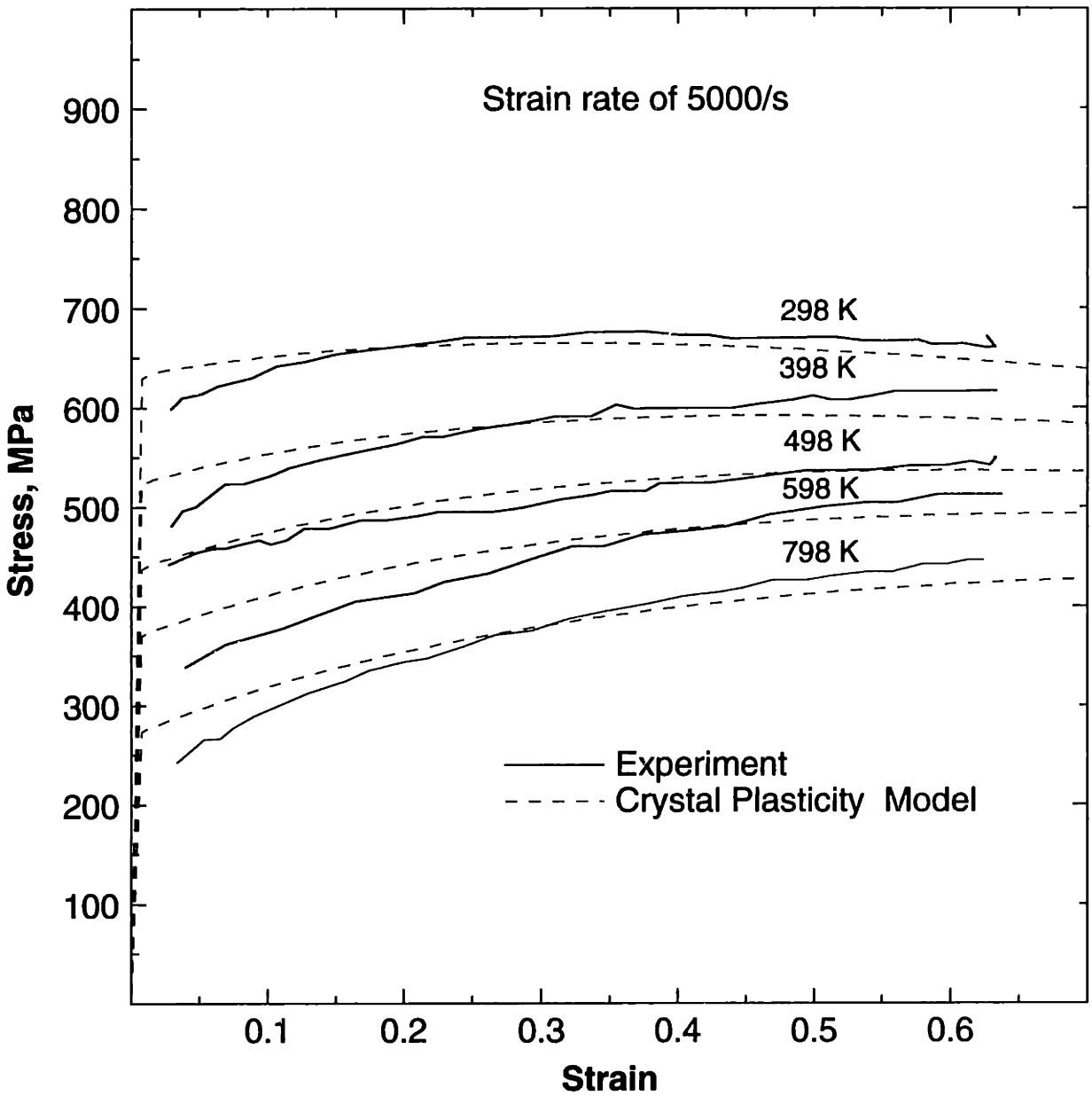

Figure 4-7: Comparison of the predictions from the Taylor-type crystal plasticity model against the *adiabatic* experiments of Nemat-Nasser and Issacs (1996).

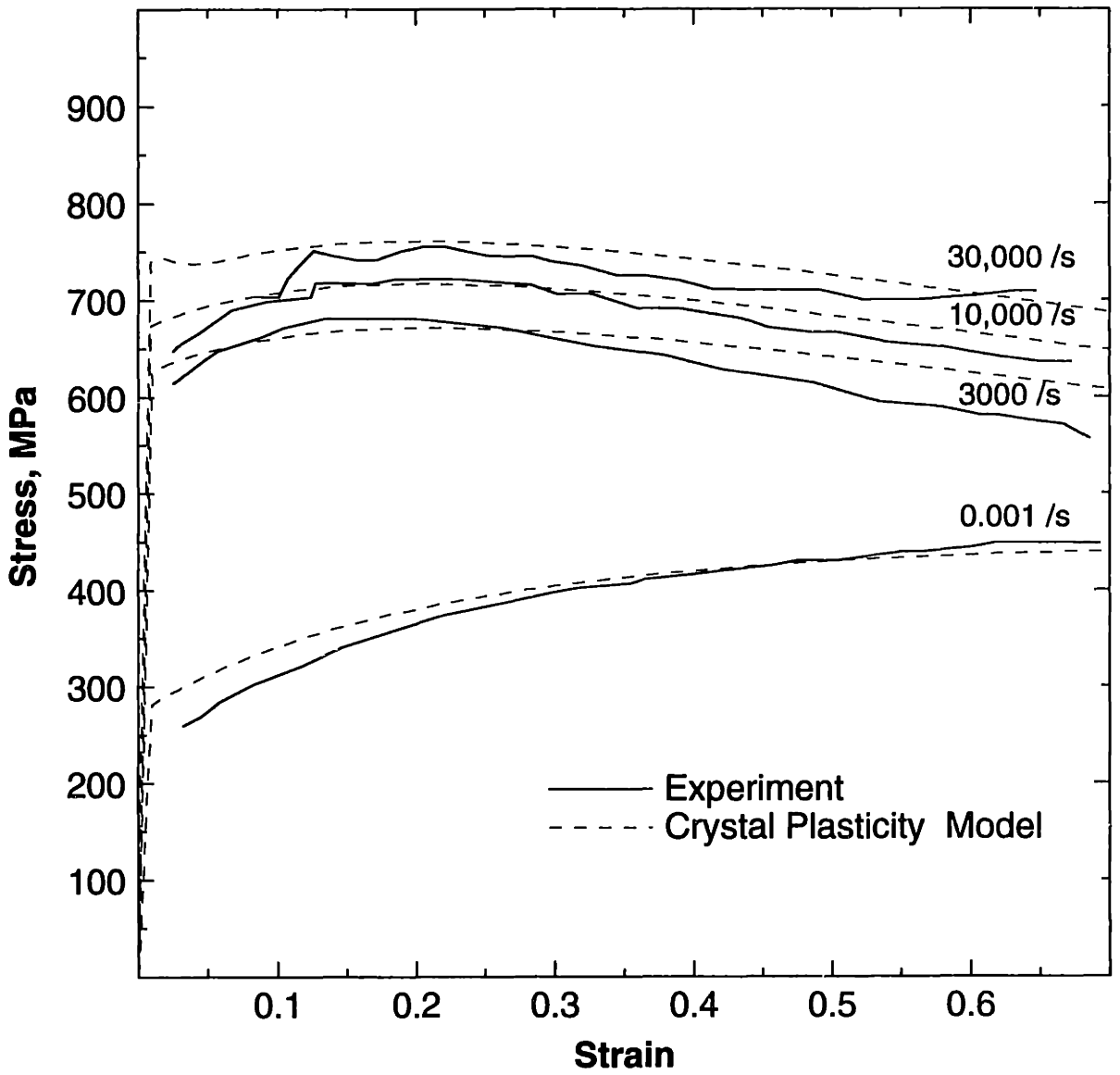

Figure 4-8: Comparison of the predictions from the Taylor-type crystal plasticity model against the experimental data of Vecchio (1994).

Chapter 5

Texture Evolution in Quasi-static Homogeneous Deformations

In this chapter the accuracy of the Taylor-type crystal plasticity model for polycrystalline b.c.c. tantalum is evaluated by comparing the predictions of the evolution of crystallographic texture and the stress-strain response in (i) simple compression and tension, (ii) plane-strain compression, and (iii) torsion on an initially-annealed, but pre-textured tantalum rod, against corresponding experiments.

All our experiments were performed on 99.9 % pure tantalum (RO5200) obtained from the Rembar Company[1] in the form of a half inch round rod. Specimens for micrographs and texture measurement were prepared by grinding on ABRAPOL automatic polishers. The specimens were first polished using SiC paper of 1000 and 4000 grit size. For the final finish, oxide polishing (**OP-U**) is employed. Colloidal silica, with a grain size of approximately 0.04 μm and a pH of about 9.8 is used[2]. The combination of chemical activity and fine, gentle abrasion produces scratch-free specimens. The etchant used is a $50\% - 50\%$ mixture of Hydroflouric (HF) and Nitric acid (HNO_3) respectively, and the etching time is around 30 - 60 seconds.

The microstructure and the initial texture of the as received tantalum rod is shown in Fig. 5-1 and Fig. 5-2 respectively. As the grains are highly deformed, the tantalum rod was annealed at 1200^oC for half hour in a vacuum furnace at a vacuum level of 10^{-6} torr.

[1] Address:67 Main Street, Dobbs Ferry, New York - 10522. Tel.no. : 914-693-2620.

[2] The colloidal silica solution, called the Mastermet, was purchased from Buehler.

Fig. 5-3 is a photomicrograph of the annealed tantalum. The grains are equiaxed and the grain size is around 50 μm. The initial crystallographic texture of the annealed rod is shown in Fig. 5-4. The annealed texture, presented in Fig. 5-4(a), is very similar to that of the as received texture, Fig. 5-2. This indicates that texture of tantalum does not change on annealing. In all the numerical simulations reported in this chapter, the initial texture of the specimens is represented by the 400 weighted grain orientations, Fig. 5-4(b), used to reproduce the experimentally-measured texture of Fig. 5-4(a).

The flow parameters $\{\dot{\gamma}_0, \Delta F^*, p, q, s_*\}$ are taken to be the same as those obtained in the previous section, equation (4.1). The initial value of the athermal resistance $s_{a,0}$, together with the hardening parameters $\{h_0, r, s_{a,s}, q_l\}$, is determined by fitting the stress-strain data from a constant true strain rate simple compression test performed along the rod axis. The experiment was performed at an axial strain rate of -0.001s^{-1} to a final strain of -1.1 on a cylindrical specimen 0.5 inch in diameter and 0.75 inch in length. Teflon film of 0.001 inch thickness and MoS_2 grease was used for lubrication. Axial displacement was obtained by measuring the displacement of the actuator, which was corrected for the compliance in the load train. The resulting stress-strain curve is shown in Fig. 5-5. The simulation of this quasi-static simple compression experiment was performed using our Taylor crystal plasticity model implemented in ABAQUS/Standard. A single cubic ABAQUS-C3D8 (continuum, 3-D, eight-noded) element was used for the simulation. The values estimated by our curve-fitting procedure are

$$s_{a,0} = 15\,\text{MPa},\ h_0 = 70\,\text{MPa}, s_{a,s} = 160\,\text{MPa},\ r = 1.1,\ q_l = 1.4.$$

The correspondence between the stress-strain response from the simulation and the experimental data (from which the material parameters were determined), shown in Fig. 5-5, is reasonable. As seen from this figure, tantalum shows a pronounced upper and a lower yield point. The yield drop observed in tantalum is due to the stress-activated unlocking of dislocations which are pinned by the interstitials namely, oxygen and nitrogen. Our model, as formulated cannot capture this yield point phenomenon.

The experimentally-measured and numerically-predicted {222}, {110} and {200} pole figures at a strain of -1.1 are presented in Fig. 5-6. The agreement is reasonable. The compression texture is axi-symmetric with respect to the loading direction.

The specimen for the simple tension experiment was 0.315 inch in diameter and had a gauge length of 0.475 inch with the tension axis aligned with the rod axis. Strain was measured by using an axial extensometer. The experiment was performed at an axial strain rate of $0.001s^{-1}$ to a final strain of of 0.3. We were limited to this small strain level to avoid the onset of diffuse necking. For the simulation, a single ABAQUS-C3D8 element was used. Each integration point was assigned a set of 400 weighted grain orientations corresponding to Fig. 5-4(b). As seen in Fig. 5-7, the crystal plasticity model predicts the stress-strain response in simple tension reasonably well. The simulated tension texture, Fig. 5-8, is also in reasonable agreement with the experiment.

The predictions of the stress-strain curves along with the corresponding measurements for the simple compression and tension experiments are presented in Fig. 5-9. We observe from Fig. 5-9(a) that the measured tension stress-strain curve lies slightly above the measured compression stress-strain curve. However, the initial yield strength in tension is slightly lower than in compression. The crystal plasticity calculations correctly predicts these differences in the tension and compression flow curves, Fig. 5-9(b).

The specimen for the plane-strain compression experiment was machined so that the compression direction is perpendicular to the rod axis, and the constraint direction is along the rod axis. The specimen was 0.339 inch long along the compression direction, 0.356 inch long along the compression direction and 0.335 inch long along the free direction. The specimen was lubricated on all four contact surfaces inside the plane strain fixture with both Teflon film of 0.001 inch thickness and MoS_2 grease. The sliding contact surfaces of the fixture are also lubricated with the MoS_2 lubricant. The plane-strain compression experiment was performed at a strain rate of $-0.001s^{-1}$ to a final strain level of -1.0. In the numerical simulation a single ABAQUS-CPE4 (continuum, plane strain, four-noded) element was used. The predicted stress-strain response is compared against the experimental measurement in Fig. 5-10, and the predicted crystallographic texture is compared against the experimentally-measured one in Fig. 5-11. The predicted stress-strain curve and texture approach the corresponding experimental measurements, but the agreement could be better. The model overpredicts the experimental flow stress for plane strain compression at large strains. Examination of the microstructure of the sample after deformation shows that the grains have flattened and localized bands of deformation have appeared within individual grains, Fig. 5-12. Clearly, the deformation within the grains are

no longer uniform and a simple Taylor model cannot capture this deformation field. This may explain the observed differences in the stress-strain response and the crystallographic texture between the experiment and the simulation.

A fixed-end, thin-walled tubular torsion experiment was performed to a plastic shear strain of 1.0. The specimen geometry is shown in Fig. 5-13. The two important geometric ratios in the tubular torsion experiment are $\frac{l}{d}$ and $\frac{d}{t}$, where l, d, t denote the gauge length, the mean diameter and the wall thickness respectively (White [1992]). From Fig. 5-13, $\frac{l}{d} = 0.61$ and $\frac{d}{t} = 13$ for our specimen geometry. A specimen whose wall thickness is only a small fraction of the mean diameter of the tube will have a reasonably uniform shear strain distribution through the wall thickness. A large $\frac{l}{d}$ ratio can cause the specimen to buckle. The ratio $\frac{l}{d} = 0.31$ and $\frac{d}{t} = 26$ were used for the tubular torsion specimen by White *et al.* [1990] to avoid buckling and have a reasonably uniform shear strain distribution in the wall. The $\frac{d}{t}$ ratio for our specimen is smaller than that used by White *et al.* and therefore, the shear strain distribution in the wall of our specimen is only approximately uniform. As tantalum is very expensive, about $ 40/lb, we were limited to the half inch rod. Starting from a half inch rod, this was the optimum specimen geometry that we could obtain.

The torsion experiment was simulated by subjecting a single ABAQUS-CPE4 element to simple shear. The experimentally-measured and predicted shear stress and the normal stress response are shown in Fig. 5-14. As seen from this figure, although the shear stress is reasonably well predicted by the model, the normal stress is overpredicted at shear strain levels above 60%. The experimentally-measured texture and the predicted texture are shown in Fig. 5-15. The agreement is reasonable.

Having examined the capability of the model to predict reasonably satisfactorily the anisotropic stress-strain response and evolution of crystallographic texture under a few different monotonic strain paths to large strains under quasi-static conditions, in the next chapter we evaluate the predictive capability of the model to simulate the important geometry changes in the quasi-static cup-drawing experiments and the Taylor cylinder-impact experiments under dynamic loading conditions.

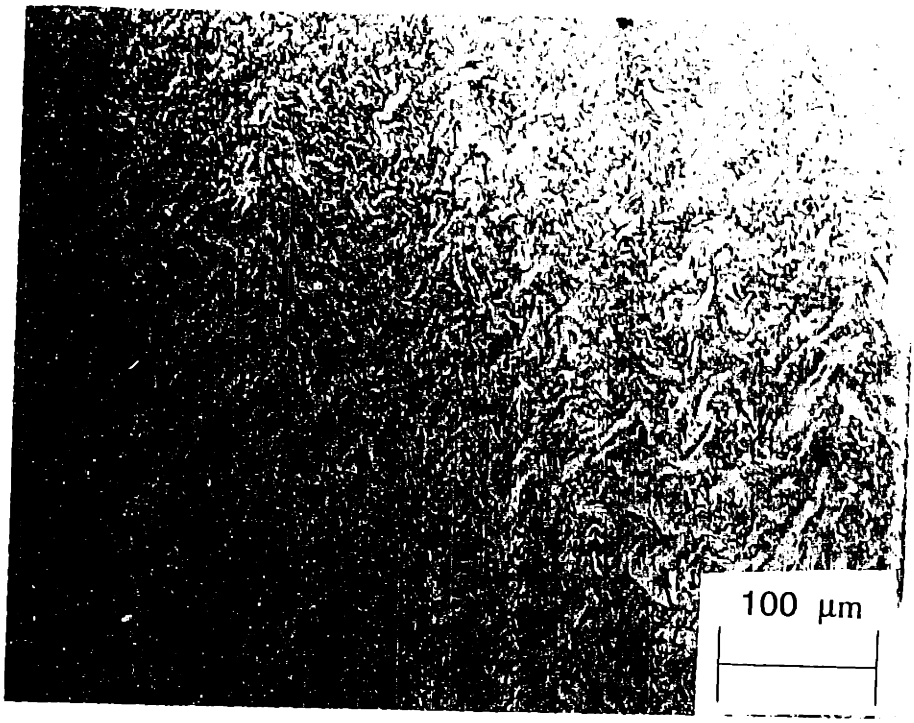

(a)

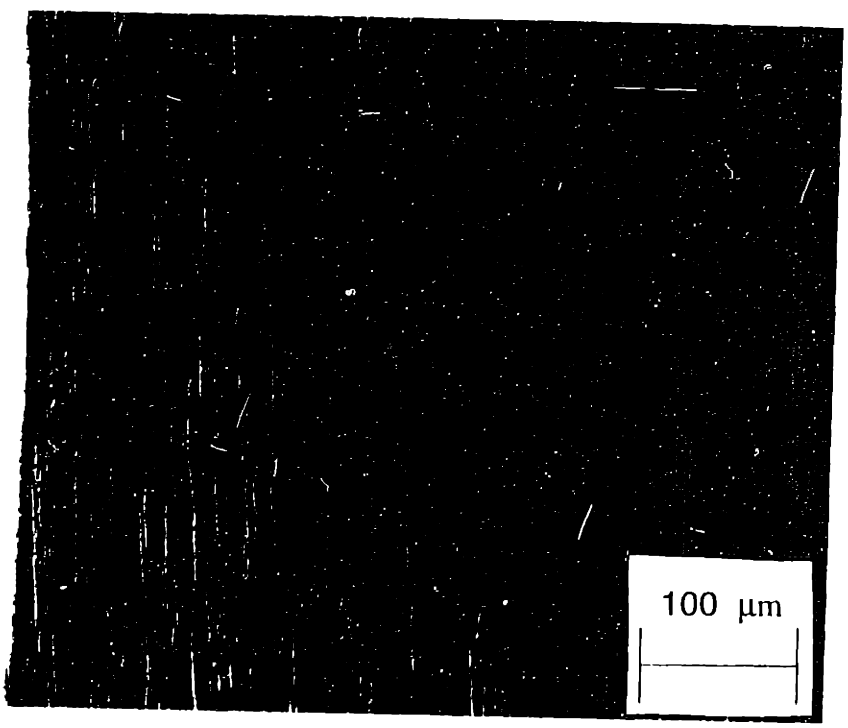

(b)

Figure 5-1: Optical micrograph of as-received tantalum rod : (a) section perpendicular to rod axis (b) section parallel to rod axis.

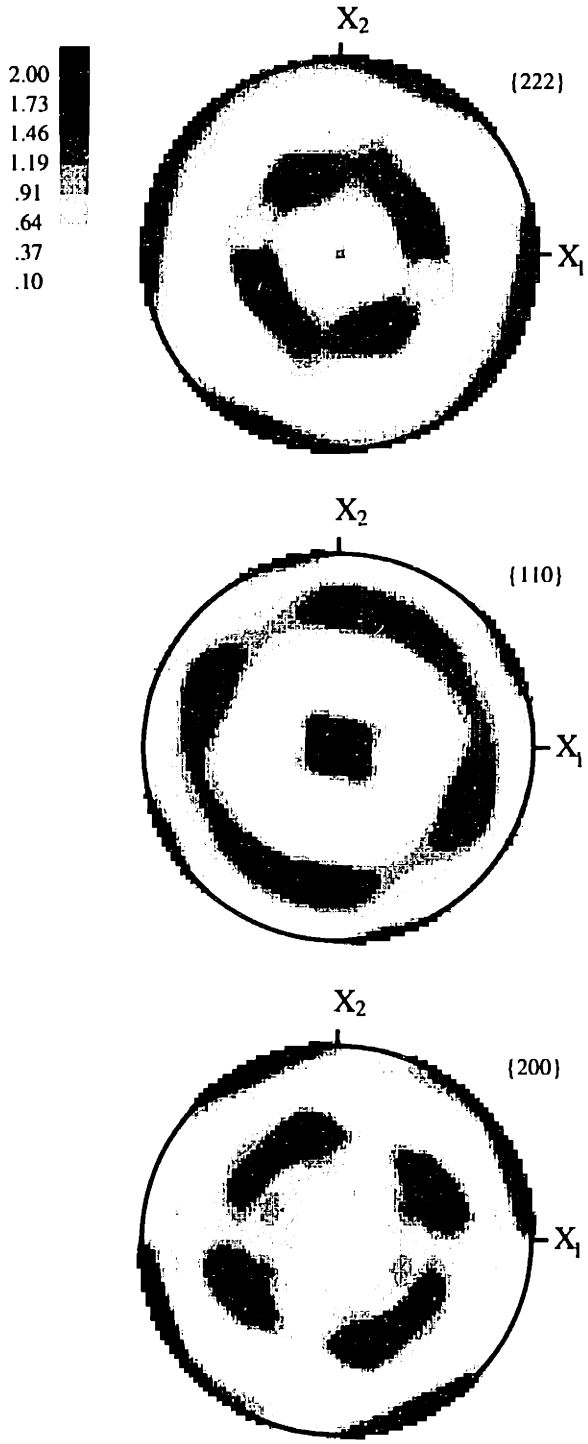

Figure 5-2: As-received texture of tantalum rod.

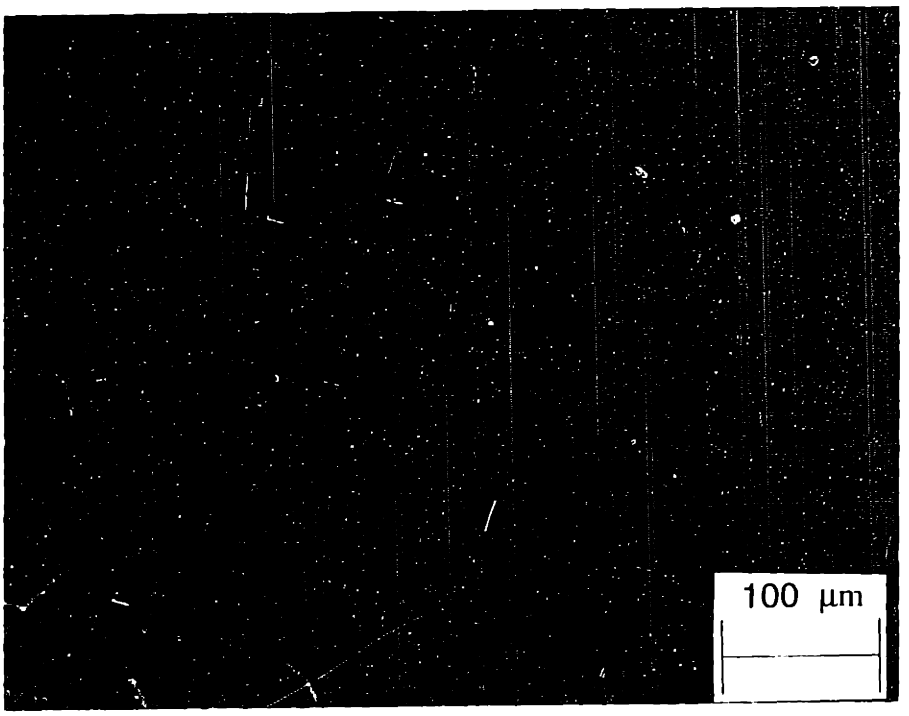

(a)

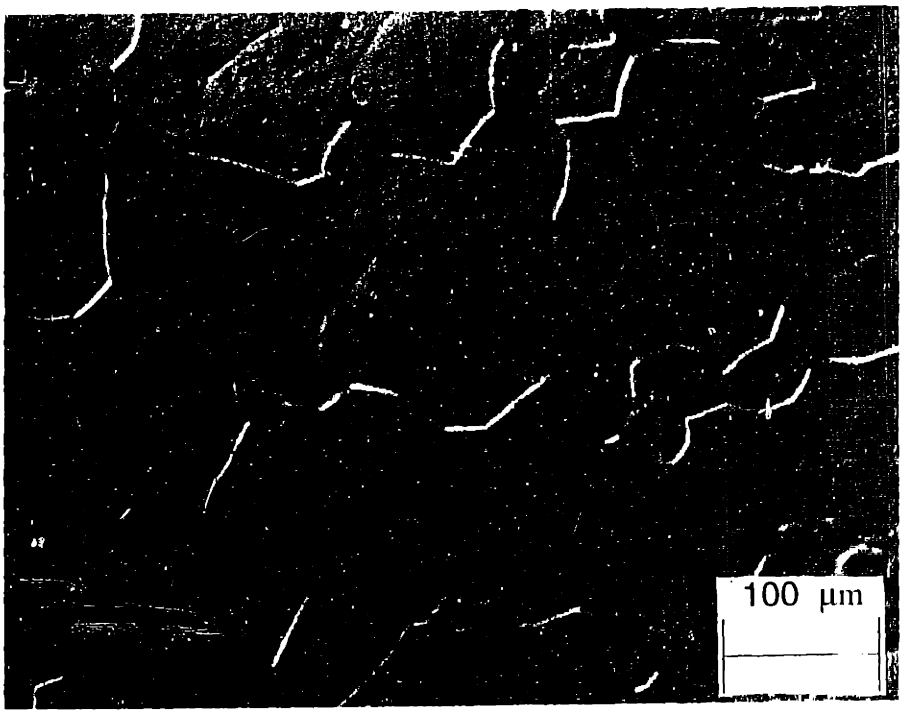

(b)

Figure 5-3: Optical micrograph of annealed tantalum rod : (a) section perpendicular to rod axis (b) section parallel to rod axis.

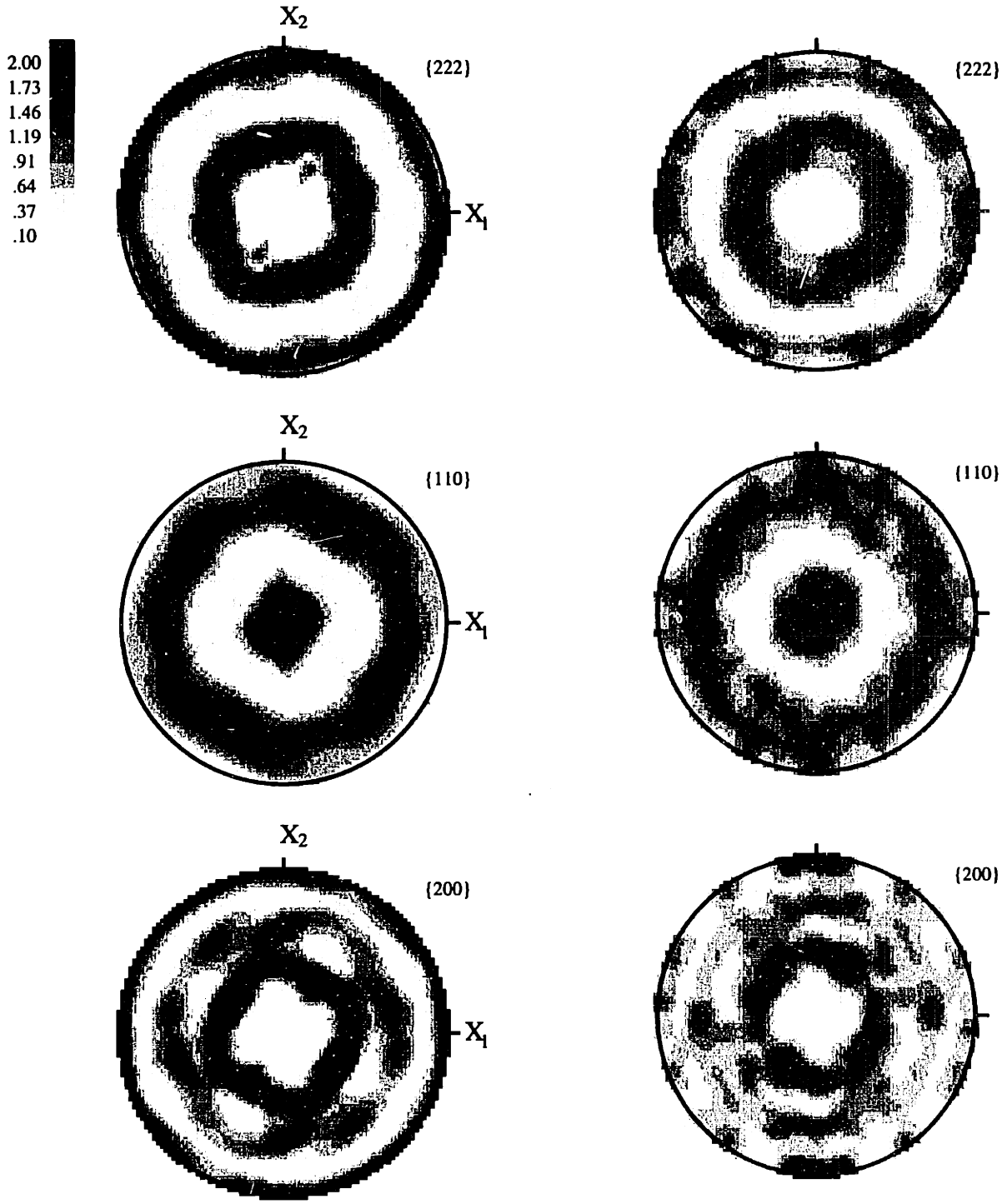

Figure 5-4: Representation of the texture of annealed b.c.c. tantalum with 400 weighted grains.

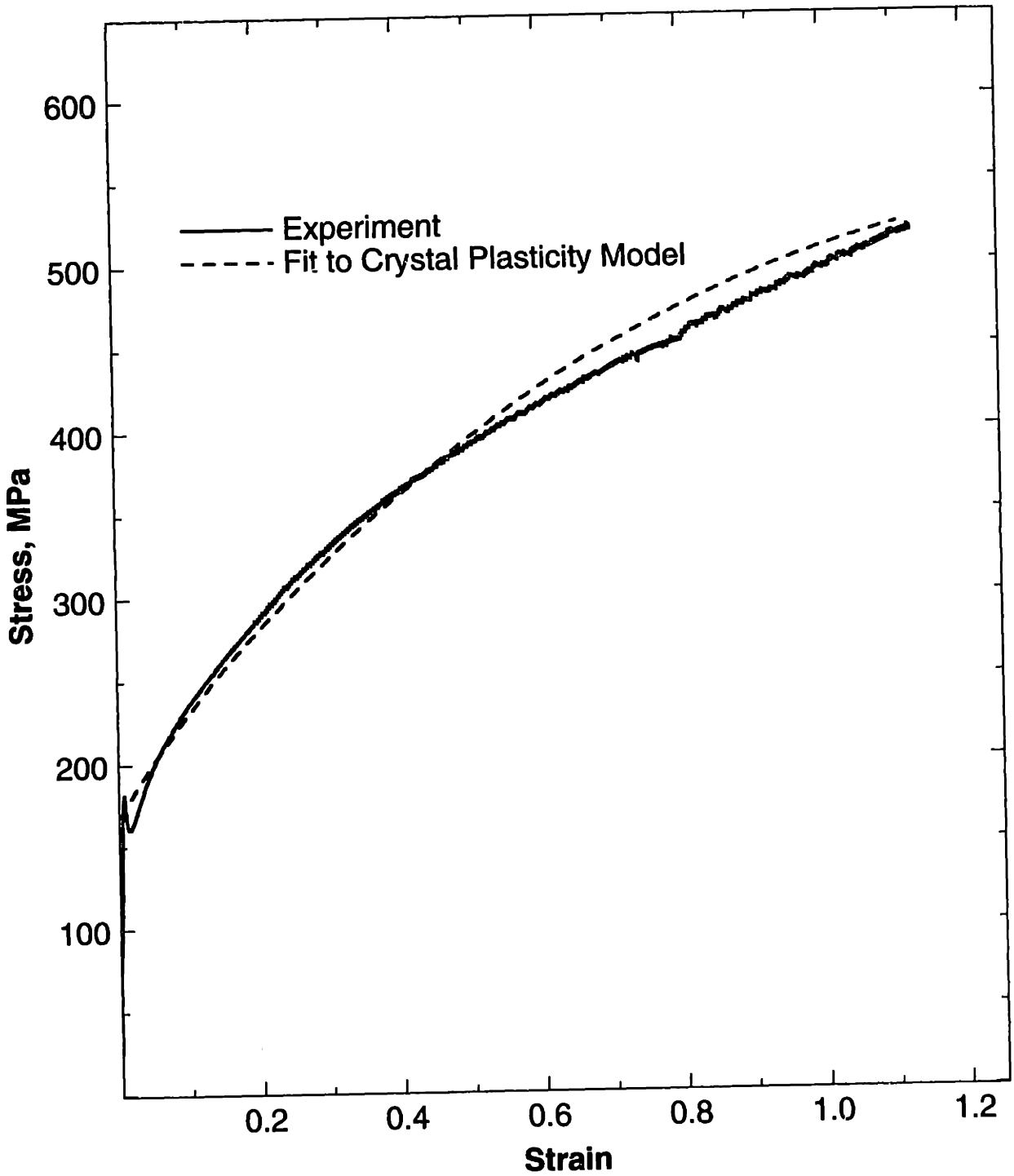

Figure 5-5: Fit of the prediction from the Taylor-type crystal plasticity model against the measured stress-strain response in simple compression experiment on annealed b.c.c. tantalum.

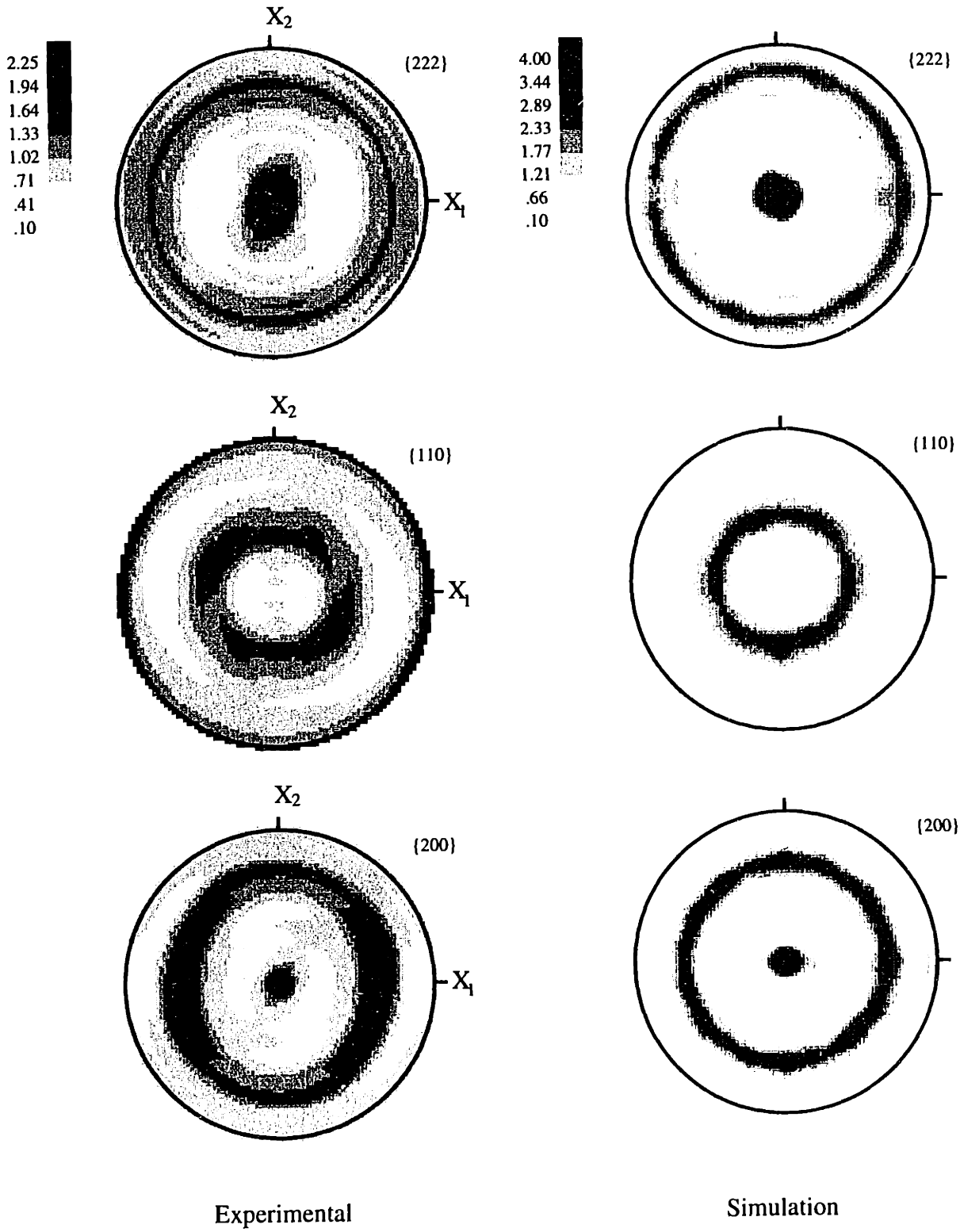

Figure 5-6: Comparison of the measured texture in the simple compression experiment on annealed b.c.c. tantalum against the texture predicted by the Taylor-type crystal plasticity model.

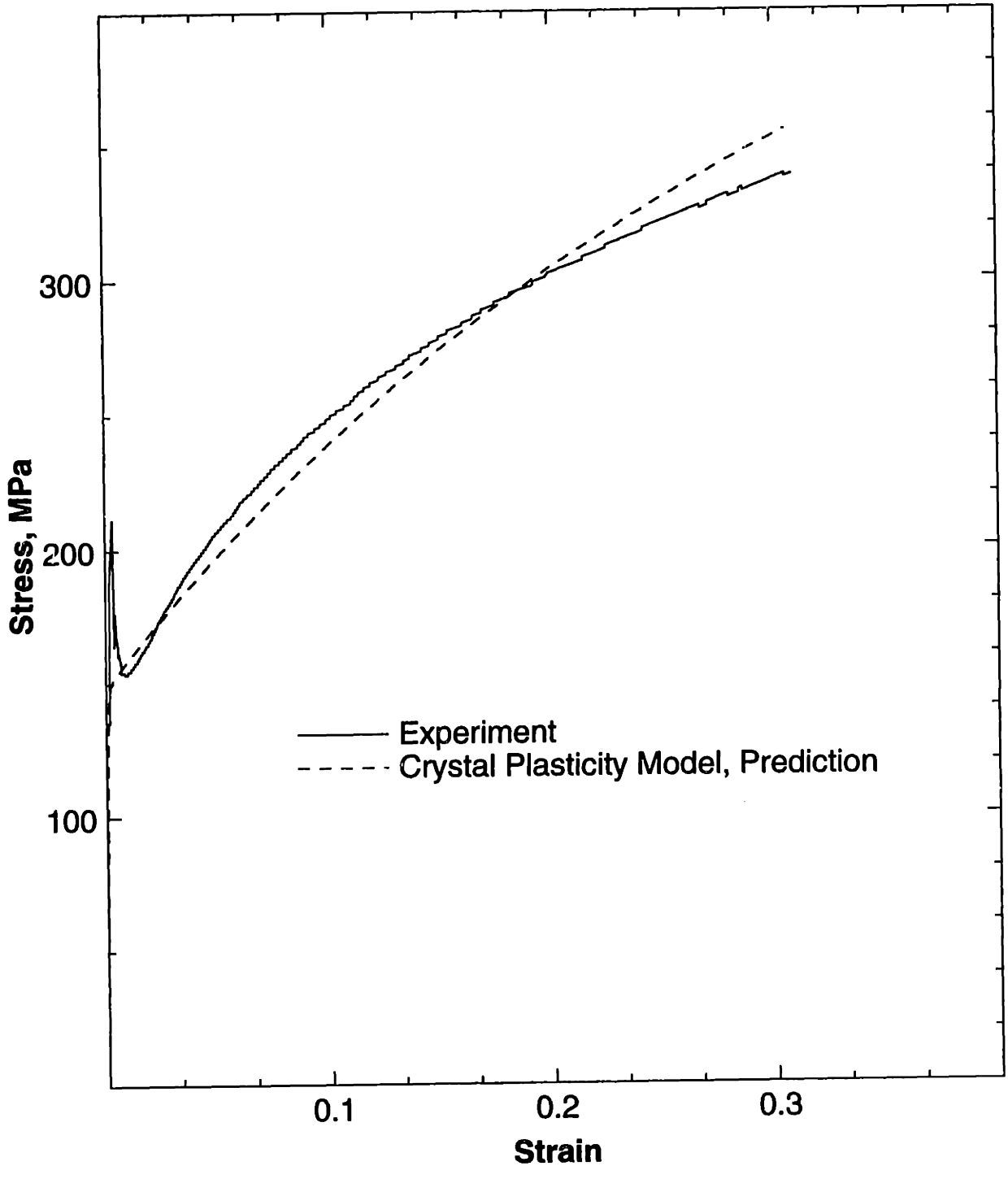

Figure 5-7: Measured and simulated stress-strain response from the Taylor-type crystal plasticity model for the simple tension experiment on annealed b.c.c. tantalum.

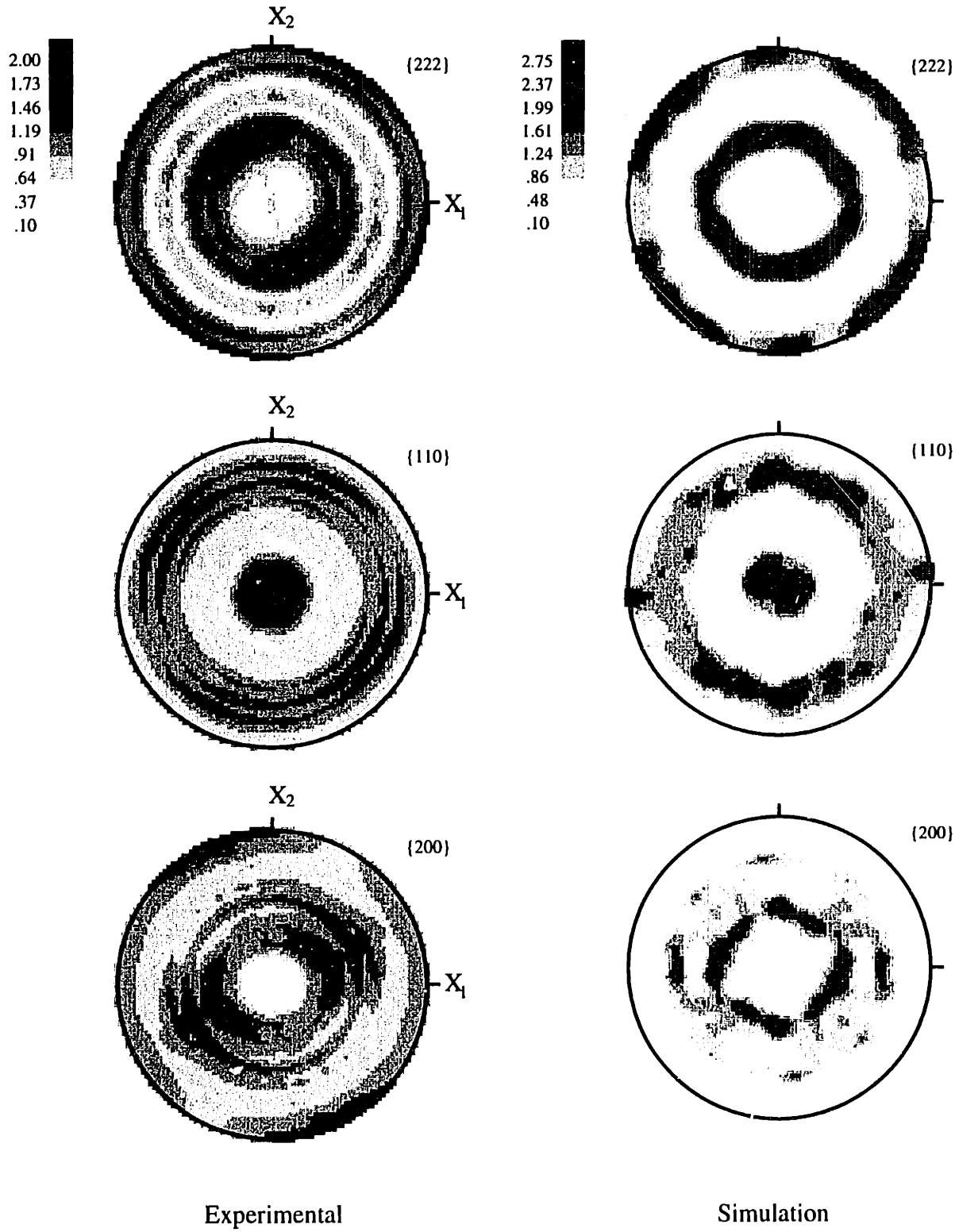

Figure 5-8: Comparison of the measured texture in the simple tension experiment on annealed b.c.c. tantalum against the texture predicted by the Taylor-type crystal plasticity model.

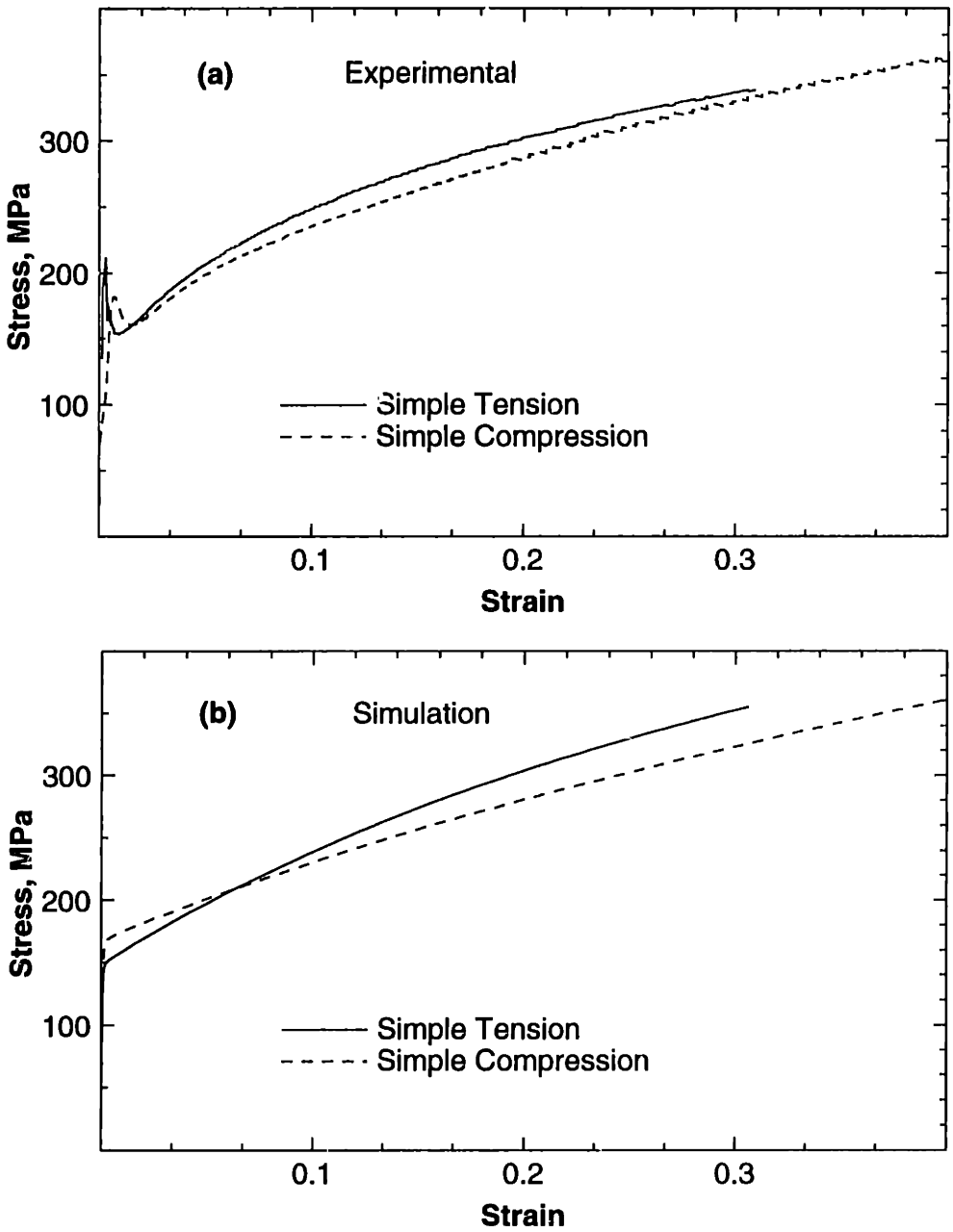

Figure 5-9: (a) Measured stress-strain response for simple compression and simple tension. (b) Simulation using the Taylor model.

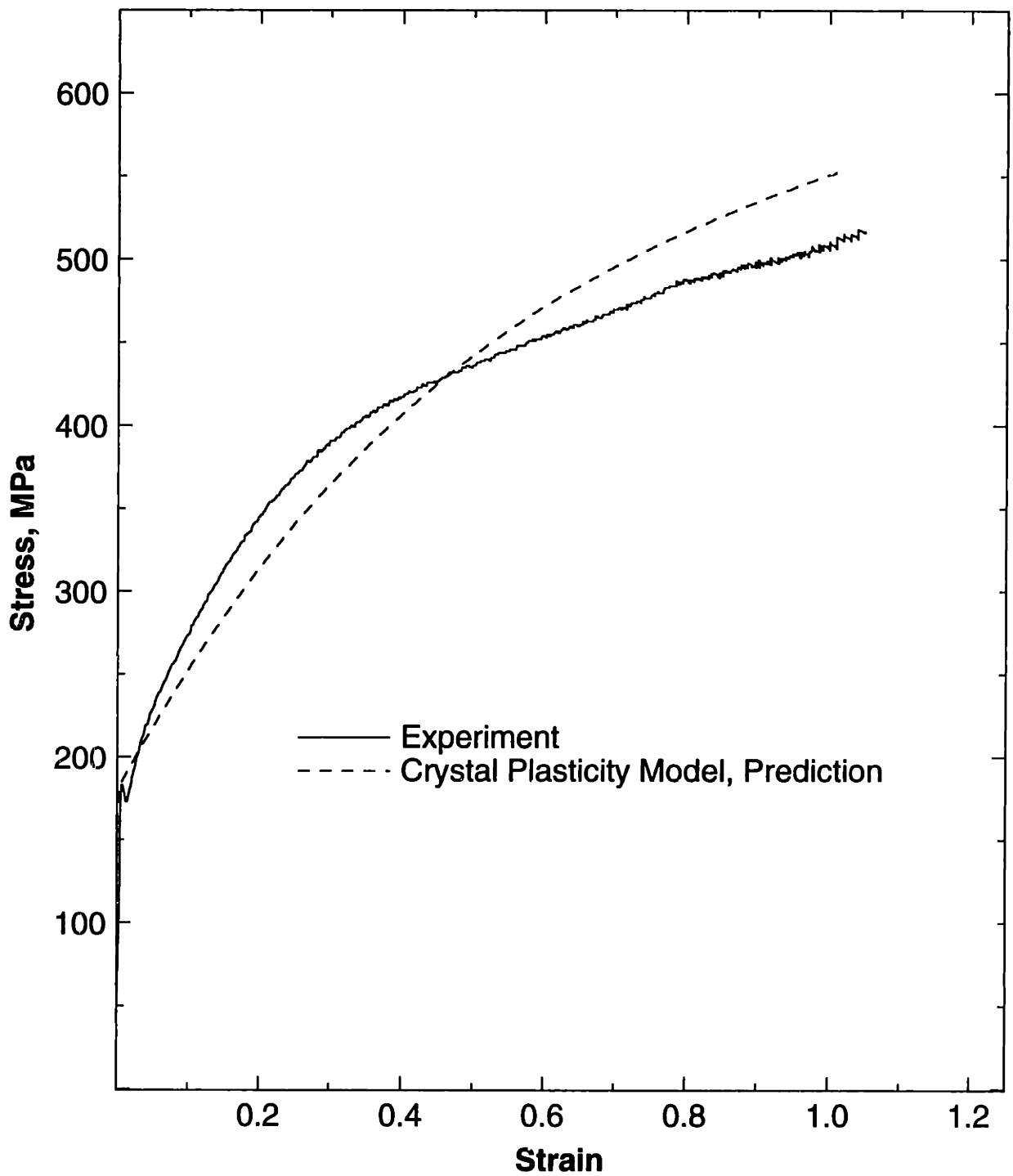

Figure 5-10: Measured and simulated stress-strain response from the Taylor-type crystal plasticity model for the plane strain compression experiment on annealed b.c.c. tantalum.

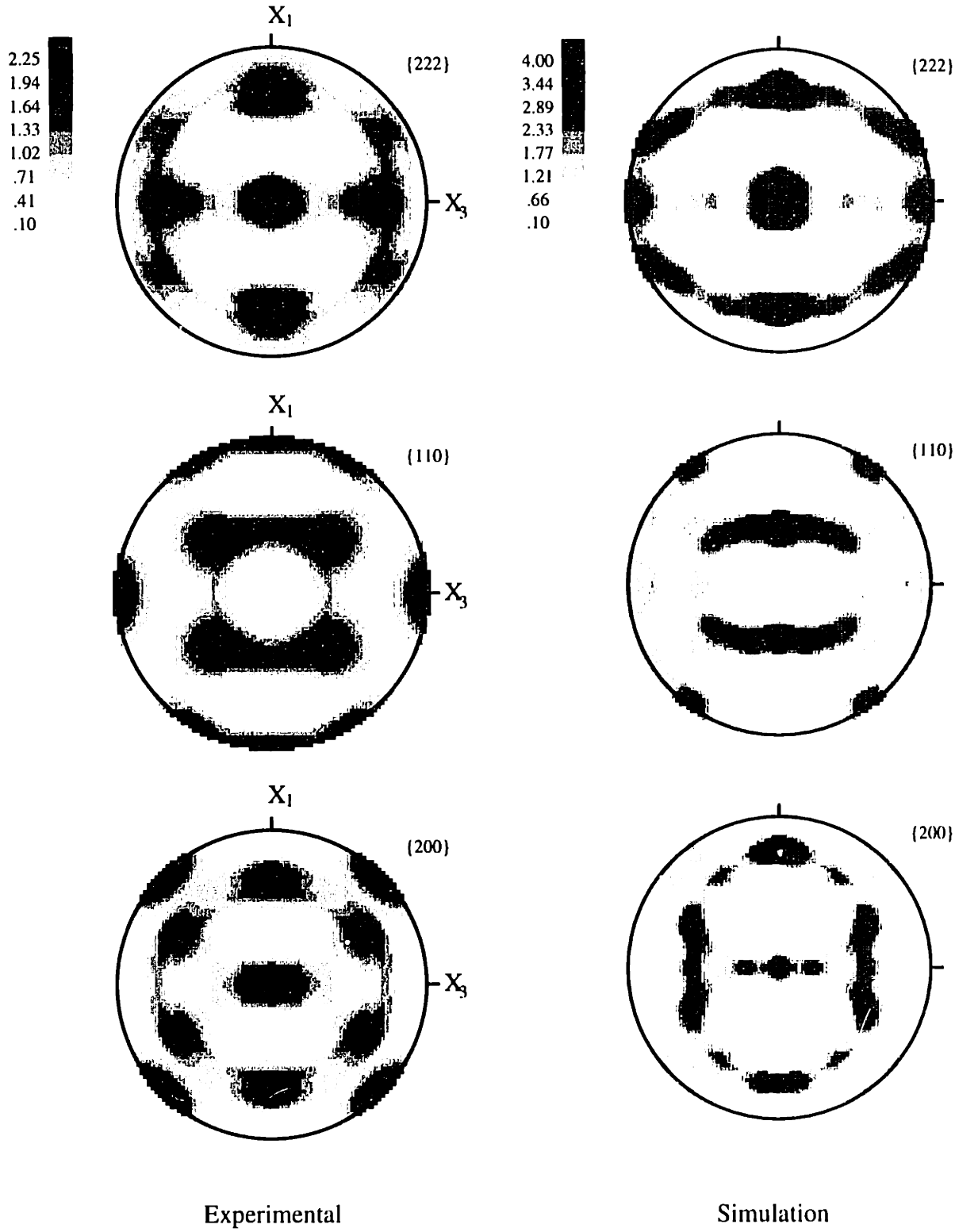

Figure 5-11: Comparison of the measured texture in the plane strain compression experiment on annealed b.c.c. tantalum against the texture predicted by the Taylor-type crystal plasticity model.

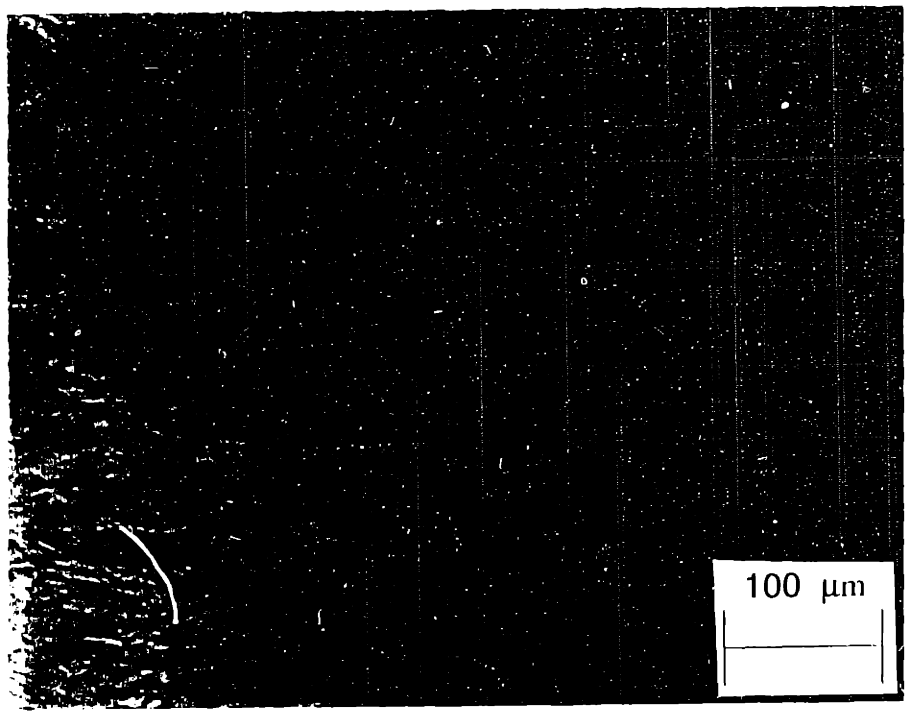

Figure 5-12: Optical micrograph of tantalum deformed by plane strain compression at a strain level of -1.0.

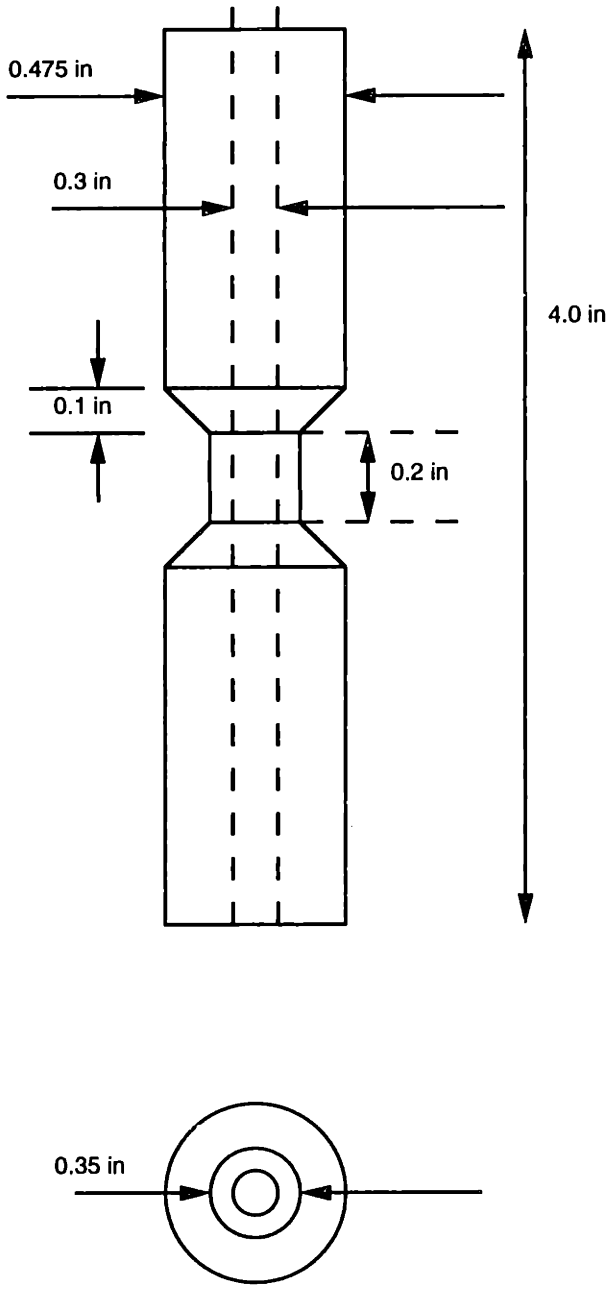

Figure 5-13: Thin-walled tubular torsion specimen.

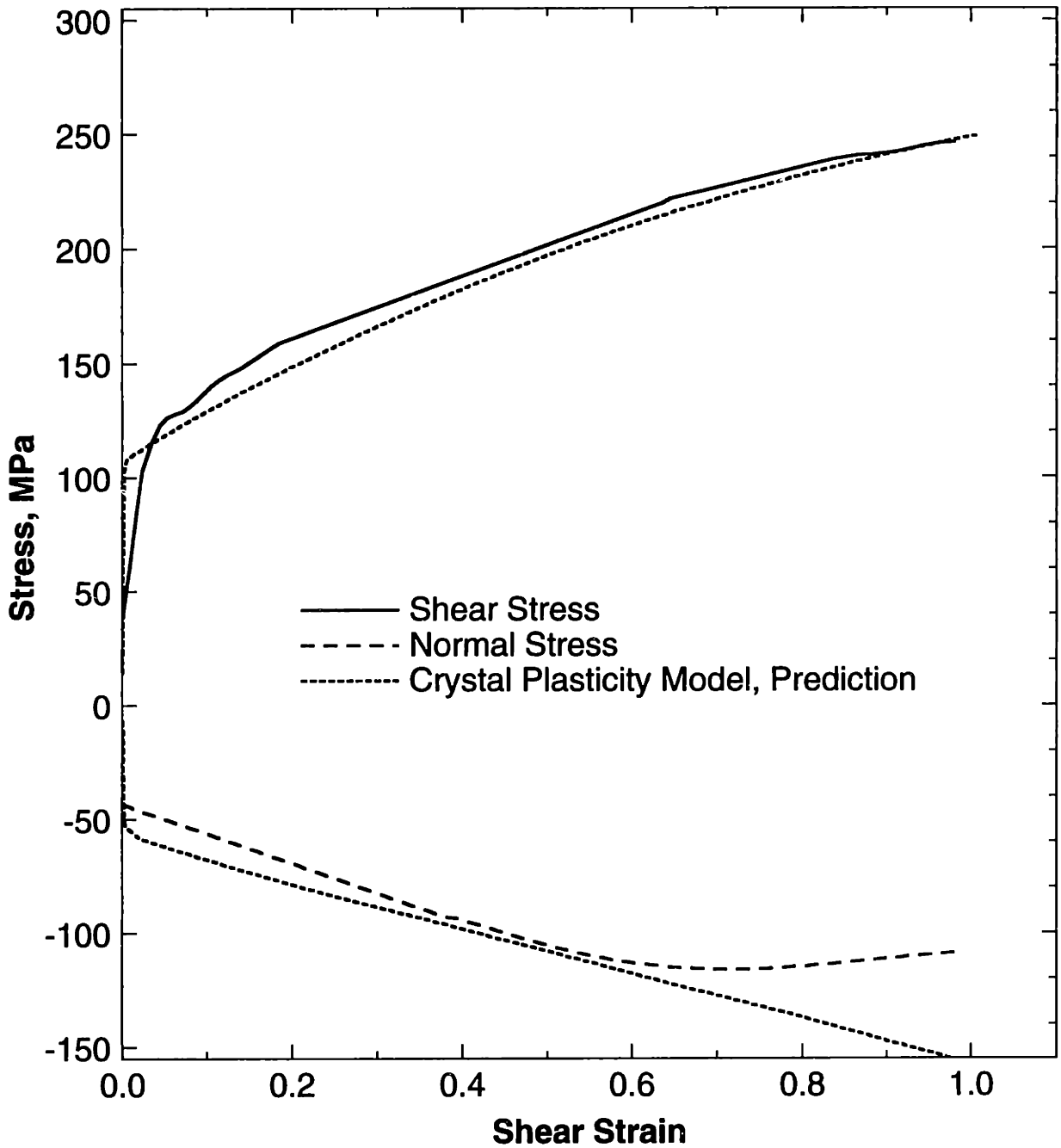

Figure 5-14: Measured and simulated stress-strain response from the Taylor-type crystal plasticity model for the simple torsion experiment on annealed b.c.c. tantalum.

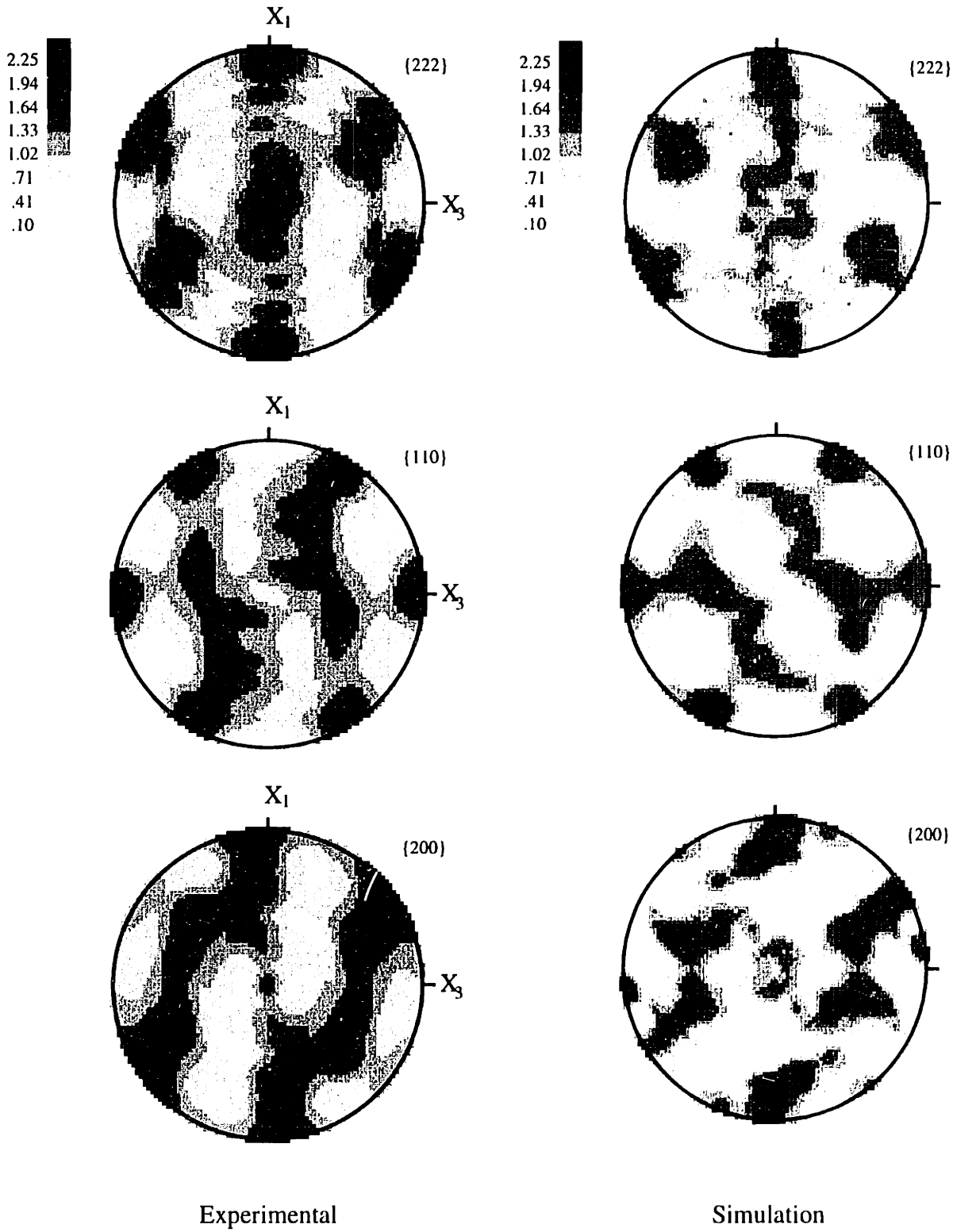

Figure 5-15: Comparison of the measured texture in the simple torsion experiment on annealed b.c.c. tantalum against the texture predicted by the Taylor-type crystal plasticity model.

Chapter 6

Non-Homogeneous Deformations on Pre-Textured Tantalum

In this chapter, we turn our attention to the simulation of non-homogeneous deformations. Specifically, we consider (i) quasi-static cup drawing experiments on sheets of tantalum, and also on a tantalum - 2.5% tungsten alloy, and (ii) dynamic rod-impact experiments on pre-textured tantalum cylinders. The numerical predictions are compared against experimentally measured macroscopic shape changes and the load-displacement response.

6.1 Quasi-Static Cup Drawing Experiments

Cup drawing tests are considered to provide a good measure of the drawability of sheet metals (e.g., Wilson and Butler [1961]; Hosford and Caddell [1993]). In this experiment, a flat blank is constrained while the center portion of the sheet is pressed into a die opening to draw the metal into a shape of cylindrical cup without folding of the corners. An important defect that forms during the cup drawing operation is earing. This defect is strongly dependent on the initial crystallographic texture of the sheet (Underwood [1961]).

The quantitative prediction of the earing behavior is a classical problem of anisotropic plasticity (e.g., Tucker [1961]; Wilson and Butler [1961]; Becker *et al.* [1993]; Balasubramanian and Anand [1996]). Only recently, Balasubramanian and Anand [1997] have shown that a crystal plasticity model can quantitatively predict the number, location and height of the ears as well as the punch load-displacement response in cup drawing operations on sheets of a f.c.c. aluminum alloy.

For b.c.c. metals, the quantitative prediction of the earing pattern has been based on Tucker's theory [1961]; for example see Inagaki [1991] and Kanetake [1991]. In these calculations, the stress state in the flange of the cup is assumed to be plane stress which consists of tensile stress in the radial direction, and an equal and opposite compressive stress in the circumferential direction. The stress in the through thickness direction of the flange is assumed to be zero. The Sachs [1928] polycrystalline model is used wherein the stress state in each crystal in the polycrystalline aggregate is assumed to be identical. With the slip systems known for b.c.c. crystals, the radial strain is determined for a given level of circumferential stress. Since the wall height of the drawn cup is proportional to the radial strain, the earing behavior is predicted from the variation of the radial strain with the angle from the rolling direction. Some of the limitations of these models are :

- The assumption of plane stress in the flange is only approximately correct. The presence of blankholder force and friction can change the stress state in the flange significantly.
- The accuracy of the Sachs assumption for b.c.c. crystals has not yet been demonstrated.
- The punch load-displacement respone cannot be predicted by these models as the calculations are carried out without using finite element methods.

Hence, there is a need for crystal plasticity models which can accurately predict both the earing pattern and the load-displacement response in cup drawing of b.c.c. metals.

In this work, we carried out quasi-static cup drawing experiments on rolled tantalum and tantalum - 2.5% tungsten sheet[1]. The initial crystallographic texture of the as-received sheets was measured by x-ray irradiation. Figs. 6-1 and 6-2 shows the measured and the numerical representation of the initial texture by a weighted average over 200 and 25 grains for tantalum and tantalum - 2.5% tungsten sheet respectively. Although the numerical representation of the initial texture using 200 weighted crystal orientations is more accurate than the 25 weighted crystal orientations, it is computationally very expensive to use in the simulations with the crystal plasticity model. Therefore, we use the 25 weighted crystal

[1]Mr. Chris Michaluk from Cabot Corporation kindly provided us with the tantalum - 2.5% tungsten sheet. (Address: Cabot Performance Materials, P.O. Box 1608, County Line Road, Boyertown, PA ; Tel. no: 610-367-2181).

orientations for the representation of the initial texture of the sheets in our numerical simulations.

The rolling textures in metals are typically represented by the notation $(hkl)[uvw]$, where (hkl) refers to the rolling plane normal and $[uvw]$ refers to the rolling direction. Inverse pole figures are often used to represent the rolling textures of metals. The normal to the sheet and the rolling direction of the sheet are plotted with respect to the crystallographic axes. For the tantalum and tantalum - 2.5% tungsten sheet, the inverse pole figures, computed from the measured pole figures using popLA, is presented in Figs. 6-3(a) and 6-3(b) respectively. As seen from this figure, the tantalum sheet has a strong component of (111) planes parallel to the rolling plane, whereas the rolling direction is more or less equally represented by all crystallographic directions. This is referred to as the (111) $< uvw >$ type texture. One of the texture components in the tantalum - 2.5% tungsten sheet is also of the (111) $< uvw >$ type. In addition, there is a component of (100) planes parallel to the rolling plane, and [100] directions parallel to the rolling direction, a component referred to as the (100)[100] type, or cube texture.

Sheet-tension tests (ASTM E8) were performed to obtain the material parameters for the two sheets. Fig. 6-4(a) shows a schematic of the sheet-tension specimen. The tests were performed at a constant cross-head velocity of 0.05 mm/sec. The measured load-displacement and the stress-strain curves are presented in Figs. 6-5(a) and 6-5(b) respectively. The displacement in Fig. 6-5(a) was measured using the cross-head displacement, while the strain in Fig. 6-5(b) was measured by using an extensometer with a gauge length of 25.4 mm and a traverse of $\pm$ 2.54 mm. Once the limits of the extensometer were reached, the test was momentarily stopped to remove the extensometer and re-started to measure the load-displacement response until failure. Note that a displacement of 20 mm in Fig. 6-5(a) corresponds to a engineering strain level of $\approx$ 79%. This is much larger than the strain measured by the extensometer in Fig. 6-5(b).

The effect of tungsten alloying on the mechanical properties of tantalum can be seen in the sheet-tension tests on tantalum and tantalum - 2.5% tungsten alloy, Fig. 6-5. The tantalum - 2.5% tungsten alloy has (a) a higher yield strength, (b) a higher strain-hardening rate, and (c) a lower ductility than pure tantalum. The lower ductility observed in the sheet-tension test on Ta-2.5W is also due to its initial crystallographic texture. It is known that in b.c.c. metals, the normal anisotropy, as measured by the Lankford Parameter R, is

higher for a sheet containing a component of (111) planes parallel to the rolling plane when compared to a sheet containing a component of (100) planes parallel to the rolling plane (Goodman and Hu [1970]; Hu [1978]). A larger value of R results in a greater resistance to through-thickness thinning and hence, a larger ductility. This behavior is consistent with the measured initial textures of our sheets, the tantalum sheet with a (111) $< uvw >$ type texture exhibits a larger cross-head displacement before failure in comparison to the Ta-2.5W sheet that has a combination of (111) $< uvw >$ and (100)[100] type texture.

The flow parameters in the crystal plasticity model for tantalum are the same as those used previously, equation (4.1). Ta-2.5W alloy has a higher yield strength than pure tantalum due to solid solution strengthening, Fig. 6-5(b). The yield strength of tantalum at a strain rate of $10^{-3}\,\mathrm{sec}^{-1}$ as a function of tungsten alloying content has been recently measured by Chen and Gray [1996] and is is plotted in Fig. 6-6. The increase in the yield strength with tungsten content is approximately linear. We model this strengthening effect by increasing the thermal part of the deformation resistance s_* as the solute particles act like short-range obstacles to dislocation motion[2] (Conrad [1964]). For a tungsten content of 2.5%, the increase in the yield stress is 75 MPa. Dividing by a "Taylor Factor"[3] of $M = 3$, we take the increase in s_* to be equal to 25 MPa. With the other flow parameters $\{\dot{\gamma}_0, \Delta F^*, p, q\}$ assumed to be the same as for tantalum, equation (4.1), the flow parameters estimated for Ta-2.5W are

$$\dot{\gamma}_0 = 1.73 \times 10^7\,\mathrm{sec}^{-1},\ \Delta F^* = 2.77 \times 10^{-19}\mathrm{J},\ p = 0.28,\ q = 1.34,\ s_* = 425\mathrm{MPa}. \quad (6.1)$$

The strain-hardening parameters for the Ta and Ta-2.5W sheets were obtained by fitting the load-displacement and the stress-strain curves measured in the sheet-tension tests. The simulation of the sheet-tension experiment was performed in ABAQUS/Explicit. A finite element representation of the specimen using 180 ABAQUS-C3D8R continuum elements is shown in Fig. 6-4(b). The values for the hardening parmeters were adjusted so that the numerical results from the finite element calculation of the sheet-tension experiment matched the corresponding experimental data. The load-displacement curve is only fit to

[2]The solute particles can also increase the free-energy barrier, ΔF_*, to dislocation motion if the concentration of the particles is high enough. As the tungsten content in tantalum is small, we make an approximation that the value of ΔF_* in tantalum-2.5% tungsten is identical to that of tantalum.

[3]$M = 3$ only for an initally random aggregate of grains. Since our sheet is pre-textured, this value for M is an approximation.

a displacement level corresponding to the onset of diffuse necking. A refined finite element mesh is needed to capture the localization and the subsequent failure due to necking of the sheet in the thickness direction, Fig. 6-5(a). The material parameters obtained from the fit for tantalum are

$$s_{a,0} = 26\,\text{MPa},\ h_0 = 75\,\text{MPa}, s_{a,s} = 155\,\text{MPa},\ r = 1.1,\ q_l = 1.4,$$

and for tantalum - 2.5% tungsten are

$$s_{a,0} = 40\,\text{MPa},\ h_0 = 250\,\text{MPa}, s_{a,s} = 175\,\text{MPa},\ r = 1.1,\ q_l = 1.4.$$

The numerical fit to the data, as shown in Fig. 6-7, is reasonable. Note that the strain hardening response of Ta-2.5W is different from that of tantalum.

6.1.1 Cup-drawing Experiment

The cup drawing experiment was conducted using a double-action servo-controlled forming press developed by Lee [1983]. A schematic diagram of the geometry of the cup drawing apparatus is shown in Fig. 6-8(a). The apparatus comprises of a round-nosed punch, die and a blankholder of diameters 50.8 mm, 53.035 mm and 58.42 mm, respectively. All surfaces in contact with the deforming metal were polished to a surface finish of 4. The die set [4] consisting of the punch, die and blankholder is constructed of AISI/SAE steel type D2, hardened to a minimum of Rockwell 62. Circular blanks of tantalum and tantalum -2.5% tungsten with a radius 50.8 mm and a thickness of 0.889 mm and 0.762 mm respectively were drawn in the apparatus. Teflon sheets were used as lubricants so as to minimize the friction in the interface between the punch and the blank, the blank and the blankholder, and the blank and the die. To ensure that the Teflon sheets stick and remain in contact with the blank at all times, a small amount of lubricanting oil (SAE20W motor oil) was applied to both sides of the blank before placing the Teflon sheets on them. The cup drawing experiment proceeds through the following stages :

1. The blankholder clamps the blank against the die with a pre-determined force.

2. The punch moves with pre-determined velocity causing deformation of the blank, and drawing in material from between the die and the blankholder.

3. The operation is complete when the entire cup is formed (or when the material fails).

In our experiments, a constant blankholder force of 10 kN was applied, and the cups were drawn with a punch speed of 1mm/sec.

The drawn cups showed four ears: two along the rolling direction and two along the transverse direction of the sheet, Fig. 6-9(a) and Fig. 6-9(b). Small wrinkles can be seen near the ears in the Ta-2.5W cup, Fig. 6-9(b), while no wrinkles appear in the Ta cup. This wrinkling occurs due to the buckling between the ears or the high parts of the cup wall. Ear wrinkling appears late in the draw, when the outer edge of the flange was no longer round, but was already showing evidence of earing. When the low points between the developing ears entered the region of the die lip and were no longer in contact with the blankholder, the compressive circumferential stresses, which are locally increased at these points due to the eccentricity of the flange, were sufficient to cause buckling in these localized regions. Clearly, higher the degree of planar isotropy in the material, lower is the chance of occurence of ear wrinkling. Hence, we observed no ear wrinkling in the Ta cup which has a $\{111\} < uvw >$ type texture.

Fig. 6-10(a) and Fig. 6-11(a) show the cup height as a function of the angle from the rolling direction. The average height of the ears and the troughs for the tantalum cup is 42.8 mm and 41.53 mm, respectively. The average difference between the heights of the ears and the troughs is 1.27 mm. In comparison, the average height of the ears and the troughs of the Ta-2.5W cup is 42.94 mm and 38.93 mm, the average difference being 4.01 mm. As the tantalum sheet has a $(111) < uvw >$ type texture, it exhibits planar isotropy and therefore the difference in the height of the ears and the troughs is small. This difference in the heights is much more pronounced in the tantalum - 2.5% tungsten sheet due to the presence of the cube components - (100)[100] of texture.

The thickness strain in the bottom, corner and the wall of the Ta and Ta-2.5W cups was measured at 0^o, 45^o, and 90^o from the rolling direction, Fig. 6-12 and Fig. 6-13. As seen from these figures, the thinnest region occurs in the cup corner for both Ta and Ta-2.5W. The thickness of the Ta and Ta-2.5W cup increases along its wall. Note that the thickness strain in the wall is higher at at 45^o than at 0^o or 90^o from the rolling direction for the Ta-2.5W cup due to the formation of troughs along this direction. Since the Ta cup shows very little earing behavior, the difference in the thickness strain in the wall along the different directions to the rolling direction is smaller.

6.1.2 Simulation of Cup-Drawing

Fig. 6-8(b) shows the finite element mesh used for the numerical simulation. A total of 672 ABAQUS continuum C3D8R and C3D6 elements were used, with 2 elements through the thickness. Since the initial texture of the sheets possesses orthotropic symmetry, only a 90° sector of the circular blank was considered in the analysis. The interfaces between the punch and the blank, the blank and the blankholder, and the blank and the die were modeled as frictionless. The die, blankholder and punch were treated as rigid surfaces. A mass is attached to the blankholder rigid surface to apply the blankholder force. To speed-up the simulation, density of the blank is artificially increased to increase the stable time increment[5]. The simulation is carried out in two steps : (a) apply a blankholder force of 2500N ($= \frac{10000}{4}$) on the blank in a ramp profile, and (b) keep the blankholder force constant at 2500N and move the punch with a velocity of 1 mm/sec.

The predicted shapes of the fully-drawn tantalum and tantalum - 2.5% tungsten cups are shown in Figs. 6-9(c) and 6-9(d) respectively. These figures also shows the equivalent tensile plastic strain $\bar{\epsilon}^p$ contours in the cup at the end of the drawing process. The prediction of the number of ears and their positions is accurate. The small wrinkling behavior observed near the ears in the Ta-2.5W cup cannot be captured by our simulation as there are only two elements through the thickness of the sheet. The comparison of the predicted cup-height and the punch load-displacement curve against the experiment is shown in Fig. 6-10 for the tantalum cup and in Fig. 6-11 for the tantalum - 2.5% tungsten cup. The predictions of the model are reasonably accurate. The jumps in the calculated punch load-displacement curve occur when an element of the blank, initially under the blankholder, enters the die. These jumps can be minimized by refining the mesh. The prediction of the thickness strain in the bottom, corner and wall of the Ta and Ta-2.5W cup is compared against the corresponding measurements in Figs. 6-14 and 6-15 respectively. The calculations are able to capture the thickness profile in the cups reasonably accurately.

Overall, we conclude that the crystal plasticity model is able to capture the effect of the initial crystallographic texture and its evolution on the macroscopic loads and shape-changes in non-homogenous forming operations as seen from the cup drawing simulations of

[5]In such "density-scaled" simulations one must ensure that the inertial effects remain small. To do this one must monitor the ratio of the total kinetic energy to the total internal (stored elastic plus dissipated plastic) energy during the simulation, and ensure that this ratio does not exceed $\approx 0.01 - 0.05$ at any time during the simulation.

the two sheets with different initial textures. To the best of our knowledge, this is the first-time that complete calculations of the cup-drawing operation has been carried out using the crystal plasticity model for b.c.c. materials.

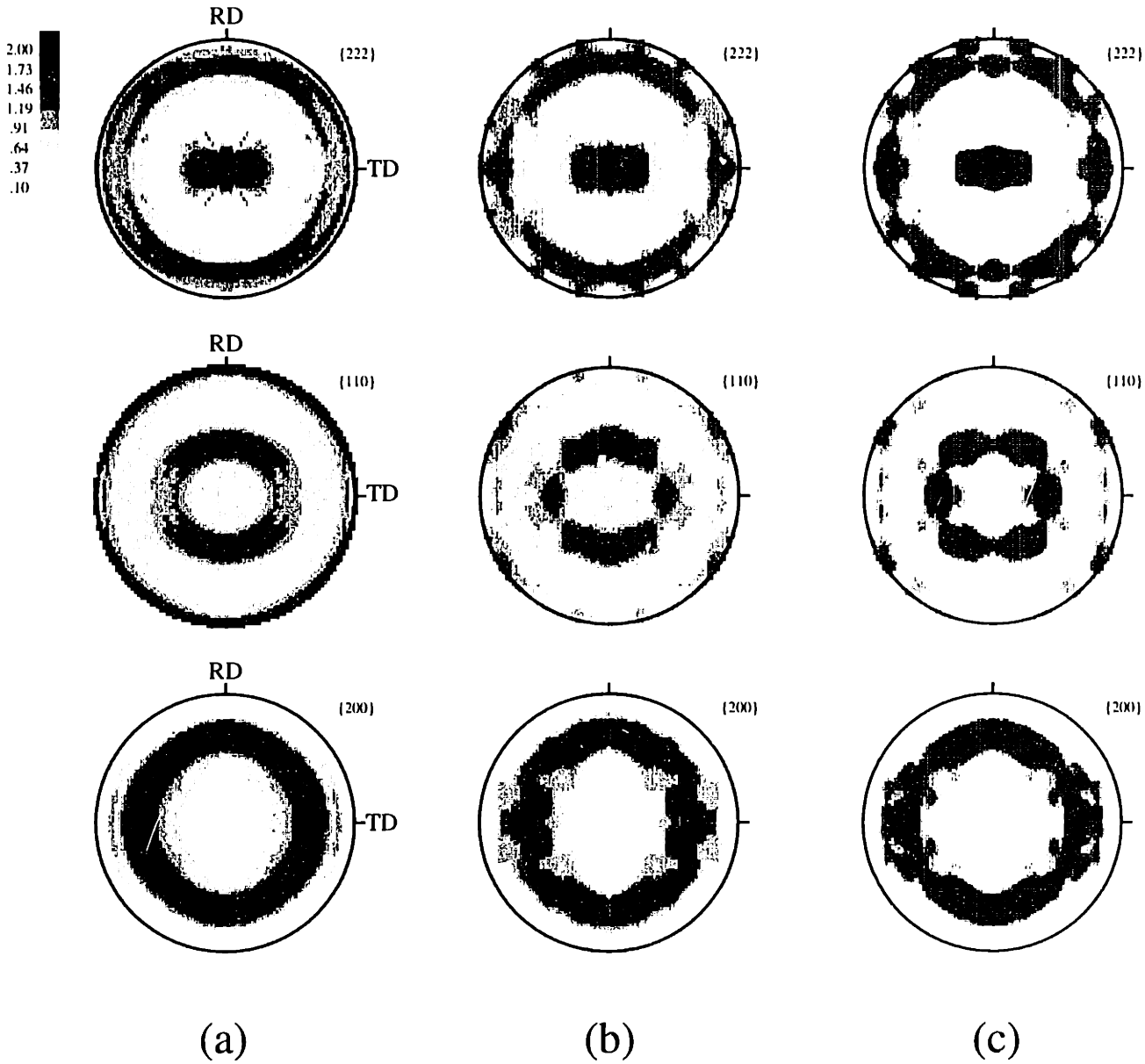

Figure 6-1: Experimentally measured texture of tantalum sheet and it's numerical representation: (a) Measured texture. (b) Numerical representation using 200 weighted grain orientations. (c) Numerical representation using 25 weighted grain orientations.

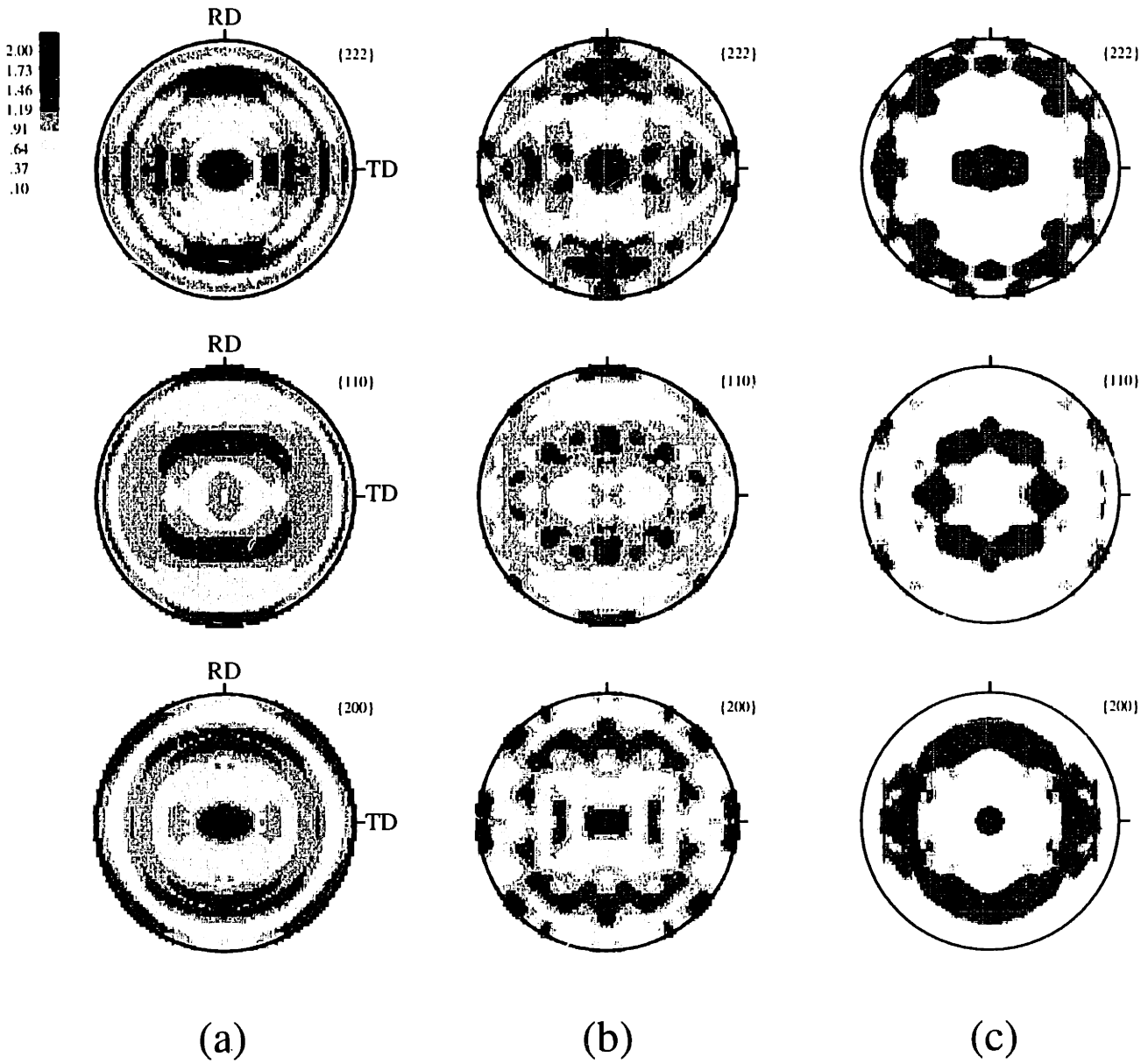

Figure 6-2: Experimentally measured texture of tantalum - 2.5% tungsten sheet and it's numerical representation: (a) Measured texture. (b) Numerical representation using 200 weighted grain orientations. (c) Numerical representation using 25 weighted grain orientations.

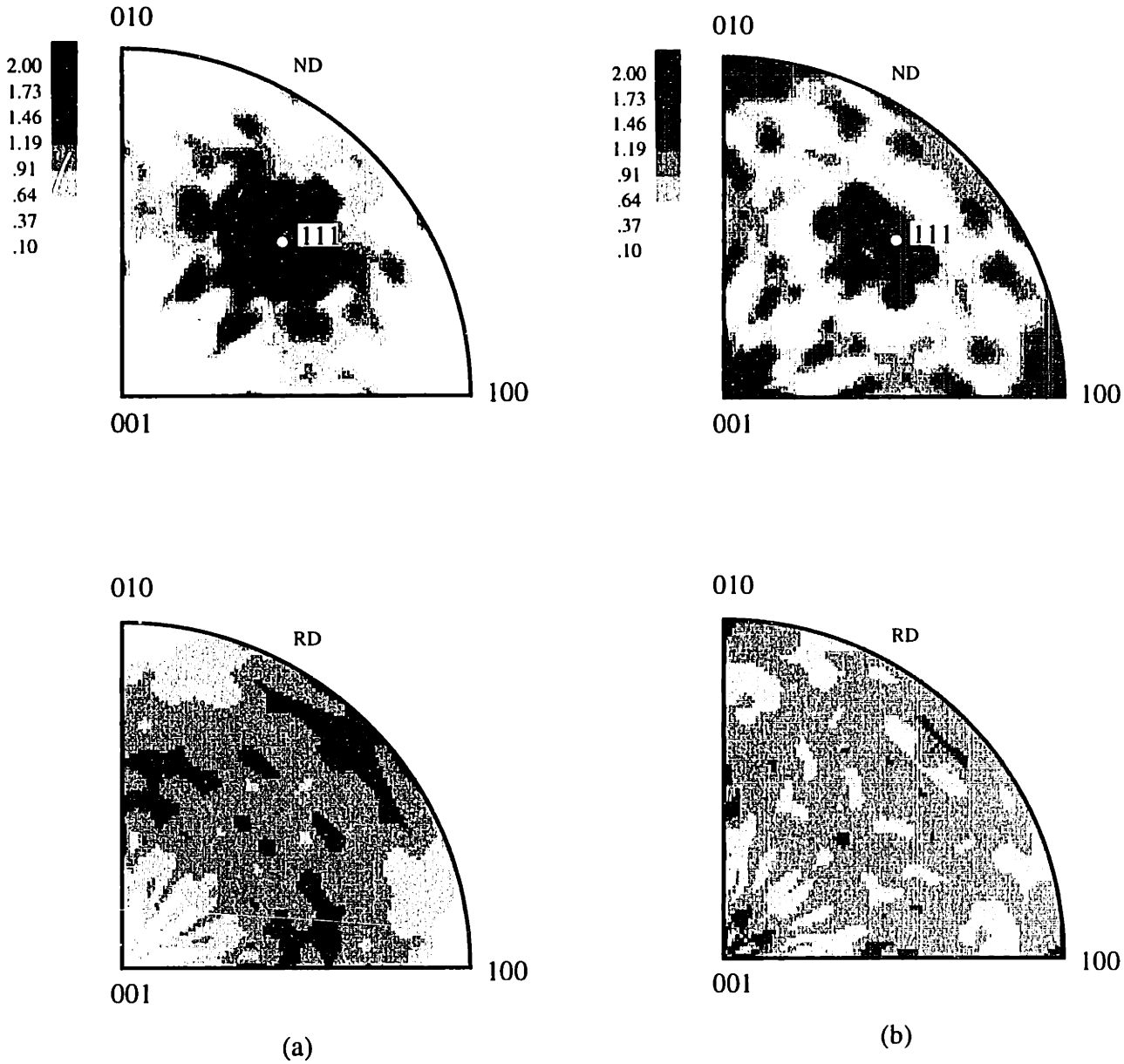

Figure 6-3: Inverse pole figures computed from the measured texture for (a) tantalum sheet, and (b) tantalum - 2.5% tungsten sheet.

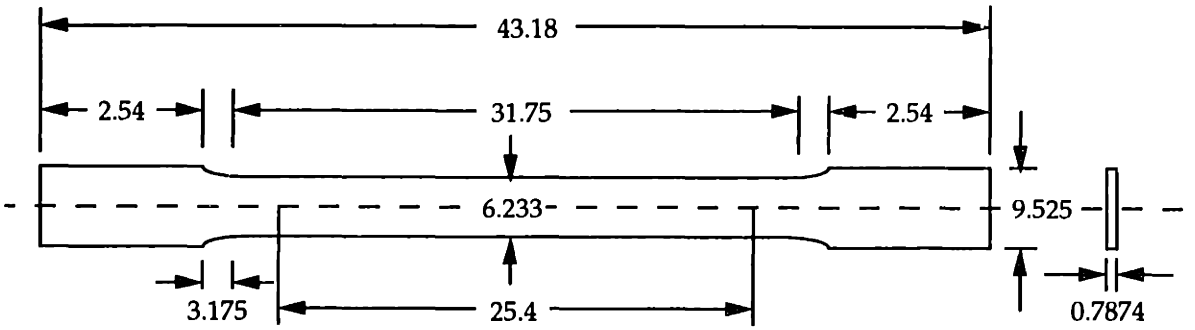

(a)

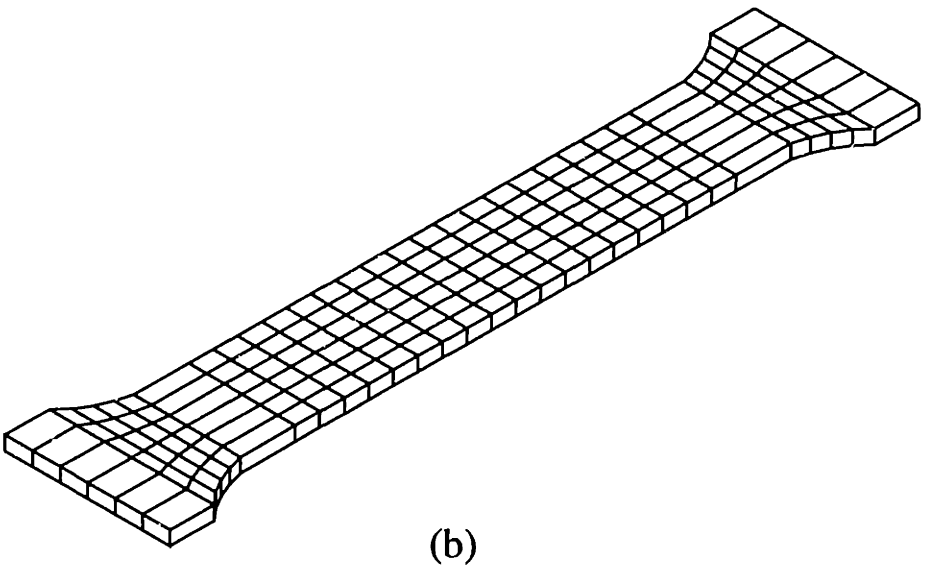

(b)

Figure 6-4: (a) Geometry of the sheet-tension specimen (ASTM E8) (All dimensions are in millimeters). (b) Finite element mesh used for the sheet-tension simulation.

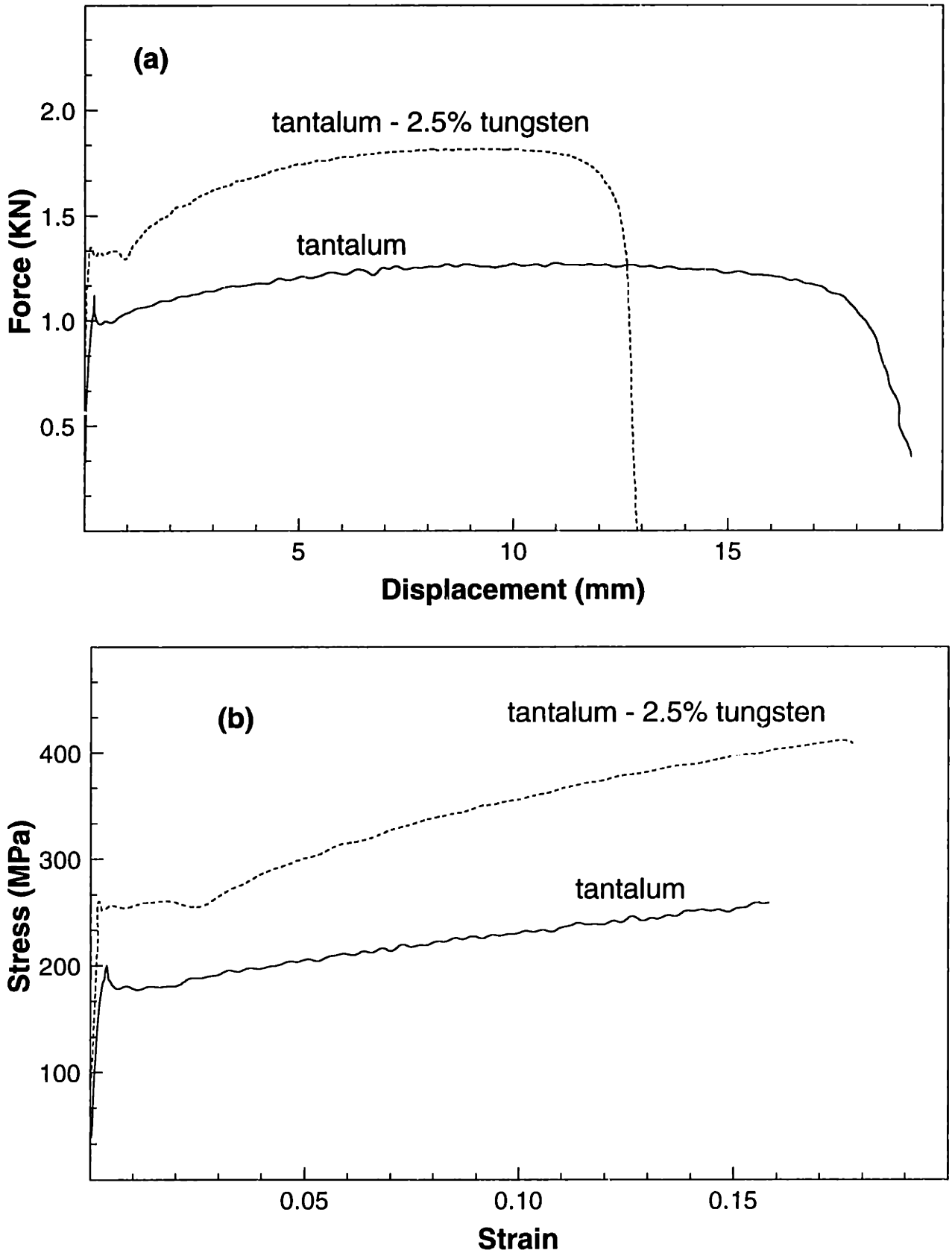

Figure 6-5: (a) The load-displacement response, and (b) the stress-strain response in the tension experiment on tantalum and tantalum 2.5% tungsten sheet along the rolling direction.

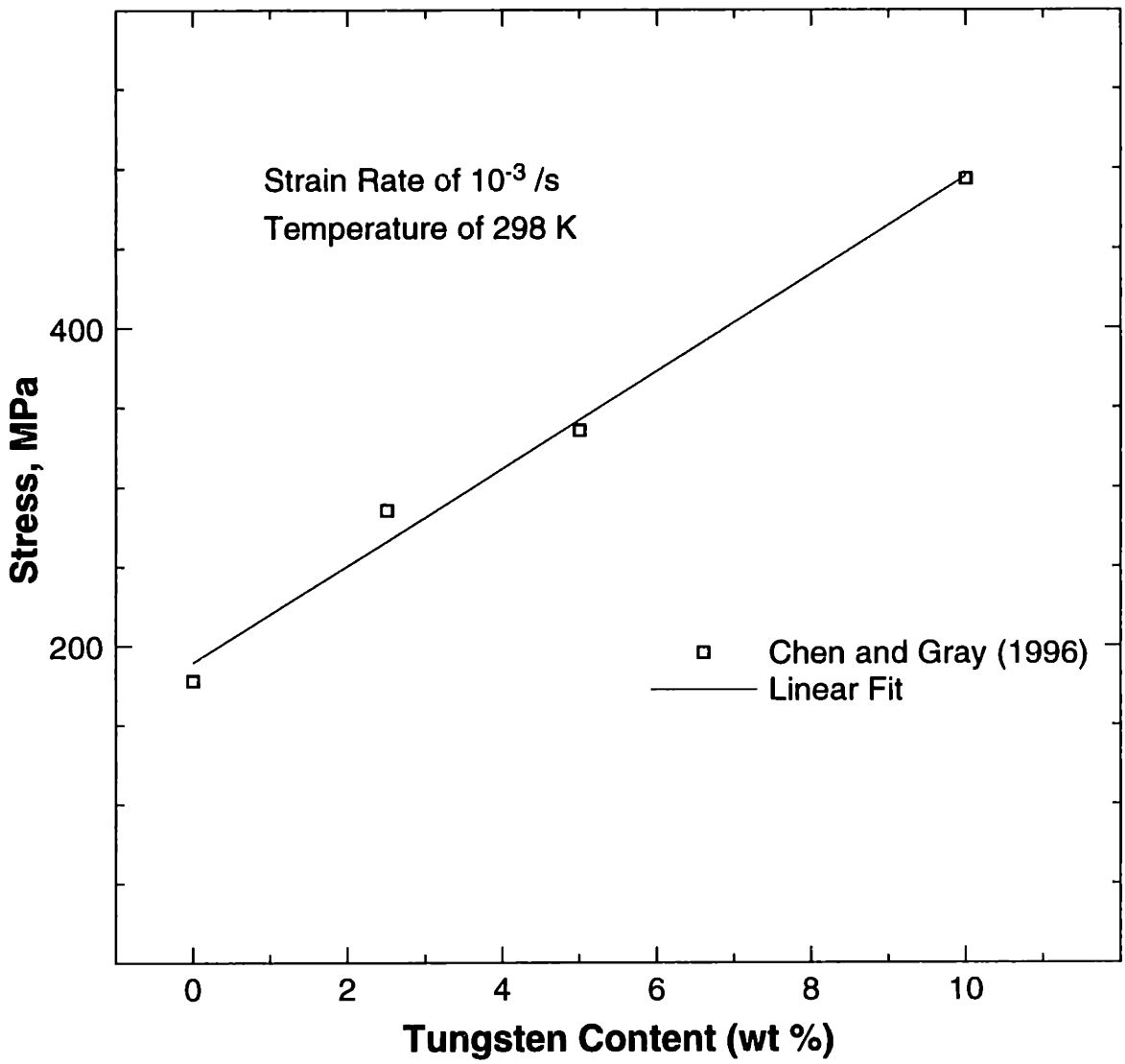

Figure 6-6: Linear fit to the increase in the yield strength as a function of tungsten alloying content in tantalum-tungsten alloys plotted from the experimental data of Chen and Gray (1996).

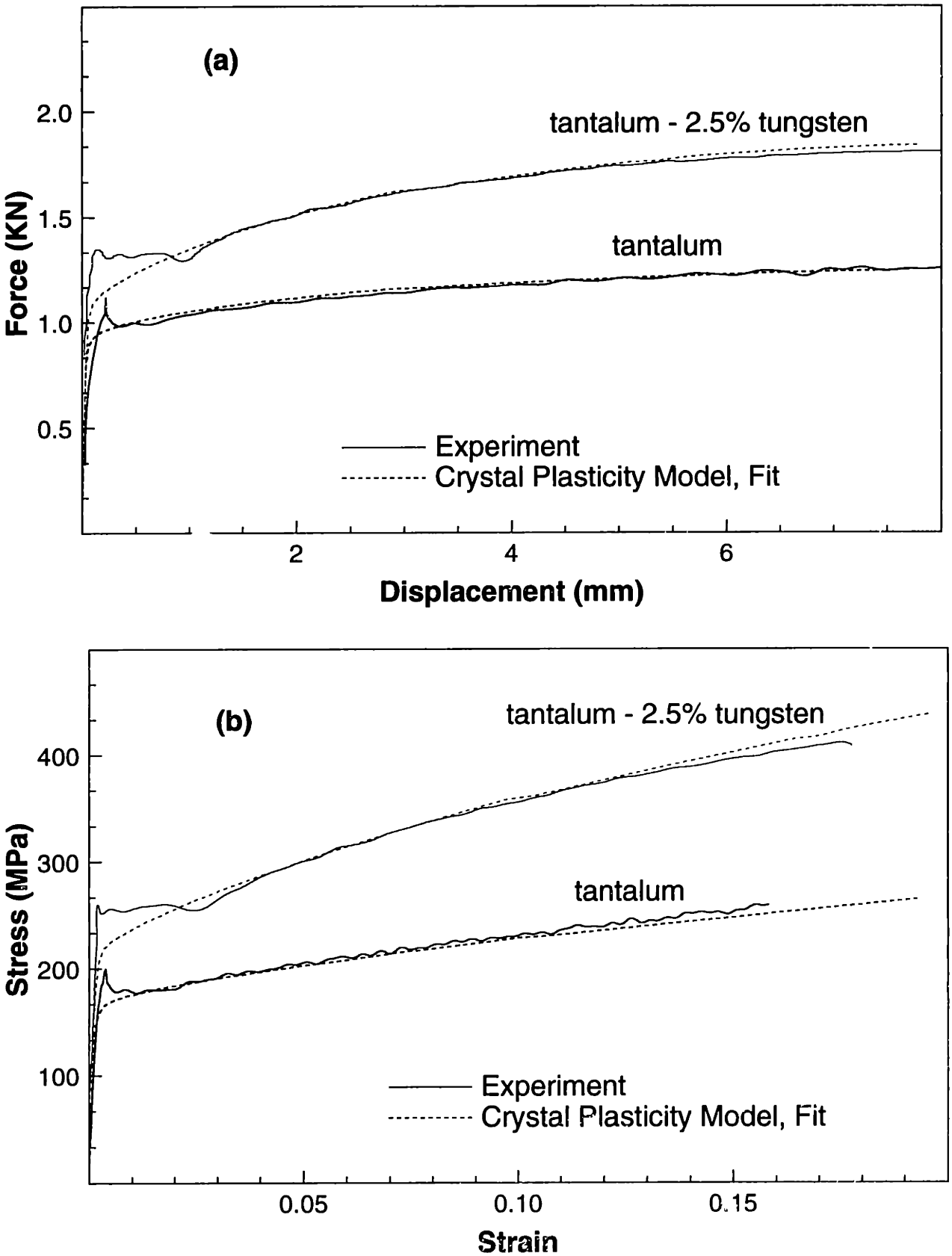

Figure 6-7: Fit of the crystal plasticity model to (a) the load-displacement response, and (b) the stress-strain response in the tension experiment on tantalum and tantalum 2.5% tungsten sheet along the rolling direction.

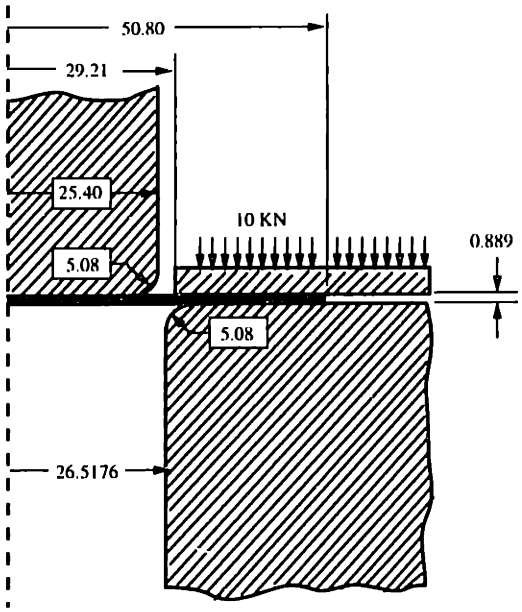

(a)

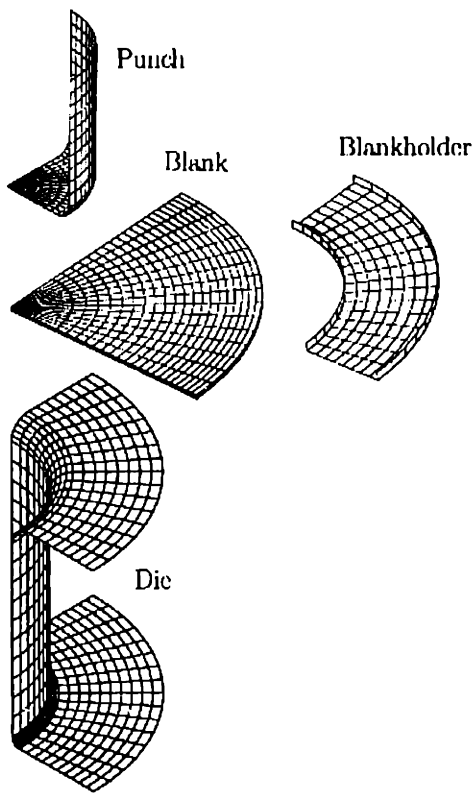

(b)

Figure 6-8: (a) Geometry of the cup drawing apparatus (All dimensions are in millimeters). (b) Exploded view of the finite element mesh used in the simulation.

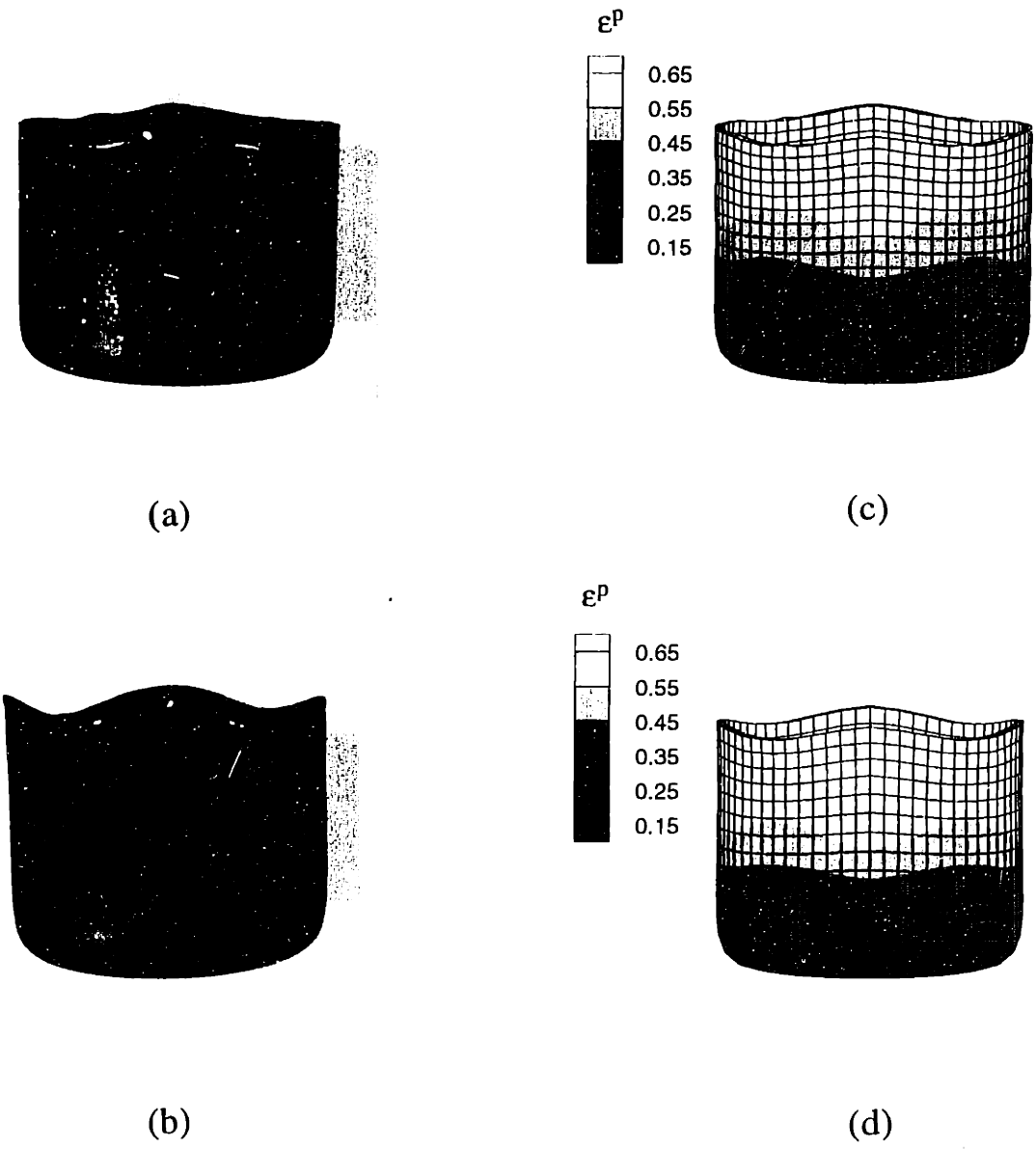

Figure 6-9: The experimentally observed earing pattern in (a) tantalum, and (b) tantalum - 2.5% tungsten. Numerically predicted predicted earing pattern in (c) tantalum, and (d) tantalum-2.5% tungsten (The rolling direction is from the left to the right). The numerical simulations also shows the equivalent plastic strain contours.

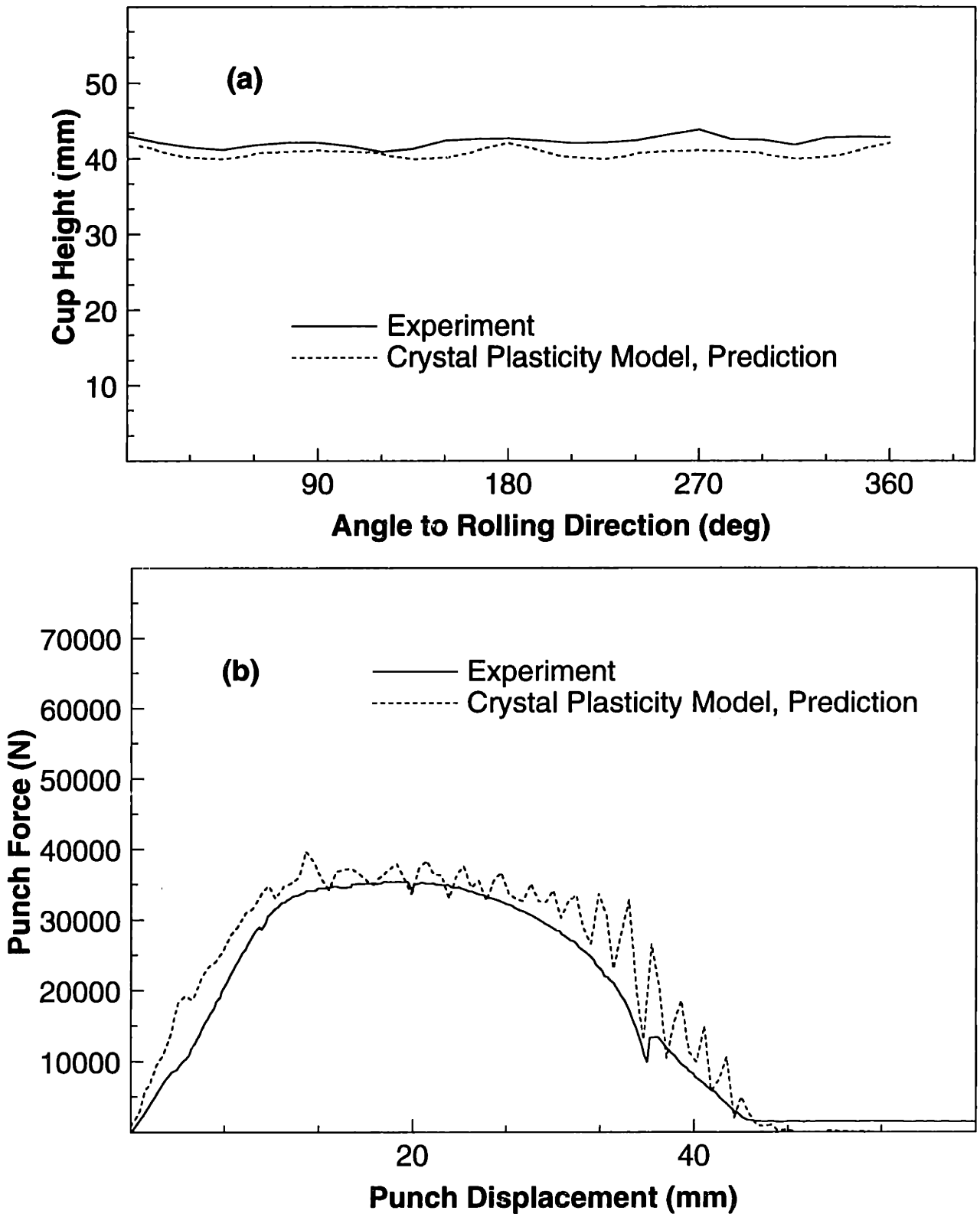

Figure 6-10: Comparison of the numerical prediction against the measured (a) cup-height profile, and (b) the load-displacement response in the cup drawing experiment on tantalum sheet.

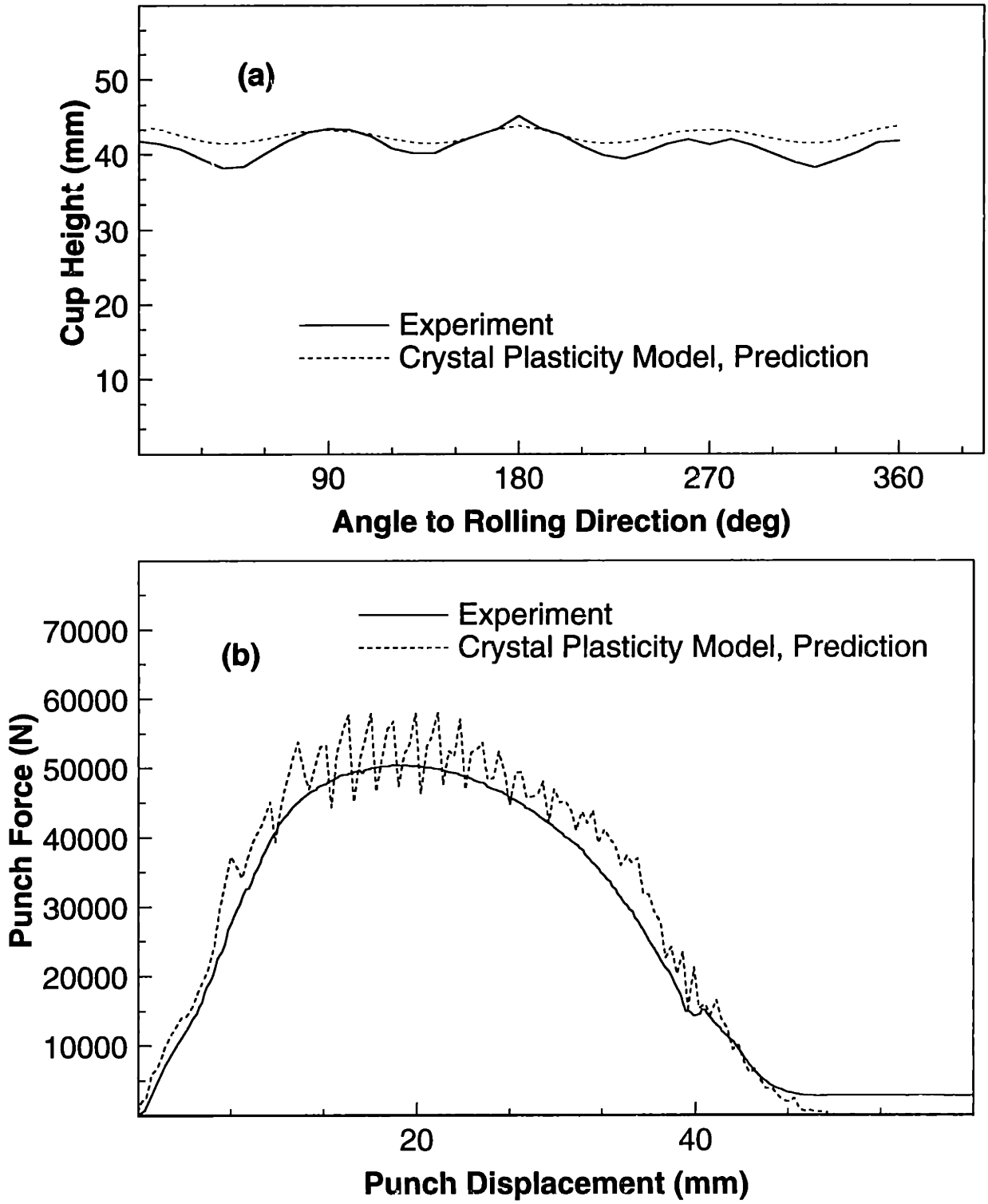

Figure 6-11: Comparison of the numerical prediction against the measured (a) cup-height profile, and (b) the load-displacement response in the cup drawing experiment on tantalum - 2.5% tungsten sheet.

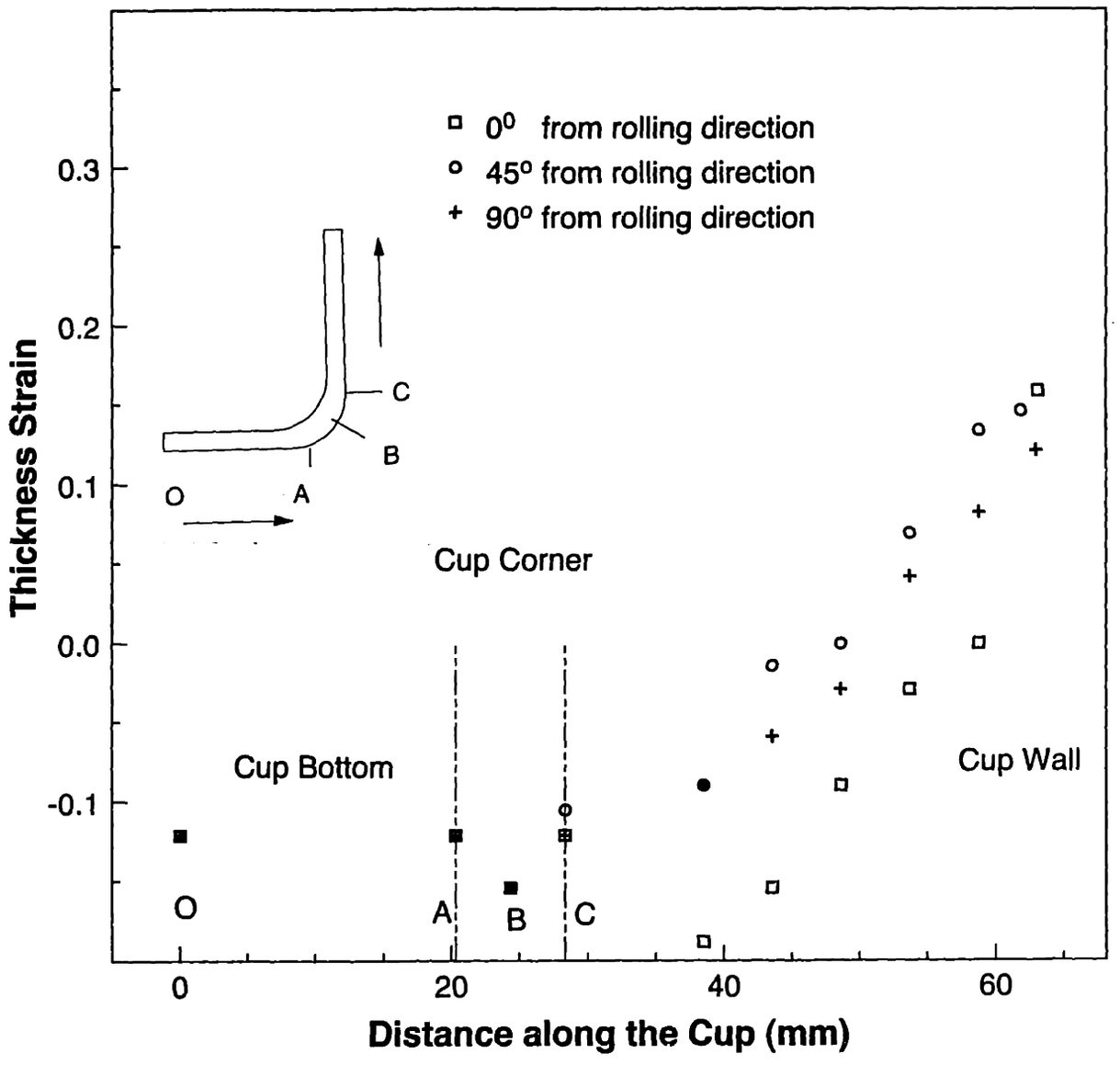

Figure 6-12: Experimentally measured thickness strain profile for the tantalum cup

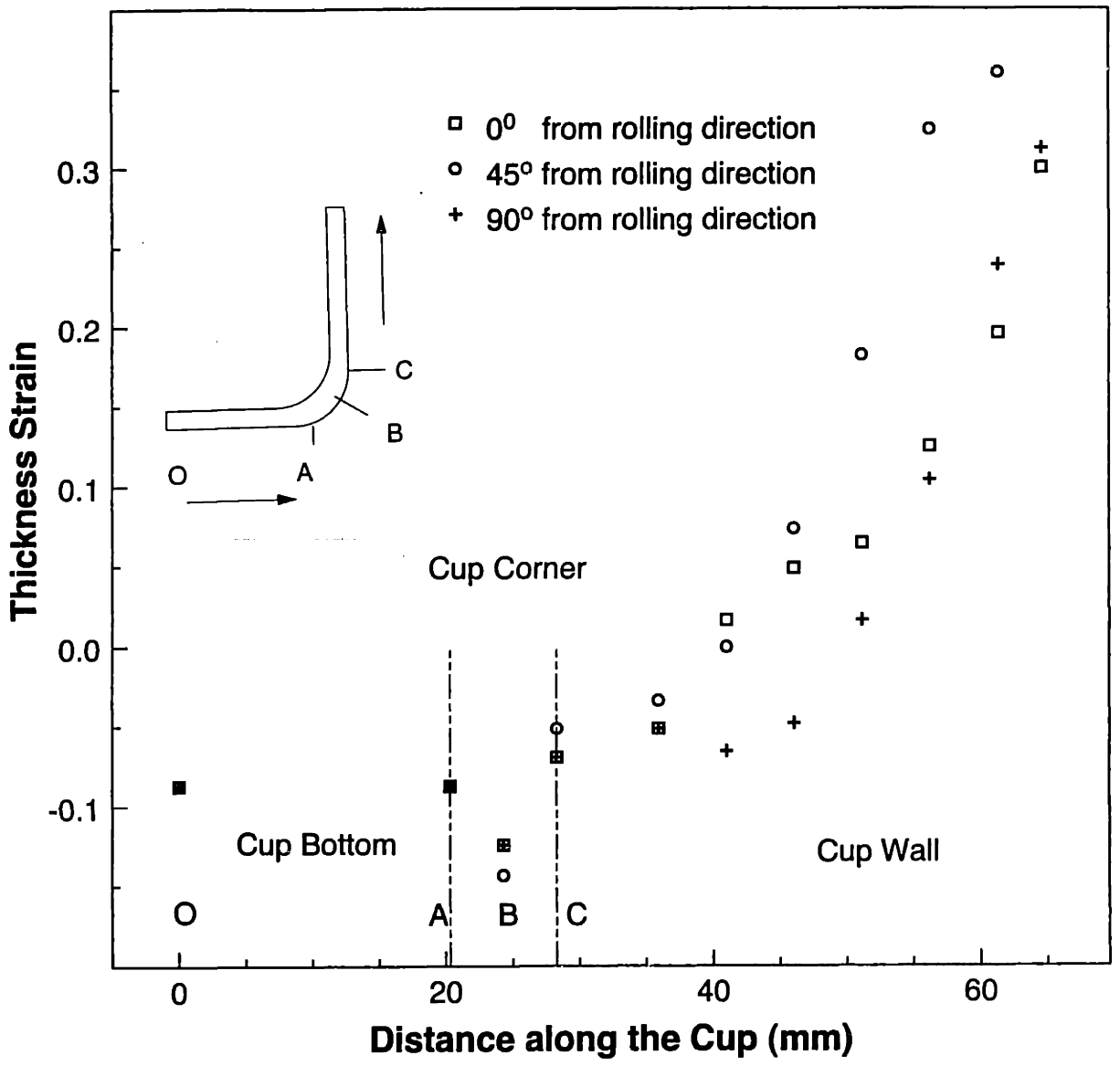

Figure 6-13: Experimentally measured thickness strain profile for the tantalum - 2.5% tungsten cup

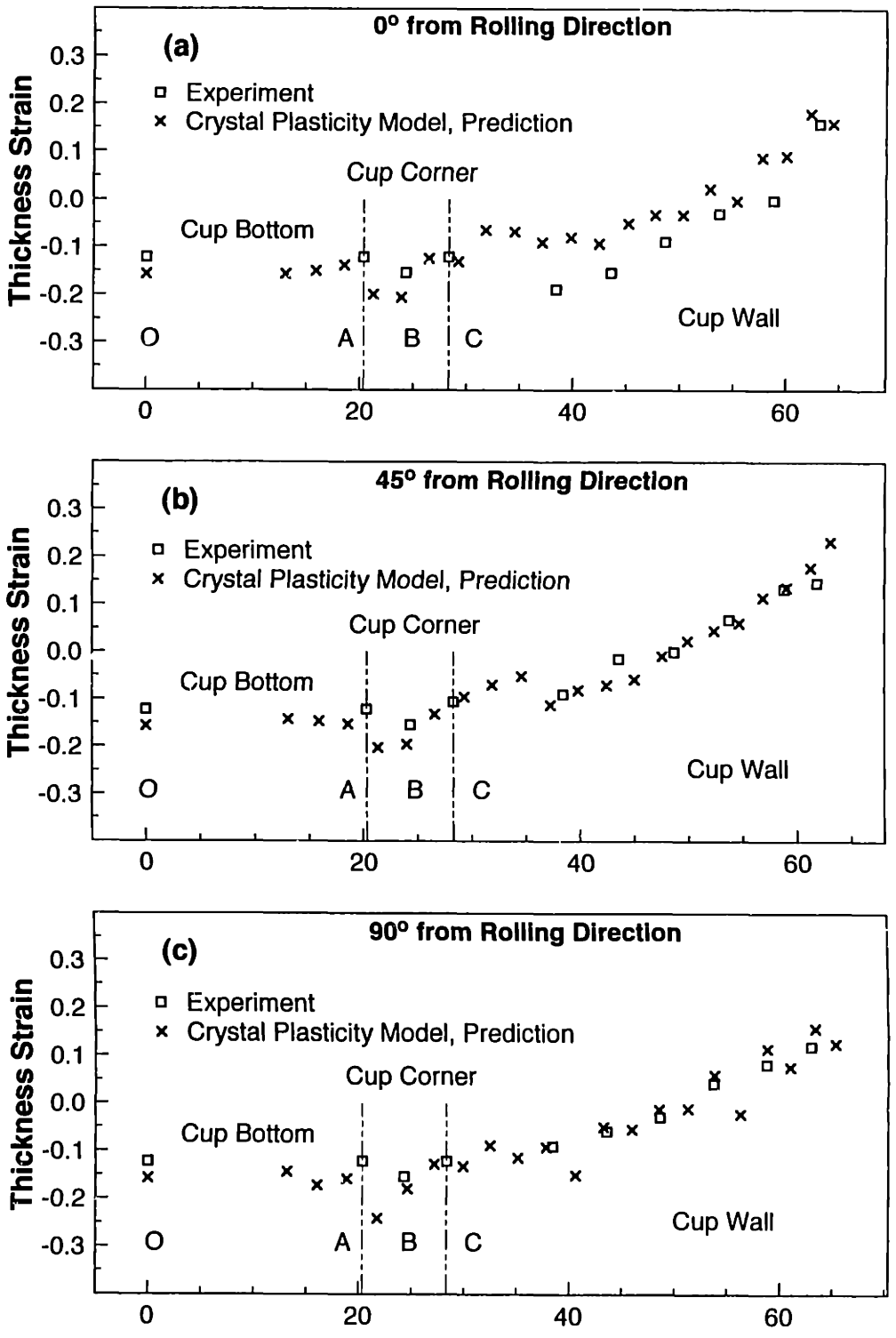

Figure 6-14: Comparison of the experimentally measured and predicted thickness strain profile for the tantalum cup along (a) 0^o from the rolling direction, (b) 45^o from the rolling direction, (c) 90^o from the rolling direction.

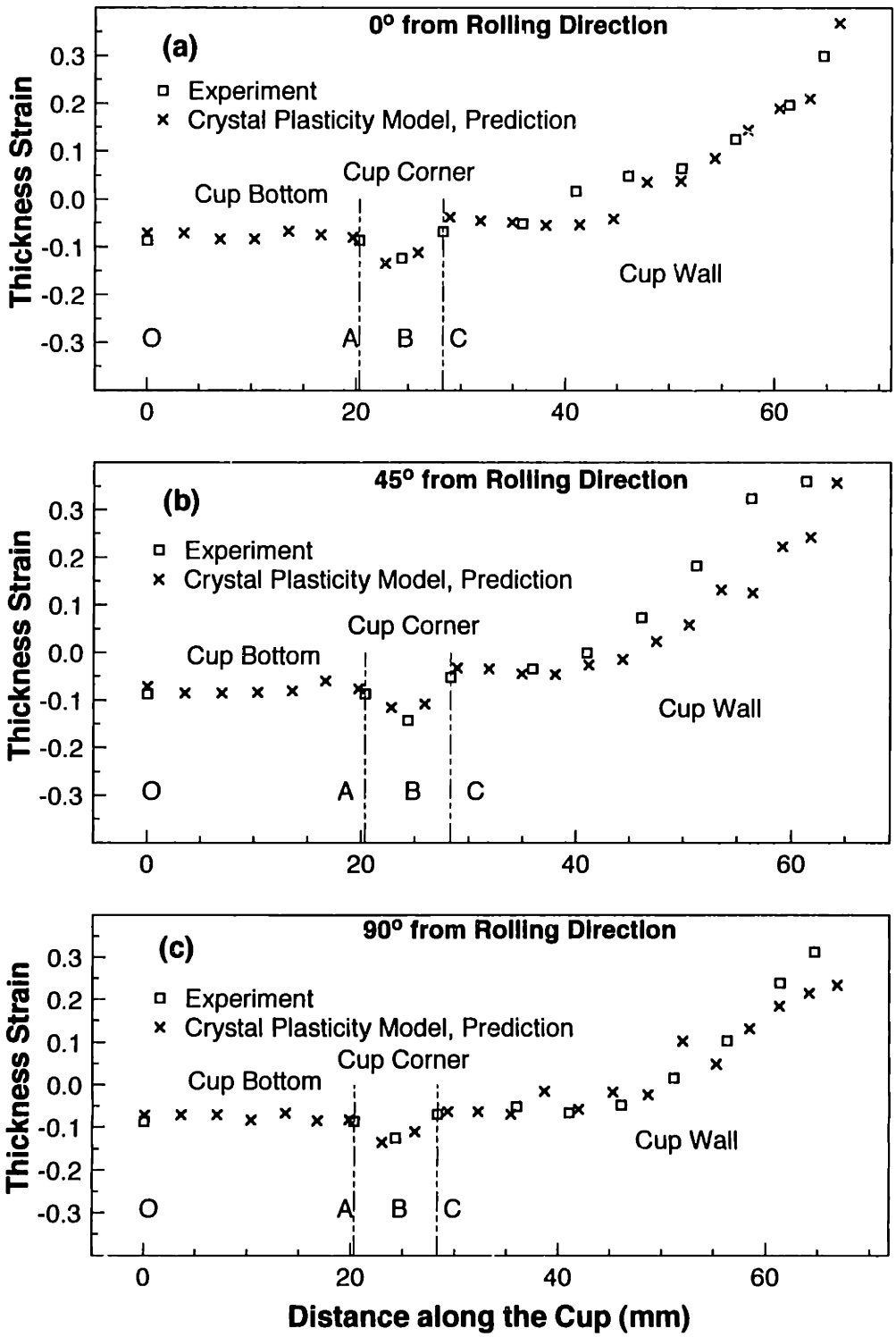

Figure 6-15: Comparison of the experimentally measured and predicted thickness strain profile for the tantalum - 2.5% tungsten cup along (a) 0^o from the rolling direction, (b) 45^o from the rolling direction, (c) 90^o from the rolling direction.

6.2 Taylor Cylinder-Impact Experiment of Pre-textured Tantalum

The cylinder-impact test (Taylor [1948]) has long been used to estimate the "dynamic flow strength" of metals at high strain rates and large plastic strains. In this experiment, cylindrical specimens are fired at a "rigid plate" and the final length, together with additional details of the deformed geometry, are measured. The material parameters in an assumed constitutive model for a material are then estimated by simulating the geometry of the deformed rod, and by varying the constitutive parameters in the material model until the computed final shape reasonably agrees with those determined experimentally. Such experiments on tantalum have been carried out by a number of investigators (e.g., Zerilli and Armstrong [1987, 1990]; Rajendran and Garret [1992]; Qiang *et al.* [1993]). Ting [1992] has also recently reported on Taylor cylinder-impact experiments on tantalum, and his own attempts at indirectly calibrating an isotropic constitutive model for this material. In his experiments, the cylinders were machined from a 6.35 mm-thick plate which was single-directionally rolled. The machined cylinders were nominally 28 mm long and 5.6 mm in diameter. The longitudinal axis of the cylinder was parallel to the rolling direction. Reverse ballistic techniques were applied in conducting the cylinder-impact experiments. In these experiments, a cylinder at a given initial temperature was kept stationary and impacted on one end by a 25 mm-diameter alumina disk mounted on a steel projectile. A powder gun was used to launch the projectile. Heating of the tantalum cylinder to elevated initial temperatures was accomplished by an electric furnace which was quickly removed from the stationary test specimens just before the gun was fired. The impacted specimens were recovered in a soft-catch box filled with a low-density material. In his paper Ting reports on eight such experiments at different initial temperatures and impact velocities. We use Ting's experimental data from two of his experiments: (i) an initial velocity of 154 m/s and temperature of 296 K; and (ii) an initial velocity of 161 m/s and temperature of 1003 K to check *directly* the predictive capabilities of our constitutive model by comparing the measured and the predicted final shape of the specimens.

The initial texture of the tantalum cylinders machined from the uni-directionally-rolled plate was experimentally measured and numerically represented by 200, and 18, weighted crystal orientations, using popLA, as shown in Fig. 6-16. The numerical representation

using 200 weighted crystal orientations is more accurate than the one using 18 weighted orientations. However, use of a large number of crystal orientations in a 3-D finite element simulation of the cylinder-impact experiment is time-consuming. In our simulations of the cylinder-impact experiments, we use the numerical representation of the initial texture by 18 weighted crystal orientations.

The flow parameters for the crystal plasticity model are the same as those used previously, equation (4.1). The initial value of the athermal slip resistance $s_{a,0}$ and the hardening parameters for the tantalum used by Ting [1992] are determined by curve-fitting the prediction of the stress-strain response from the crystal-plasticity model for the simple compression experiment along the rolling direction. The simulation was carried out using ABAQUS/Standard by subjecting a single ABAQUS-C3D8 element to simple compression at a true strain rate of $-0.001\,\mathrm{sec}^{-1}$. The initial texture in this Taylor-model calculation was represented by 18 weighted grain orientations. The hardening parameters obtained by the curve-fitting procedure are:

$$s_{a,0} = 52\,\mathrm{MPa},\ h_0 = 110\,\mathrm{MPa}, s_{a,s} = 130\,\mathrm{MPa},\ r = 1.1,\ q_l = 1.4.$$

Fig. 6-17 shows the quality of the fit. The predicted crystallographic texture after the compression is compared with the corresponding measurement in Fig. 6-18.

The finite element simulations are performed using ABAQUS/Explicit. Since the rod specimens have an initial orthotropic texture, only one quarter of the geometry is modeled. The mesh consists of 1280 ABAQUS-C3D8R elements. The nodes at one end of the rod are subjected to zero axial displacements to represent a rigid "frictionless" plate, while all the other nodes are subjected to initial velocities as in the experiments of Ting. The computed profiles after impact are reflected to obtain the complete rod profile, and then superimposed on the experimentally-measured profiles in Fig. 6-19 for two of the experiments reported by Ting [1992]. Although the ovalized impacted ends are not quite ellipitical, the experimentally measured and numerically calculated major and minor "diameters" are shown in Table 3, together with the measured final lengths. In Table 3, l_f denotes the final length, and (a, b) denotes the major and the minor diameters of the impact end of the cylinder.

Table 6.1. Comparison of the rod-impact simulations against experiments

Initial Temperature	296 K			1003 K		
	l_f (mm)	a (mm)	b (mm)	l_f (mm)	a (mm)	b (mm)
Experiment	22.1	10.3	9.8	16.7	11.9	11.5
Simulation	21.7	10.9	10.4	16.4	12.7	12.1

Overall, the simulations capture the macroscopic shapes, including the ovalization at the impact end of the cylinders, reasonably accurately.

In the next chapter, we turn our attention to polycrystalline b.c.c. iron and evaluate the accuracy of the Taylor-type model in some quasi-static homogeneous and non-homogeneous experiments.

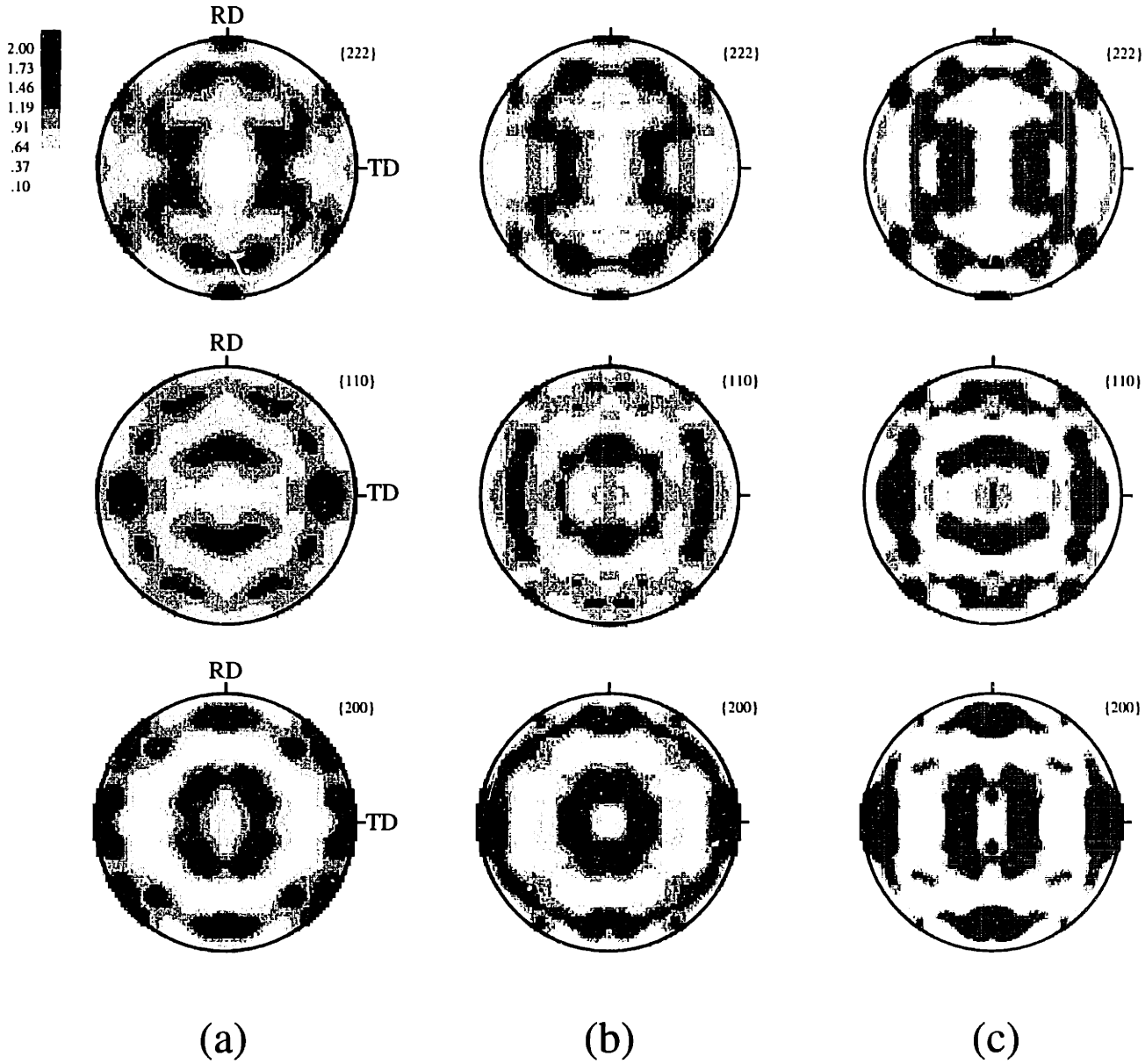

Figure 6-16: Experimentally measured texture of tantalum plate (Ting (1992)) and it's numerical representation: (a) Measured texture. (b) Numerical representation using 200 weighted grain orientations. (c) Numerical representation using 18 weighted grain orientations.

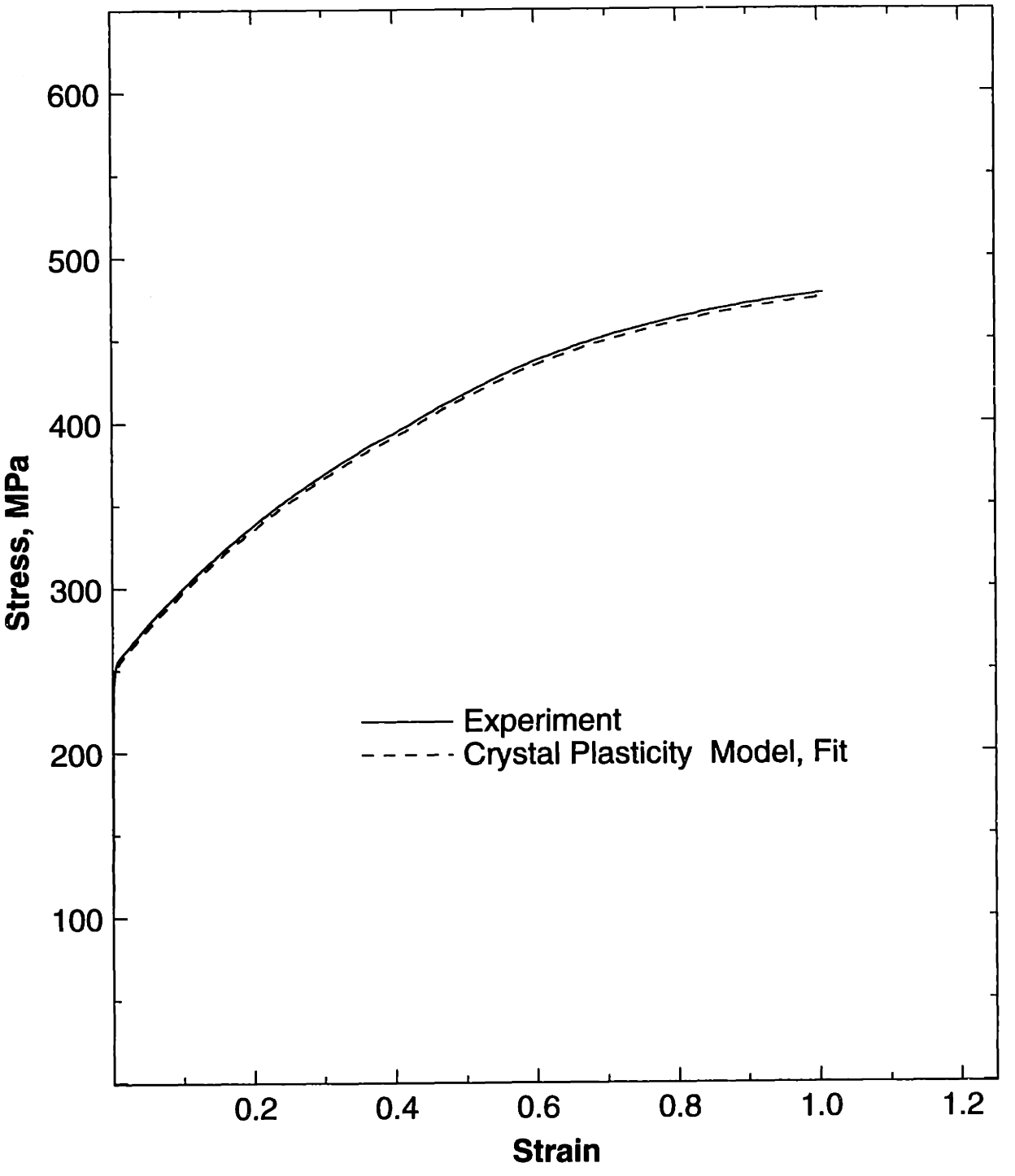

Figure 6-17: Fit of the prediction from the Taylor-type crystal plasticity model to the measured stress-strain response in simple compression experiment on tantalum rod specimen of Ting (1992).

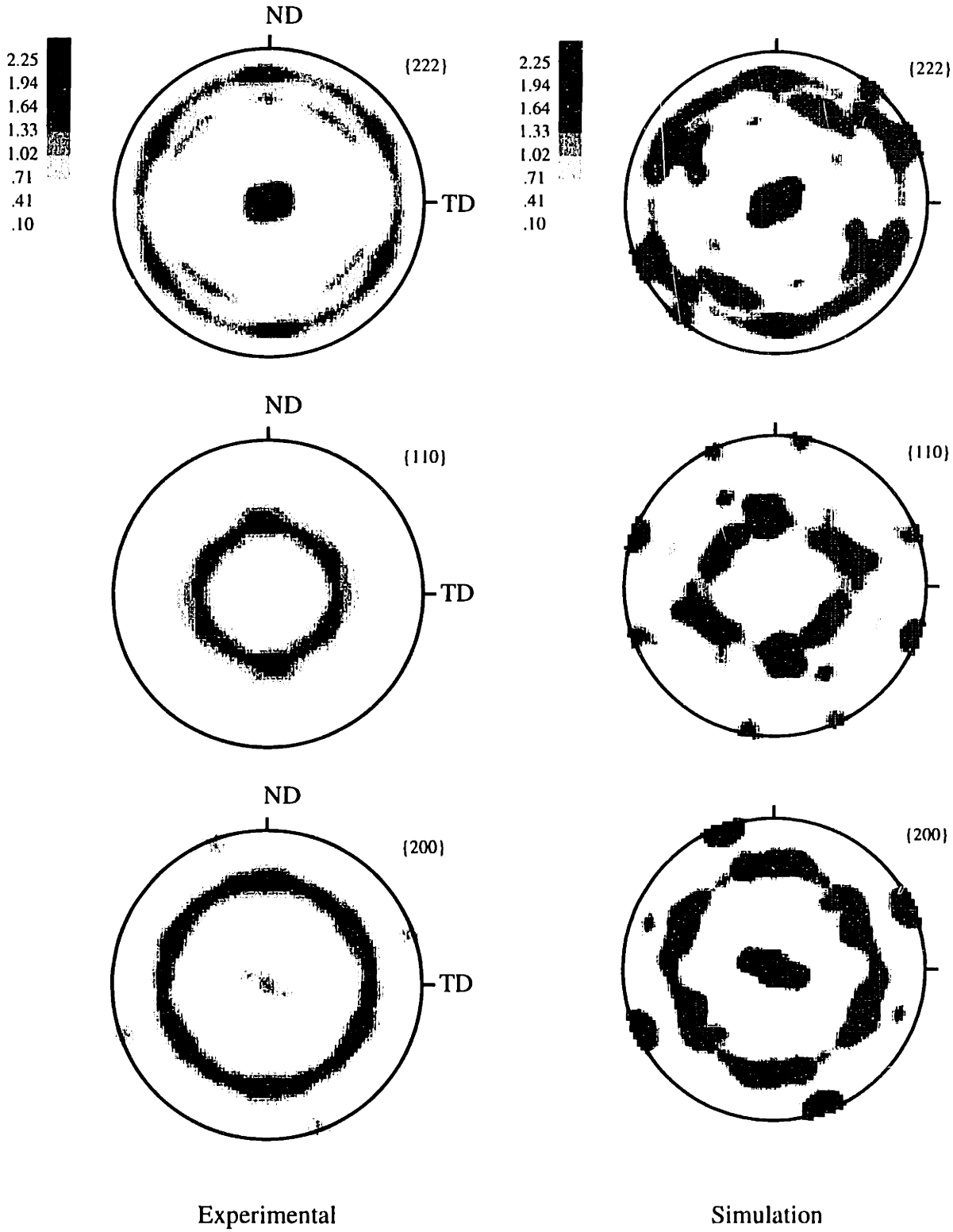

Figure 6-18: Comparison of the measured texture in the simple compression experiment on tantalum rod specimen of Ting (1992) against the texture predicted by the Taylor-type crystal plasticity model.

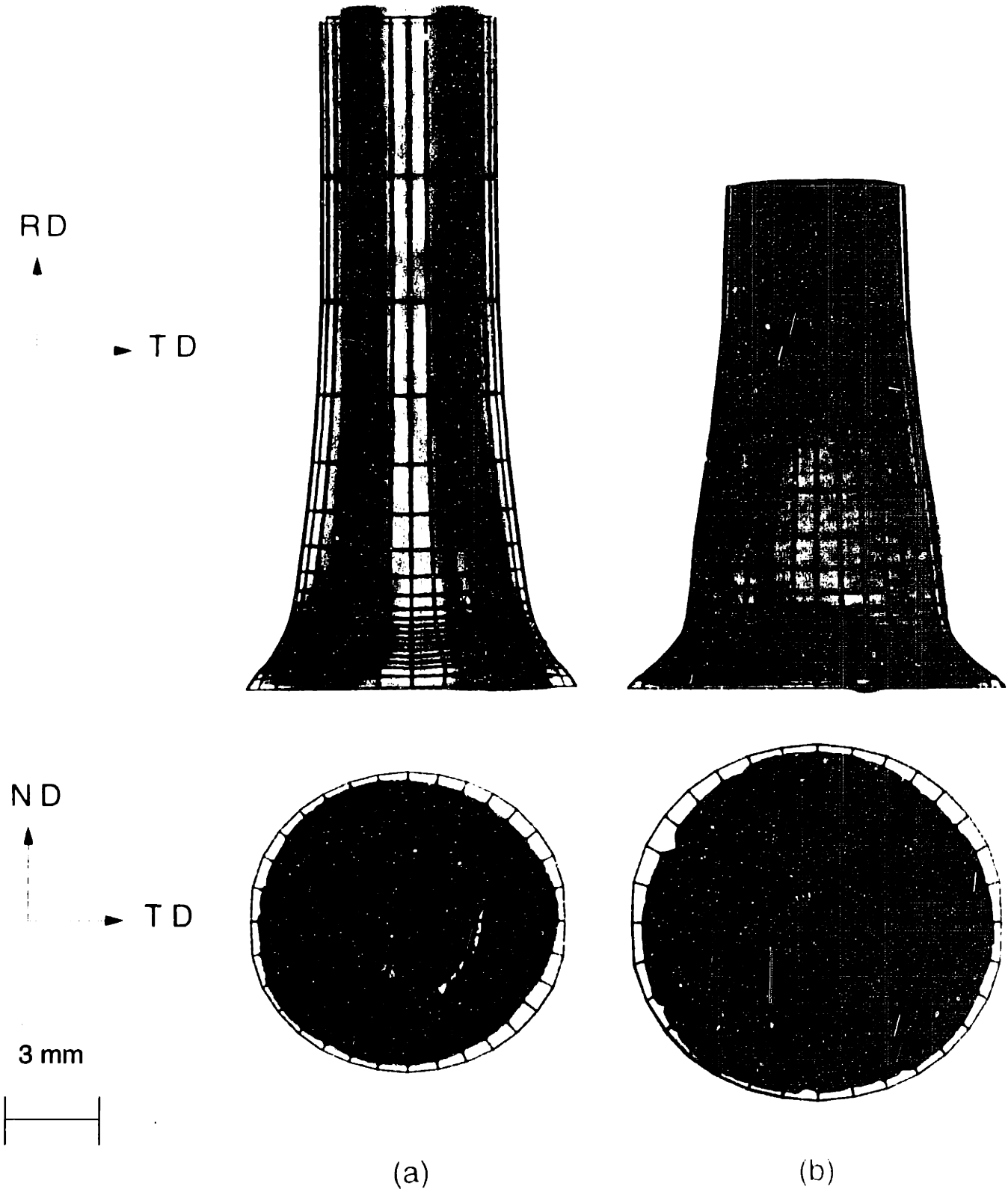

Figure 6-19: Comparison of the prediction of the Taylor-type crystal plasticity model to the rod impact data : (a) impact test at an initial velocity of 154 m/s and temperature of 296° K, and (b) impact test at an initial velocity of 161 m/s and temperature of 1003° K.

Chapter 7

Application to B.C.C. Iron

In this chapter, we evaluate the applicability of the crystal plasticity model to b.c.c. iron. After determining the material parameters, the accuracy of the crystal plasticity model is evaluated by comparing the predictions against (i) experimental results for nominally homogeneous simple compression, tension, and plane-strain compression on iron, and (ii) results from a quasi-static cup-drawing experiment on a low-carbon steel sheet.

7.1 Material Parameters for Iron

A procedure similar to that presented in Chapter 3 is followed here for the determination of the material parameters for iron. The values of the elastic parameters for iron as a function of temperature (in degree Kelvin) are taken as (Simmons and Wang [1971]):

$$\begin{aligned} C_{11} &= (247.2 - 0.06\,\theta) \text{ GPa}, \\ C_{12} &= (139.8 - 0.022\,\theta) \text{ GPa}, \\ C_{44} &= (123.6 - 0.023\,\theta) \text{ GPa}. \end{aligned}$$

As for tantalum, we assume that the operative slip systems in iron are the twelve $\{110\} < 111 >$ type, and the twelve $\{112\} < 111 >$ type. Futher, the slip on the $\{112\}$ planes is modeled to be symmetric. As we shall see, this choice of the slip systems reproduces the stress-strain curves and the crystallographic textures reasonably well for b.c.c. iron. The slip systems have been previously listed in Table 3.1.

The other necessary material parameters are the quantities $\{\dot{\gamma}_0, \Delta F^*, p, q, s_*\}$ in the

flow equations (2.14, 2.15), the quantities $\{\hat{h}_0^\alpha(|\dot{\gamma}^\alpha|,\theta), r, \hat{s}_{a,s}^\alpha(|\dot{\gamma}^\alpha|,\theta), q_l\}$ in the hardening equations (2.22, 2.23, 2.24, 2.25), and the initial value of the athermal slip-system resistance $s_{a,0}$, which are taken to be identical for all the slip systems.

The flow parameters, $\{\dot{\gamma}_0, \Delta F^*, p, q, s_*\}$, are determined by fitting the experimental data of Leslie [1972] for the temperature sensitivity of the yield strength of titanium-gettered (Fe - 0.15% Ti) iron rod. The experiments reported by Leslie were performed at a strain rate of $2.5 \times 10^{-4}\,\mathrm{sec}^{-1}$. As the initial texture of the iron rod was not reported by Leslie, we approximated this initial texture as that measured on our own commercially-procured[1] and annealed iron rod (annealing temperature - $800°C$, annealing time - 30 minutes). The {110} and {200} pole figures were measured using the Schulz-reflection method with Copper K_α radiation. This texture was represented by a set of 400 weighted grain orientations by using the texture conversion program popLA (Kallend, *et al.* [1994]). The experimentally-measured and numerically-represented pole figures are presented in Fig. 7-1.

To calculate the yield strength of iron at different temperatures, a Taylor-model simple compression ABAQUS/Standard simulation is performed on a single ABAQUS-C3D8 (continuum, 3-D, eight-noded) element subjected to the appropriate strain rate and initial temperature in the experiment. The integration point in the element is assigned the 400 weighted grain orientations corresponding to the initial texture of the rod, Fig. 7-1. The flow parameters obtained by the fitting procedure are [2]:

$$\dot{\gamma}_0 = 1.73 \times 10^7\,\mathrm{sec}^{-1},\ \Delta F^* = 1.38 \times 10^{-19}\mathrm{J},\ p = 0.62,\ q = 1.5,\ s_* = 365\mathrm{MPa}, \qquad (7.1)$$

with

$$s_{a,0} = 10\mathrm{MPa}.$$

The quantities s_* and $s_{a,0}$ are taken to be the same for all slip systems. The fit of the model

[1]The iron rod was purchased from Surepure Chemetals, Inc. (Address: 23 Woodbine Road, Florham Park, NJ 07932. Tel. no. : 201-377-4081.)

[2]Similar to the procedure followed for tantalum, the data for iron is first fit to an isotropic version of the model (see Appendix A), and the values of the material parameters so determined are then used as guides for initial estimates for the numerical calculations based on the crystal-plasticity model. In particular, the flow parameters $\{\Delta F^*, p, q\}$ are taken to be equal to those obtained for the isotropic model, and the parameter $\dot{\gamma}_0$ is obtained from the corresponding quantity $\dot{\epsilon}_0$ in the isotropic model by setting $\dot{\gamma}_0 = \sqrt{3}\,\dot{\epsilon}_0$. Initial estimates for the resistance parameters s_* and $s_{a,0}$ are taken as the values obtained for the isotropic model, divided by a "Taylor Factor" of $M \approx 3$.

against the experimental data of Leslie [1972] for the temperature sensitivity of the yield strength of iron as presented in Fig. 7-2 is reasonable.

The critical temperature θ_c in equation (2.19) depends on the flow parameters of the material and the applied strain rate. Using the flow parameters for tantalum (4.1) and iron (7.1), the variation of the parameter m defined in (4.2) is plotted for two different strain rates as a function of the normalized temperature ($\frac{\theta}{\theta_c}$) in Fig. 7-3. As seen from this figure, tantalum has a higher rate-sensitivity. Iron is found to twin at high strain rates and low temperatures (Bolling and Richman [1965]; Qiang [1993]). Therefore, the comparison of the rate sensitivity is valid as long as plastic deformation in iron occurs by crystallographic slip alone.

The hardening parameters were determined by fitting the predictions from the crystal-plasticity model against the isothermal simple compression experiment performed on pure annealed iron rod at a strain rate of $1 \times 10^{-3}\,\mathrm{sec}^{-1}$. The simulation is carried out by subjecting a single ABAQUS - C3D8 element to simple compression. Each integration point is assigned the 400 weighted grain orientations, Fig. 7-1. The hardening parameters obtained from the fitting procedure are

$$s_{a,0} = 30\,\mathrm{MPa},\ h_0 = 310\,\mathrm{MPa}, s_{a,s} = 205\,\mathrm{MPa},\ r = 2.2,\ q_l = 1.4.$$

The fit, as shown in Fig. 7-4, is reasonable.

7.2 Quasi-static Homogeneous Experiments on Iron

Nominally homogeneous simple compression, tension and plane strain compression experiments were performed on pure annealed iron rod at quasi-static rates. The accuracy of the crystal plasticity model in its applicability to b.c.c. iron was evaluated by comparing the measured macroscopic stress-strain curve and the crystallographic texture against the predictions.

A simple compression experiment was performed on the annealed iron rod along the rod axis at a strain rate of $1 \times 10^{-3}\,\mathrm{sec}^{-1}$ to a final strain of -1.0. The measured stress-strain response and the fit from the crystal-plasticity model was presented in the previous section, Fig. 7-4. The {110} and {200} pole figures predicted by the model is compared with the experimentally measured pole figures in Fig. 7-5. As seen from this figure, the agreement is

reasonable. The compression texture is axi-symmetric with {111} and {200} poles along the loading direction. The compression texture of iron is similar to that of tantalum, Fig. 5-4.

A simple tension experiment was performed on iron along the rod axis at a strain rate of $0.001s^{-1}$ to a final strain of 0.21. As seen from Figs. 7-6 and 7-7, the correspondence between the predictions and the experimentally-measured stress-strain response and the crystallographic texture is reasonable. In tension, the {200} poles are unstable and rotate away from the tension axis. This can be seen by comparing the initial texture in Fig. 7-1 and the tension texture in Fig. 7-6. Note that the intensity of the {200} poles along the tension axis is decreased considerably after tension. However, in compression, the {200} poles are stable, see Fig. 7-5.

A plane-strain compression experiment was performed on iron at a strain rate of -$0.001s^{-1}$ to a final strain level of 0.9. As in the plane strain compression experiment for tantalum, the iron specimen was machined such that the compression direction is perpendicular to the rod axis and the constraint direction is along the rod axis. In the numerical simulation a single ABAQUS-CPE4 (continuum, plane strain, four-noded) element was used. The predicted stress-strain response and the crystallographic texture are compared against the corresponding experimental measurements in Fig. 7-8 and Fig. 7-9, respectively. The agreement is good.

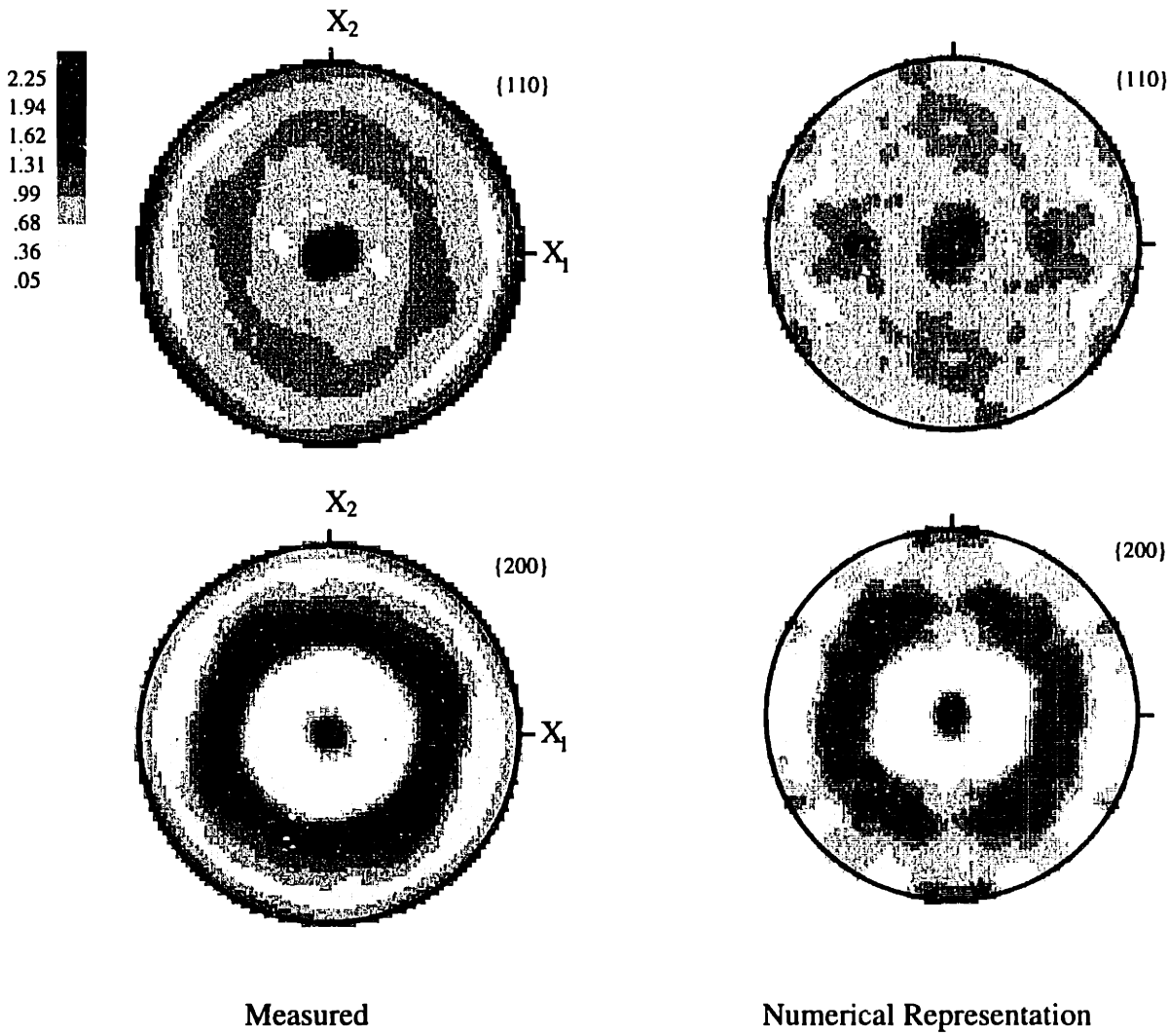

Figure 7-1: Representation of the texture of annealed b.c.c. iron with 400 weighted grains.

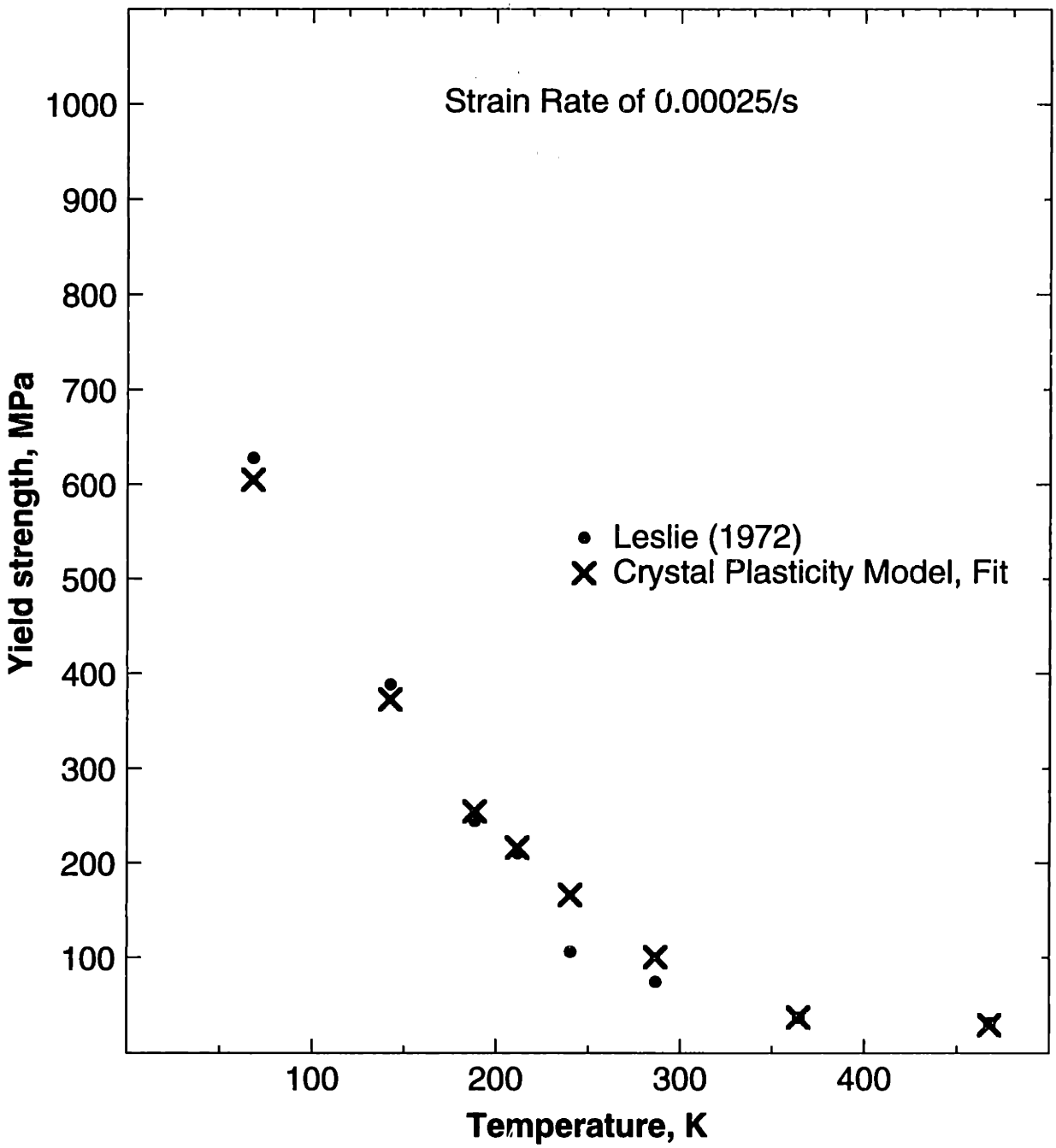

Figure 7-2: Fit of the Taylor-type crystal plasticity model to the data of Leslie (1972) on the temperature dependence of the yield strength of b.c.c. iron.

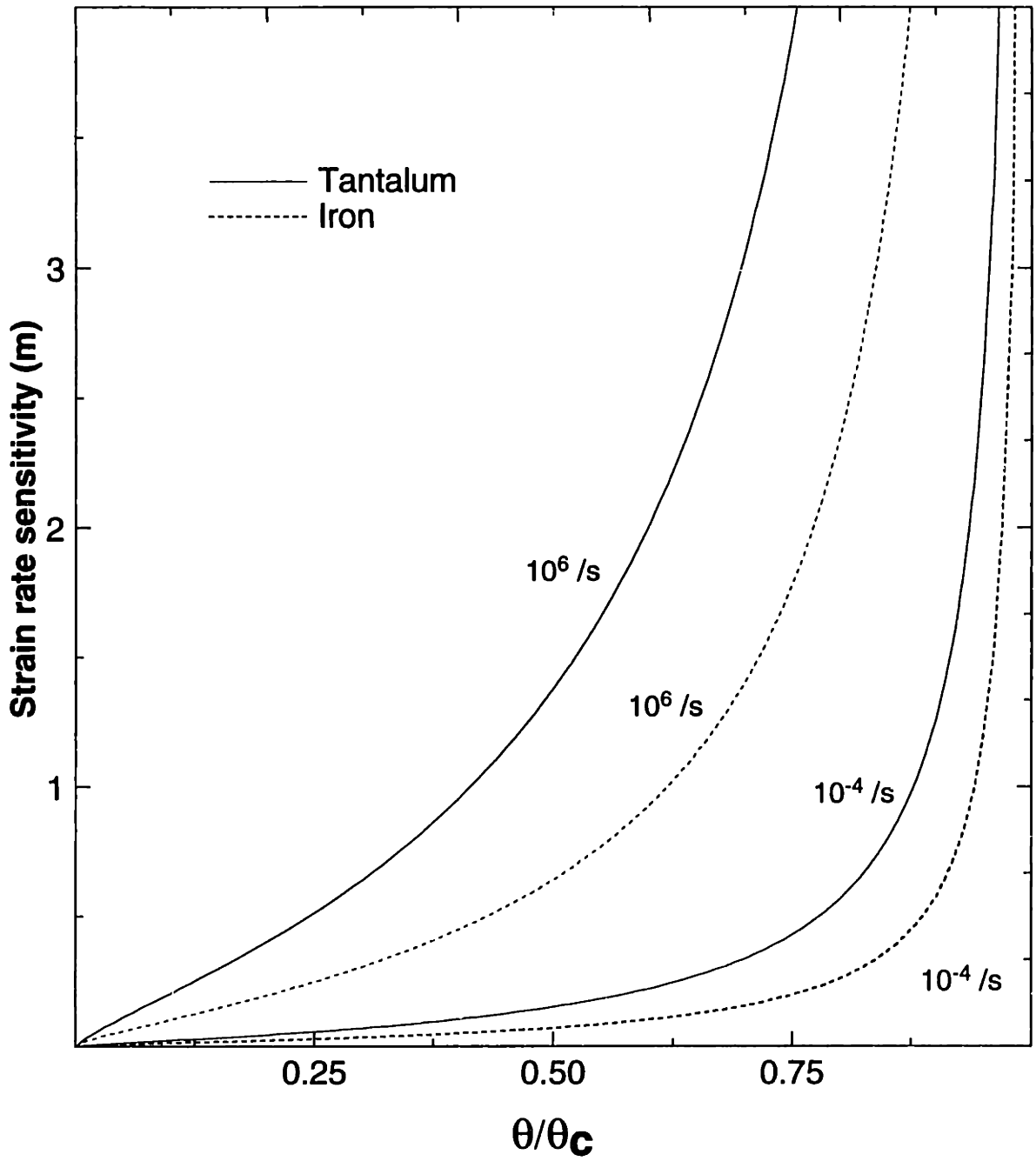

Figure 7-3: The variation of the strain rate sensitivity parameter m for tantalum and iron with normalized temperature ($\frac{\theta}{\theta_c}$) at fixed strain rates.

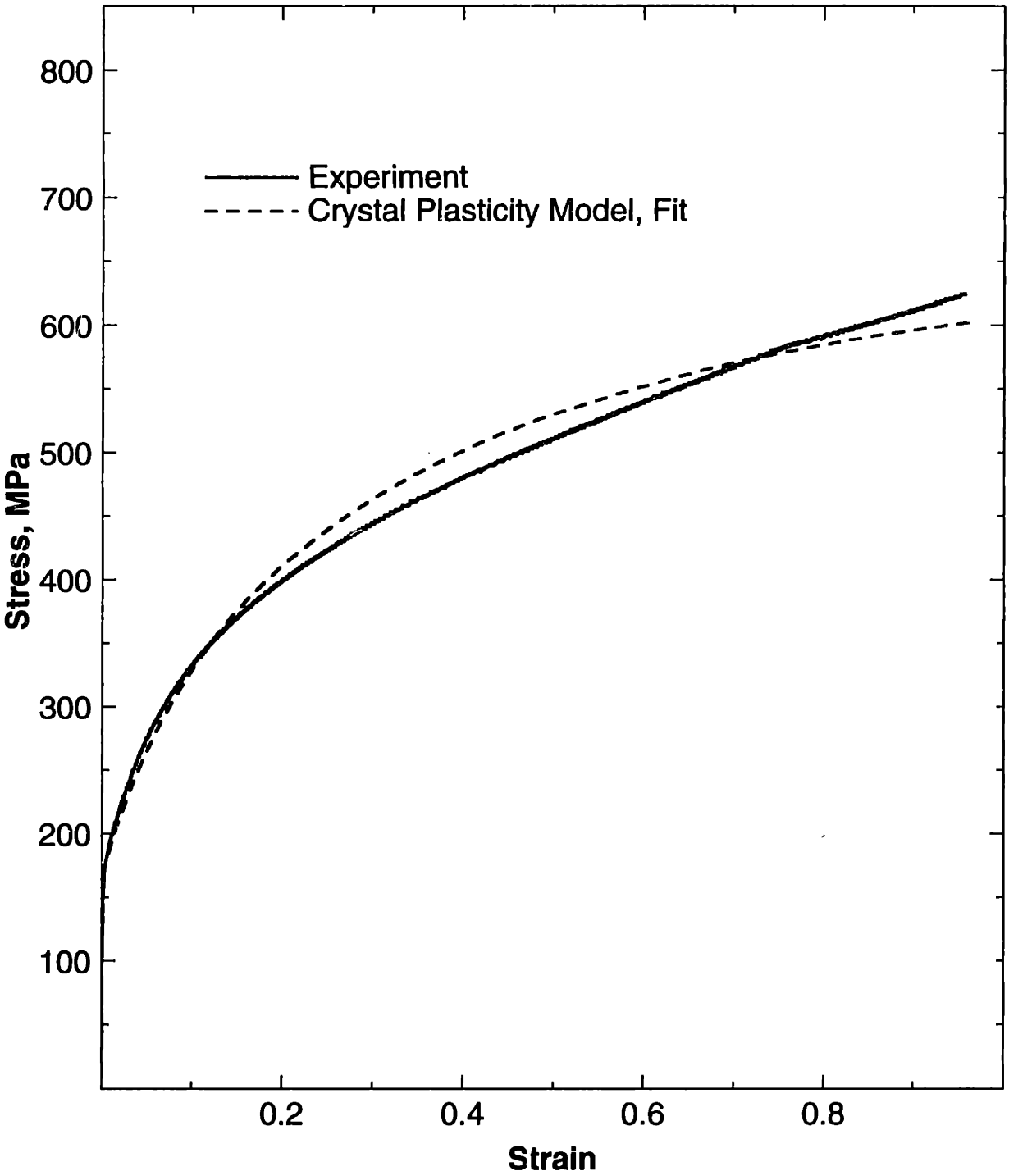

Figure 7-4: Fit of the prediction from the Taylor-type crystal plasticity model against the measured stress-strain response in simple compression experiment on annealed b.c.c. iron.

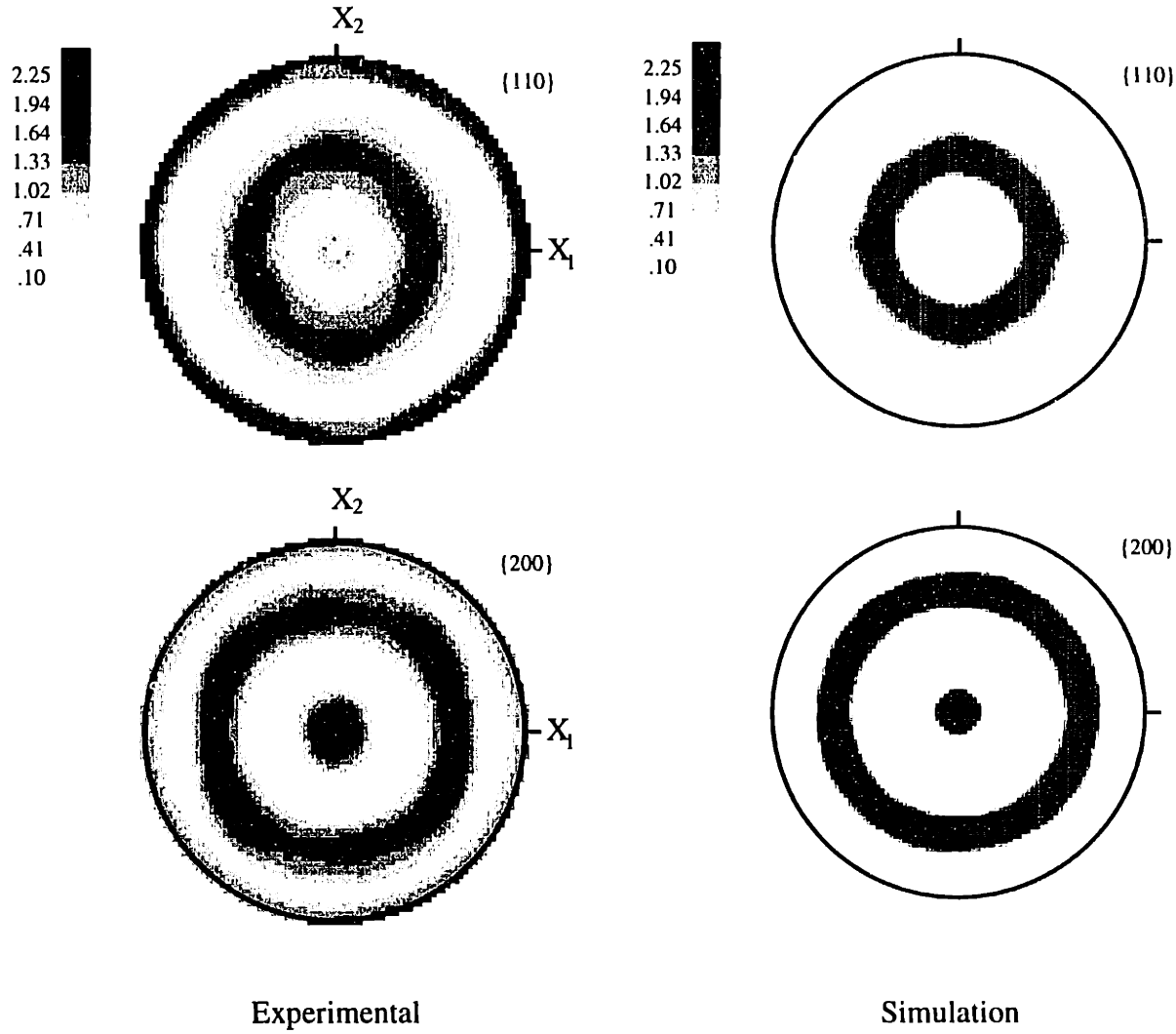

Figure 7-5: Comparison of the measured texture in the simple compression experiment on annealed b.c.c. iron against the texture predicted by the Taylor-type crystal plasticity model.

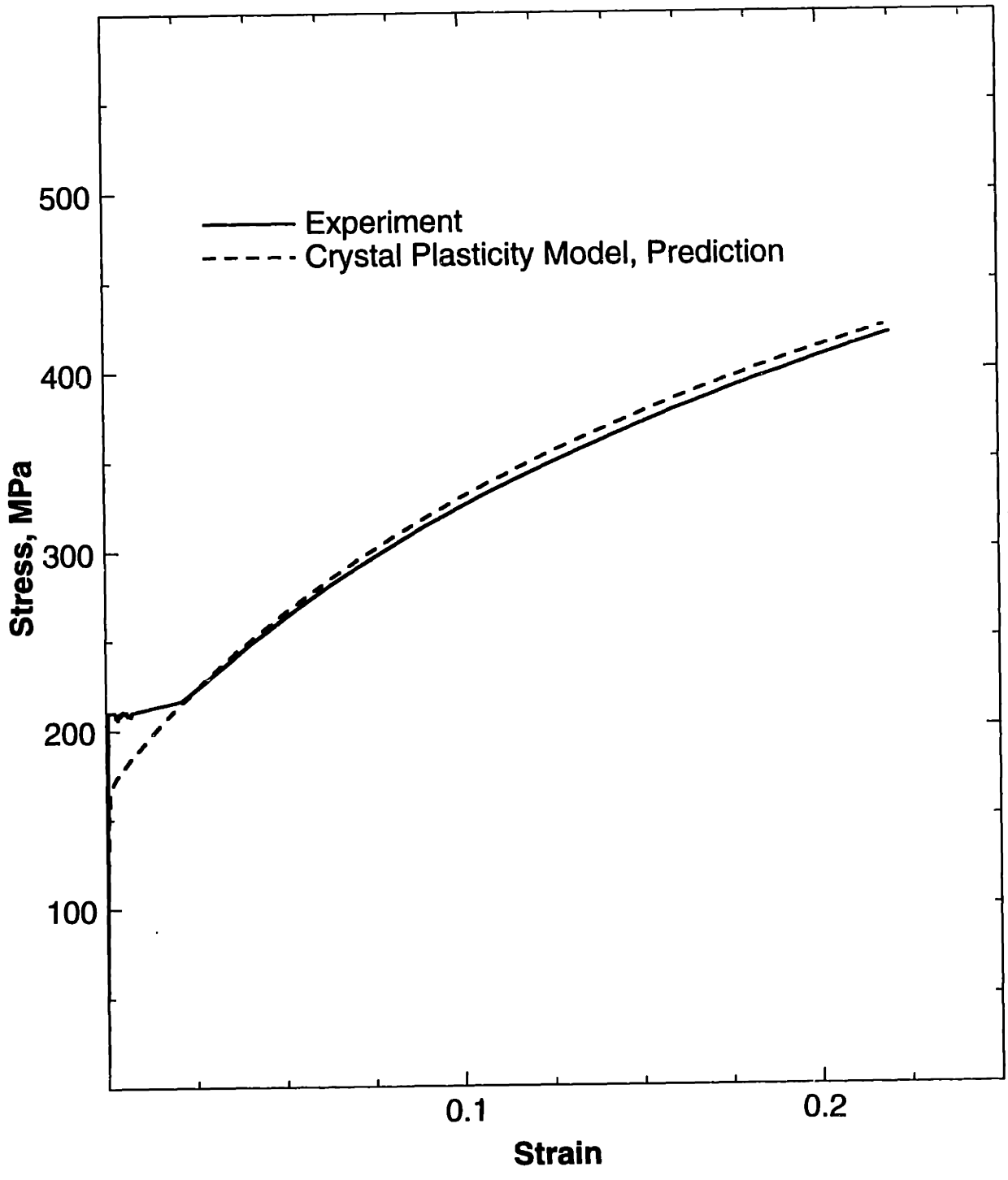

Figure 7-6: Measured and simulated stress-strain response from the Taylor-type crystal plasticity model for the simple tension experiment on annealed b.c.c. iron.

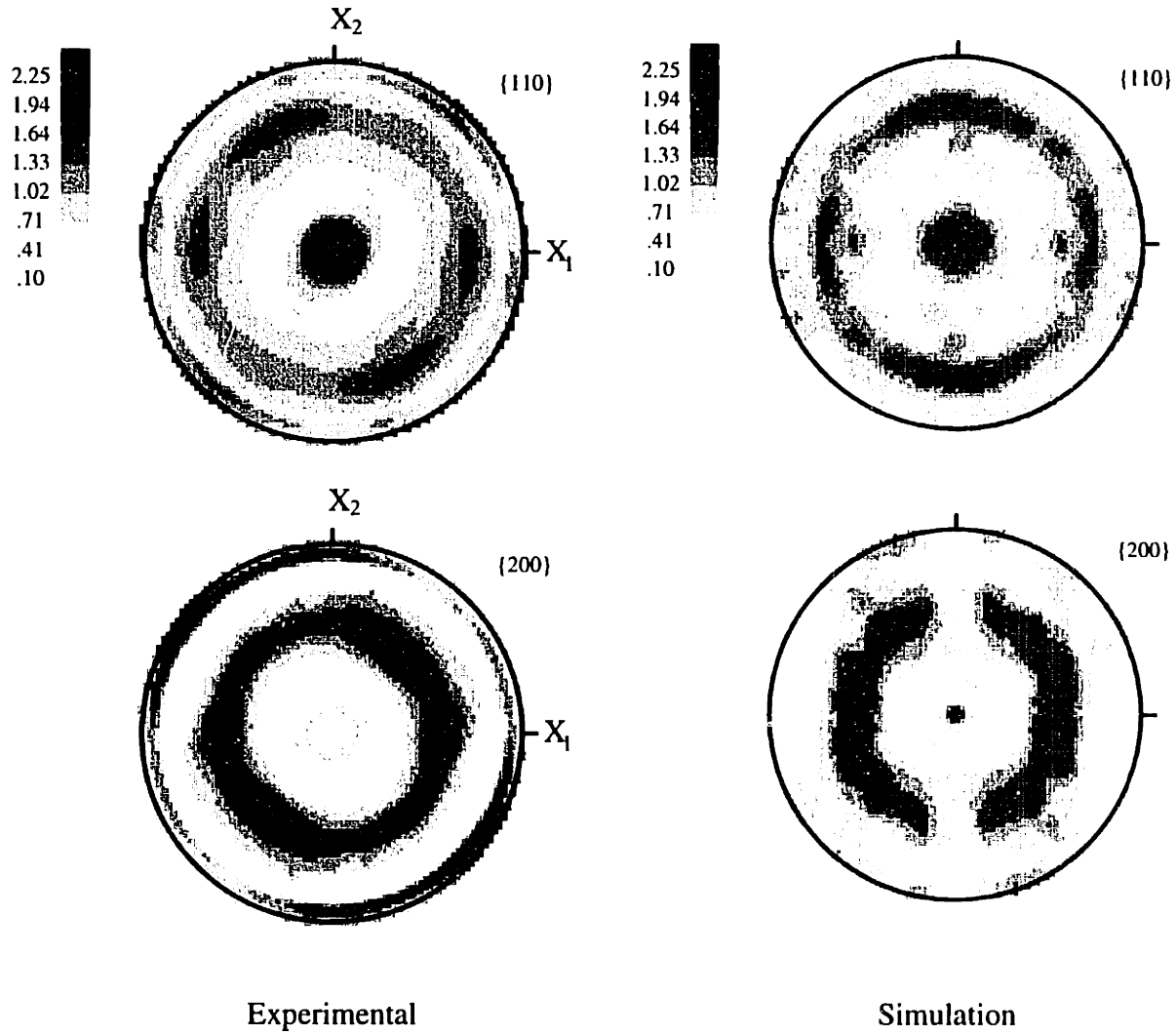

Figure 7-7: Comparison of the measured texture in the simple tension experiment on annealed b.c.c. iron against the texture predicted by the Taylor-type crystal plasticity model.

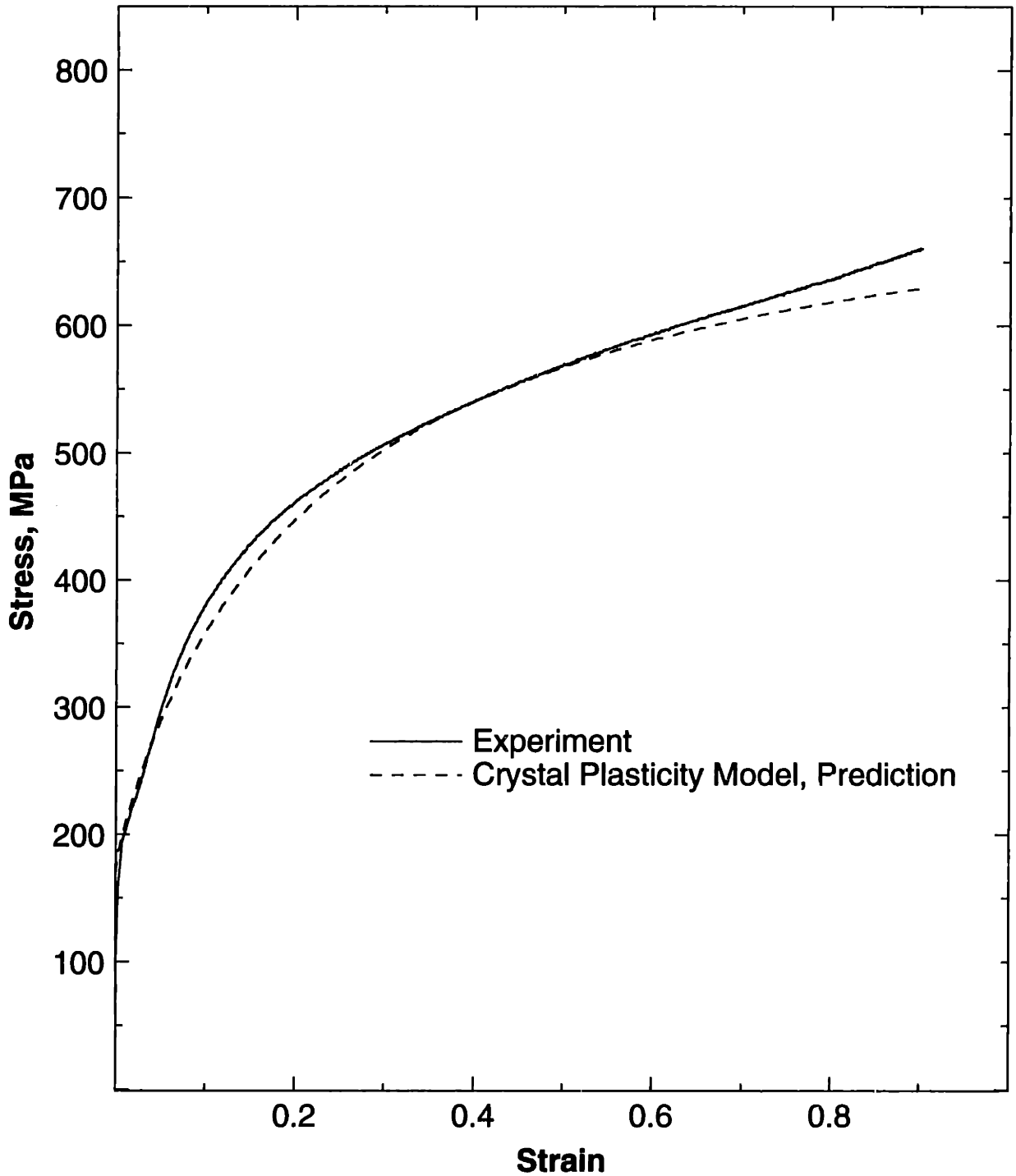

Figure 7-8: Measured and simulated stress-strain response from the Taylor-type crystal plasticity model for the plane strain compression experiment on annealed b.c.c. iron.

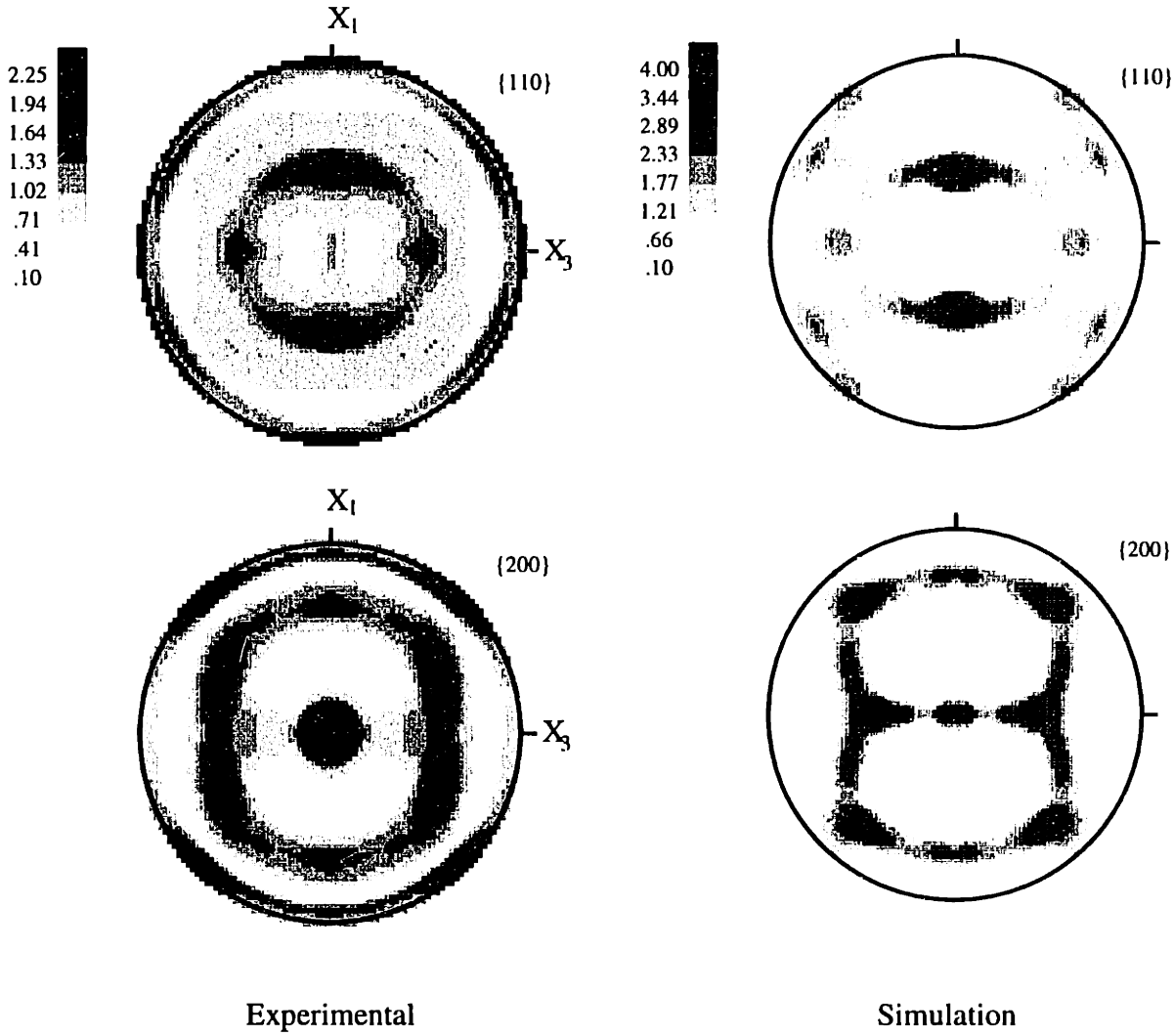

Figure 7-9: Comparison of the measured texture in the plane strain compression experiment on annealed b.c.c. iron against the texture predicted by the Taylor-type crystal plasticity model with different intensity scales.

7.3 Quasi-static Cup-Drawing Experiment on Low-Carbon Steel

Quasi-static cup-drawing experiment was performed on a polycrystalline low-carbon steel (LC1010) sheet. The initial crystallographic texture of the sheet and its numerical representation using 200 and 25 weighted orientations is plotted in Fig. 7-10. As in the cup drawing calculations on tantalum in Chapter 5, we use 25 weighted grain orientations for simulation using the crystal plasticity model. Inverse pole figures, computed from the measured as-receieved pole figures using popLA, are shown in Fig. 7-11. As seen from this figure, the low-carbon sheet has a strong (111)[110] type rolling texture.

The elastic constants at room temperature for the low-carbon steel are taken as (Simmons and Wang [1971]):

$$C_{11} = 237\,\text{GPa}, C_{12} = 141\,\text{GPa}, C_{44} = 116\,\text{GPa}.$$

Carbon atoms can interact with dislocations in iron in two different ways. First a small amount of carbon goes in as interstitial solid solution in iron, and often segregates to the dislocations present in the material, acting like pinning agents for the dislocations. This interstitial carbon is responsible for the upper and lower yield strength observed in steels, however its effect on the strain-rate and temperature sensitivity of yield strength is expected to be relatively small. Therefore, we take the flow parameters for the low-carbon steel to be the same as obtained for iron, equation (7.1). Secondly, the carbon which does not go in as an interstitial solid solution precipates out as Fe_3C particles, or platelets in pearlite, and this affects the yield strength and strain-hardening characteristics of steels. Accordingly, we determine the hardening parameters for the low-carbon steel by fitting the load-displacement and the stress-strain response as measured in a sheet-tension experiment. The test was performed at a constant veloctity of 0.05 mm/sec. The numerical simulation of the experiment was performed in ABAQUS/Explicit using 180 ABAQUS - C3D8R elements. The hardening parameters were obtained by fitting the measured load-displacement and stress-strain response. The material parameters obtained from the fit are:

$$s_{a,0} = 67\,\text{MPa},\ h_0 = 260\,\text{MPa}, s_{a,s} = 160\,\text{MPa},\ r = 1.1,\ q_l = 1.4.$$

The numerical fit to the data is shown in Figs. 7-12(a) and 7-12(b).

Circular blank of 50.8 mm in diameter and 1.067 mm thick was drawn in the cup-drawing apparatus presented in Chapter 5 (Fig. 6-8(a)). A constant blankholder force of 10 kN was applied and the cup was drawn with a punch speed of 1mm/sec. Teflon sheets were used as lubricants so as to minimize the friction in the interface between the punch and the blank, the blank and the blankholder, and the blank and the die. Examination of the cup at the end of the experiment revealed that the teflon sheet had torn apart and the cup had gouge marks. Clearly, this was due to the presence of significant friction between the sheet and the die set consisting of the punch, the die and the blankholder. The gap between the punch and the die is 1.117 mm and the thickness of the sheet is 1.067 mm. With teflon sheet present on both sides of the blank, this gap is narrowed even further.

As in the cups of tantalum and tantalum - 2.5% tungsten, the steel cup also showed four ears: two along the rolling direction and two along the transverse direction of the sheet, Fig. 7-13(a). The scoring marks on the cup due to friction can also be seen in this figure. The average height of the ear and the trough for the cup is 42.85 mm and 40.66 mm, the average difference being 2.14 mm (see Fig. 7-14(a)). The experimentally-measured earing behavior in low-carbon steel, tantalum and tantalum - 2.5% tungsten is compared in Table 4.1.

Table 6.1 Comparison of the earing behavior in sheets of low-carbon steel, tantalum and tantalum - 2.5% tungsten

Material	Average cup height (mm)			Initial texture
	ear height	trough height	difference	
Low-carbon steel	42.85	40.66	2.14	(111)[110]
Tantalum	42.8	41.53	1.27	$(111) < uvw >$
Tantalum - 2.5% tungsten	42.94	38.93	4.01	$(111) < uvw > +(100)[100]$

The tantalum - 2.5% tungsten cup shows the most pronounced earing as evident from the difference between the height of the ear and the trough. The presence of cube-components or the (100)[100] type texture results in a high degree of planar anisotropy in the sheet and hence a more pronounced earing behavior.

The thickness strain in the bottom, corner and the wall of the cup measured at 0^o,

45^o, and 90^o from the rolling direction is shown in Fig. 7-15. As seen from this figure, the thinnest region occurs in the cup corner. The thickness of the cup increases along its wall and saturating at a thickness strain of 0.0465. The wall thickness cannot increase beyond 1.117 mm, which is equal to the gap between the punch and the die. For an initial sheet thickness of 1.067 mm, this corresponds to a thickness strain of 0.0465.

The numerical simulation of the experiment was performed in ABAQUS/Explicit using a combination of 672 ABAQUS C3D8 and C3D6 elements, with two elements through the thickness of the sheet, Fig. 6-8(b). Since the initial texture of the sheet possesses orthotropic symmetry, only a 90° sector of the circular blank was considered in the analysis. Initially, the interfaces between the punch and the blank, the blank and the blankholder, and the blank and the die was modeled as frictionless. The comparison of the predicted cup-height and the punch-load displacement curve for the frictionless case against the experiment is shown in Figs. 7-14(a) and 7-14(b) respectively. Although the number and the location of the ears is accurate, the simulation under-predicts the punch load and the cup height. This difference between the experiment and the prediction is due to the modeling of the interfaces between the die set and the sheet as frictionless. We repeated the calculation with a friction coefficient of 0.15. As seen from Figs. 7-14(a) and 7-14(b), the prediction of the punch load-displacement curve is now in much better agreement with the experiment; however, the cup-height is slightly over-predicted. By fine-tuning the friction coefficient, we can get the prediction of the cup-height be in better aggrement with the experiment. Fig. 7-13(b) shows the predicted shape of the fully-drawn steel cup from this simulation. This figure also shows the equivalent tensile plastic strain $\bar{\epsilon}^p$ contours in the cup at the end of the drawing process. The prediction of the number of ears and their positions is also accurate. The calculated and the measured thickness strain in the bottom, corner and wall of the cup is shown in Fig. 7-16. The agreement is reasonable.

Overall, we conclude that the Taylor-type crystal plasticity model is reasonably accurate in predicting the macroscopic stress-strain response, the evolution of crystallographic texture and the shape changes in quasi-static homogenous as well as non-homogenous experiments on b.c.c. iron and low-carbon steel.

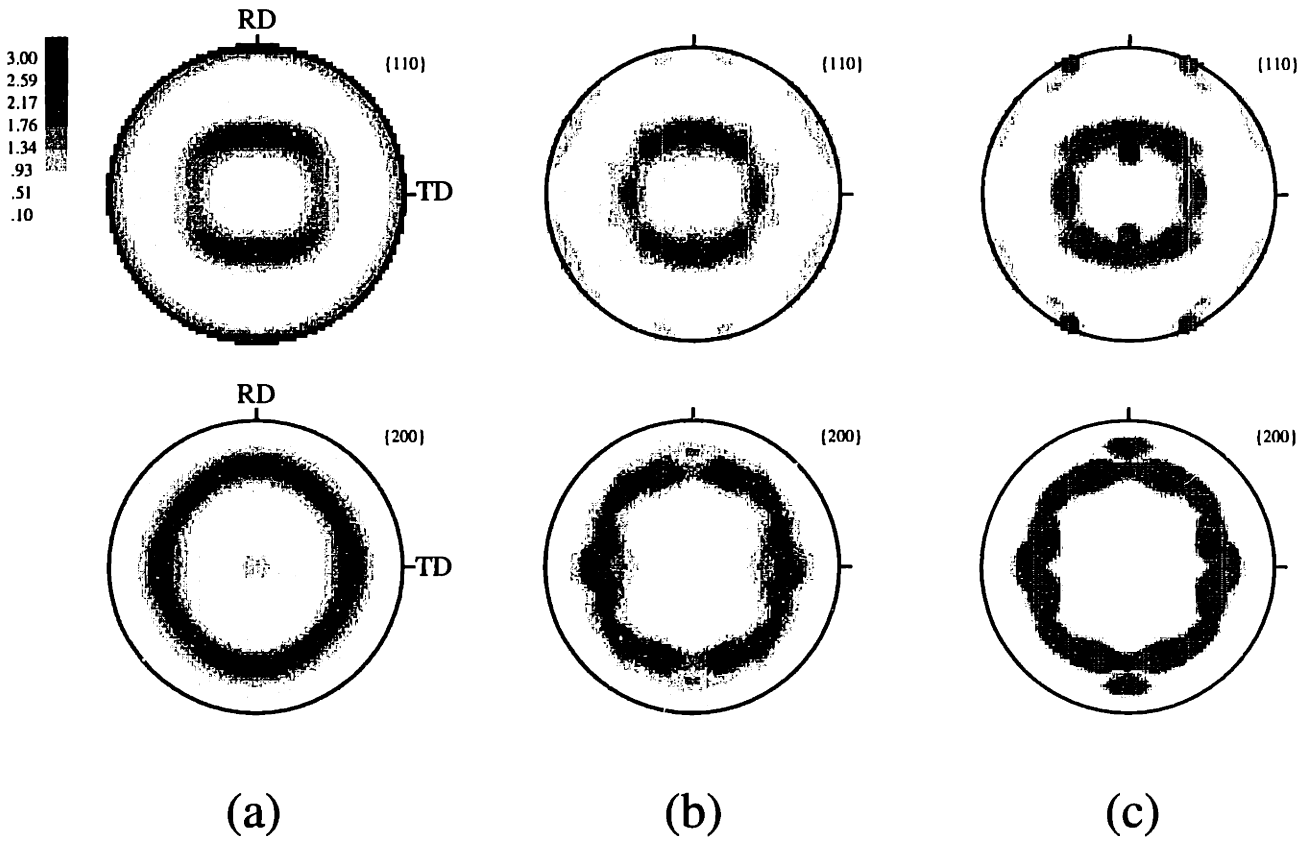

Figure 7-10: Experimentally measured texture of low-carbon sheet and it's numerical representation: (a) Measured texture. (b) Numerical representation using 200 weighted grain orientations. (c) Numerical representation using 25 weighted grain orientations.

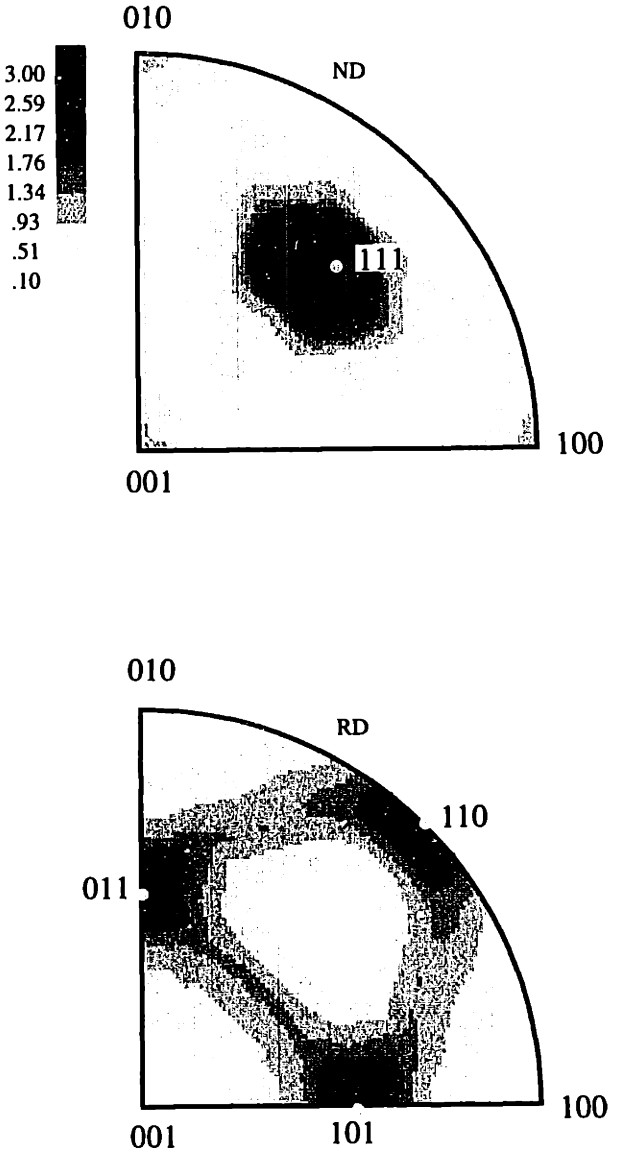

Figure 7-11: Inverse pole figures computed from the measured texture for low-carbon steel sheet.

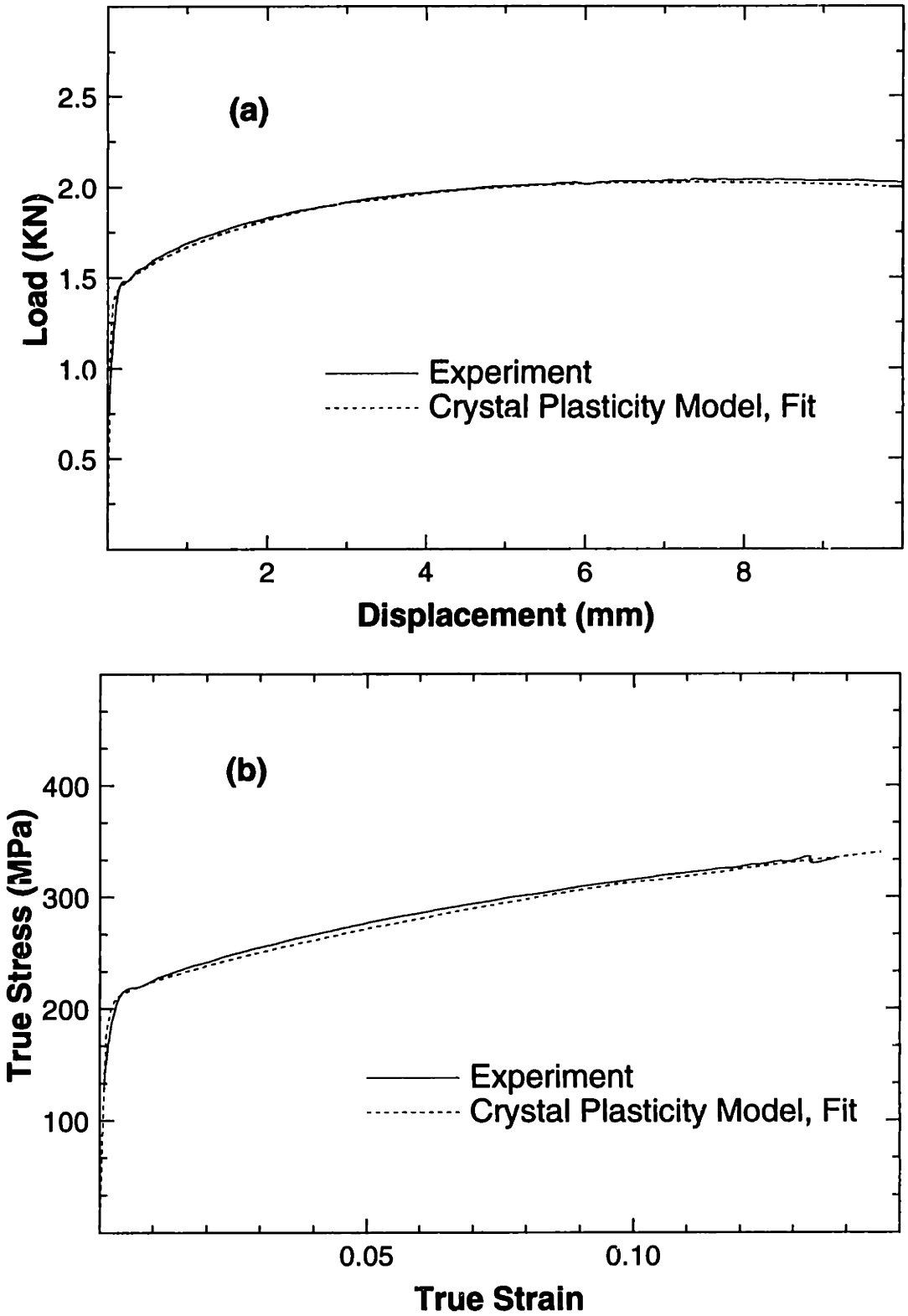

Figure 7-12: Fit of the crystal plasticity model to (a) the load-displacement response, and (b) the stress-strain response in the tension experiment on low-carbon sheet along the rolling direction.

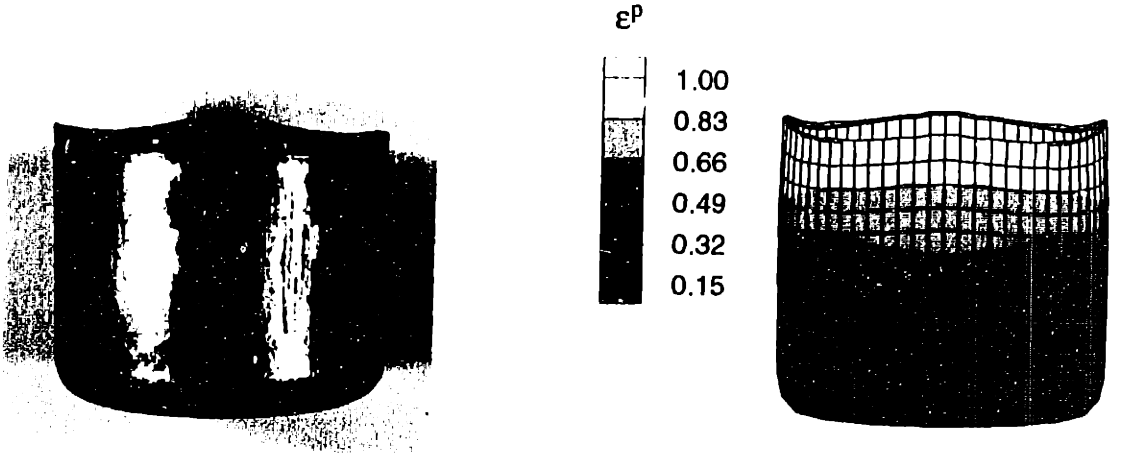

Figure 7-13: Comparison of the predicted earing pattern against that observed in the experiment. (a) Observed earing pattern (The rolling direction is from the left to the right). (b) Numerical prediction. The numerical simulation also shows the equivalent plastic strain contours.

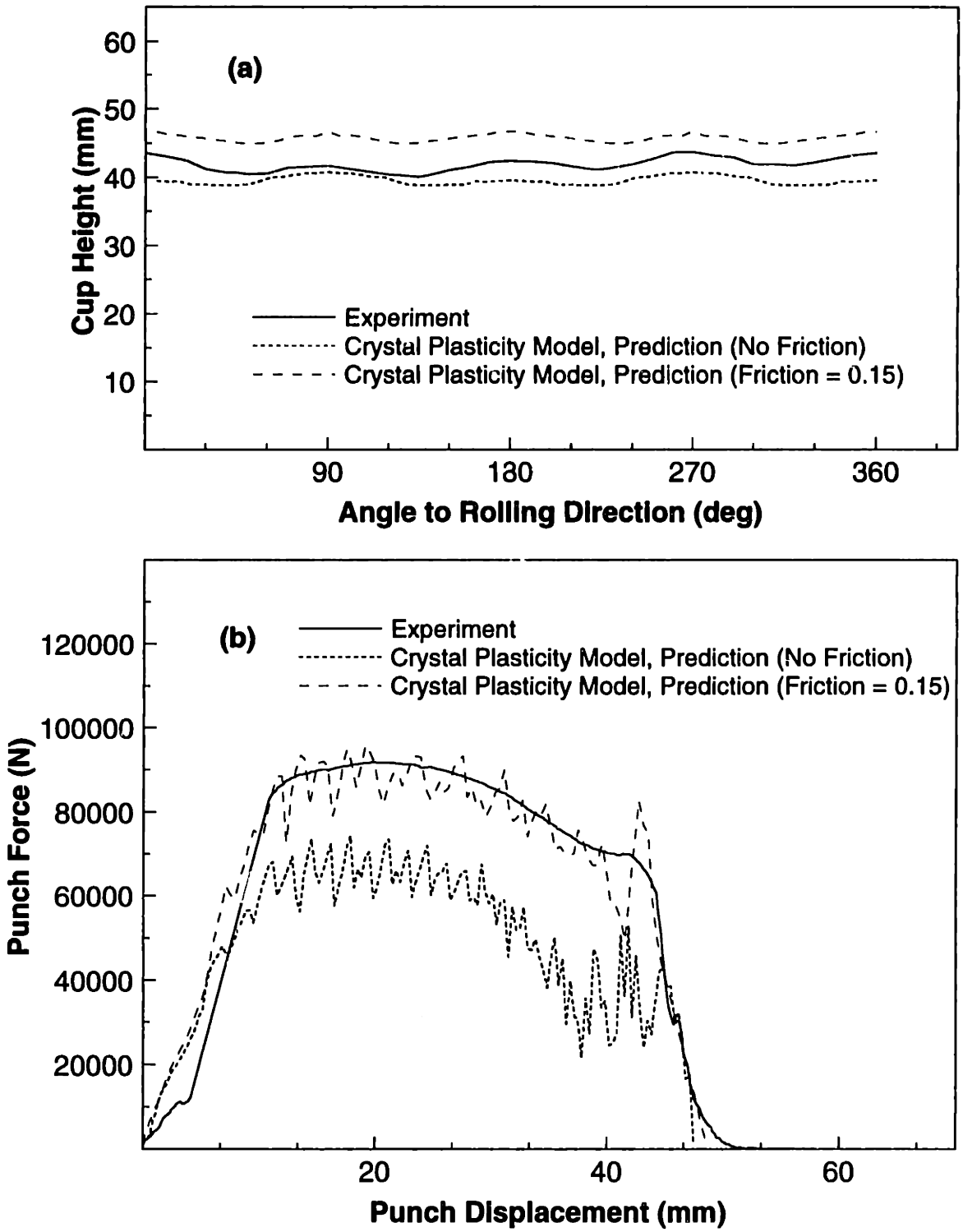

Figure 7-14: Comparion of the numerical prediction against the measured (a) cup-height profile, and (b) the load-displacement response in the cup-drawing experiment on low-carbon steel sheet.

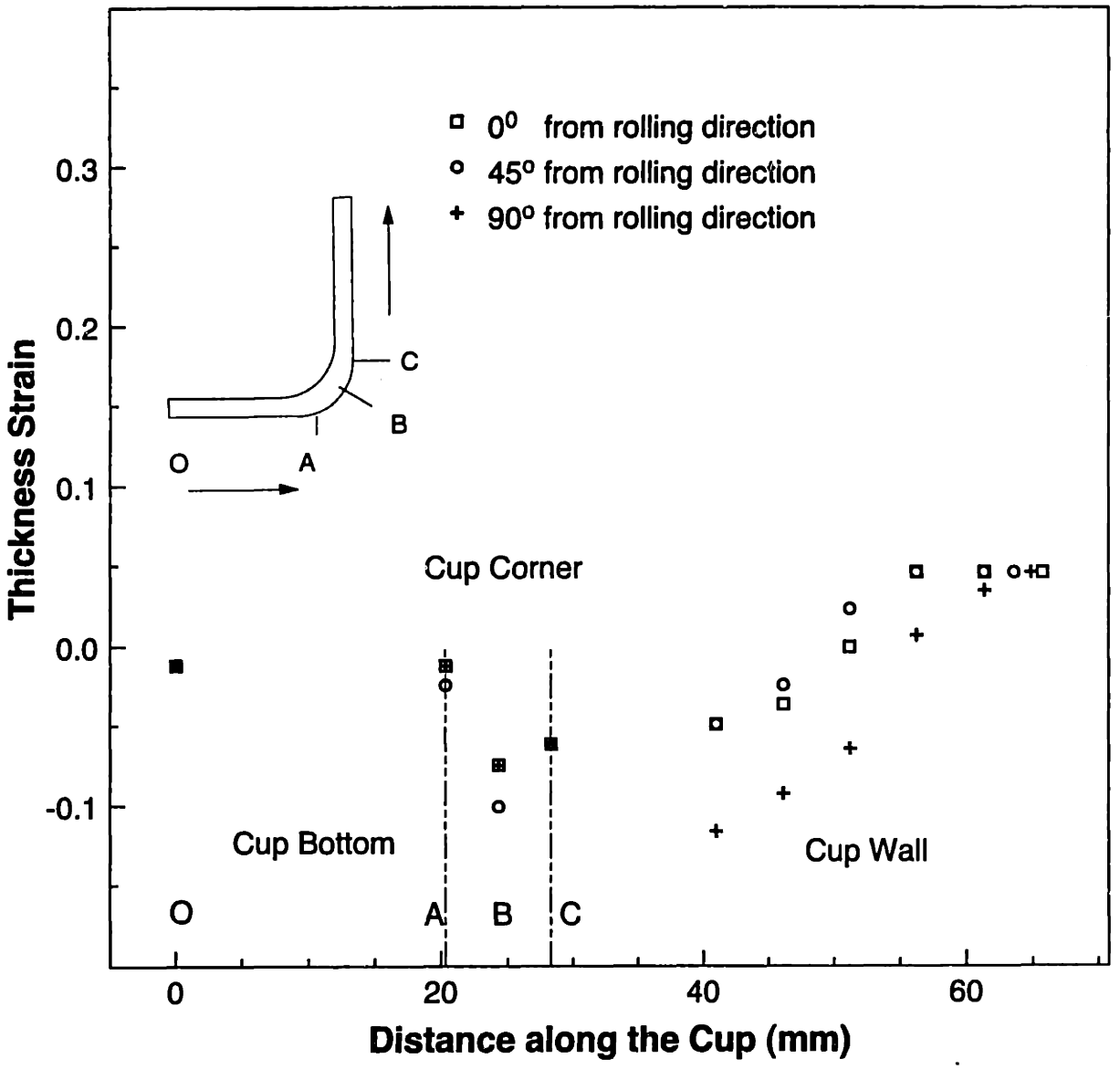

Figure 7-15: Experimentally measured thickness strain profile for the low-carbon steel cup

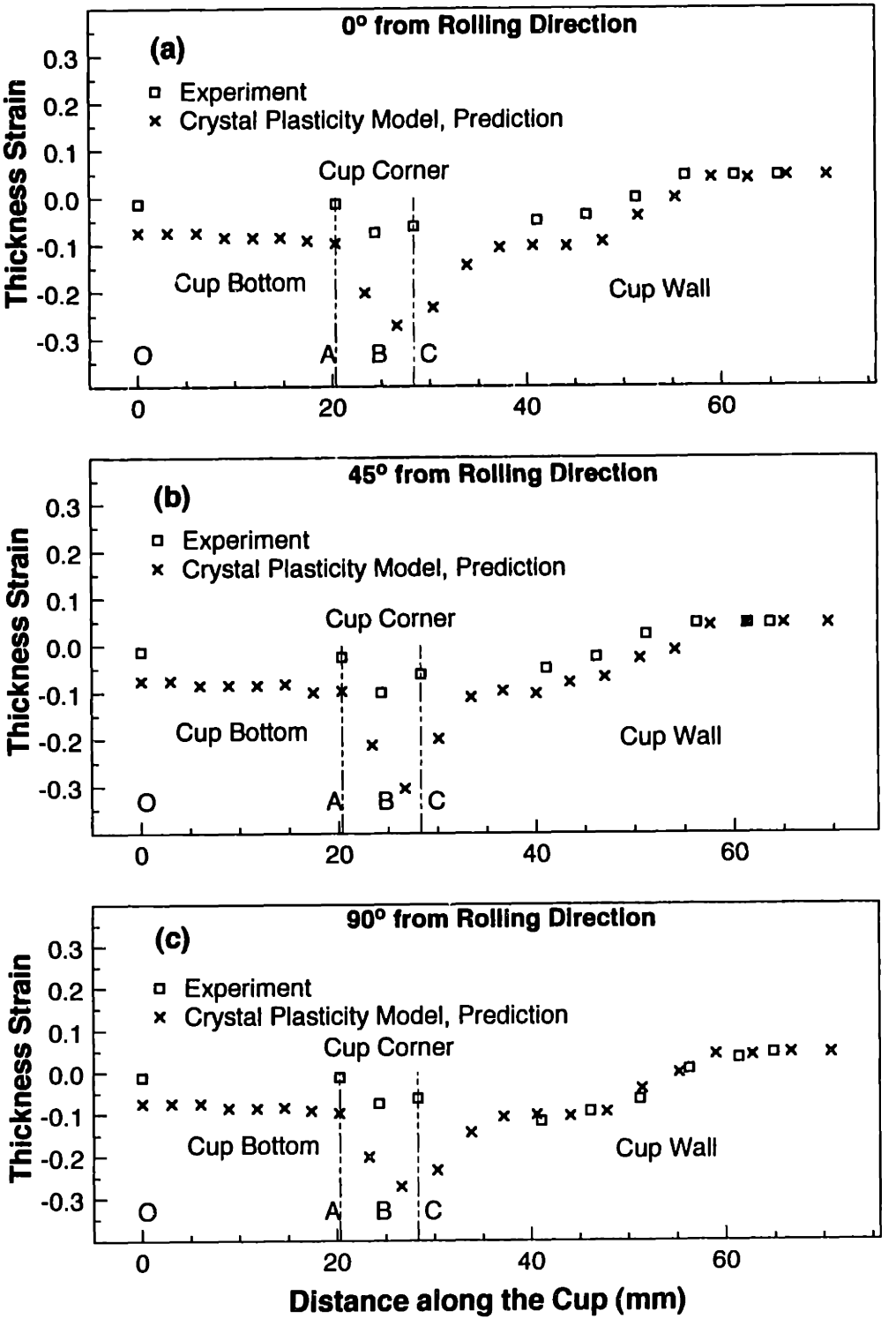

Figure 7-16: Comparison of the experimentally measured and predicted thickness strain profile for the low-carbon steel cup along (a) 0^o from the rolling direction, (b) 45^o from the rolling direction, (c) 90^o from the rolling direction.

Chapter 8

Conclusion

A Taylor-type crystal plasticity model has been developed for b.c.c. tantalum deforming by crystallographic slip. In essence, the model extends the previous work of Anand and co-workers (e.g., Kalidindi *et al.*, 1992; Bronkhorst *et al.*,1 992; Anand and Kalidindi, 1994) on f.c.c. materials to b.c.c. materials, and replaces the simple power-law relation (1.1) for the shearing rates used previously, with a more accurate relation based on thermal-activation theory of dislocation glide (e.g. Kocks *et al.*, 1975). The constitutive model has been implemented in the finite element program ABAQUS (1995). The material functions and parameters in the model are determined by calibrating the model against existing experimental data on commercially-pure tantalum (Hoge and Mukherjee, 1977; Vecchio, 1994; Nemat-Nasser and Isaacs, 1996) for large-strain ($\approx 60\%$) and high-strain rates (up to $\approx 10^5\,\mathrm{sec}^{-1}$) at low homologous temperatures (< 0.3). The model reproduces these experiments reasonably well.

To evaluate the predictive capability of the model, the following experiments were performed:

- Quasi-static experiments in (*i*) simple compression, (*ii*) plane-strain compression, and (*iii*) torsion of pre-textured tantalum have been conducted, and the resulting macroscopic stress-strain curves and crystallographic-texture evolution have been measured. A comparison of these results against corresponding predictions from our constitutive model and computational procedures shows the model to be reasonably accurate.

- The ability of the constitutive model and computational procedures to capture the

effect of initial texture on the final shape and load-displacement response under quasi-static rates is evaluated by carrying out cup-drawing experiments on tantalum and tantalum-2.5% tungsten sheets. The agreement between the predicted earing phenomenon and the load-displacement response with the experiments is very good.

- The performance of the model under high strain rates and large strains is also evaluated by carrying out a simulation of a Taylor cylinder-impact experiment, and by comparing the predicted final shape to that observed experimentally by Ting (1992). The final shapes, including the ovalization of the impact end of the pre-textured rod used by Ting, are quantitatively well predicted by our simulations.

To the best of our knowledge, this is the first demonstration of the applicability of a Taylor-type crystal plasticity model for both quasi-static and dynamic deformations of polycrystalline tantalum.

The applicability of the crystal plasticity model to b.c.c iron has also been demonstrated by performing quasi-static homogeneous experiments on iron, and quasi-static cup-drawing experiments on a low-carbon steel.

8.1 Suggestions for Future Research

Following are some areas for future research :

- Adiabatic shear localization is an important mode of failure in polycrystalline b.c.c. materials such as tantalum and iron at high strain-rates (Qiang [1993]). The effect of textural and thermal softening on the localization phenomenon can be studied by using the constitutive equations presented here.

- To predict failures during deformation processing, there is a need to develop a failure criteria. Other details of microstructure such as porosity, localized shear bands, etc. and their evolution need to be incorporated in the constitutive model.

- Twinning is a major contributor to plastic deformation in many important b.c.c. metals. For example, iron twins profusely at high strain-rates or low temperatures. The incorporation of twinning in a rate-dependent crystal plasticity model would facilitate simulations of dynamic deformations in materials. For a recent rate-

independent model incorporating both crystallographic slip and twinning, see Staroselsky and Anand [1997].

Appendix A

Isotropic Model

The simplest and most commonly-used phenomenological model for "isotropic" infinitesimal elastic-plastic deformations is the classical rate-independent J_2 flow theory with isotropic hardening. The set of constitutive equations considered here is essentially a generalization of this widely-used theory to model finite plastic deformations, and rate-dependence of plastic flow. This isotropic model substantially aids in the determination of the material parameters in the anisotropic crystal-plasticity model described in Chapter 2 of this thesis. When the complete details of a crystal-plasticity based calculation are not needed, then this isotropic model is useful in its own right for representing the large-strain, strain-rate and temperature-dependent behavior of b.c.c. materials.

In the isotropic model, the governing variables are taken as $\{\mathbf{T}, \mathbf{F}, \theta; \mathbf{F}^p, s\}$, where now $\mathbf{F}^p$ with $\det(\mathbf{F}^p) = 1$ is a macroscopic plastic deformation gradient, and $s > 0$ is a macroscopic "isotropic" deformation resistance.

Constitutive Equation For Stress:

The constitutive equation for stress is taken as

$$\mathbf{T}^* = \mathcal{C}\left[\mathbf{E}^e - \mathbf{A}\,(\theta - \theta_0)\right], \tag{A.1}$$

where, now $\mathcal{C} = 2\,\mu\mathcal{I} + (\kappa - (2/3)\mu)\,\mathbf{1} \otimes \mathbf{1}$ is a fourth-order isotropic elasticity tensor, with μ and κ the shear and bulk moduli, respectively; and $\mathbf{A} = \alpha\,\mathbf{1}$, with α the coefficient of thermal expansion, is a second-order isotropic thermal expansion tensor. Also, $\mathbf{E}^e$ and $\mathbf{T}^*$

are strain and stress measures defined by

$$\mathbf{E}^e \equiv (1/2)\left\{\mathbf{F}^{eT}\mathbf{F}^e - \mathbf{1}\right\} \quad \text{and} \quad \mathbf{T}^* \equiv (\det \mathbf{F}^e)\, \mathbf{F}^{e-1}\mathbf{T}\mathbf{F}^{e-T}. \tag{A.2}$$

Flow Rule:

The evolution equation for $\mathbf{F}^p$ is given by the flow rule

$$\dot{\mathbf{F}}^p\mathbf{F}^{p-1} = \mathbf{D}^p + \mathbf{W}^p, \tag{A.3}$$

$$\mathbf{D}^p = (3/2)\dot{\bar{\epsilon}}^p\,(\mathbf{T}^{*\prime}/\bar{\sigma}), \tag{A.4}$$

$$\mathbf{W}^p = \mathbf{0}. \tag{A.5}$$

The quantity $\mathbf{T}^{*\prime}$ is the deviatoric part of $\mathbf{T}^*$,

$$\bar{\sigma} = \sqrt{(3/2)\mathbf{T}^{*\prime}\cdot\mathbf{T}^{*\prime}}$$

is the equivalent tensile stress, and

$$\dot{\bar{\epsilon}}^p = f\,(\bar{\sigma}, \theta, s) \tag{A.6}$$

is an equivalent tensile plastic strain rate.

This large-deformation isotropic elastic-viscoplastic model is specialized to represent plastic flow by thermally-activated glide of dislocations at low (< 0.3) homologous temperatures as follows. First, we decompose s as

$$s = s_a + s_*, \tag{A.7}$$

where, the part s_a denotes the athermal part, and s_* the thermally-activatable part of s. Next, with

$$\bar{\sigma}_* = \bar{\sigma} - s_a, \tag{A.8}$$

denoting an "effective stress," we take the equivalent tensile plastic strain rate to be given by

$$\dot{\bar{\epsilon}}^p = \left\{ \begin{array}{ll} 0 & \text{if } \bar{\sigma}_* \leq 0, \\ \dot{\epsilon}_0 \exp\left\{-\frac{\Delta G_*(\bar{\sigma}_*, s_*)}{k_B\theta}\right\} & \text{if } 0 < \bar{\sigma}_* < s_*, \end{array} \right\}, \tag{A.9}$$

with

$$\Delta G_* = \Delta F_* \left[1 - \left(\frac{\bar{\sigma}_*}{s_*}\right)^p\right]^q, \tag{A.10}$$

and where ΔF_*, the activation free energy required to overcome the obstacles to plastic shear increments without the aid of an applied shear stress. The quantities p and q are taken to lie in the ranges

$$0 \leq p \leq 1, \quad \text{and} \quad 1 \leq q \leq 2, \tag{A.11}$$

and the pre-exponential term is taken to have a typical magnitude of $\dot{\epsilon}_0 \approx 10^6$ to 10^7sec^{-1}.

For the case of non-zero plastic strain rate, equations (A.9, A.10) may be rearranged as

$$\bar{\sigma} = s_a + Z\left(\theta, \dot{\bar{\epsilon}}^p\right) s_*, \tag{A.12}$$

with

$$Z = \left[1 - \left(\frac{\theta}{\theta_c}\right)^{1/q}\right]^{1/p} \leq 1, \quad \text{and} \quad \theta_c = \left\{\frac{\Delta F_*}{k_B \ln\left(\frac{\dot{\epsilon}_0}{\dot{\bar{\epsilon}}^p}\right)}\right\}. \tag{A.13}$$

Evolution Equation for Deformation Resistance:

The evolution equation for the deformation resistance is taken as

$$\dot{s} = h\,\dot{\bar{\epsilon}}^p, \qquad h = \hat{h}\left(\bar{\sigma}, \theta, s\right). \tag{A.14}$$

Since s_* for b.c.c. materials is controlled by interactions with the Peierl's lattice resistance, it is reasonable to assume that

$$s_* \approx \text{constant}, \tag{A.15}$$

and

$$\dot{s} \doteq \dot{s}_a = h\,\dot{\bar{\epsilon}}^p, \tag{A.16}$$

with

$$h = h_0 \left|1 - \frac{s_a}{s_{a,s}}\right|^r \text{sign}\left(1 - \frac{s_a}{s_{a,s}}\right), \tag{A.17}$$

where

$$h_0 = \hat{h}_0\left(\dot{\bar{\epsilon}}^p, \theta\right) \tag{A.18}$$

is the initial hardening rate, and

$$s_{a,s} = \hat{s}_{a,s}\left(\dot{\bar{\epsilon}}^p, \theta\right) \tag{A.19}$$

is a saturation value of s_a, where we have indicated that both h_0 and $s_{a,s}$ are possibly strain-rate and temperature-dependent.

The computational problem for the isotropic model is much simpler than the crystal-plasticity model because one does not have to consider explicitly the slip systems, the individual slip-system resistances, and their evolution. For a detailed discussion of the time-integration procedure for the isotropic plasticity model[1] see Weber and Anand [1990].

A.1 Material Parameters for Tantalum

The material parameters in the isotropic model for tantalum are as follows. The isotropic elasticity tensor $\mathcal{C}$ is specified in terms of two parameters, μ and κ, the shear and bulk moduli, respectively. The values of these parameters for tantalum as a function of temperature are taken as (Simmons and Wang [1971]):

$$\begin{aligned} \mu &= \left(68.8 - 9.9 \times 10^{-3}\,\theta\right) \text{ GPa}, \\ \kappa &= \left(176.5 - 11 \times 10^{-3}\,\theta\right) \text{ GPa}. \end{aligned}$$

Determination of Flow Parameters :

Step 1. Determination of the initial value of the athermal deformation resistance $s_{a,0}$.

Repeating equation (A.12) and (A.13) for convenience, we have

$$\bar{\sigma}_0\left(\theta, \dot{\bar{\epsilon}}^p\right) = s_{a,0} + Z\left(\theta, \dot{\bar{\epsilon}}^p\right) s_*, \tag{A.20}$$

with

$$Z = \left[1 - \left(\frac{\theta}{\theta_c}\right)^{1/q}\right]^{1/p} \leq 1, \quad \text{and} \quad \theta_c = \left\{\frac{-\Delta F_*}{k_B \ln\left(\frac{\dot{\bar{\epsilon}}^p}{\dot{\epsilon}_0}\right)}\right\}. \tag{A.21}$$

$\bar{\sigma}_0\left(\theta, \dot{\bar{\epsilon}}^p\right)$ denotes the yield strength at a strain rate of $\dot{\epsilon}$ (when the plastic flow is fully developed, we may assume that $\dot{\bar{\epsilon}}^p \approx |\dot{\epsilon}|$) and at a temperature θ. At a given strain rate $\dot{\epsilon}$, the strain rate and temperature parameter $Z = 0$ at a temperature $\theta = \theta_c$ and

[1]The difference between the model considered by Weber and Anand, and that used here, lies essentially in the choice of the stress and strain measures for the constitutive equation for stress. In their paper, instead of (A.2), Weber and Anand used $\mathbf{E}^e \equiv \ln \mathbf{U}^e$ and $\mathbf{T}^* \equiv (\det \mathbf{U}^e)\, \mathbf{R}^{eT} \mathbf{T} \mathbf{R}^e$, where $\mathbf{F}^e = \mathbf{R}^e\, \mathbf{U}^e$ is the polar decomposition of $\mathbf{F}^e$. For infinitesimal elastic stretches, the difference between the two models is indistinguishable.

the above equation reduces to

$$\bar{\sigma}_0\left(\theta_c, \dot{\bar{\epsilon}}^p\right) = s_{a,0} \;\; \forall \theta \geq \theta_c$$

To determine $s_{a,0}$, we need to know the critical temperature θ_c at a given strain rate $\dot{\epsilon}$ and the yield stress at this temperature. The critical temperature θ_c depends also on the flow parameters ΔF_* and $\dot{\epsilon}_0$ which are yet to be determined. Therefore, as a first guess, determine θ_c from the yield strength vs. temperature data at a constant strain rate by finding the temperature at which the yield strength appears to saturate and take this value to be equal to $s_{a,0}$. From Fig. A-2, at a strain rate of 10^{-4}sec^{-1}, the yield strength of tantalum appears to saturate around 800 K and $s_{a,0} = \bar{\sigma}_0 \approx 66$ MPa at this temperature.

Step 2. Determination of the thermal deformation resistance s_*.

From (A.20) and (A.21), it can be seen that at 0 K, the strain rate and temperature parameter $Z = 1$ and $s_* = \bar{\sigma}_0 - s_{a,0}$, where $\bar{\sigma}_0$ is the yield strength obtained by extrapolating the experimental data on the temperature sensitivity of yield strength to 0 K. From Fig. A-2, $\bar{\sigma}_0 \approx 1141$ MPa at 0 K and with $s_{a,0} = 66$ MPa from step 1, the thermal deformation resistance $s_* = 1075$ MPa for tantalum.

Step 3. Determination of $\Delta F^*, p, q$ and $\dot{\epsilon}_0$.

With $s_{a,0}$ and s_* as obtained above, the flow parameters $\{\Delta F^*, p, q, \dot{\epsilon}_0\}$ are obtained by performing a non-linear least squares fit of the experimental data on the temperature and strain rate sensitivity of yield strength to (A.20). The values of the flow parameters obtained by the curve fitting procedure are

$$\dot{\epsilon}_0 = 10^7\,\text{sec}^{-1},\;\; \Delta F^* = 2.77 \times 10^{-19}\text{J},\;\; p = 0.28,\;\; q = 1.34,\;\; s_* = 1075\text{MPa}$$

with

$$s_{a,0} = 66\text{MPa}$$

Step 4. Determine the critical temperature θ_c in step 1.

With the flow parameters as obtained in step 3, determine the critical temperature θ_c. If this critical temperature is different from the the temperature at which $s_{a,0}$ was

determined, go back to step 1 and reiterate with a temperature θ_c as obtained in this step. For tantalum, at a strain rate of $10^{-4}\,\mathrm{sec}^{-1}$ the temperature $\theta_c \approx 800K$. As $s_{a,0}$ was obtained in step 1 at a temperature around 800 K, the iterative procedure for the determination of the flow parameters has converged.

The fit from the isotropic model and the experimental data for the strain rate dependence of the yield strength at 298^o K is presented in Fig. A-1 and for the temperature dependence of the yield strength at a strain rate of $10^{-4}\mathrm{sec}^{-1}$ in Fig. A-2. As seen from the figures, the model is able to capture the strain rate and temperature sensitivity of the yield strength of tantalum reasonably well.

Determination of the hardening parameters :

With the flow parameters as determined above, the hardening parameters, with h_0 and $s_{a,s}$ taken as independent of strain-rate and temperature, are determined by curve-fitting the isothermal and adiabatic experimental stress-strain curves of Vecchio [1994]) and Nemat-Nasser and Isaacs [1996] against the predictions from the isotropic model. This yields:

	$s_{a,0}$	h_0	$s_{a,s}$	r
Nemat-Nasser and Isaacs (1996)	90 MPa	1000 MPa	375 MPa	1.1
Vecchio (1994)	150 MPa	2000 MPa	300 MPa	1.1

These different values of the hardening parameters may be attributed to the different initial states of the specimens used in the two sets of experiments by the two sets of authors.

The fit from the isotropic model against the experiments of Nemat-Nasser and Isaacs [1996] and Vecchio [1994] are presented in Fig. A-3 through A-5. The model is able to capture the strain hardening and thermal softening behavior of tantalum reasonably well upto strain rates of the order of 10^4 sec^{-1}, temperatures upto 800^o K and strains upto 60%.

A.2 Material Parameters for Iron

The material parameters in the isotropic model for iron are as follows. The isotropic elasticity tensor $\mathcal{C}$ is specified in terms of two parameters, μ and κ, the shear and bulk moduli, respectively. The values of these parameters for iron as a function of temperature

are taken as (Simmons and Wang [1971]):

$$\begin{aligned} \mu &= \left(81.5 - 22.5 \times 10^{-3}\theta\right) \text{GPa}, \\ \kappa &= \left(138.5 - 30.6 \times 10^{-3}\theta\right) \text{GPa}. \end{aligned}$$

The data of Leslie [1972] on the temperature dependence of the yield strength of titanium-gettered iron (Fe-0.15% Ti) is used for the determination of the flow parameters, Fig. A-6. Following the procedure presented in the previous section, the flow parameters obtained by the fitting procedure are

$$\dot{\epsilon}_0 = 10^7 \,\text{sec}^{-1},\ \Delta F^* = 1.38 \times 10^{-19}\text{J},\ p = 0.62,\ q = 1.5,\ s_* = 1000\text{MPa}$$

with

$$s_{a,0} = 30\text{MPa}$$

The fit, as presented in Fig. A-6, is reasonable.

The hardening parameters are determined for the individual cases by fitting the measured stress-strain curve.

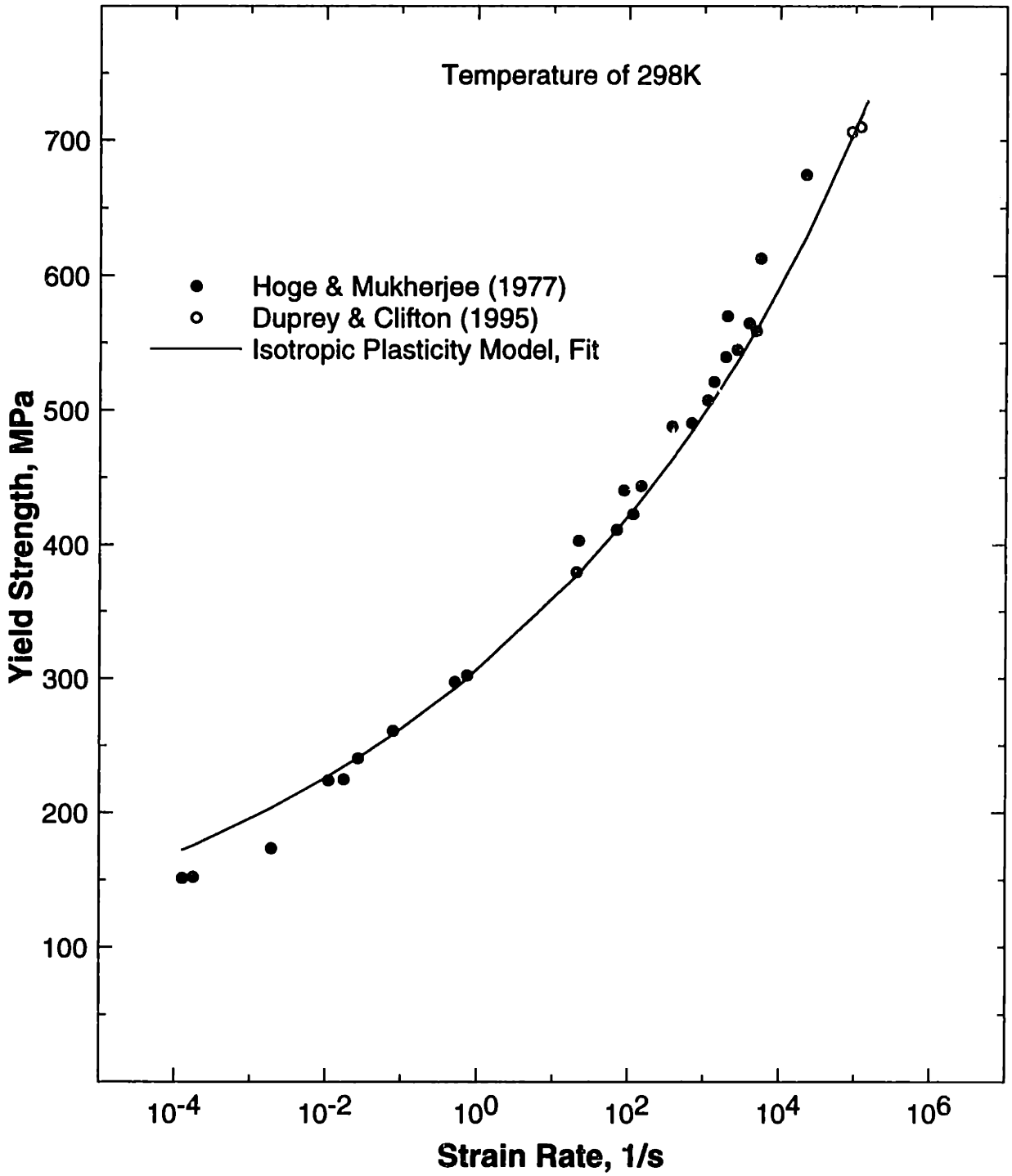

Figure A-1: Fit of the isotropic model to the data of Hoge and Mukherjee (1977) and Duprey and Clifton (1995) on the strain rate dependence of the yield strength of b.c.c. tantalum.

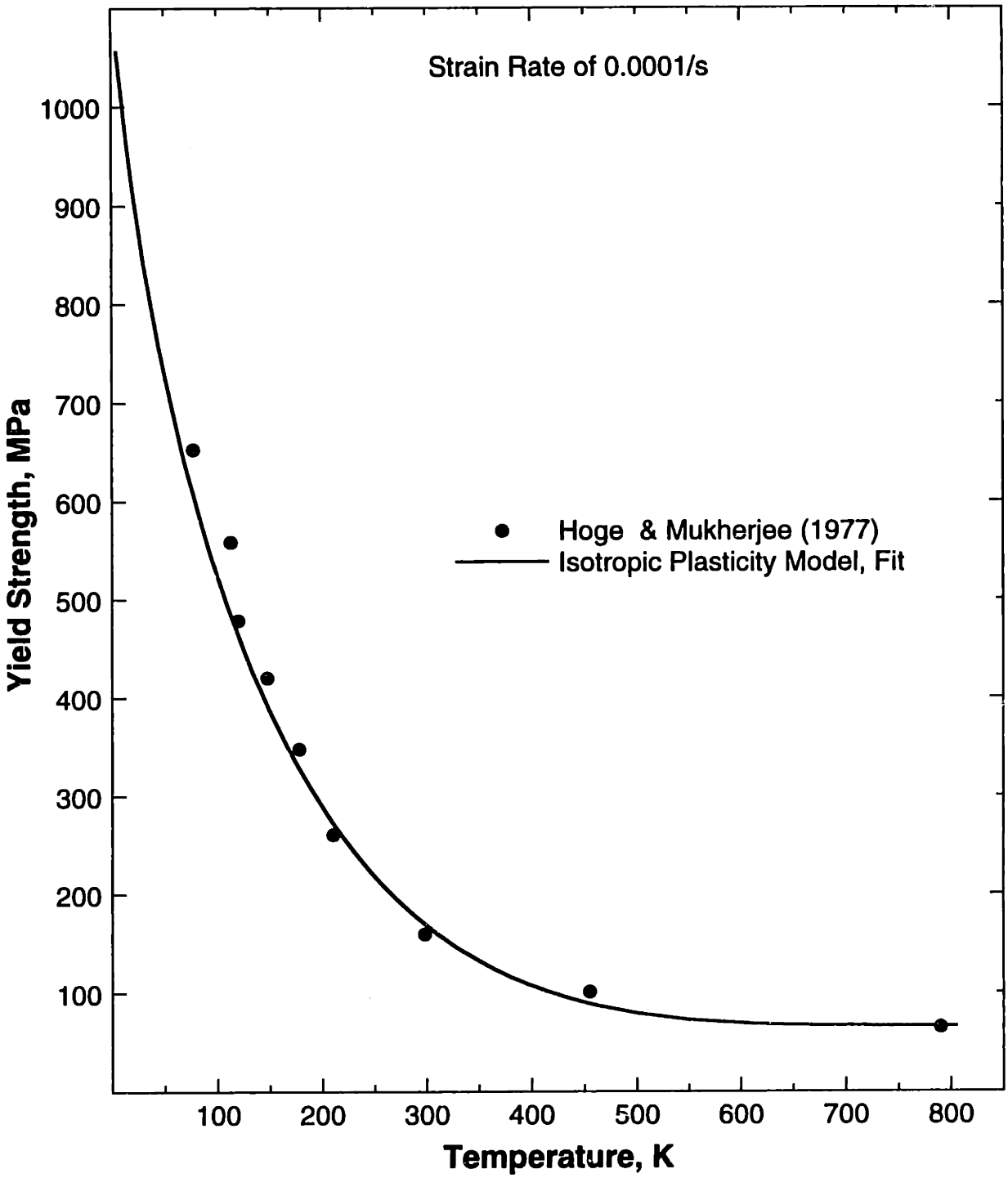

Figure A-2: Fit of the isotropic model to the data of Hoge and Mukherjee (1977) on the temperature dependence of the yield strength of b.c.c. tantalum.

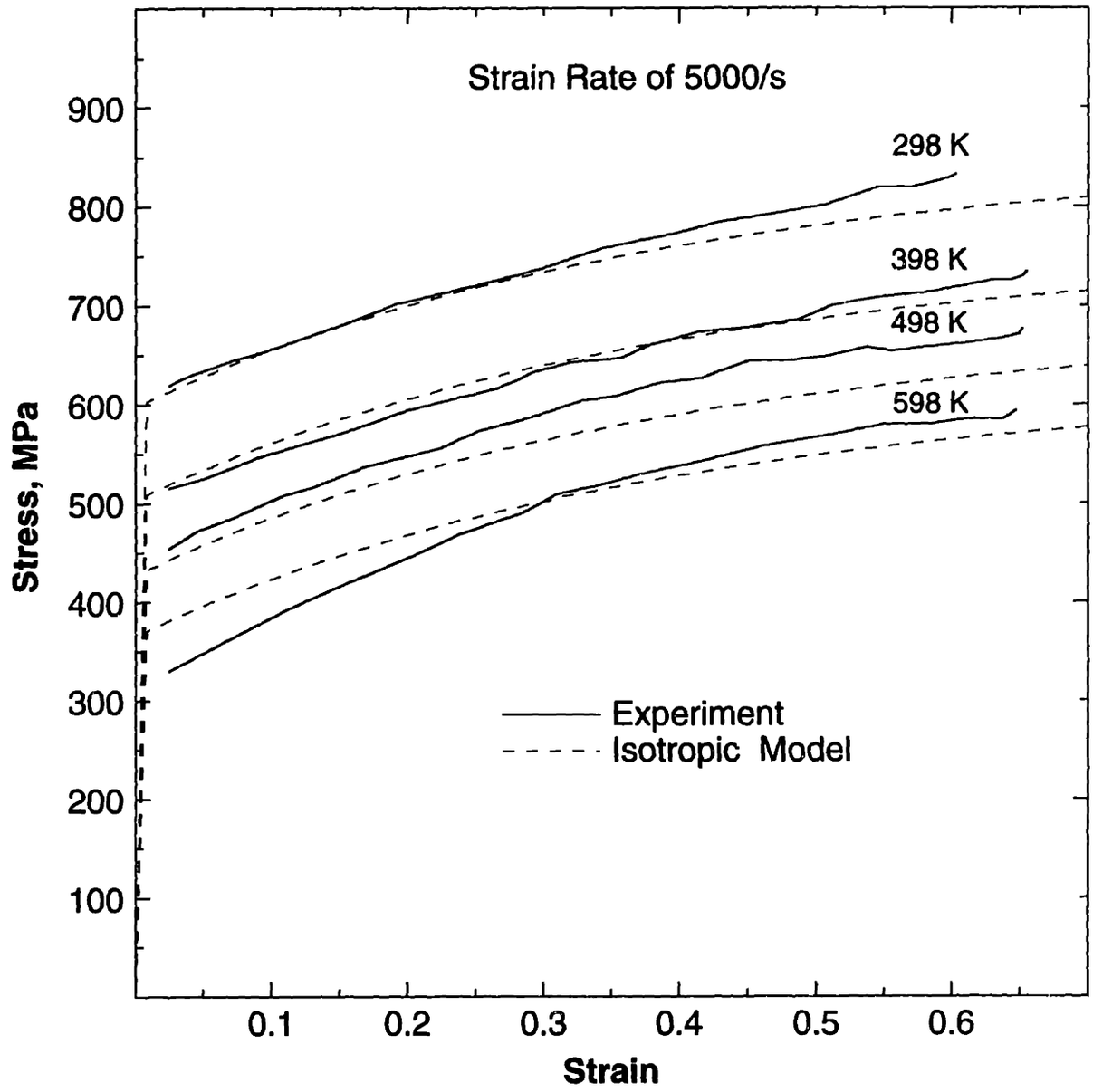

Figure A-3: Comparison of the predictions from the isotropic model against the *isothermal* experiments of Nemat-Nasser and Issacs (1996).

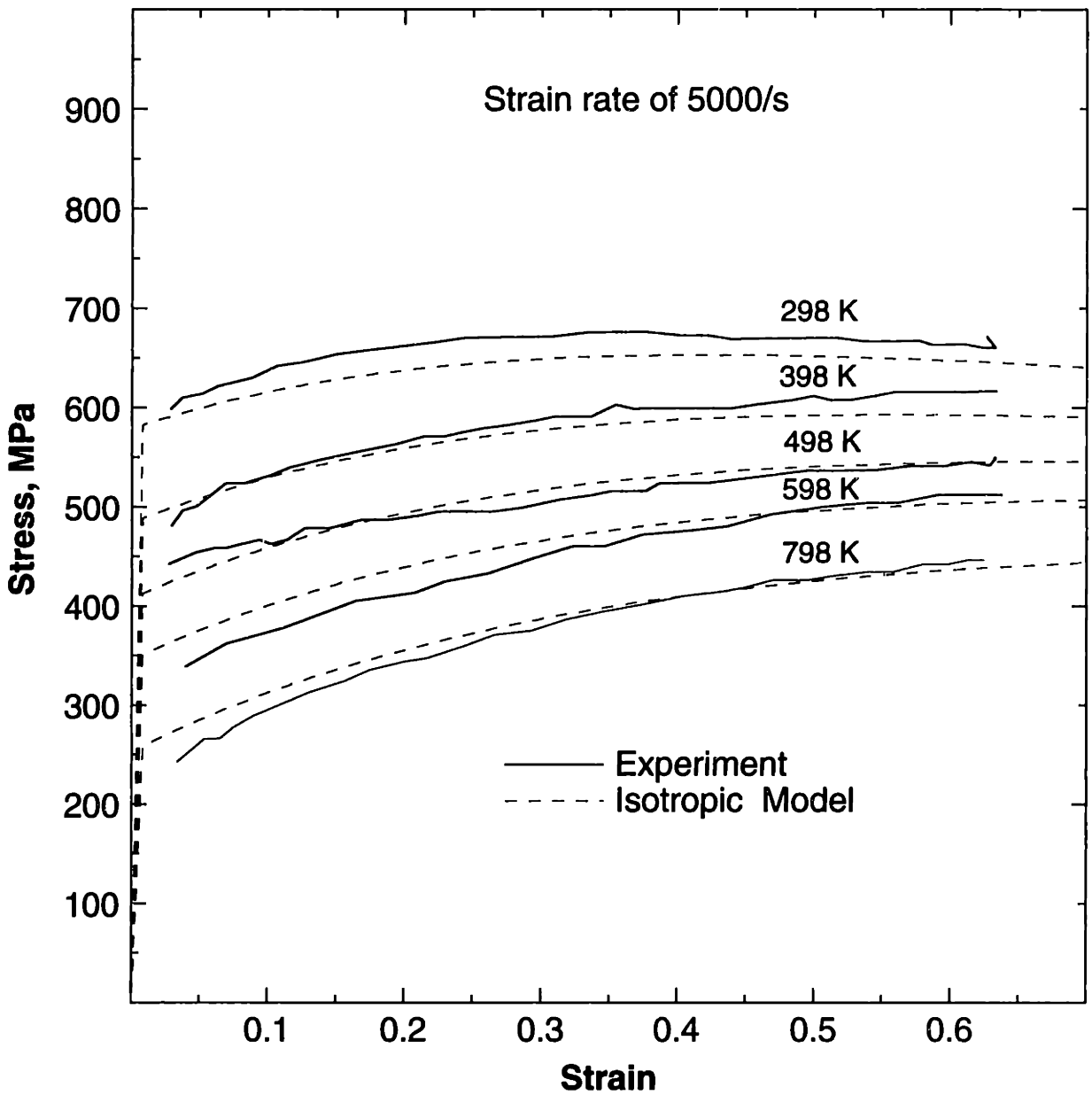

Figure A-4: Comparison of the predictions from the isotropic model against the *adiabatic* experiments of Nemat-Nasser and Issacs (1996).

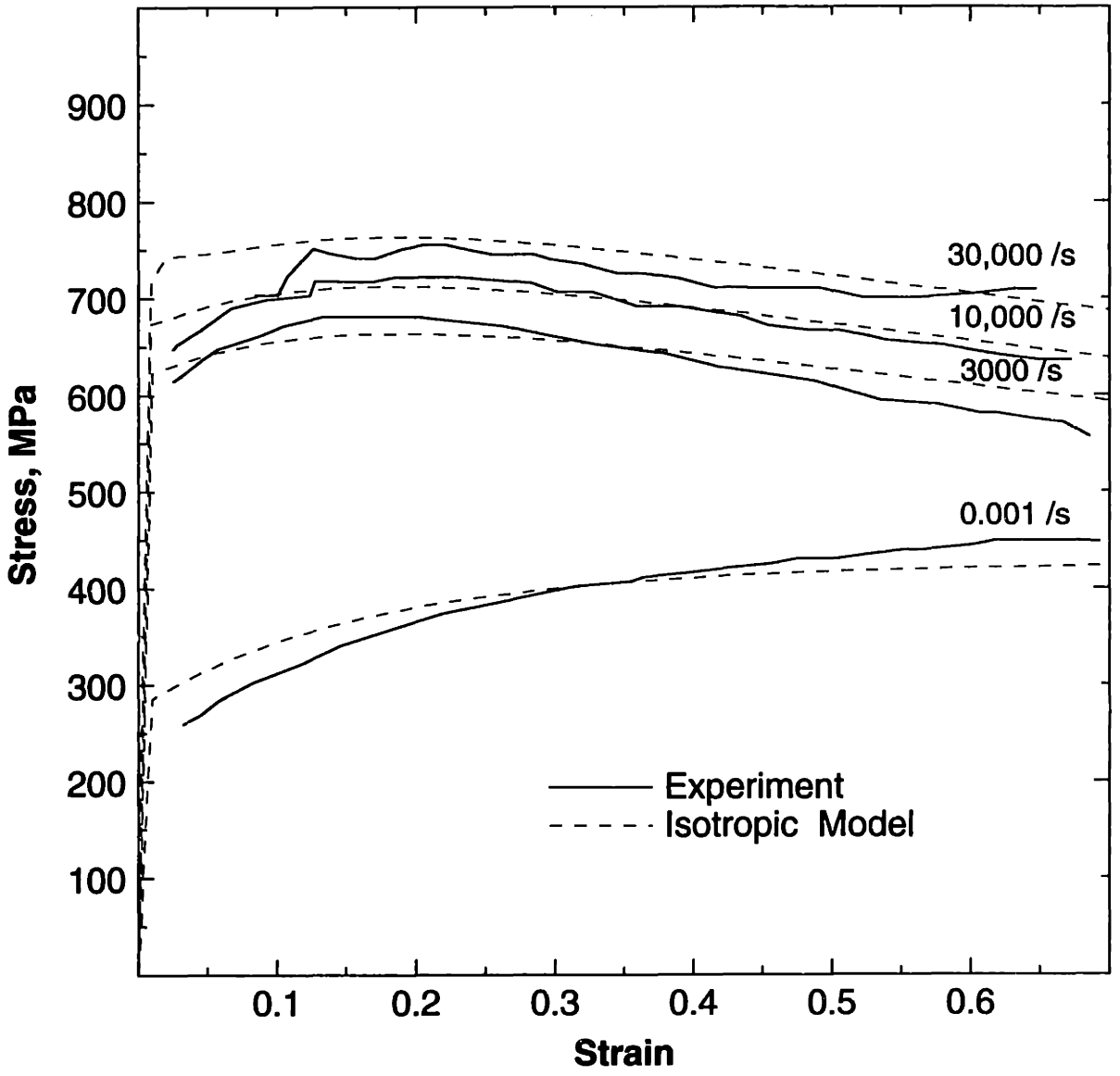

Figure A-5: Comparison of the predictions from the isotropic model against the experimental data of Vecchio (1994).

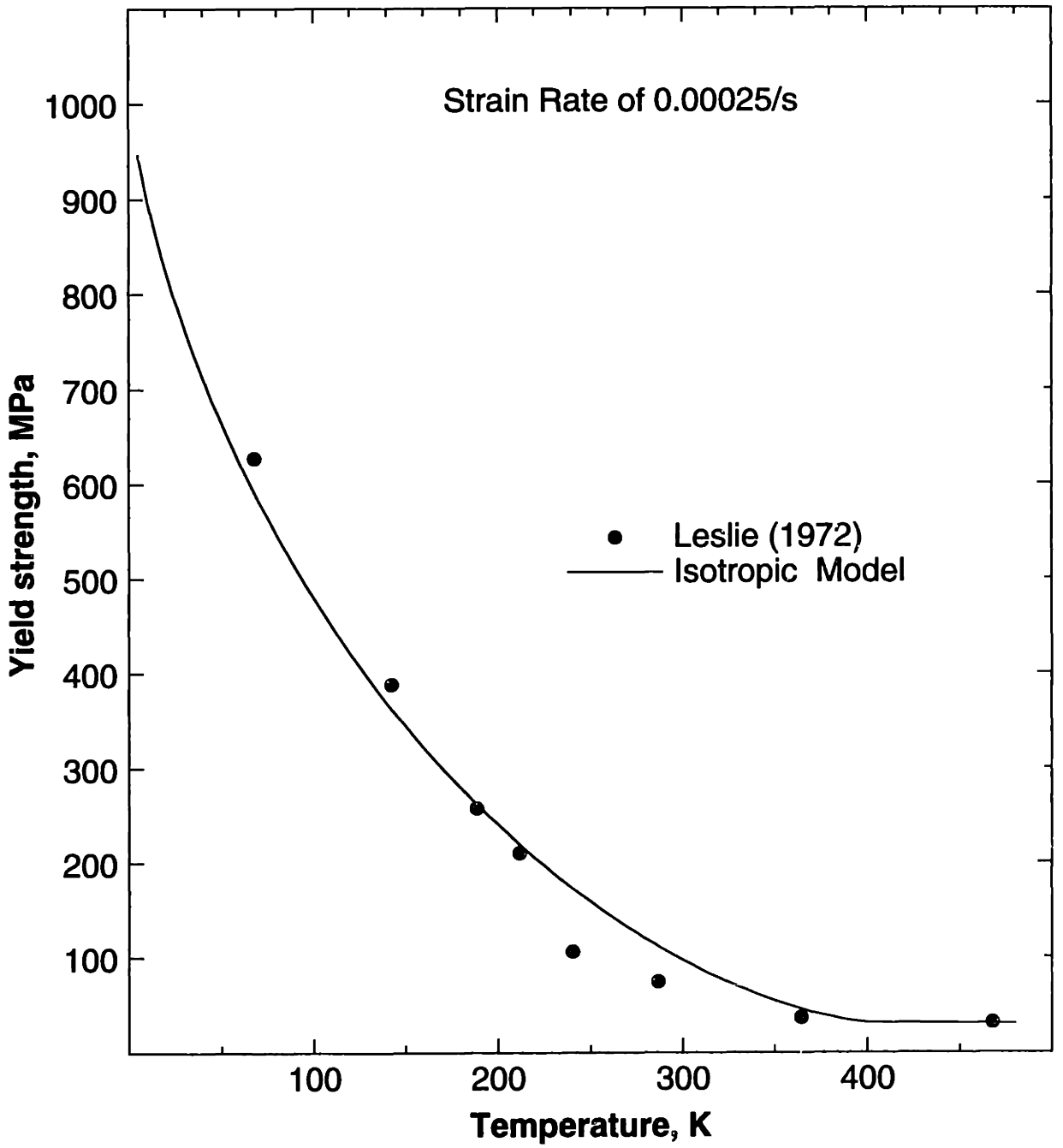

Figure A-6: Fit of the isotropic model to the data of Leslie (1972) on the temperature dependence of the yield strength of b.c.c. iron.

Appendix B

Simple Compression and Tension Simulations on B.C.C. Single Crystals

In this chapter, we analyze the effect of the different choices of the slip systems on the evolution of texture and the stress-strain response in simple compression and tension experiments on b.c.c. single crystals.

The single crystal orientations considered are the corner multi-slip orientation [$\bar{1}11$], and the single-slip orientation [$\bar{2}36$] inside the primary stereographic triangle [001] - [011] - [$\bar{1}11$] as shown in the Figure B-1. These initial orientations are specified by three Euler angles {θ, ϕ and ω} (Kalidindi [1992], Allan [1995]):

Orientation	θ	ϕ	ω
[$\bar{1}11$]	-54.7356	45.0	0.
[$\bar{2}36$]	-31.0	33.7	0.

The simple compression and tension simulations were performed for the 4 different choices of the slip systems namely, 12, 24, 36 and 48, respectively. Henceforth, we shall refer to these cases by (12), (24), (36), and (48), respectively. The flow parameters for these

cases are identical to those used in Chapter 3 (see equations (3.2 and 3.4).

B.1 Simple Compression

The simple compression simulations were carried out at an axial strain rate of $0.001\,s^{-1}$ fo a final true strain of 1.0. The simulation were performed using the FEM package ABAQUS/Standard with a user subroutine for crystal plasticity developed at MIT by Anand and co-workers (Kalidindi *et al.* [1992]; Bronkhorst *et al.* [1992]). A single eight-noded ABAQUS - C3D8 element was used.

The slip system activity for the simple compression simulation in the orientation $[\bar{2}36]$ is presented in Fig. B-2. This figure shows the accumulated shear strains on the active slip systems as a function of the imposed axial strain. In the orientation $[\bar{2}36]$, the primary slip systems contain the slip direction [111], Fig. B-1(a). The slip planes are $(\bar{1}01)$ (slip system no. 2), $(2\bar{1}\bar{1})$ (slip system no. 13s) and $(\bar{3}12)$ (slip system no. 29), Table 3.1. The conjugate slip systems contain the slip direction $[\bar{1}\bar{1}1]$ and the slip plane normals are (011) (slip system no. 4), $(1\bar{2}\bar{1})$ (slip system no. 17s) and $(\bar{1}32)$ (slip system no. 32). At first, there is significant slip acitivity only on the primary slip systems during which the compression axis rotates on a great circle towards the slip plane normal $[\bar{1}01]$ until it reaches the $[001]-[\bar{1}11]$ boundary of the stereographic triangle around a strain of ~ 0.12 for the cases (12) and (24), Fig. B-3. As the slip activity on slip system 13s is very small in case (24), it does not affect the rotation of the compression axis. In addition to slip system no. 2 and 13s, slip system no. 29 also shows significant slip activity in case (48). Therefore, the compression axis rotates towards a direction that is a vector sum, weighted by the slip shears, of the slip plane normals $(\bar{1}01)$, $(2\bar{1}\bar{1})$ and $(\bar{3}12)$. The rate of rotation towards the $[001]-[\bar{1}11]$ boundary of the stereographic triangle is slower when compared to the case (12) and (24), reaching the boundary at a strain of ~ 0.2, Fig. B-2 and Fig. B-3. Once the compression axis reaches the $[001]-[\bar{1}11]$ boundary of the stereographic triangle, the shearing rates on the conjugate slip systems become significant. If the crystal were to slip only on the conjugate slip system, the compression axis would now rotate towards the conjugate slip plane normal. In the case (12), there is same slip rate on the primary slip system, 2, and the conjugate slip system, 4, the net result is a slow rotation of the compression axis along the $[001]-[\bar{1}11]$ boundary of the stereographic triangle towards

the limit orientation $[\bar{1}12]$ (which is the vector sum of $[\bar{1}01]$ and $[011]$), Fig. B-3. In the case (24), the conjugate slip systems are slip system no. 4 and 17s. The shear activity on the slip systems 13s and 17s begins to increase around a strain of ~ 0.8. As a result, the compression axis rotates beyond the orientation $[\bar{1}12]$ towards the stable orientation $[\bar{1}11]$. The compression axis rotates also rotates towards the orientation $[\bar{1}11]$ in the case (48) due to the similar reason, slip acitivity on slip systems 13s, 17s, 29 and 32 in addition to 2 and 4. However, the rate of rotation towards $[\bar{1}11]$ is much faster than case (24), Fig. B-3.

The change in the orientation of the crystal axis affects the stress-strain response. The stress-strain curves for the simple compression simulations with 12, 24 and 48 slip systems in the $[\bar{2}36]$ orientation are almost identical until the compression axis reaches the $[001]-[\bar{1}11]$ boundary, Fig. B-4. Note that the yield stress is slightly higher in case (12) when compared to case (24) and (d). Beyond this point, the stress-strain curves begin to diverge, being higher in case (24) and (d), due to the different rate and path of rotation of the compression axis.

The orientation $[\bar{1}11]$ belongs to 6 stereographic triangles of the [001] - [011] - [111] type, Fig. B-1(a). The primary slip systems belonging to each stereographic triangle will show significant slip activity in this orientation. There are 6, 9 and 15 slip systems with significant slip acitivity in the $[\bar{1}11]$ orientation in the simple compression simulation with 12, 24 and 48 slip systems,Fig. B-5. The slip activity on the slip systems of the same type, namely $\{2,3,4,6,10,11\}$ of the $\{110\} < 111 >$ type, $\{13s,17s,24s\}$ of the $\{112\} < 111 >$ type, and $\{29,30,32,34,43,45\}$ of the $\{123\} < 111 >$ type are equal (see Table 3.1). The orientation of the crystal does not change with axial strain for each of the different cases, (12), (24) or (48), Fig. B-6. However, there is a considerable softening effect on the stress-strain response, highest being the simulation with 12 slip systems and the lowest with 48 slip systems, Fig. B-7.

B.2 Simple Tension

In the compression simulations along the $[\bar{1}11]$ and $[\bar{2}36]$ directions, the slip systems with significant slip activitity on the on the $\{112\}$ planes were of the $\{112\} < 111 > s$ type, (13s, 17s, 24s) along the $[\bar{1}11]$ orientation, and (13s, 17s) along the $[\bar{2}36]$ orientation. To evaluate the influence of the asymmetry of slip on the $\{112\}$ planes, simple tension simulations were

performed along the $[\bar{2}36]$ and $[\bar{1}11]$ orientations so as to activate the slip systems of the $\{112\} < 111 > h$ type. The element was deformed in tension at an axial strain rate of $0.001\, s^{-1}$ fo a final true strain of 0.25.

The slip systems with significant slip acitivity in tension along the orientation $[\bar{2}36]$ are slip system no. 2 for case (12), slip system no. 2 and 13h for case (24), slip system no. 2 for case (36), and slip system no. 2 and 29 for case (48), Fig. B-8. The slip activity on the slip system 13h is negligible in the case (36) as the deformation resistance, s_0, is higher on this slip system when compared to the slip system 2. The change in the orientation of the tensile axis for the 4 cases is presented in Fig. B-9. The tensile axis rotates towards the slip direction [111]. The direction of the rotation of the tensile axis is towards the symmetry boundary [001] - [011] in comparison to the compression axis which rotates towards the symmetry boundary $[001] - [\bar{1}11]$. Due to identical slip activity, the tensile axis in the cases (a) and (c) rotate along the same path. The stress-strain response for the four cases are almost similar, Fig. B-10.

In tension, the orientation $[\bar{1}11]$ is unstable. The tensile axis for a crystal in this orientation could rotate in to one of the six stereographic triangles of the [001] - [011] - [111] type, Fig. B-1(a). Therfore, we perturbed this orientation by a degree so that it lies just inside the primary stereographic triangle [001] - [011] - $[\bar{1}11]$. The slip activity and the rotation of the tensile axis are shown in Figs. B-11 and B-12 respectively. Note that eventhough there is considerable slip activity on the slip system 13h in case (36), the rotation of the tensile axis is identical to that in case (12). The macroscopic stress-strain curves show softening due to the rotation of the tensile axis away from the hard orientation $[\bar{1}11]$. The yield stress of the crystal is the highest for the case (12) and is considerably lower for the cases (b) and (d) due to the availibility of a larger number of slip systems. However, the yield stress in case (36) is closer to that in (a) due to shearing on the hard slip system 13h.

B.3 Conclusions

From the simple compression and tension simulations on a single crystal, the following conclusions can be made :

1. Larger the number of available slip systems, lower is the yield stress. (See Figs. B-4, B-7, B-10 and B-13.)

2. The behavior of a crystal with the assumption of asymmetry of slip on the $\{112\}$ planes, case (36), is similar to that with only 12 slip systems, case (12). This can be seen in the predicted stress-strain response (Figs. B-10 and B-13) and the evolution of the tensile axis (Figs. B-9 and B-12).

3. Depending on the initial orientation, the rotation of the crystal axis in simple compression and tension can be slightly different with 12, 24 and 48 slip systems.

4. In f.c.c. crystals, the slip systems are of the $\{111\} < 110 >$ type. Hence, the behavior of the b.c.c. crystals in compression along the $[\bar{1}11]$ and $[\bar{2}36]$ orientation with the $\{110\} < 111 >$ type slip systems is qualitatively similar to that predicted for f.c.c. crystals in tension by Anand and Kothari [1996].

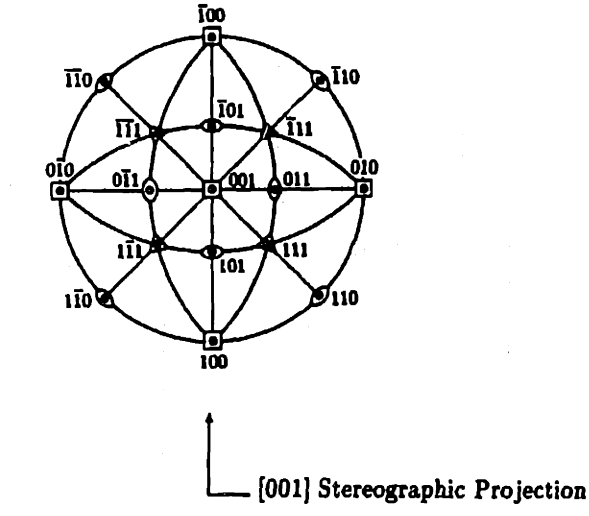

(a)

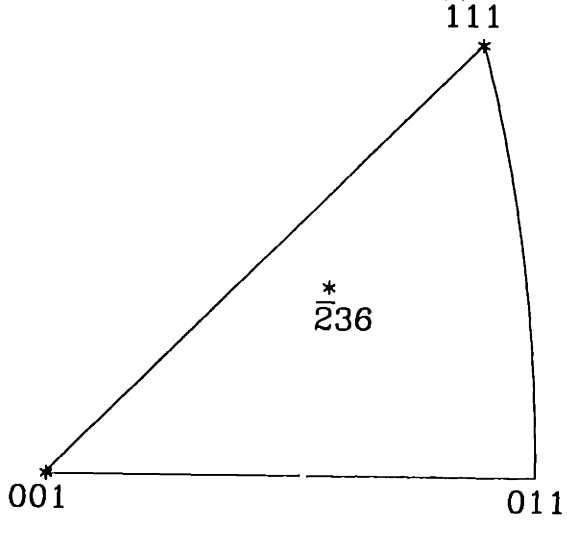

(b)

Figure B-1: (a) A [001] stereographic projection (Cullity [1978]). (b) Primary orientation triangle in a [001] steregraphic projection.

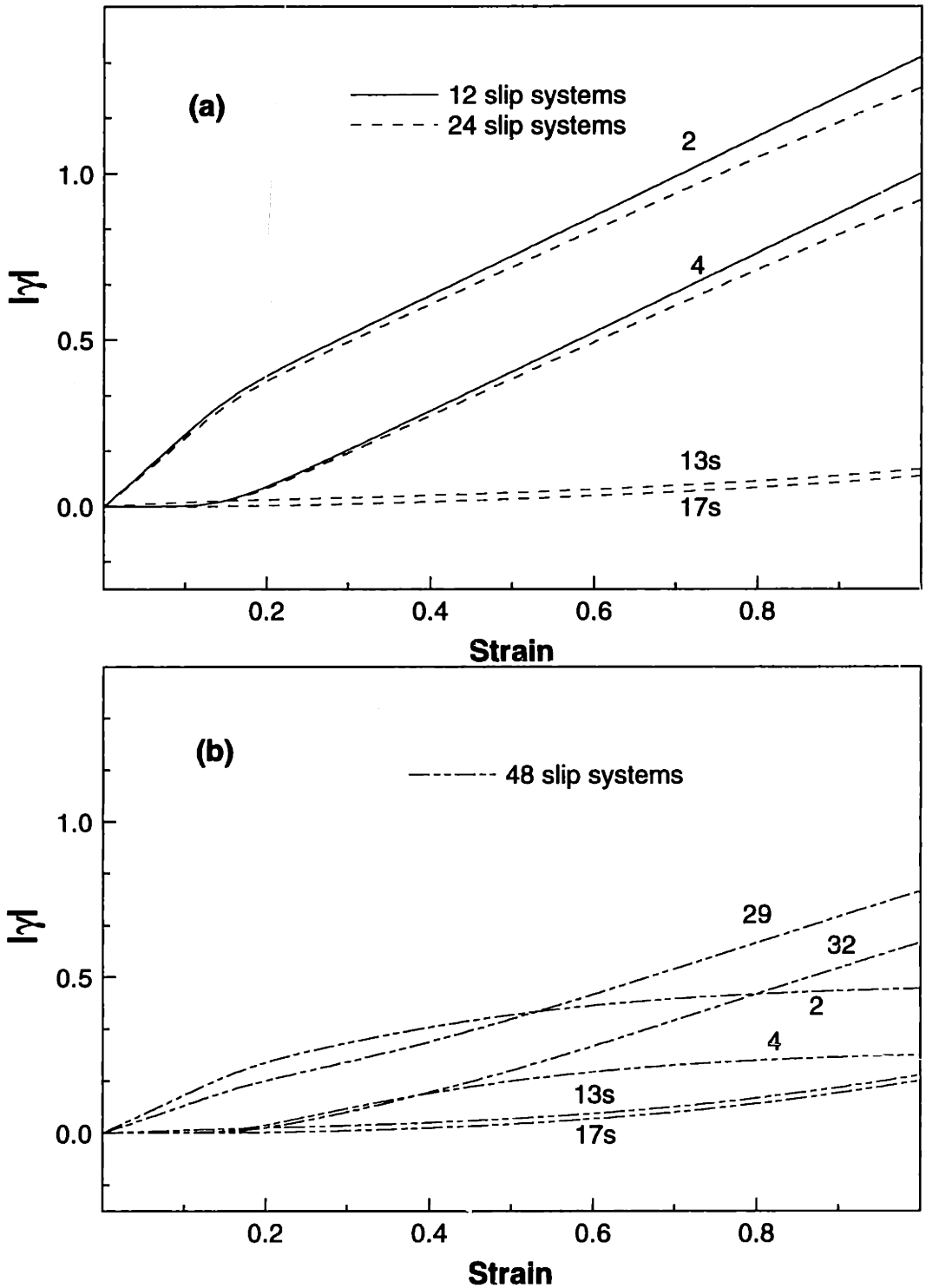

Figure B-2: The slip system activity in a simple compression simulation on a b.c.c. crystal initially oriented along the [$\bar{2}$36] direction with (a) 12 and 24 slip systems, and (b) 48 slip systems.

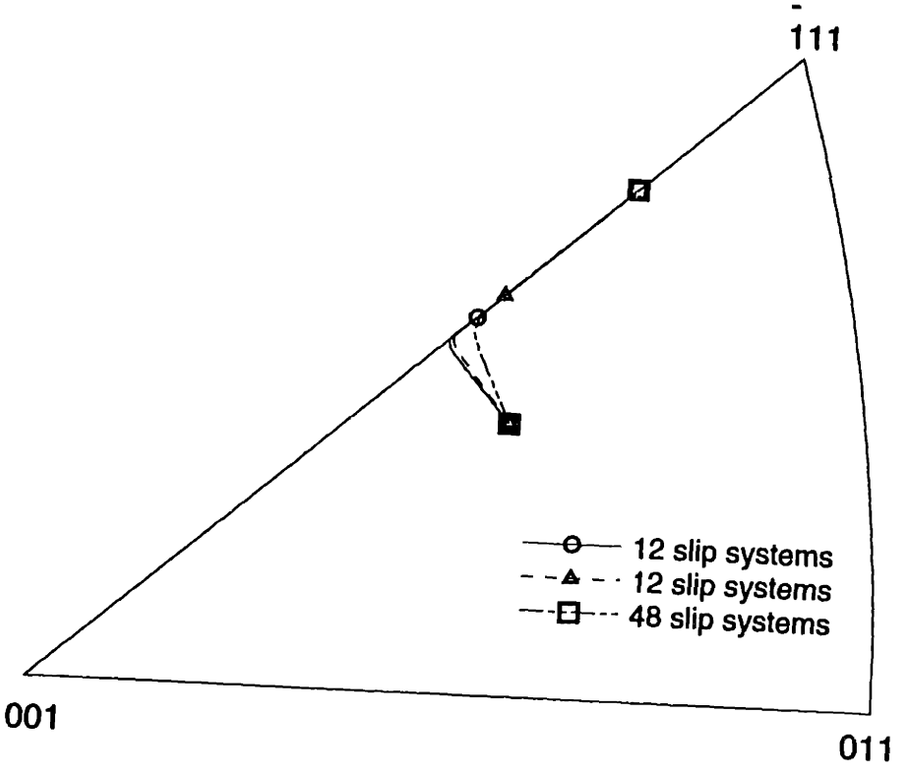

Figure B-3: The inverse pole figures for the change in the orientation of the compression axis in a simple compression simulation on a b.c.c. crystal initially oriented along the [$\bar{2}$36] direction. The symbols are plotted at the initial and the final orientation of the compression axis.

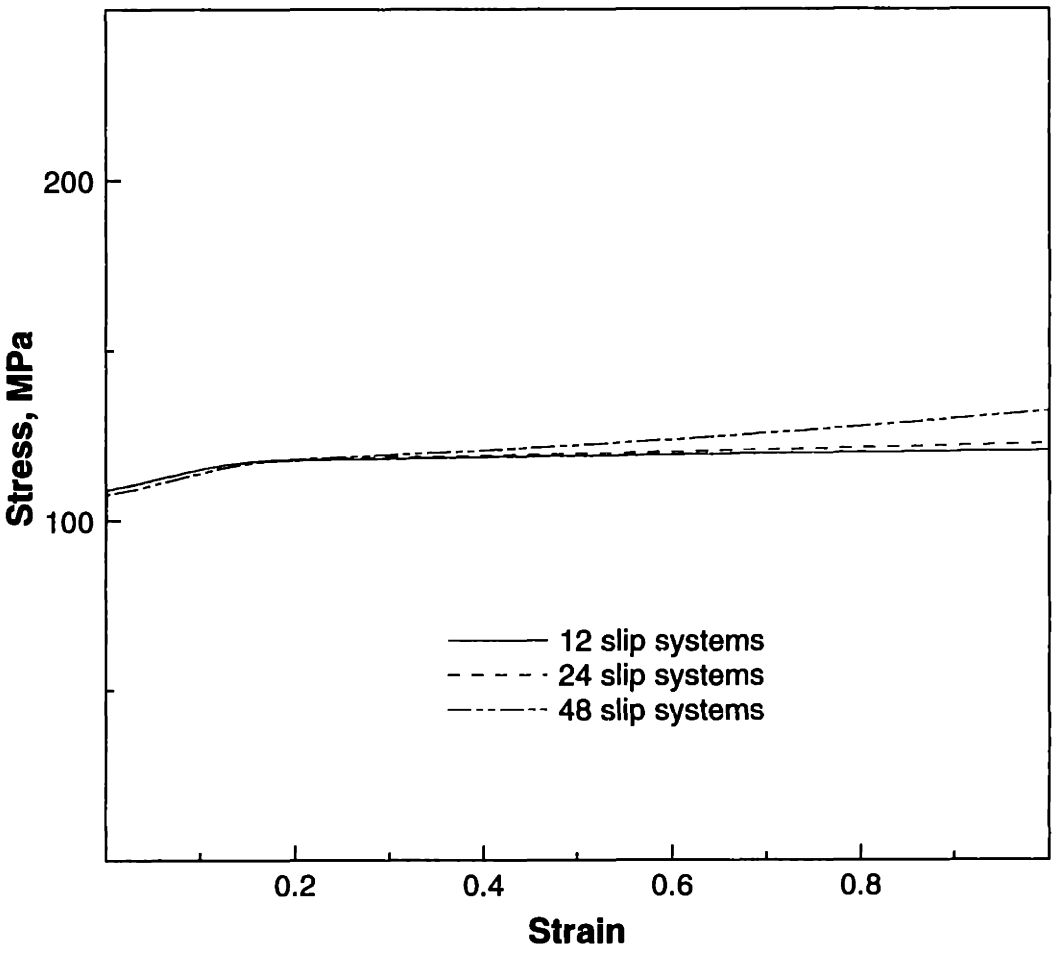

Figure B-4: The stress-strain response in a simple compression simulation on a b.c.c. crystal initially oriented along the $[\bar{2}36]$ direction.

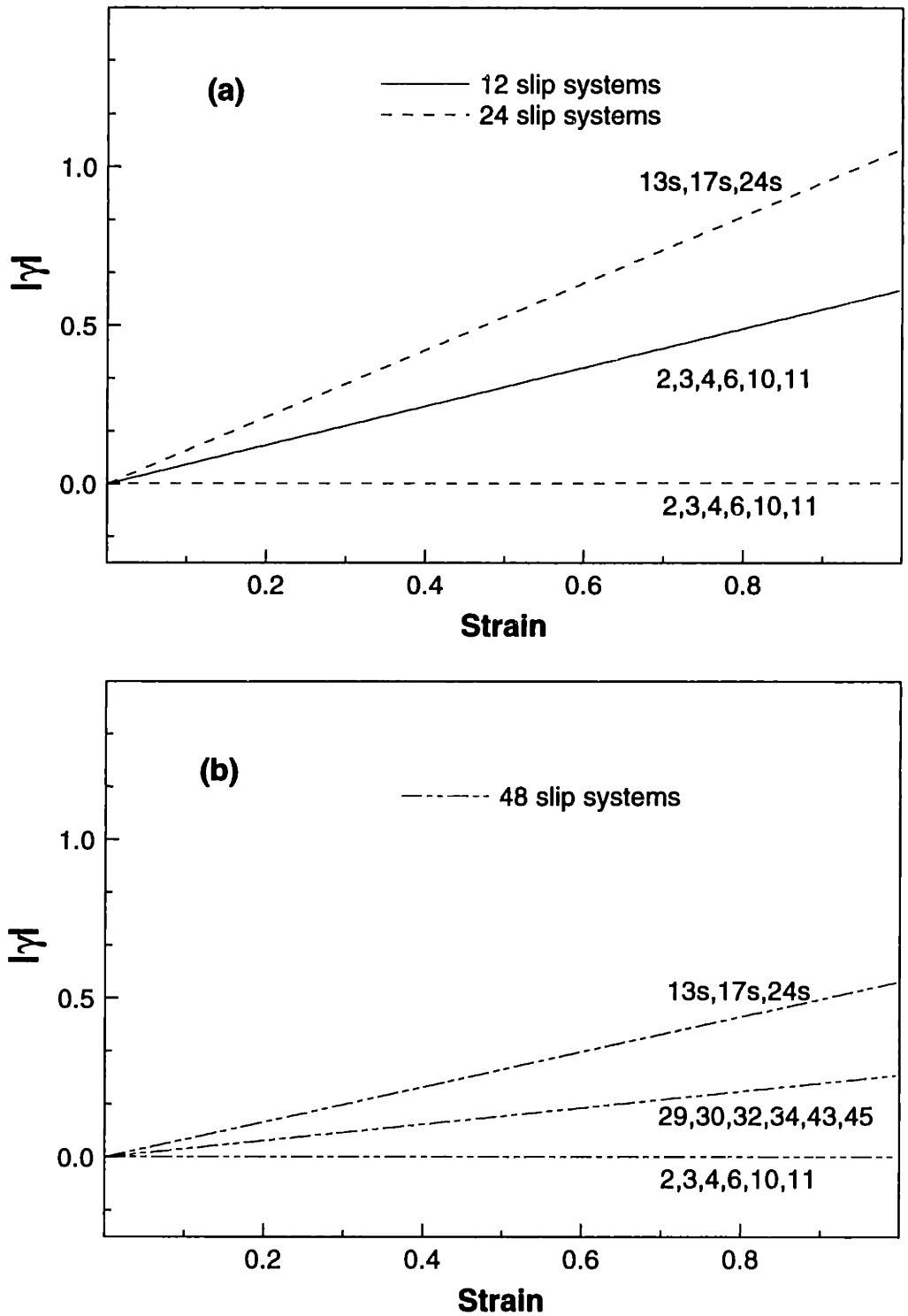

Figure B-5: The slip system activity in a simple compression simulation on a b.c.c. crystal initially oriented along the $[\bar{1}11]$ direction with (a) 12 and 24 possible slip systems, and (b) 48 possible slip systems.

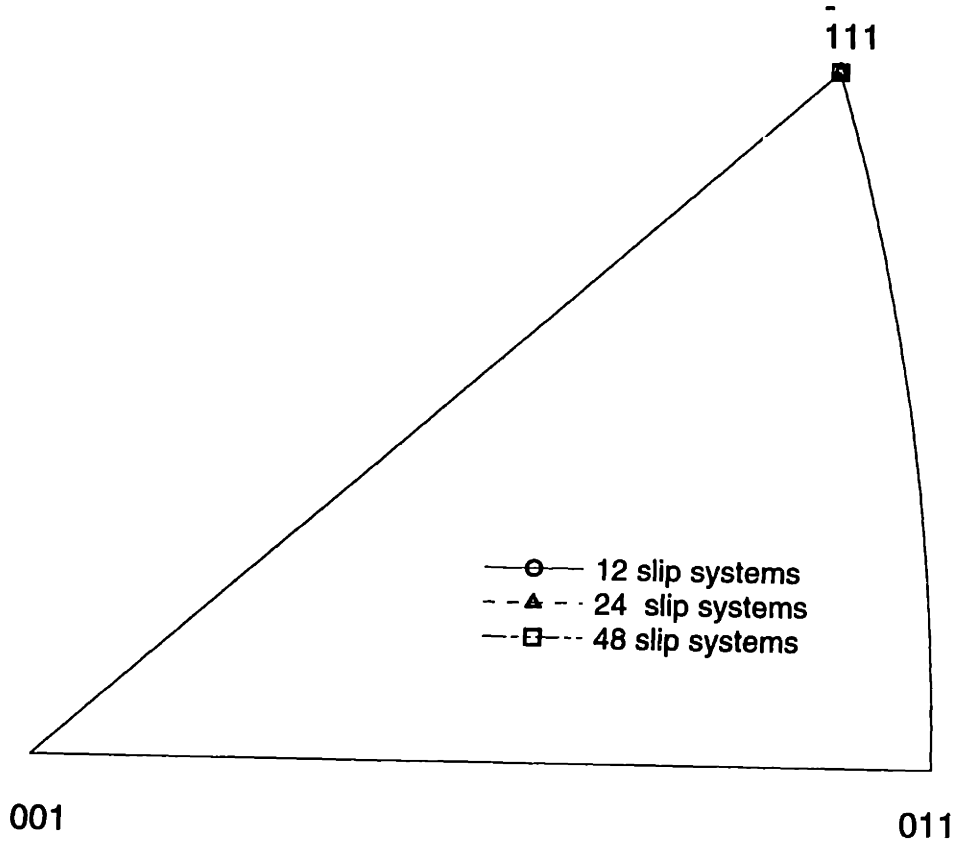

Figure B-6: The inverse pole figures for the change in the orientation of the compression axis in a simple compression simulation on a b.c.c. crystal initially oriented along the [$\bar{1}$11] direction. The symbols are plotted at the initial and the final orientation of the compression axis. For this case, the initial and the final orientations are identical.

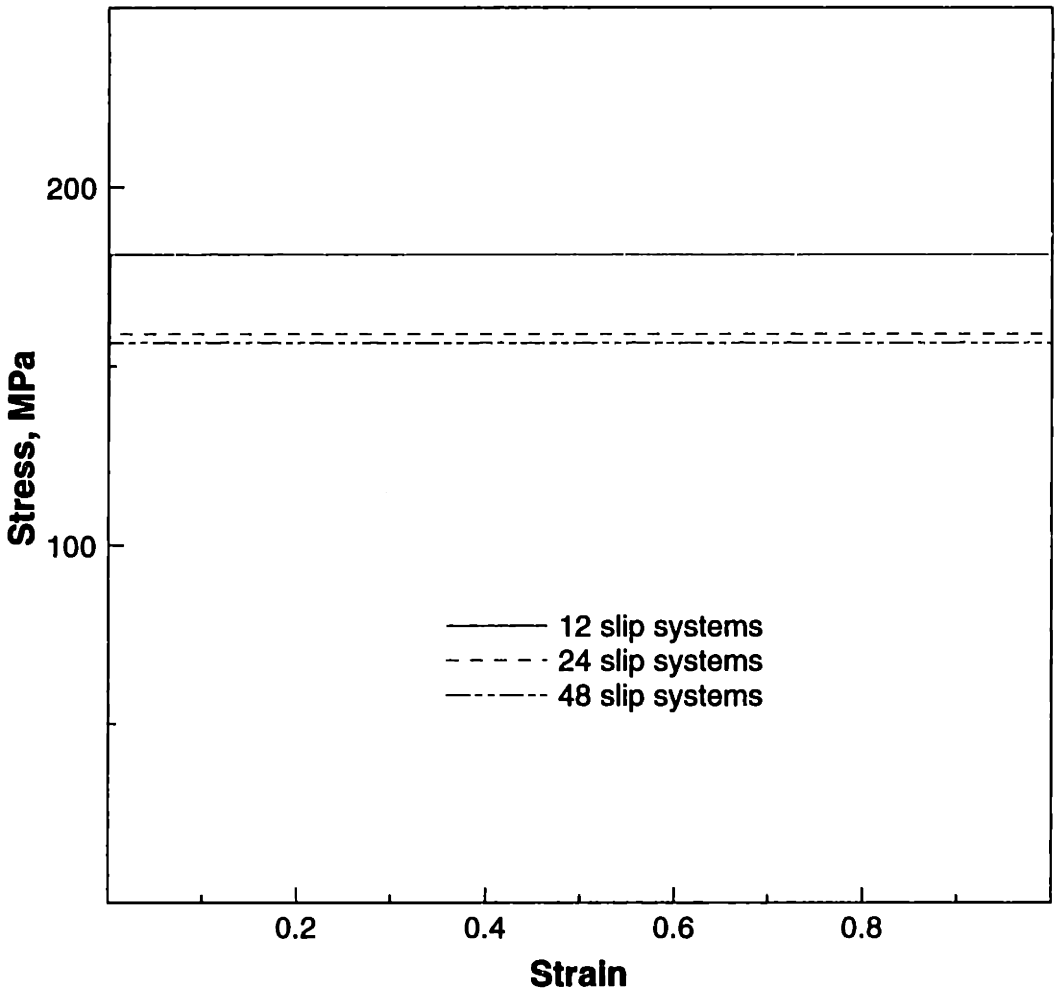

Figure B-7: The stress-strain response in a simple compression simulation on a b.c.c. crystal initially oriented along the $[\bar{1}11]$ direction.

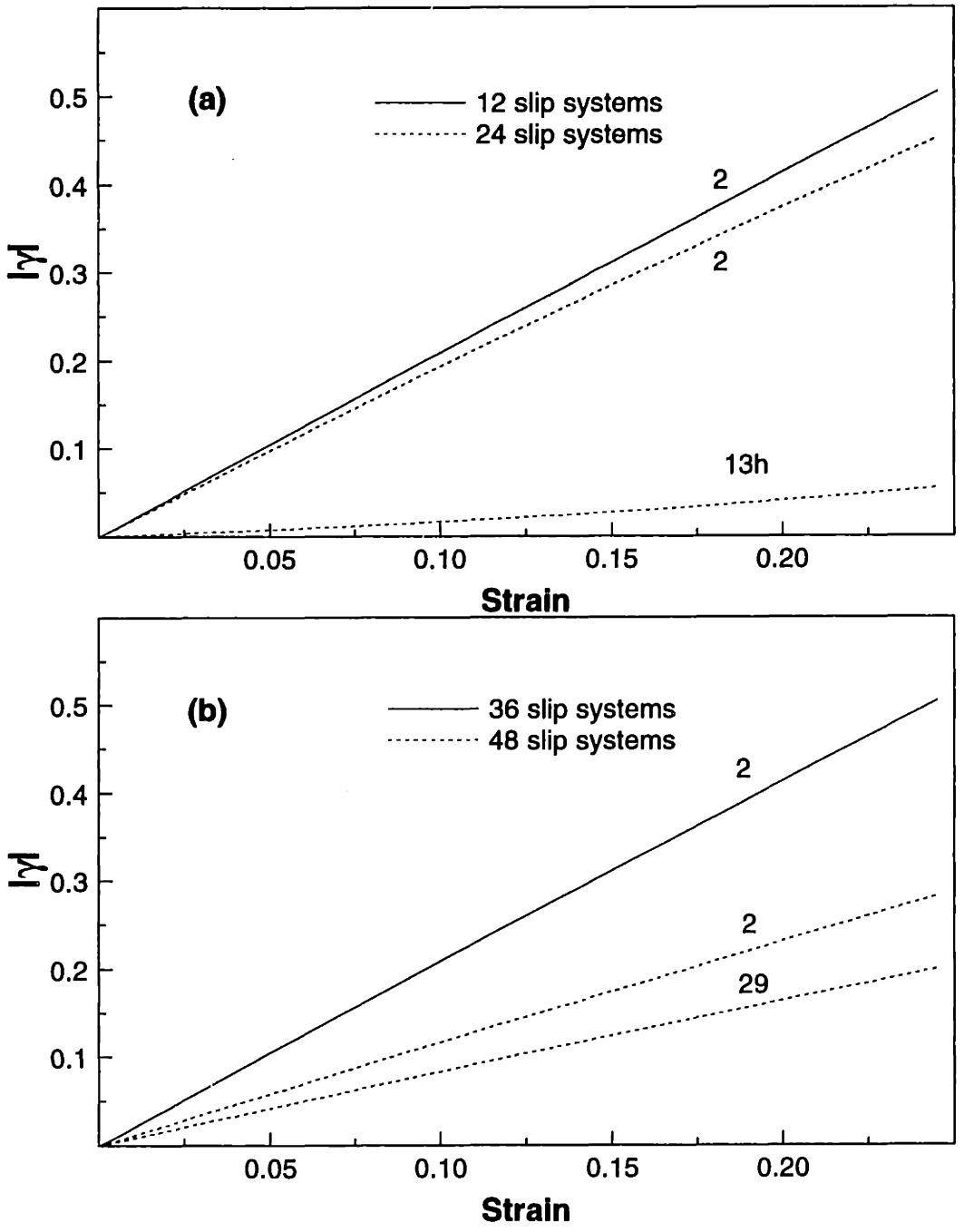

Figure B-8: The slip system activity in a simple tension simulation on a b.c.c. crystal initially oriented along the [$\bar{2}$36] direction with (a) 12 and 24 slip systems, and (b) 36 and 48 slip systems.

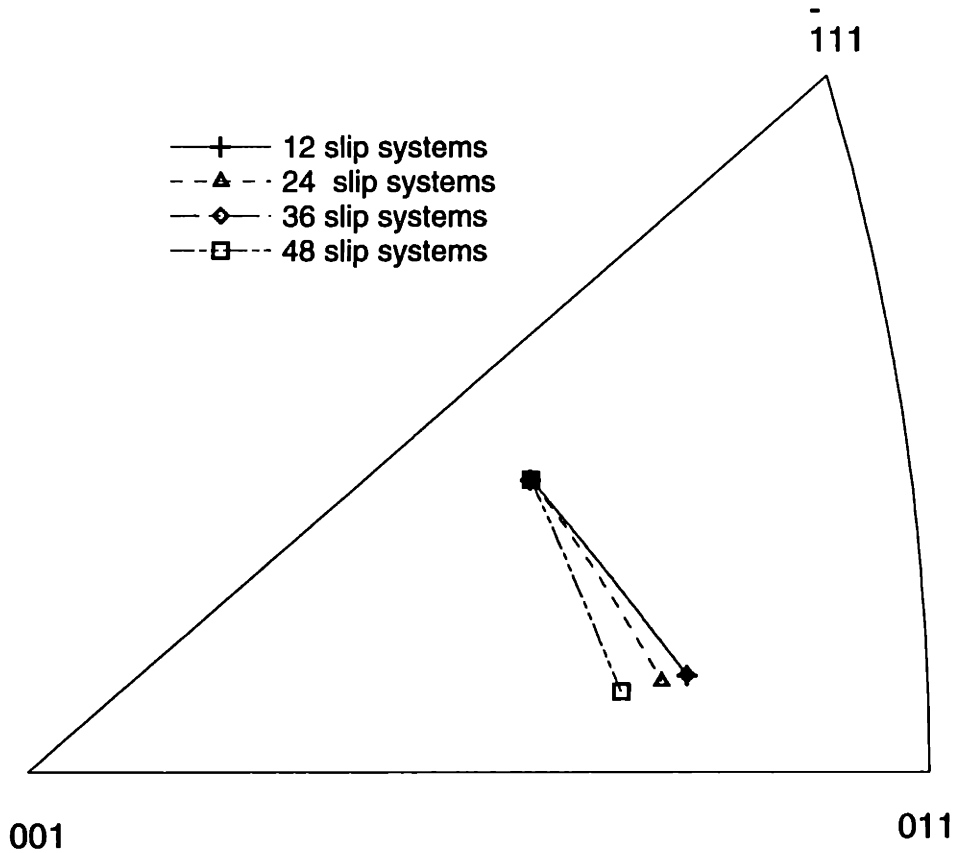

Figure B-9: The inverse pole figures for the change in the orientation of the tensile axis in a simple tension simulation on a b.c.c. crystal initially oriented along the $[\bar{2}36]$ direction. The symbols are plotted at the initial and the final orientation of the tensile axis.

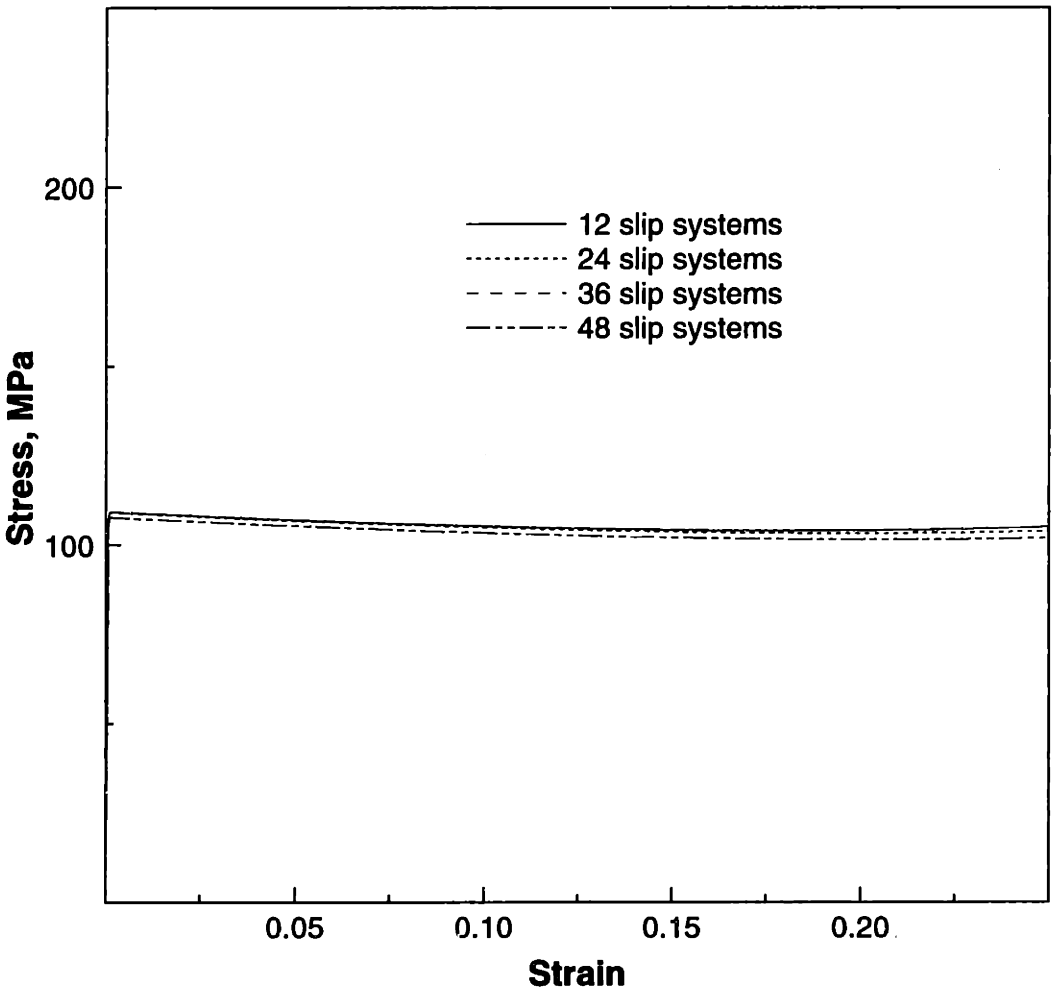

Figure B-10: The stress-strain response in a simple tension simulation on a b.c.c. crystal initially oriented along the $[\bar{2}36]$ direction.

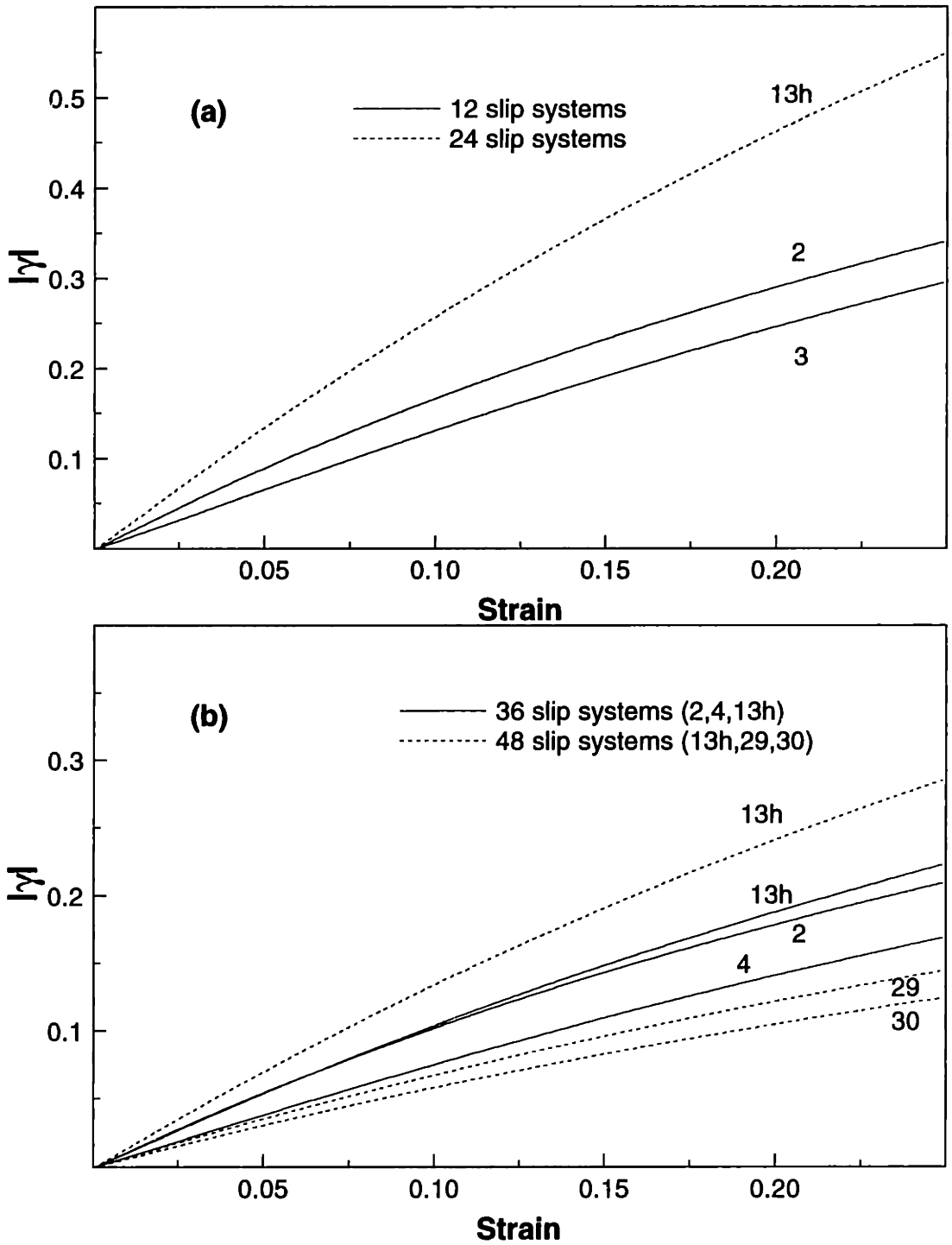

Figure B-11: The slip system activity in a simple tension simulation on a b.c.c. crystal initially oriented along the $[\bar{1}11]$ direction with (a) 12 and 24 slip systems, and (b) 36 and 48 slip systems.

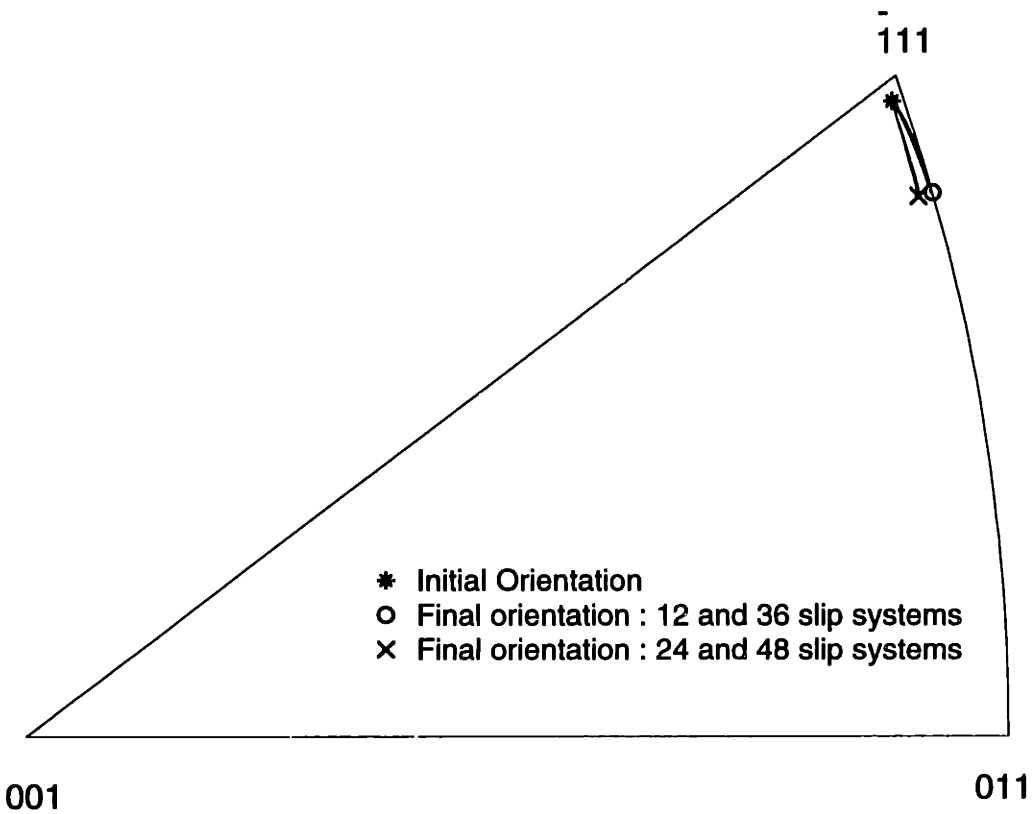

Figure B-12: The inverse pole figures for the change in the orientation of the tensile axis in a simple tensile simulation on a b.c.c. crystal initially oriented along the [$\bar{1}$11] direction. The symbols are plotted at the initial and the final orientation of the tensile axis.

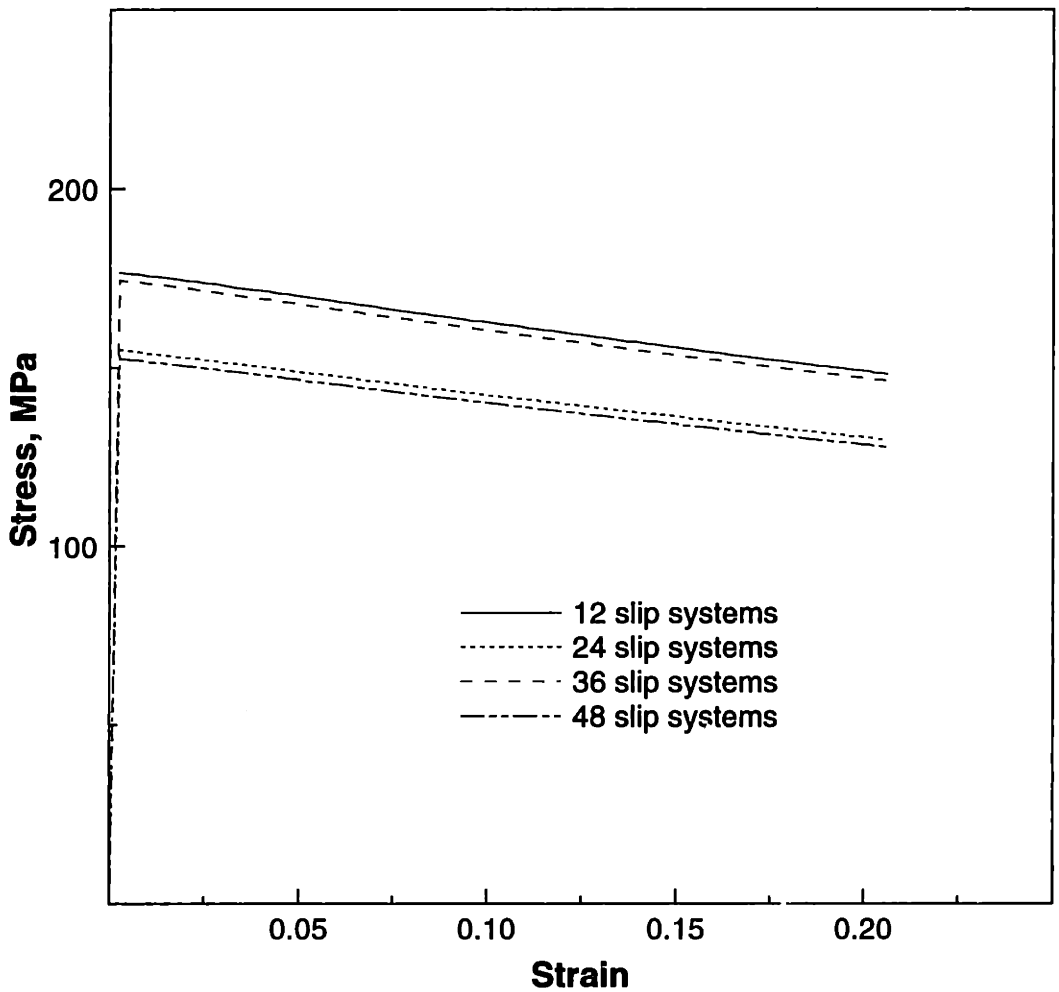

Figure B-13: The stress-strain response in a simple tension simulation on a b.c.c. crystal initially oriented along the $[\bar{1}11]$ direction.

Bibliography

[ABAQUS, 1994] Hibbit , Karlsson & Sorenson, Inc., Providence, R.I. *ABAQUS Reference Manuals*, 1994.

[Allan, 1995] C. D. Allan. *Plasticity of Nickel Based Single Crystal Super Alloys.* PhD thesis, Massachusetts Institute of Technology, February 1995.

[Anand and Kalidindi, 1994] L. Anand and S.R. Kalidindi. The process of shear band formation in plane strain compression of fcc metals: effects of crystallographic texture. *Mechanics of Materials*, 17:223–243, 1994.

[Anand and Kothari, 1996] L. Anand and M. Kothari. A computational procedure for rate-independent crystal plasticity. *Journal of the Mechanics and Physics of Solids*, 44:525–558, 1996.

[Argon, 1995] A.S. Argon. Mechanical Properties of Single Phase Crystalline Media: Deformation at Low Temperatures. In R.W. Cahn and P. Hassen, editors, *Physical Metallurgy.* Elsevier, Amsterdam, 1995.

[Asaro and Needleman, 1985] R.J. Asaro and A. Needleman. Texture development and strain hardening in rate dependent polycrystals. *Acta Metallurgica*, 33:923–953, 1985.

[Asaro and Rice, 1977] R.J. Asaro and J.R. Rice. Strain localisation in ductile single crystals. *Journal of the Mechanics and Physics of Solids*, 25:309–338, 1977.

[Asaro, 1983a] R.J. Asaro. Crystal plasticity. *ASME Journal of Applied Mechanics*, 50:921–934, 1983.

[Asaro, 1983b] R.J. Asaro. Micromechanics of crystals and polycrystals. *Advances in Applied Mechanics*, 23:1–115, 1983.

[Balasubramanian and Anand, 1996] S. Balasubramanian and L. Anand. Single crystal and polycrystal elasto-viscoplasticity: Application to earing in cup drawing of F.C.C. materials. *Computational Mechanics*, 17:209–225, 1996.

[Balasubramanian and Anand, 1997] S. Balasubramanian and L. Anand. Polycrystalline Plasticity: Application to Earing in Cup Drawing of Al2008-T4 Sheet. *Submitted to Journal of Applied Mechanics*, 1997.

[Barrett *et al.*, 1937] C.S. Barrett, G. Ansel, and R.F. Mehl. *Transactions of A.I.M.E.*, 127:516, 1937.

[Bassani, 1993] J.L. Bassani. Plastic flow of crystals. *Advances in Applied Mechanics*, 30:191–258, 1993.

[Beaudoin *et al.*, 1994] A.J. Beaudoin, P.R. Dawson, K.K. Mathur, U.F. Kocks, and D.A. Korzekwa. Application of Polycrystalline Plasticity to Sheet Forming. *Computer Methods in Applied Mechanics and Engineering*, 117:49–70, 1994.

[Bechtold, 1955] J.H. Bechtold. Tensile Properties of Annealed Tantalum at Low Temperatures. *Acta Metallurgica*, 3:249–254, 1955.

[Becker *et al.*, 1993] R. Becker, R.E. Smelser, and S. Panchanadeeswaran. Simulations of Earing in Aluminum Single Crystals and Polycrystals. *Modeling and Simulations in Materials Science and Engineering*, 1:203–224, 1993.

[Bishop and Hill, 1951a] J.F.W. Bishop and R. Hill. A theoretical derivation of the plastic properties of a polycrystalline face-centered cubic metal. *Philosophical Magazine*, 42:1298–1307, 1951.

[Bishop and Hill, 1951b] J.F.W. Bishop and R. Hill. A theory of plastic distortion of a polycrystalline aggregate under combined stresses. *Philosophical Magazine*, 42:414–427, 1951.

[Bolling and Richman, 1965] G.F. Bolling and R.H. Richman. Continual mechanical twinning. *Acta Metallurgica*, 13:745–757, 1965.

[Bronkhorst *et al.*, 1992] C.A. Bronkhorst, S.R. Kalidindi, and L. Anand. Polycrystalline plasticity and the evolution of crystallographic texture in fcc metals. *Philosophical transactions of the Royal Society of London A*, 341:443–477, 1992.

[Brown *et al.*, 1989] S. Brown, K. Kim, and L. Anand. An Internal Variable Constitutive Model for Hot Working of Metals. *International Journal of Plasticity*, 5:95–130, 1989.

[Carpay *et al.*, 1975] F.M.A Carpay, G.Y Chin, S. Mahajan, and J.J Rubin. Constrained Deformation of Molybdenum Single Crystals. *Acta Metallurgica*, 23:1473–1478, 1975.

[Chen and Gray, 1996] S.R. Chen and G.T. Gray. Constitutive Behavior of Tantalum and Tantalum-Tungsten Alloys. *Metallurgical and Materials Transactions A*, 27A:2994–3006, 1996.

[Chin and Mammel, 1967] G.Y. Chin and W.L. Mammel. Computer solutions of the taylor analysis for axisymmetric flow. *Transactions of the Metallurgical society of AIME*, 239:1400–1405, 1967.

[Chin, 1972] G.Y. Chin. Competition among {110}, {112}, and {123} $<$ 111 $>$ slip modes in bcc metals. *Metallurgical Transactions*, 3:2213–2216, 1972.

[Christian, 1970] J.W. Christian. Plastic deformation of bcc metals. *Proceedings of the 2nd International Conference on Strength of Metals and Alloys*, 1:29–70, 1970.

[Conrad, 1964] H. Conrad. Thermally Activated Deformation of Metals. *Journal of Metals*, pages 582–588, 1964.

[Cullity, 1978] B.D. Cullity. *ELEMENTS OF X-RAY DIFFRACTION.* Addison-Wesley Publishing Company, Inc, 2nd edition, 1978.

[Dawson *et al.*, 1994] P.R. Dawson, A.J. Beaudoin, and K.K. Mathur. Finite Element Modeling of Polycrystalline Solids. In S.I. Andersen, J.B. Bilde-Soremsem, T. Lorentzen, O.B. Pedersen, and N.J. Sorensen, editors, *Proceedings of the 15th RISO International Symposium on Materials Science*, pages 33–43. Springer-Verlag, 1994.

[Duesbery *et al.*, 1973] M.S. Duesbery, V. Vitek, and D.K. Brown. The effect of shear stress on the screw dislocation core structure in body-centered cubic lattices. *Proceedings of the Royal Society of London, A*, 332:85–111, 1973.

[Duprey and Clifton, 1994] K. Duprey and R.J. Clifton. Plastic Flow of Tantalum at High Strain Rates. In A. Bose and R.J. Dowding, editors, *Proceedings of the 2nd International Conference on Tungsten and Refractory Metals.* 1994.

[Franciosi, 1983] P. Franciosi. Glide mechanisms in b.c.c. crystals: An investigation of the case of α-iron through multislip and latent hardening tests. *Acta Metallurgica*, 31:1331–1342, 1983.

[Frost and Ashby, 1982] H.J. Frost and M.F. Ashby. *Deformation Mechanism Maps.* Pergamon Press, New York, 1982.

[Gilbert *et al.*, 1962] A. Gilbert, D. Hull, W.S. Owen, and C.N. Reid. The Yield of Polycrystalline Tantalum. *Jorunal of the Less-Common Metals*, 4:399–408, 1962.

[Goodman and Hu, 1970] S.R. Goodman and H. Hu. Effect of Hot-Rolling Texture on the Plastic Strain Ratio of Low-Carbon Steels. *Metallurgical Transactions*, 1:1629–1640, 1970.

[Gray III and Rollet, 1992] G.T. Gray III and A.D. Rollet. The High Strain Rate and Spallation Response of Tantalum, Ta-10W and T-111. In R. Asfahani, E. Chen, and A. Crowson, editors, *High Strain Rate Behavior of Refractory Metals and Alloys*, pages 303–315. 1992.

[Havner, 1992] K.S. Havner. *Finite Plastic Deformation of Crystalline Solids.* Cambridge University Press, 1st edition, 1992.

[Hill and Rice, 1972] R. Hill and J.R. Rice. Constitutive analysis of elastic-plastic crystals at arbitrary strain. *Journal of the Mechanics and Physics of Solids*, 20:401–413, 1972.

[Hoge and Mukherjee, 1977] K.G. Hoge and A.K. Mukherjee. The Temperature and Strain Rate Dependence of the Flow Stress of Tantalum. *Journal of Material Science*, 12:1666–1672, 1977.

[Hosford and Caddell, 1993] W.F. Hosford and R.M. Caddell. *Metal Forming: Mechanics and Metallurgy.* Prentice Hall, 2nd edition, 1993.

[Hu, 1978] H. Hu. Mechanisms of recrystallization texture formation in deep-drawing steels. In G. Gottstein and K. Lucke, editors, *Proceedings of the Fifth International Conference on Textures of Materials* , pages 3–20. Springer-Verlag, 1978.

[Hull and Bacon, 1984] D. Hull and D.J. Bacon. *Introduction to Dislocations.* Pergamon Press, New York, 3 edition, 1984.

[Inagaki, 1991] H. Inagaki. Basic Earing Behavior of fcc and bcc Metals in Cup Drawing. *Zeitschrift Für Metallkunde*, 82:361–372, 1991.

[Kalidindi *et al.*, 1992] S.R. Kalidindi, C.A. Bronkhorst, and L. Anand. Crystallographic texture evolution in bulk deformation processing of fcc metals. *Journal of the Mechanics and Physics of Solids*, 40:536–569, 1992.

[Kalidindi, 1992] S. R. Kalidindi. *Polycrystal Plasticity: Constitutive Modeling and Deformation Processing.* PhD thesis, Massachusetts Institute of Technology, June 1992.

[Kallend *et al.*, 1994] J.S. Kallend, U.F. Kocks, A.D. Rollett, and J.R. Wenk. popLA: the Preferred Orientation Package from Los Alamos. 1994.

[Kanetake, 1991] N. Kanetake. Quantitative Application of Texture Data to Sheet Metal Forming. *Textures and Microstructures*, 14-18:1001–1006, 1991.

[Kocks *et al.*, 1975] U.F. Kocks, A.S. Argon, and M.F. Ashby. Thermodynamics and Kinetics of Slip. In *Progress in Material Science.* Pergamon Press, London, 1975.

[Krausz and Eyring, 1975] A.S. Krausz and H.E. Eyring. *Deformation Kinetics.* Wiley, New York, 1975.

[Lee, 1983] C.G.Y. Lee. Closed Loop Control of Sheet Metal Stability During Forming. Master's thesis, Massachusetts Institute of Technology, 1983.

[Leslie, 1972] W.C. Leslie. Iron and Its Dilute Substitutional Solid Solutions. *Metallurgical Transactions*, 3:5–26, 1972.

[Lucke and Holscher, 1991] K. Lucke and M. Holscher. Rolling and Recrystallization Textures of BCC Steels. *Textures and Microstructures*, 14-18:585–596, 1991.

[Mandel, 1974] J. Mandel. Thermodynamics and Plasticity. In D. Domingos, J.J. Nina, M. N.R, and J.H Whitlaw, editors, *Proceedings of the International Symposium on Foundations of Continuum Thermodynamics*, page 283. McMillan, London, 1974.

[Mathur and Dawson, 1989] K.K. Mathur and P.R. Dawson. On Modeling the Development of Crystallographic Texture in Bulk Forming Processes. *International Journal of Plasticity*, 5:67–94, 1989.

[Mathur and Dawson, 1990] K.K. Mathur and P.R. Dawson. Texture Development During Wire Drawing. *ASME Journal of Engineering Materials and Technology*, 112:292–297, 1990.

[Meyers *et al.*, 1995] M.A. Meyers, Y.J. Chen, F.D.S. Marquis, and D.S. Kim. High-Strain, High Strain-Rate Behavior of Tantalum. *Metallurgical and Materials Transactions A*, 26A:2493–2501, 1995.

[Meyers, 1994] M.A. Meyers. *Dynamic Behavior of Materials.* John Wiley & Sons, New York, 1994.

[Mitchell and Spitzig, 1965] T.E. Mitchell and W.A. Spitzig. Three-Stage Hardening in Tantalum Single Crystals. *Acta Metallurgica*, 12:1169–1179, 1965.

[Mordike and Rudolf, 1967] B.L. Mordike and G. Rudolf. Three-Stage Hardening in Tantalum Deformed in Compression. *Journal of Material Science*, 2:332–338, 1967.

[Nemat-Nasser and Isaacs, 1996] S. Nemat-Nasser and J.B. Isaacs. Direct Measurement of Isothermal Flow Stress of Metals at Elevated Temperatures and High Strain Rates with Application to Ta and Ta-W Alloys. In *Internal Report, Center of Excellence for Advanced Materials.* UCSD, San Diego, 1996.

[Nemat-Nasser *et al.*, 1994] S. Nemat-Nasser, Y.F. Li, and J.B. Isaacs. Experimental/computational evaluation of flow stress at high strain rates with application to adiabatic shear banding. *Mechanics of Materials*, 17:111–134, 1994.

[Orowan, 1940] E. Orowan. Problems of plastic gliding. *Philosophical transactions of the Royal Society of London A*, 52:8–22, 1940.

[Peirce *et al.*, 1982] D. Peirce, R.J. Asaro, and A. Needleman. An analysis of nonuniform and localized deformation in ductile single crystals. *Acta Metallurgica*, 30:1087–1119, 1982.

[Piehler and Backofen, 1971] H.R. Piehler and W.A. Backofen. A theoretical examination of the plastic properties of b.c.c. crystals deforming by $< 111 >$ pencil glide. *Metallurgical Transactions*, 2:249–280, 1971.

[Qiang *et al.*, 1993] N. Qiang, P. Niessen, and R.J. Pick. Dynamic-loading-induced damage in tantalum and Armco iron. *Materials Science and Engineering*, 160A:49–56, 1993.

[Qiang, 1993] N. Qiang. *Numerical and Experimental Simulation of Adiabatic Shear Localization in Tantalum and Armco Iron.* PhD thesis, University of Waterloo, 1993.

[Rajendran and Garrett Jr., 1992] A.M. Rajendran and R.K. Garrett Jr. Effects of Texture and Strain rate on Flow and Fracture in Pure Tantalum. In R. Asfahani, E. Chen, and A. Crowson, editors, *High Strain Rate Behavior of Refractory Metals and Alloys*, pages 289–302. 1992.

[Reid, 1981] C.N. Reid. The Association of Twinning and Fracture in bcc Metals. *Metallurgical Transactions A*, 12A:371–377, 1981.

[Rice, 1971] J.R. Rice. Inelastic constitutive relations for solids: An internal variable theory and its application to metal plasticity. *Journal of the Mechanics and Physics of Solids*, 19:433–455, 1971.

[Royer *et al.*, 1991] F. Royer, A. Nadari, F. Yala, P. Lipinski, D. Ceccaldi, M. Berveiller, and P. Pennelle. Plastic Deformation of BCC Polycrystals: Comparison Between Experimental Datas and Results of Several Modelling Codes. *Textures and Microstructures*, 14-18:1129–1134, 1991.

[Sachs, 1928] G. Sachs. *Z. Verein Duet. Ing.*, 72:734, 1928.

[Simmons and Wang, 1971] G. Simmons and H. Wang. *Single Crystal Elastic Constants and Calculated Aggregate Properties.* The M.I.T Press, Cambridge, 1971.

[Staroselsky and Anand, 1997] A. Staroselsky and L. Anand. Inelastic deformation of f.c.c. materials by slip and twinning. *Submitted to Journal of the Mechanics and Physics of Solids*, 1997.

[Taylor, 1938a] G.I. Taylor. Analysis Of Plastic Strain In A Cubic Crystal. In *Stephen Timoshenko 60th Anniversary Volume*, pages 218–224. McMillan, New York, 1938.

[Taylor, 1938b] G.I. Taylor. Plastic Strain in Metals. *Journal of the Institute of Metals*, 62:307–324, 1938.

[Taylor, 1948] G.I. Taylor. The use of flat-ended projectiles for determining dynamic yield stress. *Proceedings of the royal society of London*, 194:289–299, 1948.

[Teodosiu and Sidoroff, 1976] C. Teodosiu and F. Sidoroff. A theory of finite elastoviscoplasticity of single crystals. *International Journal of Engineering Science*, 14:165–176, 1976.

[Teodosiu, 1970] C. Teodosiu. A dynamic theory of dislocations and its applications to the theory of the elastic-plastic continuum. In R. Simmons J.A., de Wit and R. Bullough, editors, *Proceedings of the Conference on Fundamental Aspects of Dislocation Theory*, page 837. 1970.

[Ting, 1992] Chang-Sheng Ting. Constitutive Modeling of Tantalum Dynamic Plasticity based on the Theory of Thermal Activation and the Evolution of Strain Hardening. In R. Asfahani, E. Chen, and A. Crowson, editors, *High Strain Rate Behavior of Refractory Metals and Alloys*, pages 249–265. 1992.

[Tucker, 1961] G.E.G. Tucker. Texture and Earing in Deep Drawing of Aluminum. *Acta Metallurgica*, 9:275–286, 1961.

[Underwood, 1961] F.A. Underwood. *Textures in Metal Sheets.* Macdonald, London, 1961.

[Van Houtte, 1978] P. Van Houtte. Influence of the critical shear stress ratio of {112} and {110} slip planes on the rolling texture of bcc metals. In G. Gottstein and K. Lucke, editors, *Proceedings of the Fifth International Conference on Textures of Materials* , pages 347–356. Springer-Verlag, 1978.

[Vecchio, 1994] K.S. Vecchio. High-Strain, High Strain-Rate Deformation of Tantalum and Tantalum-Tungsten Alloys. *Supplement J. de. Physique III*, 4:301–306, 1994.

[Vitek, 1976] V. Vitek. Computer simulation of the screw dislocation motion in b.c.c. metals under the effect of the external shear and uniaxial stresses. *Proceedings of the Royal Society of London, A*, 352:109–124, 1976.

[Wagner *et al.*, 1991] F. Wagner, G. Canova, P. Van Houtte, and M. Molinari. Comparisons of Simulated and Experimental Deformation Textures For BCC Metals. *Textures and Microstructures*, 14-18:1135–1140, 1991.

[Weber *et al.*, 1989] G. Weber, A.M. Lush, A. Zavaliangos, and L. Anand. An objective time-integration procedure for isotropic rate-independent and rate-dependent elastic-plastic constitutive relations. *International Journal of Plasticity*, 6:95–130, 1989.

[White *et al.*, 1990] C.S. White, C.A. Bronkhorst, and L. Anand. An improved isotropic-kinematic hardening model for moderate deformation metal plasticity. *Mechanics of Materials*, 10:127–147, 1990.

[White, 1992] C.S. White. An analysis of the thin-walled torsion specimen. *Journal of Engineering Materials and Technology*, 114:384–389, 1992.

[Wilson and Butler, 1961] D.V. Wilson and R.D. Butler. The Role of Cup-Drawing Tests in Measuring Drawability. *Journal of the Institute of Metals*, 90:473–483, 1961.

[Zerilli and Armstrong, 1987] F.J. Zerilli and R.W. Armstrong. Dislocation-Mechanics-Based Constitutive Relations for Material Dynamics Calculations. *Journal of Applied Physics*, 61:1816–1825, 1987.

[Zerilli and Armstrong, 1990] F.J. Zerilli and R.W. Armstrong. Description of Tantalum Deformation Behavior by Dislocation Mechanics Based Constitutive Relations. *Journal of Applied Physics*, 68:1580–1591, 1990.